Study of Intrinsically Curved Elastic Rods Under External Loads with Applications to Concentric Tube Continuum Robots and their Control

Dissertation

zur Erlangung des Grades eines Doktors der Naturwissenschaften
(Dr. rer. nat.)

am Fachbereich Mathematik und Informatik
der Freien Universität Berlin

vorgelegt von

SIVA PRASAD CHAKRI DHANAKOTI

Berlin, 2023

Betreuer/Erstgutachter:	Prof. Dr. Christof Schütte Professor Department of Mathematics and Computer Science Freie Universität Berlin Room 132, Arnimalle 6 Berlin 14195
Zweitgutachter:	Prof. Dr. John H. Maddocks Professor Emeritus Institute of Mathematics École Polytechnique Fédérale de Lausanne MA C1 582 (Bâtiment MA) Station 8 CH-1015 Lausanne
Tag der Disputation:	05/09/2023

ABSTRACT

Using variational principles, we investigate elastic rod structures under external loads that are clamped at one end and free at the other. Their stability properties are analyzed using second order conditions by generalizing the *Jacobi theory* of *conjugate points*. The notion of the *index*, which quantifies the dimension of the subspace of variations over which the second variation is negative, is also generalized to this class of problems. The variational structure of the parameter-dependent calculus of variations problems can be exploited to detect the changes in the *index* at the folds as the parameter is varied, with the assistance of *distinguished bifurcation diagrams*. We generalize these plots to cover our current case with fixed-free ends. Furthermore, we extend the investigation to the problems with discontinuous integrands by generalizing the concept of *conjugate points*, *index*, and *distinguished bifurcation diagrams* to them. For this purpose, second-order matching conditions are derived at the points of discontinuity.

These techniques are developed with the aim of employing them in soft robotic applications, a field that is increasingly gaining popularity. Applications such as Concentric Tube Continuum Robots (CTCRs) employ intrinsically curved rods to generate flexible mechanisms. We emphasize the impact of intrinsic curvature, which is often a source of complex mechanics, on the equilibria of elastic rods and their stability. The interplay between geometric non-linearities, external load, and intrinsic curvature leads to intriguing and complex behavior such as snap-back instability. We study the influence of the parameters, such as intrinsic curvature, length, tip load, and lever arm of the load on this behavior. This study aids in their efficient utilization in practical applications. We extend this investigation to CTCRs, which resemble an intrinsically curved elastic rod with slightly different physics. These robots consist of multiple sections, and their properties change abruptly at the boundary of each section. This research has the potential to advance the design and control of robots for tackling more complex tasks.

Finally, an open-loop gradient-based navigation is devised to model the robot maneuver using *optimal control* techniques. Through this approach, various tasks can be modelled in terms of objective functions that are subsequently optimized. We consider *optimal control* of CTCRs parameterized over pseudo-time, primarily focusing on minimizing the robot's working volume during its motion. A numerical strategy to implement this optimization task is also discussed. This *optimal control-based* methodology can be adapted to any backbone-based continuum robots.

Keywords: *Jacobi Condition*, *Stability*, *Conjugate points*, *Intrinsic Curvature*, *Distinguished Bifurcation Diagram*, *Hysteresis*, *Concentric Tube Continuum Robot*, *Optimal Control*.

Dedicated to my Amma and Nanna (Mom and Dad)

ACKNOWLEDGEMENT

I would like to express my sincere thanks to Prof. Dr. John H. Maddocks for sharing his profound expertise across a spectrum of topics in Mathematics and Mechanics. His invaluable guidance has been instrumental throughout this Ph.D. journey and contributed to my academic development. I am equally grateful to Dr. Martin Weiser for imparting his extensive knowledge on the topics of Optimal Control and Optimization and for introducing me to several relevant scientific questions. His guidance has significantly broadened my understanding and fueled my curiosity in these fields. Additionally, I would like to extend my thanks to Prof. Dr. Christof Schütte, who is instrumental in managing the machinery behind this work.

I would like to express my gratitude to the members of LCVMWWW including Rahul, Roushan, Harmeet, Thomas, and Giulio for their scientific and non-scientific discussions that always kept me motivated. Special thanks to the secretaries Carine, Marina, Jana Jerosh, and Doro for easing my life with bureaucratic procedures both in Berlin and Lausanne. Additionally, I would also offer my sincere thanks to Dr. Sebastian Krumschied and Dr. Jannes Quer who guided me through various aspects of life in FU Berlin and Berlin.

I am deeply grateful to my *akka* (sister), *annayya* (brother), *bava* (brother-in-law), and *vadina* (sister-in-law) for their constant unwavering support throughout this period. I also want to give a special mention to my nieces Hema, Harshini, and Samhi, who always cherished me with their constant affection and encouragement. I am filled with gratitude for Sukirti, Jia Xuan, Jessica, Fahamida, Harish, Anand, Lakshmi, and Abhishek whose presence made this journey look simple and tireless. A heartfelt thanks to my friends at ICCB for providing me with some relaxation and leisure by playing cricket during weekends. I would like to extend my appreciation to my departmental comrades, particularly Abhishek and Sarai for engaging in enriching discussions across a wide spectrum of topics in Mensa. I am also thankful to friends GTK, Sabbi, Bond, Prasen, and Manohar who enriched my life with their presence (online) and experiences. Special thanks to my friend GTK who shared his Netflix account during the difficult pandemic period.

This work is made possible through the funding provided by the Einstein Foundation Berlin and Math+. I extend my heartfelt gratitude for their support.

TABLE OF CONTENTS

CHAPTER 1

Introduction

Rods are slender structures with lengths much greater than their diameters. These structures exhibit nonlinear behavior, involving large deformations and rotations, while the constituent material undergoes only smaller strains. In the absence of external forces, these rods assume a shape referred to as *intrinsic shape* or *natural shape*, which can be straight, helical, or any other shape. Rod-like structures with intrinsic curvatures, such as curly hair, DNA, plant tendrils, and cables, are ubiquitous in nature and technology. They are also employed in soft robotic applications to create compliant mechanisms. Inspiration is often drawn from nature to mimic the mechanisms, such as that of octopus tentacle or elephant trunk, and to utilize them in practical applications (Laschi et al., 2012; Majidi, 2014) as they offer increased dexterity and manipulation capabilities. The recent development of highly deformable elastic materials has significantly contributed to the development of these mechanisms.

When a naturally straight elastic rod, clamped at one end and with a dead load attached to the other end, is rotated using the clamp, it exhibits a snap-back instability for certain combinations of length and load. This well-known catapult behavior has the potential to be utilized in the design of soft robotic arms (Armanini et al., 2017). Likewise, a naturally curved elastic rod with a tip load may exhibit a snap-back instability when its clamped end is rotated. The presence of intrinsic curvature introduces additional complexity to the problem, as it leads to complex mechanics and geometrical non-linearities in elastic rods. In our current research, we focus on studying these structures. But before going into further depth, we shall present a few examples highlighting the effect of intrinsic curvature in elastic rods, which are closely linked to the current research. When a naturally curved elastic wire is held at fixed locations (not clamped), and one end is slowly twisted, the wire tends to *ratchet*, i.e., there is an abrupt change in the torque required to twist the wire. This phenomenon has direct implications in surgical procedures, such as angioplasty, where thin wires are inserted into blood vessels and guided. Usually, a smooth twisting action is desired without any sudden rotations. Even though these guide wires are intended to be straight, the manufacturing processes and coil storage impart a natural curvature. Warner (1997) numerically studied this behavior using *Kirchhoff rod theory*. Another interesting example on the effect of intrinsic curvature can be noticed in an elastic rod that hangs under its own weight (Miller et al., 2014). For smaller intrinsic curvatures, the rod adopts planar equilibria. In this instance, the rod is straight near the clamped end and develops a curled hook at the tips. However, higher intrinsic curvatures lead to non-planar rod equilibria,

which are classified into two types: *localized helix*, which consists of a helix beneath a straight portion, and *globalized helix*, which is wholly composed of a helical portion. The configurations of curly hair or analogous filamentary structures concur with this behavior. These examples demonstrate the non-intuitive behavior that intrinsic curvature imparts to the elastic rods. Apart from its complex effects, intrinsic curvature in elastic rods also offers prospective benefits that can be harnessed in various applications. For instance, it can enhance the maximum reachout (distance between the endpoints) of a tip-loaded robotic arm (Sipos and Várkonyi, 2020). A tip-loaded elastic rod with a natural curvature facilitates more reachout (distance between the endpoints) compared to a tip-loaded naturally straight rod. On the other hand, the majority of research on rods with intrinsic curvature has primarily focused on symmetric boundary conditions, which consist of clamped boundary conditions at both ends (Neukirch and Henderson, 2002; Domokos and Healey, 2005; Lazarus et al., 2013b), or rods of infinite length (McMillen et al., 2002). To date, the investigation of the tip-loaded intrinsically curved elastic rods of finite length remains limited in scope. This problem is of current interest as naturally curved elastic structures are increasingly being utilized in the field of soft robotics, such as in the case of Concentric Tube Continuum Robots (CTCRs).

Recently developed CTCRs, also called active cannulas, consist of perfectly concentric elastic tubes of different stiffness and pre-curvatures (Rucker et al., 2010). These tubes are usually made of materials such as Nitinol alloy, which can undergo significant elastic deformations without showing any sign of plasticity. The ends of the tubes are fixed to the actuators in the base, which can either mechanically translate or rotate the tubes independently. The concentric tubes are constrained to assume the shape of a common centerline referred to as the *backbone*, which can be controlled by relatively sliding and rotating the tubes one inside the other using the actuators. The robot's tip, equipped with an instrument, is steered by appropriate relative slides and twists of the tubes at its root. The slim diameters of order 2mm and compliant nature of CTCRs encouraged many researchers to utilize them in confined spaces, such as in minimally invasive surgeries (Burgner et al., 2011; Burgner et al., 2013; Alfalahi et al., 2021). Overall, this CTCR *backbone* is analogous to the naturally curved elastic rod with slightly different mechanics and, consequently, it inherits certain aspects of their behavior.

This thesis primarily aims to explore the behavior of intrinsically curved rod structures when subjected to a conservative tip load. In the first part, we focus on tip-loaded intrinsically curved elastic rods that are clamped at one end and attached to a dead load at the other. We commence with the Hamiltonian formulation of elastic rods (Dichmann et al., 1996) to obtain the equilibria for varying clamp angles. In this formulation, the spatial orientation of the rod is characterized using quaternions. The equilibria are numerically examined using *parameter continuation* with *AUTO-07p* software package. The second part extends this formulation to determine the equilibria of CTCRs when attached to a dead load. In the final part, using the equilibria from the second part, we propose an *optimal control*-based navigation strategy for CTCRs. However, the mere determination of the equilibria is insufficient, and further analysis of their stability is necessary.

Generally, a flexible rod under a load can exhibit multiple equilibria. Then, a natural question arises about which equilibria are stable. The stability analysis of rod equilibria using variational principles has a long history. The variational structure of the problem correlates the stability of the equilibria to the local minimum of the energy functional. The absence of *conjugate points*, often termed as the *Jacobi condition*, along with the *Legendre's strengthened condition* is the necessary condition for the equilibria to be the local minimum of the functional (Bolza, 1904; Gelfand and Fomin, 1963). Furthermore, Morse (1951) extended this concept to define an *index*, which quantifies the maximal dimension of the subspace of variations over which the second variation is negative. This *index* is equal to the number of the *conjugate points*. The equilibria are stable as long as the *index* is zero. Maddocks (1984) investigated the stability properties of elastic rods under various boundary conditions and found many previously unknown configurations of elastic rods. This analysis employs the nodal properties of the functions. The exact form of equilibria is not assumed, and *Euler angles* are employed. In his subsequent study, Maddocks (1987) employed restricted quadratic forms to address the stability of elastic rods subject to isoperimetric constraints. The notion of the isoperimetric *index* was later developed by Manning et al. (1998) for the constrained variational problems, which is determined by counting the number of *conjugate points* for an appropriately projected second variation. A numerical strategy to determine these *conjugate points* was also outlined here. This study is aimed at analyzing the stability of DNA minicircles. Subsequently, Manning and Hoffman (2001); Hoffman et al. (2002); Hoffman and Manning (2009) extended this idea to a variety of constrained elastic rod problems. In the literature, there are also alternative methods to analyze the stability properties. For example, Kuznetsov and Levyakov (2002); Levyakov and Kuznetsov (2010) determined the stability properties of planar rod equilibria under various boundary conditions using the exact solutions expressed in terms of Jacobi elliptic integrals. The second-order variation is represented as a quadratic form using the basis of the eigenfunctions of an auxiliary *Sturm-Liouville* operator. The stability analysis reduces to determining whether a certain interval contains eigenvalues of this operator. As already pointed out, this approach requires analytic solutions, which are available only for the planar cases. Kumar and Healey (2010); O'Reilly and Peters (2011); Lazarus et al. (2013a); Majumdar and Raisch (2014) have employed other alternative techniques for stability analysis. The majority of the existing literature on stability analysis has either focused on cases with *Dirichlet boundary conditions* at both ends or simple planar cases. However, a gap exists in the literature regarding the stability analysis of 3D elastic rods under fixed-free boundary conditions. This thesis aims to address this research gap by investigating their stability. Moreover, we generalize the concept of *Morse index* to this class of problems.

The highly flexible CTCRs also exhibit multiple equilibria under a given load, and therefore, their stability properties must be evaluated. This is further complicated by the fact that CTCRs consist of multiple sections, each with different overlapping tubes. As a result, we have a system of concentric rods whose properties such as stiffness, and intrinsic curvature change abruptly at the boundary between the sections. This kind of problem is classified as a variational problem with discontinuous integrand. In the past, Bliss and Mason (1906), and Graves

(1930) extended *Jacobi condition* to these variational problems with discontinuous integrand using matching conditions, while Cole (1940) extended the definition of the *index* to include these problems. Recently, O'Reilly and Peters (2011); Lane (2012) studied these problems in the context of elastic rods. In the present study, we analyze the stability properties of CTCR with multiple sections by extending *Jacobi condition* to them. Furthermore, the notion of *Morse index* is also extended to these problems.

In general, the variational problems depend on the parameter and yield a family of parameter-dependent equilibria. These parameters either describe the functional or boundary conditions. Such problems are termed parameter-dependent variational problems. Bifurcation diagrams, consisting of a plot of a particular projection of the solutions, provide insights into the stability information as this parameter is varied. Standard Bifurcation Theory (Golubitsky and Schaeffer, 2014) predicts that folds in the parameter in these diagrams correspond to the exchange of stability. *Distinguished bifurcation diagrams* additionally convey the direction of stability exchange at the fold in parameter through its specific shape. In a previous study, Maddocks (1987) utilized the variational structure of the problems and derived the ordinate for these bifurcation diagrams. This analysis considered only the homogeneous boundary conditions, and the bifurcation parameter appears in the integrand. Hoffman (2005) extended this concept to derive bifurcation diagrams for parameter-dependent variational problems with fixed-fixed ends, where the parameter appears in boundary conditions. The shape of the diagrams accurately predicted the increase or decrease of the *Morse index* at the folds, and unstable equilibria, which have an *index* greater than zero could be easily identified. In our current research, we verify if these diagrams also agree with the cases of fixed-free ends. Furthermore, we broaden their scope to functionals with discontinuous integrands. Later, we employ these diagrams to study the hysteresis behavior in the tip-loaded elastic rods and CTCRs.

CTCRs are mainly intended for use in confined spaces such as body cavities. These applications necessitate the development of effective path planning and control strategies to perform tasks with a high degree of precision. For its attainment, accurate mechanical models, numerical methods, and *optimal control* techniques are the key. Confined spaces often impose several challenges on robot navigation. The robot must steer clear of delicate tissues and hard obstacles such as bones. The contact with the obstacles is challenging to model, and the robot's behavior cannot be predicted precisely. In most surgical procedures, minimum or no tissue damage is intended. Therefore, the robot must deviate as minimally as possible from its narrow working space and avoid interference with the neighboring regions. Therefore, paths with a minimum working space, i.e., a minimum deviation from a mean curve, are highly desirable. One significant aspect of the CTCR is the *follow-the-leader* (FTL) strategy, where the robot is deployed telescopically such that the *backbone* always lies along the path traced by prior tip locations. This strategy occupies a minimal working space during its deployment and is an ideal solution for operating in minimum working volumes. In the simpler setup for this deployment, the unstressed tubes of the robot section must be either in the shape of circular arcs or in the shape of helical arcs with equal torsions. The robot *backbone* then assumes the shape of a uniform curve

like a circular or helical arc under specific control parameters. The sections are then extended along this arc's tangent allowing the robot's body to follow the path previously traced by the tip (Gilbert et al., 2015; Garriga-Casanovas and Rodriguez y Baena, 2018). This deployment fails when the constituent tubes have unequal torsions or the robot tip is mounted to a non-zero load. The working space must lie along this helical curve so that this FTL deployment can reach it, which is not the case in general. Many tasks, for example, cardiac ablation (Yip et al., 2017), require the tip to move continuously to neighboring points, resulting in the deviation from the FTL configuration. Besides, working just with FTL configurations limits the robot's working space and degrees of freedom. So, suitable *optimal control* techniques are necessary to maneuver the robot such that the desired objective of operating at minimum working volume is fulfilled. In the third part of the thesis, we intend to mathematically model the robot maneuver by casting it as an *optimal control problem*. There are several combinations of control parameters, i.e., lengths and rotations of the tubes, which guide the robot tip to a specific point or to accomplish a task. This flexibility increases with the increase of tubes in the CTCR. Thus, it would be more beneficial to choose the optimal set of these control parameters over which the intended performance indicators are better. We focus on tasks such as minimizing the working volume and reaching a target orientation.

In the past, *optimal control* techniques have been employed in designing CTCRs to select design parameters based on the available workspace and anatomical constraints (Bergeles et al., 2015). Derivative-free optimization methods such as Nelder-Mead (Baykal et al., 2015; Granna et al., 2016) or particle swarm methods (Granna, 2019) are extensively used. Gradient-based optimization techniques are used only for simpler models (Lyons et al., 2009; Flaßkamp et al., 2019), where analytical derivatives are available. These methods lead to local minima rather than to global minima. But, they are computationally fast and useful in real-time operations. Tasks such as moving to a nearby point can usually be planned with local optimization methods. Recently, the use of nonlinear programming methods for CTCR path planning has been proposed by Flaßkamp et al. (2019) in planar robots, where the analytical representation of the robot states is available. In the final part of the thesis, we aim to model some simple navigation tasks using the *optimal control* techniques, with the aid of the CTCR equilibrium equations. Since the analytical form of the states is not unavailable, they are determined numerically inside the optimization framework.

This thesis is structured into three parts. Part 1 presents the study concerning the mechanics of elastic rods, Part 2 examines the mechanics of CTCRs, and Part 3 focuses on the *optimal control* of CTCRs. Each chapter is organized as follows.

Chapter 2 gives a brief overview of the variational principles that are required throughout the thesis. We describe unconstrained *conjugate point theory* and an *index* for the calculus of variations problem subject to fixed boundary conditions at one end and free boundary conditions at the other. Here, we also present the *distinguished bifurcation diagram* for the parameter-dependent variational problems in which the varying parameter is present in the boundary con-

ditions at the fixed end.

Chapter 3 contains a description of the *Kirchhoff theory* of elastic rods. We discuss kinematics, strains, equilibrium equations, and constitutive law. We review the quaternions, which relate the orientation of the rod cross-section to the fixed laboratory frame. Then, we derive the Hamiltonian form of equilibria for elastic rods clamped at one end and attached to a conservative tip load that exerts a tip force as well as a moment due to the arm of loading. Then, we present the Hamiltonian form of the *Jacobi equations* and provide a suitable numerical algorithm to compute the *conjugate points*.

Chapter 4 is devoted to the numerical procedures employed in solving the equilibrium equations. The *AUTO-07p* software is employed for numerical parameter continuation and orthogonal collocation. This chapter provides a concise review of these methods, offering insights into how the problem is implemented in *AUTO-07p*.

In Chapter 5, we study the prototypical model of an elastic rod with a tip load and investigate its hysteresis behavior. We compute the *conjugate points* and assign the *Morse index* to the equilibria. *Distinguished bifurcation diagrams* are plotted, and their prediction on the exchange of stability near folds is verified.

We commence part 2 with chapter 6 discussing the mechanics of CTCRs. We model the equilibria of the CTCRs with a load attached using the Hamiltonian formulation. The *Jacobi condition* is extended to these cases of functional with discontinuous integrand. We also present a numerical algorithm to compute the *conjugate points* for this class of problems.

In Chapter 7, we present some examples which demonstrate the hysteresis behavior in the CTCRs. *Conjugate points* are computed for these equilibria across the sections. Surface plots are plotted against several parameters to gain better insight into the hysteresis behavior and its dependence on the parameters.

We begin part 3 with chapter 8 briefing the preliminaries of *optimal control problem* and Nonlinear Programming problem.

In Chapter 9, we model the navigation of CTCR by casting it as an *optimal control problem*. We proposed several objective functions here, required for efficient navigation. And in Chapter 10, present some prototype navigation tasks to test out the proposed *optimal control* approach.

Finally, Chapter 11 provides a conclusion, including a summary of the work and suggestions for future research.

Part I

Variational principles and their Application to Elastic Rods

CHAPTER 2

Variational Principles including Second-Order Conditions

In this chapter, we present the *conjugate point theory* for unconstrained calculus of variations problems. The results for the problems with both ends subject to fixed (or *Dirichlet*) boundary conditions can be found in any standard textbook on the calculus of variations (Bolza, 1904; Gelfand and Fomin, 1963; Hestenes, 1966; Sagan, 1969; Caratheodery, 1967). However, the results for the case of fixed boundary conditions at one end and free (or *Neumann*) conditions at the other end are not so common. Therefore, we extend *conjugate point theory* to cover this case. To solve the given variational problem, we must choose a function space and associated norm. In our problem, we choose the function space $\mathcal{C}^1[0,l]$ (the set of continuously differentiable functions) with *weak* norm:

$$\|y\|_1 = \sup_{0<s<l} \|y(s)\| + \sup_{0<s<l} \|y'(s)\|,$$

which is also called the $\mathcal{C}^1$- norm. The $\mathcal{C}^0$- measure is defined in the $\mathcal{C}^1[0,l]$ function space as

$$\|y\|_0 = \sup_{0<s<l} \|y(s)\|.$$

It is used for dealing with so-called strong extremals in the language of the classic calculus of variations.

2.1 Standard Calculus of Variations Problem

Let $\zeta : s \longrightarrow \mathbb{R}^p$ be a continuous and differentiable function in the interval $[0,l]$, where s is an independent parameter. Given a continuous mapping $\mathcal{L} : \mathbb{R}^p \times \mathbb{R}^p \times [0,l] \to \mathbb{R}$, the classic calculus of variations problem is to minimize a functional of the form

$$J(\zeta) = \int_0^l \mathcal{L}(\zeta, \zeta', s)ds, \tag{2.1}$$

with both the ends $s = 0$ and $s = l$ subject to either fixed or free boundary conditions. At the fixed end, the state ζ is imposed a fixed value, while at the free end, no conditions are imposed on the state ζ.

2.1.1 Euler-Lagrange Equations and their Hamiltonian Form

The first-order necessary condition for $\boldsymbol{\zeta}(s)$ to be a stationary point is the vanishing first variation given by

$$\delta J(\boldsymbol{\zeta})[\mathbf{h}] = \int_0^l \left(-\left(\frac{\partial \mathcal{L}}{\partial \boldsymbol{\zeta}'}\right)' + \frac{\partial \mathcal{L}}{\partial \boldsymbol{\zeta}} \right) \cdot \mathbf{h} ds + \left[\frac{\partial \mathcal{L}}{\partial \boldsymbol{\zeta}'} \cdot \mathbf{h} \right]_0^l = 0.$$

Here $\cdot$ represents the dot product between two column vectors $\mathbf{u} \cdot \mathbf{v} = \mathbf{u}^T \mathbf{v}$. The variations $\mathbf{h}$ are functions in $\mathcal{C}^1[0, l]$ and perturb the solution $\boldsymbol{\zeta}$ satisfying the imposed boundary conditions. Provided that the minimizer is piecewise smooth, the coefficient of an arbitrary variation $\mathbf{h}$ vanishes, fetching the famous *Euler-Lagrange equations*

$$-\left(\frac{\partial \mathcal{L}}{\partial \boldsymbol{\zeta}'}\right)' + \frac{\partial \mathcal{L}}{\partial \boldsymbol{\zeta}} = \mathbf{0}. \tag{2.2}$$

In addition, the first-order condition leads to *Natural boundary condition* at any free end

$$\frac{\partial \mathcal{L}}{\partial \boldsymbol{\zeta}'} = \mathbf{0}.$$

A variant of the problem, in which the functional to be minimized has an additional boundary term at any free end, say $s = l$, of the form

$$J(\boldsymbol{\zeta}) = \int_0^l \mathcal{L}(\boldsymbol{\zeta}, \boldsymbol{\zeta}', s) ds + B(\boldsymbol{\zeta}(l)),$$

where the boundary term $B(\boldsymbol{\zeta}(l))$ is a smooth scalar function of $\boldsymbol{\zeta}(l)$. In this context, the first-order condition appears as

$$\delta J(\boldsymbol{\zeta})[\mathbf{h}] = \int_0^l \left(-\left(\frac{\partial \mathcal{L}}{\partial \boldsymbol{\zeta}'}\right)' + \frac{\partial \mathcal{L}}{\partial \boldsymbol{\zeta}} \right) \cdot \mathbf{h} ds + \left[\frac{\partial \mathcal{L}}{\partial \boldsymbol{\zeta}'} \cdot \mathbf{h} \right]_0^l + \frac{\partial}{\partial \boldsymbol{\zeta}} B(\boldsymbol{\zeta}) \cdot \mathbf{h} \Big|_{s=l} = 0.$$

Subsequently, we obtain the *Euler-Lagrange equations* (2.2) and slightly revised *Natural boundary condition* at the free end $s = l$

$$\frac{\partial \mathcal{L}}{\partial \boldsymbol{\zeta}'} + \frac{\partial}{\partial \boldsymbol{\zeta}} B(\boldsymbol{\zeta}) = \mathbf{0}. \tag{2.3}$$

The solutions to the *Euler-Lagrange equations* with the corresponding boundary conditions are called critical points, equilibria, or extrema. The extrema of J with respect to the $\mathcal{C}^0$- norm are called *strong extrema* or *strong minima*, whereas the extrema of J with respect to $\mathcal{C}^1$- norm are called *weak extrema* or *weak minima*.

The equilibria correspond to the solutions of the *Euler-Lagrange equations* (2.2), which take the form of second-order Ordinary Differential Equations (ODEs). On the other hand, the Hamiltonian form (Goldstein, 1951) offers an elegant way of representing them as first-order ODEs. Generally, the Hamiltonian system is expressed in terms of canonical variables $\boldsymbol{\zeta}$ and $\mathbf{p}$,

in which the canonical momentum $\mathbf{p} \in \mathbb{R}^p$ is defined as

$$\mathbf{p} := \frac{\partial}{\partial \boldsymbol{\zeta}'} \mathcal{L}(\boldsymbol{\zeta}, \boldsymbol{\zeta}'; s).$$

If the function $\mathcal{L}(\boldsymbol{\zeta}, \boldsymbol{\zeta}', s)$ is strictly convex with respect to $\boldsymbol{\zeta}'$, then the derivative $\boldsymbol{\zeta}'$ can be expressed as a function of canonical variables $\boldsymbol{\zeta}, \mathbf{p}$:

$$\boldsymbol{\zeta}' = \boldsymbol{\phi}(\boldsymbol{\zeta}, \mathbf{p}, s). \tag{2.4}$$

Then, the Hamiltonian H is defined as the *Legendre transform* of the function $\mathcal{L}$, and is given by

$$H(\boldsymbol{\zeta}, \mathbf{p}; s) := \boldsymbol{\phi}(\boldsymbol{\zeta}, \mathbf{p}) \cdot \mathbf{p} - \mathcal{L}(\boldsymbol{\zeta}, \boldsymbol{\phi}(\boldsymbol{\zeta}, \mathbf{p}, s), s).$$

Consequently, the equilibria are obtained as solutions of a system of first-order ODEs from the Hamiltonian $H(\boldsymbol{\zeta}, \mathbf{p}, s)$ as

$$\begin{bmatrix} \boldsymbol{\zeta} \\ \mathbf{p} \end{bmatrix}' = \begin{bmatrix} \mathbf{0} & \mathbf{I} \\ -\mathbf{I} & \mathbf{0} \end{bmatrix} \begin{bmatrix} H_{\boldsymbol{\zeta}} \\ H_{\mathbf{p}} \end{bmatrix}, \tag{2.5}$$

where $H_{\boldsymbol{\zeta}}$ and $H_{\mathbf{p}}$ are partial derivatives of the function $H(\boldsymbol{\zeta}, \mathbf{p}, s)$ with respect to the variables $\boldsymbol{\zeta}$ and $\mathbf{p}$ respectively. And $\mathbf{0}$ and $\mathbf{I}$ are the zero matrix and the identity matrix, respectively, in $\mathbb{R}^{p \times p}$. At the free end, say $s = l$, the *Natural boundary condition* (2.3) in terms of the Hamiltonian phase variables $\boldsymbol{\zeta}, \mathbf{p}$ read

$$\mathbf{p}(l) + \frac{\partial}{\partial \boldsymbol{\zeta}} B(\boldsymbol{\zeta}(l)) = \mathbf{0},$$

and the *Dirichlet boundary conditions* are expressed directly in terms of the variable $\boldsymbol{\zeta}$.

2.1.2 Corner Points or Broken Extremal

So far, we have assumed that the function $\boldsymbol{\zeta}(s)$ is smooth in the interval $[0, l]$. Now, we shall relax this requirement and derive the first-order conditions. Let us consider a scenario where the function $\boldsymbol{\zeta}(s)$ is continuous in $[0, l]$, but its derivative $\boldsymbol{\zeta}'(s)$ is discontinuous at a known point $c \in [0, l]$. These points are referred to as *corner points*, and the extremals with these *corner points* are termed *broken extremals*. The integrand $\mathcal{L}(\boldsymbol{\zeta}, \boldsymbol{\zeta}', s)$ is assumed to be a continuous function of s in $[0, l]$. The necessary conditions for a broken extremal are well-known *Weierstrass-Erdmann conditions* (Bolza, 1904; Gelfand and Fomin, 1963), and the results are stated here without proof:

$$\left.\frac{\partial \mathcal{L}}{\partial \boldsymbol{\zeta}'}\right|_{s=c-} = \left.\frac{\partial \mathcal{L}}{\partial \boldsymbol{\zeta}'}\right|_{s=c+}, \tag{2.6a}$$

$$\left.\mathcal{L} - \boldsymbol{\zeta}' \cdot \frac{\partial \mathcal{L}}{\partial \boldsymbol{\zeta}'}\right|_{s=c-} = \left.\mathcal{L} - \boldsymbol{\zeta}' \cdot \frac{\partial \mathcal{L}}{\partial \boldsymbol{\zeta}'}\right|_{s=c+}. \tag{2.6b}$$

Here, the notations $c-$ and $c+$ indicate the evaluation of the expression on the left and right sides of the point c respectively. The first condition (2.6a) is required for establishing the existence of the *weak minima*, whereas the second condition (2.6b) is required for establishing the existence of the *strong minima*. If $\mathcal{L}(\boldsymbol{\zeta}, \boldsymbol{\zeta}', s)$ is a convex function of $\boldsymbol{\zeta}' \in \mathbb{R}^p$, the relations (2.4) and (2.6a) implicate

$$\boldsymbol{\zeta}'(c+) = \boldsymbol{\zeta}'(c-).$$

Hence, the extremal solution cannot have a *corner point*. If a curve $\boldsymbol{\zeta}$ is a strong extremum, then $\mathcal{L}_{\boldsymbol{\zeta}'}$ and $\boldsymbol{\zeta}' \cdot \mathcal{L}_{\boldsymbol{\zeta}'} - \mathcal{L}$ must be continuous at each corner point. A *strong minima* can be a *weak minima*, whereas the *weak minima* need not necessarily be a *strong minima*. We shall always assume that $\mathcal{L}(\boldsymbol{\zeta}, \boldsymbol{\zeta}', s)$ is a strict convex function of $\boldsymbol{\zeta}'$ and $\mathcal{L}_{\boldsymbol{\zeta}'\boldsymbol{\zeta}'}$ is strictly positive definite. Then, (2.6b) is satisfied whenever (2.6a) is satisfied, and any *weak minima* is alternatively a *strong minima* (Bolza, 1904).

2.2 Second-Order Conditions: Fixed-Fixed ends

This section discusses the well-established second-order conditions for unconstrained calculus of variations problems that are subjected to fixed (or *Dirichlet*) boundary conditions at both ends. The critical points $\boldsymbol{\zeta}_o$ obtained as a solution to the *Euler-Lagrange equations* (2.2) with the boundary conditions

$$\boldsymbol{\zeta}(0) = f_o, \quad \boldsymbol{\zeta}(l) = f_l,$$

are classified if they are local minima after analyzing the second variation of the functional $J(\boldsymbol{\zeta})$. Here, f_o and f_l are given constants. In problems of mechanics, typically the functional J corresponds to energy, and local minima represent stable configurations. Therefore, the terms locally stable and local minima are used interchangeably throughout this thesis. The second variation of the functional J at an equilibrium point $\boldsymbol{\zeta}_o$ is

$$\delta^2 J(\boldsymbol{\zeta}_o)[\mathbf{h}] = \frac{1}{2}\int_0^l \left(\mathbf{h}' \cdot \mathbf{P}\mathbf{h}' + \mathbf{h} \cdot \mathbf{C}\mathbf{h}' + \mathbf{h}' \cdot \mathbf{C}^T\mathbf{h} + \mathbf{h} \cdot \mathbf{Q}\mathbf{h}\right) ds, \tag{2.7}$$

where $\mathbf{P}, \mathbf{C}$ and $\mathbf{Q}$ are $p \times p$ Hessian matrices evaluated at the extremal $\boldsymbol{\zeta}_o$ given by

$$\begin{aligned}
\mathbf{P} &= \frac{\partial^2}{\partial \boldsymbol{\zeta}'^2}\mathcal{L}(\boldsymbol{\zeta}_o, \boldsymbol{\zeta}_o', s) \equiv \mathcal{L}_{\boldsymbol{\zeta}'\boldsymbol{\zeta}'}(\boldsymbol{\zeta}_o, \boldsymbol{\zeta}_o', s),\\
\mathbf{C} &= \frac{\partial^2}{\partial \boldsymbol{\zeta}' \partial \boldsymbol{\zeta}}\mathcal{L}(\boldsymbol{\zeta}_o, \boldsymbol{\zeta}_o', s) \equiv \mathcal{L}_{\boldsymbol{\zeta}\boldsymbol{\zeta}'}(\boldsymbol{\zeta}_o, \boldsymbol{\zeta}_o', s),\\
\mathbf{Q} &= \frac{\partial^2}{\partial \boldsymbol{\zeta}^2}\mathcal{L}(\boldsymbol{\zeta}_o, \boldsymbol{\zeta}_o', s) \equiv \mathcal{L}_{\boldsymbol{\zeta}\boldsymbol{\zeta}}(\boldsymbol{\zeta}_o, \boldsymbol{\zeta}_o', s).
\end{aligned} \tag{2.8}$$

For brevity, the dependence of $\mathbf{P}, \mathbf{C}$ and $\mathbf{Q}$ on s is not explicitly shown. The matrices $\mathbf{P}$ and $\mathbf{Q}$ are symmetric, whereas the matrix $\mathbf{C}$ may not be. The second-order necessary condition for $\boldsymbol{\zeta}_o$

to be local minima of the functional J is

$$\delta^2 J(\boldsymbol{\zeta}_o)[\mathbf{h}] \geq 0. \tag{2.9}$$

The variations $\mathbf{h}$ in the solutions must satisfy the boundary conditions, and accordingly, belong to the class of admissible variations:

$$\mathcal{A} \equiv \left\{\mathbf{h}(s) \in \mathcal{C}^1[0,l]) : \mathbf{h}(0) = \mathbf{0} = \mathbf{h}(l)\right\}. \tag{2.10}$$

On applying integration by parts on (2.7), we obtain

$$\delta^2 J(\boldsymbol{\zeta}_o)[\mathbf{h}] = \frac{1}{2}\int_0^l \left(-\frac{d}{ds}\left(\mathbf{P}\mathbf{h}' + \mathbf{C}^T\mathbf{h}\right) + \mathbf{C}\mathbf{h}' + \mathbf{Q}\mathbf{h}\right)\cdot\mathbf{h}ds + \left[\left(\mathbf{P}\mathbf{h}' + \mathbf{C}^T\mathbf{h}\right)\cdot\mathbf{h}\right]_0^l.$$

The boundary terms vanish at $s = 0$ and $s = l$ leading to an alternate form of the second variation

$$\delta^2 J[\mathbf{h}] = \frac{1}{2}\langle \mathcal{S}\mathbf{h}, \mathbf{h}\rangle, \tag{2.11}$$

where $\mathcal{S}$ is the second-order self-adjoint differential operator:

$$\mathcal{S}\mathbf{h} \equiv -\frac{d}{ds}\left(\mathbf{P}\mathbf{h}' + \mathbf{C}^T\mathbf{h}\right) + \mathbf{C}\mathbf{h}' + \mathbf{Q}\mathbf{h}, \tag{2.12}$$

and $\langle\cdot,\cdot\rangle$ denotes the standard inner-product in L^2- space. This system of ODEs along with the boundary conditions on $\mathbf{h}$ (2.9) is called the *accessory boundary value problem* or *Jacobi differential equations*, and its solutions are called *accessory extremals*. Now, we state an integration by parts result of this *Jacobi operator* $\mathcal{S}$ as a lemma that is frequently used in subsequent results.

Lemma 2.2.1. *For any two-vector valued continuous functions* $\mathbf{u}, \mathbf{v}$*,*

$$\langle \mathcal{S}\mathbf{u}, \mathbf{v}\rangle = \langle \mathbf{u}, \mathcal{S}\mathbf{v}\rangle + \left[\left(\mathbf{P}\mathbf{v}' + \mathbf{C}^T\mathbf{v}\right)\cdot\mathbf{v}\right]_0^l - \left[\left(\mathbf{P}\mathbf{u}' + \mathbf{C}^T\mathbf{u}\right)\cdot\mathbf{v}\right]_0^l. \tag{2.13}$$

Proof. On applying integration by parts twice on the L.H.S and bearing in mind that $\mathbf{P} = \mathbf{P}^T$ and $\mathbf{Q} = \mathbf{Q}^T$, we obtain

$$\begin{aligned}
\langle \mathcal{S}\mathbf{u}, \mathbf{v}\rangle &= \int_0^l \left(-\frac{d}{ds}\left(\mathbf{P}\mathbf{u}' + \mathbf{C}^T\mathbf{u}\right) + \mathbf{C}\mathbf{u}' + \mathbf{Q}\mathbf{u}\right)\cdot\mathbf{v}ds,\\
&= \int_0^l \left(\mathbf{P}\mathbf{u}' + \mathbf{C}^T\mathbf{u}\right)\cdot\mathbf{v}' + \left(\mathbf{C}\mathbf{u}' + \mathbf{Q}\mathbf{u}\right)\cdot\mathbf{v}ds - \left[\left(\mathbf{P}\mathbf{u}' + \mathbf{C}^T\mathbf{u}\right)\cdot\mathbf{v}\right]_0^l,\\
&= \int_0^l \left(\mathbf{P}\mathbf{v}' + \mathbf{C}^T\mathbf{v}\right)\cdot\mathbf{u}' + \left(\mathbf{C}\mathbf{v}' + \mathbf{Q}\mathbf{v}\right)\cdot\mathbf{u}ds - \left[\left(\mathbf{P}\mathbf{u}' + \mathbf{C}^T\mathbf{u}\right)\cdot\mathbf{v}\right]_0^l,\\
&= \int_0^l \left(-\frac{d}{ds}\left(\mathbf{P}\mathbf{v}' + \mathbf{C}^T\mathbf{v}\right) + \mathbf{C}\mathbf{v}' + \mathbf{Q}\mathbf{v}\right)\cdot\mathbf{u}ds + \left[\left(\mathbf{P}\mathbf{v}' + \mathbf{C}^T\mathbf{v}\right)\cdot\mathbf{u}\right]_0^l\\
&\qquad - \left[\left(\mathbf{P}\mathbf{u}' + \mathbf{C}^T\mathbf{u}\right)\cdot\mathbf{v}\right]_0^l,\\
&= \langle \mathcal{S}\mathbf{v}, \mathbf{u}\rangle + \left[\left(\mathbf{P}\mathbf{v}' + \mathbf{C}^T\mathbf{v}\right)\cdot\mathbf{u}\right]_0^l - \left[\left(\mathbf{P}\mathbf{u}' + \mathbf{C}^T\mathbf{u}\right)\cdot\mathbf{v}\right]_0^l.
\end{aligned}$$

□

This lemma also proves the self-adjoint nature of the $\mathcal{S}$ operator for the functions $\mathbf{u}, \mathbf{v} \in \mathcal{A}$, i.e.,

$$\langle \mathcal{S}\mathbf{u}, \mathbf{v} \rangle = \langle \mathbf{u}, \mathcal{S}\mathbf{v} \rangle.$$

The *Jacobi differential operator* $\mathcal{S}$ can be represented in the Hamiltonian form (Caratheodery, 1967) using the Hamiltonian H as

$$\begin{bmatrix} \mathbf{h} \\ \mathbf{k} \end{bmatrix}' = \begin{bmatrix} \mathbf{0} & \mathbf{I} \\ -\mathbf{I} & \mathbf{0} \end{bmatrix} \begin{bmatrix} H_{\zeta\zeta} & H_{\zeta\mathbf{p}} \\ H_{\mathbf{p}\zeta} & H_{\mathbf{pp}} \end{bmatrix} \begin{bmatrix} \mathbf{h} \\ \mathbf{k} \end{bmatrix},$$

where the additional variable $\mathbf{k}$ is the variation in the momentum $\mathbf{p}$, and it satisfies

$$\mathbf{k} = \mathbf{P}\mathbf{h}' + \mathbf{C}^T\mathbf{h}.$$

A necessary condition for the second variation quadratic functional (2.11) to be non-negative is that

$$\mathbf{P} \equiv \mathcal{L}_{\zeta'\zeta'} > 0, \quad \forall s \in [0, l], \tag{2.14}$$

i.e., the matrix $\mathbf{P}$ is positive definite, and this condition is also known as *Legendre's strengthened condition*. We shall always assume that $\mathcal{L}(\zeta, \zeta', s)$ satisfies this condition in addition to the strict convexity of $\mathcal{L}(\zeta, \zeta', s)$ with respect to ζ'. Then, the sufficient condition that the critical points ζ_o correspond to a non-negative second variation is the absence of *conjugate points* with respect to the *Jacobi differential equations* (2.12), which are defined as follows.

Definition 2.2.1. *The point $\sigma \in [0, l]$ is said to be a conjugate point with respect to the functional $\delta^2 J(\zeta_o)[h]$ if there exists a non-trivial solution $\mathbf{h}$ to*

$$\mathcal{S}\mathbf{h} = \mathbf{0}, \quad 0 < s < \sigma, \quad \mathbf{h}(0) = \mathbf{h}(\sigma) = \mathbf{0}. \tag{2.15}$$

This sufficient condition is also termed as *Jacobi condition*. Morse (1951) extended this condition to define an *index*, which quantifies the maximal dimension of subspace over which the quadratic functional $\delta^2 J$ is negative and is given by the number of *conjugate points*. The *Jacobi condition* (2.15) can be included in the eigenvalue problem:

$$\mathcal{S}\mathbf{h} = \rho(\sigma)\mathbf{h}, \quad s \in [0, \sigma], \quad \mathbf{h}(0) = \mathbf{h}(\sigma) = \mathbf{0}. \tag{2.16}$$

When σ is the *conjugate point*, this eigenvalue problem has a zero eigenvalue. The eigenvalues ρ depend continuously on σ. The combination of *Legendre's strengthened condition*, *Sturm-Liouville problem*, and *Rayleigh quotients* give rise to the following set of properties (see e.g., (Manning et al., 1998) (presented in Appendix 1)):

Property 1: For any σ, the operator $\mathcal{S}$ has countable infinity of isolated eigenvalues $\rho_1(\sigma) \leq \rho_2(\sigma) \leq \cdots \leq \rho_\infty(\sigma)$, each with finite multiplicity.

Property 2: Each eigenvalue is a monotonically decreasing function of σ.

Property 3: For σ sufficiently close to 0, $\rho_i(\sigma) > 0$ for all $\forall i$.

By the last property, the eigenvalues $\rho_i(\sigma)$, $i = 1, \ldots, \infty$ are all positive for σ close to 0. As the point σ is moved from 0 towards l, the value of the eigenvalues $\rho_i(\sigma)$, $i = 1, \ldots, \infty$ decrease in accordance with Property 2. Upon encountering the first *conjugate point*, the smallest eigenvalue ρ_1 reaches zero and undergoes a sign change from positive to negative during the traversal. In this manner, n th eigenvalue $\rho_n(\sigma)$ transitions from a positive to a negative value upon traversing the n th *conjugate point*. Therefore, the *index* I defined as the number of *conjugate points* gives the number of negative eigenvalues of (2.16). It denotes the dimension of the basis, over which the functional (2.11) yields a negative value. If $I = 0$, there are no negative eigenvalues, and $\delta^2 J[\mathbf{h}]$ is non-negative for all $\mathbf{h} \in \mathcal{A}$. If $I > 0$, there exists a subspace of variations spanned by the eigenfunctions of negative eigenvalues over which $\delta^2 J[\mathbf{h}]$ is negative.

2.3 Second-Order Conditions: Fixed-Free ends

This section will delve into the relatively less explored second-order conditions pertaining to the case of fixed-free ends. Consider a variational problem where a functional of the form

$$J(\boldsymbol{\zeta}) = \int_0^l \mathcal{L}(\boldsymbol{\zeta}, \boldsymbol{\zeta}', s) ds + B(\boldsymbol{\zeta}(l)),$$

is minimized subject to fixed boundary conditions at the end $s = 0$ and free boundary conditions at the other end $s = l$. The critical points $\boldsymbol{\zeta}_o$ obtained as the solution the *Euler-Lagrange equations* (2.2) with the boundary conditions

$$\boldsymbol{\zeta}(0) = f_o, \quad \frac{\partial}{\partial \boldsymbol{\zeta}'} \mathcal{L}(\boldsymbol{\zeta}, \boldsymbol{\zeta}', l) + \frac{\partial}{\partial \boldsymbol{\zeta}} B(\boldsymbol{\zeta}(l)) = 0, \tag{2.17}$$

can be classified as local minima, if the second variation functional evaluated as

$$\delta^2 J(\boldsymbol{\zeta}_o)[\mathbf{h}] = \frac{1}{2} \int_0^l \left(\mathbf{h}' \cdot \mathbf{P}\mathbf{h}' + \mathbf{h} \cdot \mathbf{C}\mathbf{h}' + \mathbf{h}' \cdot \mathbf{C}^T \mathbf{h} + \mathbf{h} \cdot \mathbf{Q}\mathbf{h} \right) ds + \mathbf{B}\mathbf{h}(l) \cdot \mathbf{h}(l), \tag{2.18}$$

is non-negative. The matrices $\mathbf{P}, \mathbf{Q}$ and $\mathbf{C}$ are same as defined previously (2.8), and the additional term $\mathbf{B}$ is the matrix $\frac{\partial^2 B}{\partial \boldsymbol{\zeta}^2}$ evaluated at the free end $s = l$ and is symmetric in nature. The new set of boundary conditions (2.17) leads to the following class of admissible variations

$$\mathcal{B} = \{\mathbf{h} \in \mathcal{C}^1[0, l] : \mathbf{h}(0) = \mathbf{0}, \quad \mathbf{P}\mathbf{h}'(l) + \mathbf{C}^T \mathbf{h}(l) + \mathbf{B}\mathbf{h}(l) = \mathbf{0}\}. \tag{2.19}$$

The condition $\mathbf{P}\mathbf{h}' + \mathbf{C}^T \mathbf{h} + \mathbf{B}\mathbf{h}(l) \equiv \mathcal{L}_{\boldsymbol{\zeta}'\boldsymbol{\zeta}} \mathbf{h}(l) + \mathcal{L}_{\boldsymbol{\zeta}'\boldsymbol{\zeta}'}(l)\mathbf{h}'(l) + \mathbf{B}\mathbf{h}(l) = \mathbf{0}$ is the result of the linearization of the *Natural boundary condition* at the end $s = l$. After applying integration by

parts on (2.7), we obtain

$$\delta^2 J(\zeta_o)[\mathbf{h}] = \frac{1}{2}\int_0^l \left(-\frac{d}{ds}\left(\mathbf{P}\mathbf{h}' + \mathbf{C}^T\mathbf{h}\right) + \mathbf{C}\mathbf{h}' + \mathbf{Q}\mathbf{h}\right)\cdot \mathbf{h} ds + \Big[\left(\mathbf{P}\mathbf{h}' + \mathbf{C}^T\mathbf{h}\right)\cdot \mathbf{h}\Big]_0^l + \mathbf{B}\mathbf{h}(l)\cdot\mathbf{h}(l).$$

The boundary terms vanish and the second variation takes the form

$$\delta^2 J(\boldsymbol{\zeta}_o)[\mathbf{h}] \equiv \frac{1}{2}\langle \mathcal{S}\mathbf{h}, \mathbf{h}\rangle, \tag{2.20}$$

where $\mathcal{S}$ is the second-order differential *Jacobi operator* defined in the same manner as before in (2.11). The terms containing the matrix $\mathbf{B}$ have no contribution in the second variation functional $\delta^2 J[\mathbf{h}]$, as it is cancelled by the boundary term of the allowable variation $\mathbf{h}$ at $s = l$ from (2.19).

Given the *Legendre's strengthened condition* $\mathbf{P} > 0$, the absence of *conjugate points* ensures the non-negativity of the second variation functional (2.20). In this context of fixed-free cases, the notion of a *conjugate point* is somewhat altered as given below.

Definition 2.3.2. *For a simple case of $p = 1$, a point $l^* \in [0, l]$ is defined to be a point conjugate to l with respect to the functional $\delta^2 J(\boldsymbol{\zeta}_o)[\mathbf{h}]$ if there exists a non-trivial solution $\mathbf{h} : [0, l] \to \mathbb{R}$ satisfying*

$$\mathcal{S}\mathbf{h} = 0, \qquad \mathbf{h}(l^*) = 0, \quad \mathbf{h}(l) = 1, \quad \mathbf{h}'(l) = 0.$$

A one-point boundary condition must be stated at the boundary where the requirements on the derivatives are specified in the given variational problem.

***Conjugate point* (Higher dimension):** The solution of *Jacobi operator* $\mathbf{h} : [0, l] \to \mathbb{R}^p$ is a member of $2p$- parameter family with p parameters at each boundary $s = 0$ and $s = l$. Choose a boundary with *Natural boundary condition*, i.e., $s = l$ in our case and determine the p-parameter family of solutions $\mathbf{h}(s)$ emanating from this end

$$\mathbf{h}(s) = a_1\mathbf{h}^{(1)} + \cdots + a_p\mathbf{h}^{(p)}, \quad a_1, \ldots, a_p \in \mathbb{R}, \quad \mathbf{h}^{(1)}, \ldots, \mathbf{h}^{(p)} \in \mathbb{R}^p.$$

The point $l^* \in [0, l]$ is *conjugate* to l if a non-trivial solution $\mathbf{h}(s)$ satisfies

$$\mathcal{S}\mathbf{h} = \mathbf{0}, \quad \mathbf{h}(l^*) = \mathbf{0}, \quad \mathbf{P}\mathbf{h}'(l) + \mathbf{C}^T\mathbf{h}(l) + \mathbf{B}\mathbf{h}(l) = \mathbf{0}. \tag{2.21}$$

The boundary condition $\mathbf{P}\mathbf{h}'(l) + \mathbf{C}^T\mathbf{h}(l) + \mathbf{B}\mathbf{h}(l) = \mathbf{0}$ is accommodated by using a basis of solutions for $\mathbf{h}(l)$.

Definition 2.3.3. *Let*

$$\begin{aligned}
\mathbf{h}^{(1)} &= \left(h_1^{(1)}, h_2^{(1)}, \ldots, h_p^{(1)}\right), \\
\mathbf{h}^{(2)} &= \left(h_1^{(2)}, h_2^{(2)}, \ldots, h_p^{(2)}\right), \\
&\ldots. \\
\mathbf{h}^{(p)} &= \left(h_1^{(p)}, h_2^{(p)}, \ldots, h_p^{(p)}\right)
\end{aligned}$$

be a set of p solutions to the system where i th solution corresponds to the initial conditions

$$\mathbf{h}^{(i)}(l) = \mathbf{e}_i, \quad \mathbf{P}\mathbf{h}^{(i)\prime}(l) + \mathbf{C}^T\mathbf{h}^{(i)}(l) + \mathbf{B}\mathbf{h}^{(i)}(l) = \mathbf{0}, \quad i = 1, \ldots, p.$$

A point l^* is said to be conjugate point to l if the accessory extremal $\mathbf{h}(s)$, which is the linear combination of the basis vectors $\mathbf{h^{(i)}}(s)$, $i = 1, \ldots, p$, vanishes at $s = l^*$. This condition is satisfied when the determinant

$$\begin{vmatrix}
h_1^{(1)}(s) & h_2^{(1)}(s) & \ldots & h_p^{(1)}(s) \\
h_1^{(2)}(s) & h_2^{(2)}(s) & \ldots & h_p^{(2)}(s) \\
. & . & \ldots & . \\
h_1^{(p)}(s) & h_2^{(p)}(s) & \ldots & h_p^{(p)}(s)
\end{vmatrix} = 0,$$

at $s = l^*$.

Next, we will present the proofs for the conditions on the $\mathcal{S}$ operator, which ensures that the equilibrium $\boldsymbol{\zeta}_o$ corresponds to local minima. For the sake of simplicity, we don't include the boundary term $B(\boldsymbol{\zeta}(l))$ in the subsequent analysis, i.e., $B(\zeta(l)) = 0$, and the matrix $\mathbf{B}$ is a zero matrix. Nonetheless, the presented results can be straightforwardly extended to the cases with the non-zero $B(\boldsymbol{\zeta}(l))$.

Theorem 2.3.1. *If the matrix $\mathbf{P}$ is strictly positive definite, and the interval $[0, l]$ contains no point conjugate to l, then the second variation quadratic functional $\delta^2 J(\boldsymbol{\zeta}_o)[\mathbf{h}]$ is positive for all $\mathbf{h}(s) \in \mathcal{B}$.*

Proof. This proof parallels the proof for fixed-fixed boundary conditions presented by Gelfand and Fomin (1963) and is slightly generalized. Let $\mathbf{W} : s \longrightarrow \mathbb{R}^{p\times p}$ be an arbitrary differentiable symmetric matrix. Without affecting the values of the second variation integral (2.7), we can add the following term

$$\begin{aligned}
0 &= \int_0^l \frac{d}{ds}\left(\mathbf{W}\mathbf{h}\cdot\mathbf{h}\right) ds - \left[\mathbf{W}\mathbf{h}\cdot\mathbf{h}\right]_0^l, \\
0 &= \int_0^l \mathbf{W}'\mathbf{h}\cdot\mathbf{h} + \mathbf{W}\mathbf{h}'\cdot\mathbf{h} + \mathbf{W}\mathbf{h}\cdot\mathbf{h}' ds + \left(\mathbf{W}(l)\mathbf{h}(l)\cdot\mathbf{h}(l) - \mathbf{W}(0)\mathbf{h}(0)\cdot\mathbf{h}(0)\right).
\end{aligned}$$

The matrix function $\mathbf{W}(s)$ is chosen such that the boundary terms vanish. For the current case with fixed-free ends, we have $\mathbf{h}(0) = \mathbf{0}$ at the fixed end, and we require $\mathbf{h}(l)\cdot\mathbf{W}(l)\mathbf{h}(l) = 0$ at the free end. The latter condition is satisfied for any non-trivial $\mathbf{h}(l)$ when $\mathbf{W}(l)$ is a zero matrix of order p, denoted by $\mathbf{O}$. This condition also holds if $\mathbf{W}(l)$ is a skew-symmetric matrix, but it

contradicts the symmetric matrix assumption of $\mathbf{W}(s)$ and, therefore, is disregarded. Then, the integral (2.7) becomes

$$\delta^2 J(\boldsymbol{\zeta}_o)[\mathbf{h}] = \int_0^l \mathbf{P}\mathbf{h}' \cdot \mathbf{h}' + (\mathbf{C} + \mathbf{W})\,\mathbf{h} \cdot \mathbf{h}' + (\mathbf{C} + \mathbf{W})^T \mathbf{h}' \cdot \mathbf{h} + \left(\mathbf{Q} + \mathbf{W}'\right)\mathbf{h} \cdot \mathbf{h} ds.$$

The integrand can be expressed as a perfect square of the form

$$\delta^2 J(\boldsymbol{\zeta}_o)[\mathbf{h}] = \int_0^l \left(\mathbf{P}^{1/2}\mathbf{h}' + \left(\mathbf{Q} + \mathbf{W}'\right)^{1/2}\mathbf{h}\right) \cdot \left(\mathbf{P}^{1/2}\mathbf{h}' + \left(\mathbf{Q} + \mathbf{W}'\right)^{1/2}\mathbf{h}\right) ds,$$

if the matrix $\mathbf{W}(s)$ is chosen to be the solution of

$$\mathbf{P}^{1/2}\left(\mathbf{Q} + \mathbf{W}'\right)^{1/2} = (\mathbf{C} + \mathbf{W})^T, \tag{2.22a}$$

$$\Longrightarrow \mathbf{Q} + \mathbf{W}' = (\mathbf{C} + \mathbf{W})\,\mathbf{P}^{-1}\left(\mathbf{C}^T + \mathbf{W}\right). \tag{2.22b}$$

Since $\mathbf{P}$ is assumed to be a positive definite symmetric matrix, its square root $\mathbf{P}^{1/2}$ exists and is also positive definite. Moreover, its inverse $\mathbf{P}^{-1/2}$ exists. The expression (2.22b) is called *Matrix Ricatti equation*, and the second variation integral takes the form

$$\begin{aligned}\delta^2 J(\boldsymbol{\zeta}_o)[\mathbf{h}] &= \int_0^l \left(\mathbf{P}^{1/2}\mathbf{h}' + (\mathbf{Q} + \mathbf{W})\,\mathbf{Q}^{-1/2}\mathbf{h}\right) \cdot \left(\mathbf{P}^{1/2}\mathbf{h}' + (\mathbf{Q} + \mathbf{W})\,\mathbf{Q}^{-1/2}\mathbf{h}\right) ds, \\ &= \int_0^l \mathbf{P}\left(\mathbf{h}' + \mathbf{P}^{-1/2}\,(\mathbf{Q} + \mathbf{W})\,\mathbf{Q}^{-1/2}\mathbf{h}\right) \cdot \left(\mathbf{h}' + \mathbf{P}^{-1/2}\,(\mathbf{Q} + \mathbf{W})\,\mathbf{Q}^{-1/2}\mathbf{h}\right) ds,\end{aligned}$$

where the integrand is a perfect square and is always non-negative. This expression

$$\mathbf{P}^{1/2}\mathbf{h}' + (\mathbf{Q} + \mathbf{W})\,\mathbf{Q}^{-1/2}\mathbf{h},$$

vanishes only for the trivial solution $\mathbf{h}(s) = \mathbf{0}$. If the *Matrix Ricatti equation* has a continuous solution $\mathbf{W}(s)$ defined over the interval $[0, l]$, then the second variation is positive definite. Substituting

$$\mathbf{C}^T + \mathbf{W} = -\mathbf{P}\mathbf{U}'\mathbf{U}^{-1} \Longrightarrow \mathbf{P}\mathbf{U}' + \mathbf{C}^T\mathbf{U} + \mathbf{W}\mathbf{U} = \mathbf{O}, \tag{2.23}$$

where $\mathbf{U}$ is a new unknown matrix results in

$$-\frac{d}{ds}\left(\mathbf{P}\mathbf{U}' + \mathbf{C}^T\mathbf{U}\right) + \left(\mathbf{C}\mathbf{U}' + \mathbf{Q}\mathbf{U}\right) = \mathbf{O}, \tag{2.24}$$

which is the matrix form of the *Jacobi operator* $\mathcal{S}$. Now, consider the boundary term at $s = l$. In the present case, the matrix $\mathbf{W}(l)$ is chosen to be a zero matrix, and the relation (2.23) yields the boundary condition

$$\mathbf{W}(l) = \mathbf{O} \Longrightarrow \mathbf{P}\mathbf{U}'(l) + \mathbf{C}^T\mathbf{U}(l) = \mathbf{O}.$$

This is a matrix form of the linearized *Natural boundary condition* at the boundary $s = l$. The columns in matrix $\mathbf{U}$ can be interpreted as the basis of the variations $\mathbf{h}$. If $[0, l]$ contains no point *conjugate* to l, then (2.24) has a solution $\mathbf{U}(s)$ which is non-singular in $[0, l]$. Therefore, the

Matrix Ricatti equation (2.22b) has a solution given by (2.23). Thus, there exists a matrix $\mathbf{W}(s)$ that transforms the integrand to a perfect square, producing a non-negative second variation $\delta^2 J(\boldsymbol{\zeta}_o)[\mathbf{h}]$. □

Theorem 2.3.2. *If the matrix* $\mathbf{P}$ *is positive definite and the interval* $[0, l]$ *contains a point conjugte to* l*, then the second variation quadratic functional* $\delta^2 J(\boldsymbol{\zeta}_o)[\mathbf{h}]$ *is not positive for all* $\mathbf{h} \in \mathcal{B}$.

Proof. Suppose there exists a point $s = l^*$ *conjugate* to $s = l$ in $0 < s < l$. Consequently, there exists a non-null accessory extremal $\mathbf{h}(s)$ satisfying $\mathbf{h}(l^*) = \mathbf{0}$ and $\mathbf{P}\mathbf{h}'(l) + \mathbf{C}^T\mathbf{h}(l) = \mathbf{0}$. Let $\boldsymbol{\gamma}(s)$ be a continuous arc defined as

$$\boldsymbol{\gamma}(s) = \begin{cases} \mathbf{0}, & 0 < s < l^*, \\ \mathbf{h}(s), & l^* < s < l, \end{cases}$$

and is depicted in Figure (2.1).

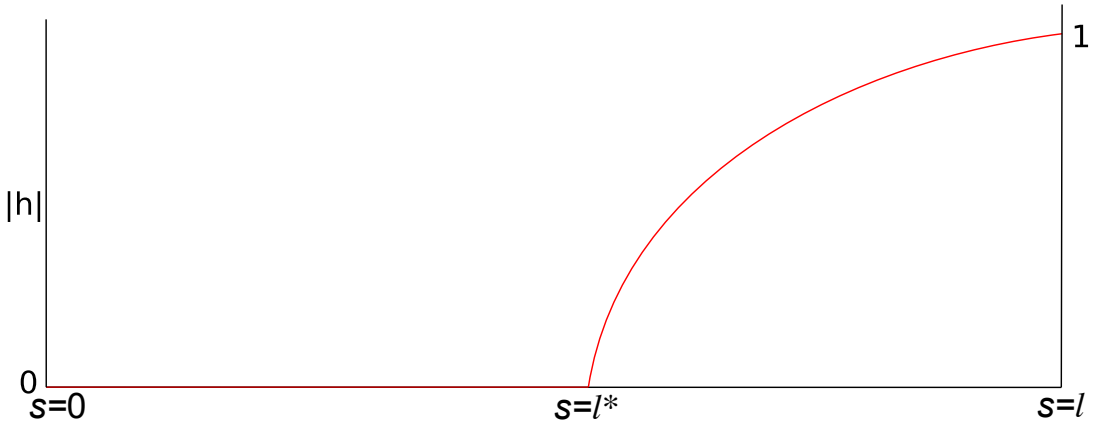

Fig. 2.1 The broken accessory extremal $\gamma(s) \in \mathcal{B}$

The second variation $\delta^2 J(\boldsymbol{\zeta}_o)$ along the arc $\boldsymbol{\gamma}$ is given by

$$\begin{aligned} \delta^2 J(\boldsymbol{\zeta}_o)[\boldsymbol{\gamma}] &= \frac{1}{2}\int_0^l \mathcal{S}\boldsymbol{\gamma}(s)\cdot\boldsymbol{\gamma}(s)ds, \\ &= \frac{1}{2}\int_{l^*}^l \mathcal{S}\mathbf{h}(s)\cdot\mathbf{h}(s)ds, \\ &= \frac{1}{2}\Big[\big(\mathbf{P}(s)\mathbf{h}'(s) + \mathbf{C}^T(s)\mathbf{h}(s)\big)\cdot\mathbf{h}(s)\Big]_l^{l^*} = 0. \end{aligned}$$

However, this arc $\boldsymbol{\gamma}(s)$ has a *corner point* at $s = l^*$, as $\mathbf{h}'(l^*-) \neq \mathbf{h}'(l^*+)$. If the matrix $\mathbf{P}(s)$ is positive definite, then by *Weierstrass-Erdmann conditions* (2.6a), the arc γ with a *corner point* cannot be the local minimizer. But, the second variation functional $\delta^2 J$ is zero along the present *broken extremal* $\gamma(s)$. Therefore, there must exist another arc $\mathbf{h}(s) \in \mathcal{B}$ which is a local minimizer and further reduces the second variation $\delta^2 J < 0$, thereby proving the theorem. □

Similar to the prior scenario, the *Jacobi condition* on a fixed-free case can be used to define the notion of *Morse index*, which quantifies the maximal subspace of variations $\mathbf{h}$ over which $\delta^2 J[\mathbf{h}]$ is negative. The present *Jacobi condition* can be reformulated into the following eigenvalue problem

$$\begin{aligned} \mathcal{S}\mathbf{h} = \rho(l^*)\mathbf{h}, \quad l^* < s < l, \quad \mathbf{P}\mathbf{h}'(l) + \mathbf{C}^T\mathbf{h}(l) = 0, \\ \mathbf{h}(l^*) = 0. \end{aligned} \tag{2.25}$$

Therefore, $\rho(l^*)$ is a zero eigenvalue when l^* is a *conjugate point*. As long as the $\mathcal{S}$ operator is self-adjoint, the properties mentioned in the prior section can be generalized to this scenario with minor modifications. The eigenvalues $\rho(l^*)$ continuously depend on l^*. Using the combination of *Legengre's strengthened condition*, *Sturm-Liouville problem*, and *Rayleigh quotients*, the following set of properties (Appendix 1) are defined:

Property 1 For any given $l^* \in [0, l]$, the operator $\mathcal{S}$ has a countably infinite number of eigenvalues. $\rho_1(l^*) \leq \rho_2(l^*) \leq \ldots$, each with finite multiplicity.

Property 2 Each eigenvalue $\rho_j(l^*)$, $j = 1, 2, \ldots, \infty$ is monotonically increasing with l^*.

Property 3 For l^* sufficiently close to l, $\rho_j(l^*) > 0$, for all $j = 1, 2, \ldots, \infty$.

The eigenvalues are positive for l^* sufficiently close to l (by Property 3). As the point l^* is moved from l to 0, each eigenvalue ρ_j, $j = 1, 2, \ldots, \infty$ decreases owing to property 2. When l^* transverses the *conjugate point* for the first time, the lowest eigenvalue ρ_1 changes its sign from positive to negative. Similarly, the eigenvalue ρ_n crosses zero, as the l^* transverses n th *conjugate point*. As a result, the *index I* given by the number of *conjugate points* corresponds to the number of negative eigenvalues of (2.25) and represents the dimension of space of eigenfunctions over which the functional $\delta^2 J$ is negative.

2.4 Distinguished Bifurcation Diagram

Calculus of Variation problems are often expressed in terms of system parameters, leading to a parameter-dependent family of equilibria. These parameters are typically involved in either the integrand or the boundary conditions. In the past, Maddocks (1984, 1985, 1987) studied the stability of rod equilibria by casting them as parameter-dependent variational problems. Generally, bifurcation diagrams were employed in the analysis of these problems, where a specific projection of the solutions conveys the stability exchange information. The key to predicting stability changes is selecting the appropriate projection to plot. The structure of the variational problem can be exploited to study the second variation without verifying the *Jacobi condition* by employing *distinguished bifurcation diagrams*. The stability properties of the solutions can be deduced from this diagram with a little observation and without any additional analysis. Maddocks (1987) derived the ordinate of bifurcation diagrams for parameter-dependent variational problems. In this instance, only homogeneous boundary conditions are considered, and the bi-

furcation parameter appears either in the integrand of the functional or as a Lagrange multiplier in a constrained calculus of variations problem. This concept is later expanded to the variational problems with non-homogeneous boundary conditions (Rogers, 1997), where the varying parameter appears in the boundary conditions. In this case, both ends are subjected to fixed boundary conditions. In this section, we verify these *distinguished bifurcation diagram* for the unconstrained calculus of variations problem if one of the fixed ends is set free.

Consider an unconstrained parameter-dependent variational problem:

$$J(\boldsymbol{\zeta}, \xi) = \int_0^l \mathcal{L}(\boldsymbol{\zeta}, \boldsymbol{\zeta}', s)ds + B(\boldsymbol{\zeta}(l)), \tag{2.26}$$

subject to a parameter-dependent *Dirichlet boundary condition* at the end $s = 0$

$$\boldsymbol{\zeta}(0) = \boldsymbol{\zeta}_o(\xi),$$

and *Natural boundary condition* at the other end $s = l$, where $\xi \in \mathbb{R}$ is the parameter. The critical points $(\boldsymbol{\zeta}(s,\tau), \xi(\tau))$ obtained as a solution to the *Euler-Lagrange equations*

$$-\mathcal{L}'_{\boldsymbol{\zeta}'} + \mathcal{L}_{\boldsymbol{\zeta}} = \mathbf{0}, \qquad \boldsymbol{\zeta}(0) = \boldsymbol{\zeta}_o(\xi), \quad \mathbf{p}(l) + \frac{\partial}{\partial \boldsymbol{\zeta}} B(\zeta(l)) = \mathbf{0}, \tag{2.27}$$

exist as a continuous curve of solutions along a branch for some pseudo-arclength parameterization τ satisfying

$$\left|\dot{\boldsymbol{\zeta}}(s,\tau)\right|^2 + \left|\dot{\xi}(\tau)\right|^2 = 1.$$

Chapter 4 provides a more extensive discussion on pseudo-arclength τ. The notation $\dot{\boldsymbol{\zeta}}(s,\tau)$ denotes the derivative with respect to pseudo-arclength τ, and $\boldsymbol{\zeta}'(s,\tau)$ denotes the derivative with respect to arc length s. These critical points $(\boldsymbol{\zeta}(s,\tau), \xi(\tau))$ must satisfy the second-order necessary condition

$$\delta^2 J(\boldsymbol{\zeta}, \xi)[\mathbf{h}] \equiv \frac{1}{2}\langle \mathcal{S}\mathbf{h}, \mathbf{h}\rangle \geq 0, \quad \forall \mathbf{h} \in \mathcal{B}, \tag{2.28}$$

so that they correspond to minima of the functional $J(\boldsymbol{\zeta}, \xi)$. This condition can also be interpreted as a requirement that the linear eigenvalue problem:

$$\begin{aligned} &\mathcal{S}\mathbf{h} = \mu\mathbf{h}, \\ &\mathbf{h}(0) = \mathbf{0}, \\ &\mathbf{P}\mathbf{h}'(l) + \mathbf{C}^T\mathbf{h}(l) + \mathbf{B}\mathbf{h}(l) = \mathbf{0}, \end{aligned} \tag{2.29}$$

has only non-negative eigenvalues. The matrices $\mathbf{P}, \mathbf{C}$ and $\mathbf{Q}$ that appear in the operator $\mathcal{S}$ depend on the pseudo-arclength τ and the parameter ξ through $\boldsymbol{\zeta}(s,\tau)$ and $\boldsymbol{\zeta}'(s,\tau)$. Consequently, the operator $\mathcal{S}$ is assumed to have eigenvalues and eigenfunctions that depend smoothly on pseudo-arclength τ. Parameter-dependent variational problems yield a family of extremals, and in the case of a single parameter ξ, they correspond to a curve of solutions. Sometimes,

these solutions are characterized by folds, the points at which the slope of this curve is vertical. Before delving into further details, we briefly describe the folds.

The *Euler-Lagrange equations* can also be represented as a stationary point of the derivative of the functional $J(\boldsymbol{\zeta}(\tau), \xi(\tau))$

$$J_{\boldsymbol{\zeta}}(\boldsymbol{\zeta}(\tau), \xi(\tau)) = 0. \tag{2.30}$$

Differentiating (2.30) with respect to pseudo-arclength τ along the solution branch fetches

$$J_{\boldsymbol{\zeta}\boldsymbol{\zeta}}\dot{\boldsymbol{\zeta}} + J_{\boldsymbol{\zeta}\xi}\dot{\xi} = 0.$$

A point $(\boldsymbol{\zeta}(\tau_o), \xi(\tau_o))$ is called a fold if $\dot{\xi}(\tau_o) = 0$. As $\left|\dot{\boldsymbol{\zeta}}\right|^2 + \dot{\xi}^2 = 1$, the vector $\dot{\boldsymbol{\zeta}}$ is the null vector of the Hessian matrix $J_{\boldsymbol{\zeta}\boldsymbol{\zeta}}$. A *simple fold* in addition also satisfies

$$\ddot{\xi}(\tau_o) \neq 0, \qquad \frac{d}{d\tau} J_{\xi}\Big|_{\tau=\tau_o} \neq 0,$$

and zero is a simple eigenvalue of the operator $J_{\boldsymbol{\zeta}\boldsymbol{\zeta}}$. Standard bifurcation theory conveys that the folds in this solution curve indicate the exchange of stability (see e.g., (Golubitsky and Schaeffer, 2014)). At these points, one of the eigenvalues of (2.29) transitions from a positive value to a negative value, or vice versa. By employing the variational structure, the direction of this change can be correlated to the derivative of the eigenvalues with respect to pseudo-arclength τ. We shall demonstrate that the eigenvalue problem (2.29) has a zero eigenvalue for the critical points at a fold. We proceed by differentiating the *Euler-Lagrange equations* (2.27) and the non-linear boundary conditions with respect to τ to yield

$$\begin{aligned} &\mathcal{S}\dot{\boldsymbol{\zeta}} = \mathbf{0}, \\ &\dot{\boldsymbol{\zeta}}(0) \equiv \frac{d\boldsymbol{\zeta}_o}{d\xi}\dot{\xi}, \quad \mathbf{P}\dot{\boldsymbol{\zeta}}'(l) + \mathbf{C}^T\dot{\boldsymbol{\zeta}}(l) + \mathbf{B}\dot{\boldsymbol{\zeta}}(l) = \mathbf{0}. \end{aligned} \tag{2.31}$$

On comparing this boundary value problem (BVP) with the eigenvalue problem (2.29), we observe that it has a zero eigenvalue when $\dot{\xi} = 0$, i.e., at a fold. The eigenvalue μ changes its sign as a fold point is traversed, and $\dot{\mu}\left(\equiv \frac{\partial \mu}{\partial \tau}\right)$ gives the direction of change. The expression for $\dot{\mu}$ is obtained by differentiating the eigenvalue problem (2.29) with respect to pseudo-arclength τ as

$$\begin{aligned} &\mathcal{S}\dot{\boldsymbol{\eta}} + \dot{\mathcal{S}}\boldsymbol{\eta} = \dot{\mu}\boldsymbol{\eta} + \mu\dot{\boldsymbol{\eta}}, \\ &\dot{\boldsymbol{\eta}}(0) = \mathbf{0}, \quad \mathbf{P}\dot{\boldsymbol{\eta}}'(l) + \mathbf{C}^T\dot{\boldsymbol{\eta}}'(l) + \mathbf{B}\dot{\boldsymbol{\eta}}'(l) + \dot{\mathbf{P}}\boldsymbol{\eta}(l) + \dot{\mathbf{C}}^T\boldsymbol{\eta}'(l) + \dot{\mathbf{B}}\boldsymbol{\eta}'(l) = \mathbf{0}. \end{aligned} \tag{2.32}$$

Here, the term $\dot{\mathcal{S}}\boldsymbol{\eta}$ is interpreted as

$$\dot{\mathcal{S}}\boldsymbol{\eta} = -\frac{d}{ds}\left(\dot{\mathbf{P}}\boldsymbol{\eta}' + \dot{\mathbf{C}}^T\boldsymbol{\eta}\right) + \dot{\mathbf{C}}\boldsymbol{\eta}' + \dot{\mathbf{Q}}\boldsymbol{\eta}, \tag{2.33}$$

where the matrices $\dot{\mathbf{P}}, \dot{\mathbf{C}}, \dot{\mathbf{Q}}$ denote the derivatives of the matrices $\mathbf{P}, \mathbf{C}, \mathbf{Q}$ respectively with

respect to pseudo-arclength τ. We assume that the $\mu = 0$ is a simple eigenvalue at the fold, and therefore, $\dot{\boldsymbol{\zeta}}$ is the corresponding eigenvector $\boldsymbol{\eta}$. Taking the L^2-inner product of the equation (2.32) at this fold point with eigenvector $\dot{\boldsymbol{\zeta}}$ yields the expression

$$\dot{\mu}\langle\dot{\boldsymbol{\zeta}},\dot{\boldsymbol{\zeta}}\rangle = \langle\mathcal{S}\dot{\boldsymbol{\eta}},\dot{\boldsymbol{\zeta}}\rangle + \langle\dot{\mathcal{S}}\dot{\boldsymbol{\zeta}},\dot{\boldsymbol{\zeta}}\rangle. \tag{2.34}$$

We use the integration by parts (2.13) to simplify the terms in this expression. The first term in R.H.S $\langle\mathcal{S}\dot{\boldsymbol{\eta}},\dot{\boldsymbol{\zeta}}\rangle$ can be rewritten as

$$\langle\mathcal{S}\dot{\boldsymbol{\eta}},\dot{\boldsymbol{\zeta}}\rangle = \langle\mathcal{S}\dot{\boldsymbol{\zeta}},\dot{\boldsymbol{\eta}}\rangle - \Big[\left(\mathbf{P}\dot{\boldsymbol{\eta}}' + \mathbf{C}^T\dot{\boldsymbol{\eta}} + \mathbf{B}\dot{\boldsymbol{\eta}}\right)\cdot\dot{\boldsymbol{\zeta}}\Big]_0^l + \Big[\left(\mathbf{P}\dot{\boldsymbol{\zeta}}' + \mathbf{C}^T\dot{\boldsymbol{\zeta}} + \mathbf{B}\dot{\boldsymbol{\zeta}}\right)\cdot\dot{\boldsymbol{\eta}}\Big]_0^l.$$

At the fold, $\mathcal{S}\dot{\boldsymbol{\zeta}} = \mathbf{0}$ and the boundary terms satisfy $\dot{\boldsymbol{\eta}}(0) = \mathbf{0}$, $\dot{\boldsymbol{\zeta}}(0) = \mathbf{0}$, and $\mathbf{P}\dot{\boldsymbol{\zeta}}'(l) + \mathbf{C}^T\dot{\boldsymbol{\zeta}}(l) + \mathbf{B}\dot{\boldsymbol{\zeta}}(l) = \mathbf{0}$. Additionally, by employing the relation (2.32), the terms $\dot{\boldsymbol{\eta}}(l)$ and $\dot{\boldsymbol{\eta}}'(l)$ can be eliminated. After the transformations, we arrive at

$$\langle\mathcal{S}\dot{\boldsymbol{\eta}},\dot{\boldsymbol{\zeta}}\rangle = -\left(\mathbf{P}\dot{\boldsymbol{\eta}}' + \mathbf{C}^T\dot{\boldsymbol{\eta}} + \mathbf{B}\dot{\boldsymbol{\eta}}\right)\cdot\dot{\boldsymbol{\zeta}}\Big|_{s=l} = \left(\dot{\mathbf{P}}\boldsymbol{\eta}' + \dot{\mathbf{C}}^T\boldsymbol{\eta} + \dot{\mathbf{B}}\boldsymbol{\eta}\right)\cdot\dot{\boldsymbol{\zeta}}\Big|_{s=l}.$$

Now consider the remaining term $\langle\dot{\mathcal{S}}\dot{\boldsymbol{\zeta}},\dot{\boldsymbol{\zeta}}\rangle$. On differentiating (2.31) with respect to pseudo-arclength τ, we get the relation $\langle\dot{\mathcal{S}}\dot{\boldsymbol{\zeta}},\dot{\boldsymbol{\zeta}}\rangle = -\langle\mathcal{S}\ddot{\boldsymbol{\zeta}},\dot{\boldsymbol{\zeta}}\rangle$ and the boundary conditions

$$\ddot{\boldsymbol{\zeta}}(0) = \frac{\partial^2\boldsymbol{\zeta}_o}{\partial\xi^{22}}\dot{\xi}^2 + \frac{\partial\boldsymbol{\zeta}_o}{\partial\xi}\ddot{\xi} = \frac{\partial\boldsymbol{\zeta}_o}{\partial\xi}\ddot{\xi}, \tag{2.35a}$$

$$\ddot{\boldsymbol{\zeta}}(l) \equiv \mathbf{P}\ddot{\boldsymbol{\zeta}} + \mathbf{C}^{\mathbf{T}}\ddot{\boldsymbol{\zeta}}' + \mathbf{B}\ddot{\boldsymbol{\zeta}}' + \dot{\mathbf{P}}\dot{\boldsymbol{\zeta}} + \dot{\mathbf{C}}^{\mathbf{T}}\dot{\boldsymbol{\zeta}}' + \dot{\mathbf{B}}\dot{\boldsymbol{\zeta}}' = \mathbf{0}. \tag{2.35b}$$

Consequently, the term $-\langle\mathcal{S}\ddot{\boldsymbol{\zeta}},\dot{\boldsymbol{\zeta}}\rangle$ can be rewritten using integration by parts result (Lemma (2.13)) as

$$-\langle\mathcal{S}\ddot{\boldsymbol{\zeta}},\dot{\boldsymbol{\zeta}}\rangle = -\langle\ddot{\boldsymbol{\zeta}},\mathcal{S}\dot{\boldsymbol{\zeta}}\rangle + \left[\left(\mathbf{P}\ddot{\boldsymbol{\zeta}}' + \mathbf{C}^T\ddot{\boldsymbol{\zeta}} + \mathbf{B}\ddot{\boldsymbol{\zeta}}\right)\cdot\dot{\boldsymbol{\zeta}}\right]_0^l - \left[\left(\mathbf{P}\dot{\boldsymbol{\zeta}}' + \mathbf{C}^T\dot{\boldsymbol{\zeta}} + \mathbf{B}\dot{\boldsymbol{\zeta}}\right)\cdot\ddot{\boldsymbol{\zeta}}\right]_0^l.$$

By enforcing the boundary conditions (2.31) that the boundary term $\mathbf{P}\dot{\boldsymbol{\zeta}}' + \mathbf{C}^T\dot{\boldsymbol{\zeta}} + \mathbf{B}\dot{\boldsymbol{\zeta}}$ at $s = l$ vanishes, and that $\dot{\boldsymbol{\zeta}}(0)$ at the fold is zero along with the relations (2.35a), $\mathbf{P} = \mathbf{P}^T$, we deduce

$$\begin{aligned}
-\langle\mathcal{S}\ddot{\boldsymbol{\zeta}},\dot{\boldsymbol{\zeta}}\rangle &= \left(\mathbf{P}\dot{\boldsymbol{\zeta}}' + \mathbf{C}^T\dot{\boldsymbol{\zeta}} + \mathbf{B}\dot{\boldsymbol{\zeta}}\right)\cdot\ddot{\boldsymbol{\zeta}}\Big|_{s=0} + \left(\mathbf{P}\ddot{\boldsymbol{\zeta}}' + \mathbf{C}^T\ddot{\boldsymbol{\zeta}} + \mathbf{B}\ddot{\boldsymbol{\zeta}}\right)\cdot\dot{\boldsymbol{\zeta}}\Big|_{s=l},\\
&= \ddot{\xi}\left(\frac{\partial\boldsymbol{\zeta}_o}{\partial\xi}\cdot\mathbf{P}\dot{\boldsymbol{\zeta}}'\right)\Big|_{s=0} + \left(\mathbf{C}^T\dot{\boldsymbol{\zeta}} + \mathbf{B}\dot{\boldsymbol{\zeta}}\right)\cdot\ddot{\boldsymbol{\zeta}}\Big|_{s=0} + \left(\mathbf{P}\ddot{\boldsymbol{\zeta}}' + \mathbf{C}^T\ddot{\boldsymbol{\zeta}} + \mathbf{B}\ddot{\boldsymbol{\zeta}}\right)\cdot\dot{\boldsymbol{\zeta}}\Big|_{s=l},\\
&= \ddot{\xi}\left(\frac{\partial\boldsymbol{\zeta}_o}{\partial\xi}\cdot\mathbf{P}\dot{\boldsymbol{\zeta}}'\right)\Big|_{s=0} + \left(\mathbf{P}\ddot{\boldsymbol{\zeta}}' + \mathbf{C}^T\ddot{\boldsymbol{\zeta}} + \mathbf{B}\ddot{\boldsymbol{\zeta}}\right)\cdot\dot{\boldsymbol{\zeta}}\Big|_{s=l},\\
&= \ddot{\xi}\left(\frac{\partial\boldsymbol{\zeta}_o}{\partial\xi}\cdot\mathbf{P}\dot{\boldsymbol{\zeta}}'\right)\Big|_{s=0} - \left(\dot{\mathbf{P}}\dot{\boldsymbol{\zeta}}' + \dot{\mathbf{C}}^T\dot{\boldsymbol{\zeta}} + \dot{\mathbf{B}}\dot{\boldsymbol{\zeta}}\right)\cdot\dot{\boldsymbol{\zeta}}\Big|_{s=l}.
\end{aligned}$$

In the last step, the relation (2.35b) is utilized in eliminating the $\ddot{\boldsymbol{\zeta}}$ and $\ddot{\boldsymbol{\zeta}}'$ terms. Finally, the

expression for the derivative $\dot{\mu}$ (2.34) after assuming $\dot{\boldsymbol{\zeta}}$ as a unit vector, takes the form

$$\begin{aligned}\dot{\mu} &= \langle \mathcal{S}\dot{\boldsymbol{\eta}}, \dot{\boldsymbol{\zeta}}\rangle - \langle \ddot{\mathcal{S}}\dot{\boldsymbol{\zeta}}, \dot{\boldsymbol{\zeta}}\rangle - \left(\dot{\mathbf{P}}\dot{\boldsymbol{\zeta}}' + \dot{\mathbf{C}}^T\dot{\boldsymbol{\zeta}} + \dot{\mathbf{B}}\dot{\boldsymbol{\zeta}}\right)\cdot\dot{\boldsymbol{\zeta}}\Big|_{s=l} + \left(\dot{\mathbf{P}}\boldsymbol{\eta}' + \dot{\mathbf{C}}^T\boldsymbol{\eta} + \dot{\mathbf{B}}\boldsymbol{\eta}\right)\cdot\dot{\boldsymbol{\zeta}}\Big|_{s=l}, \\ &= \ddot{\xi}\left(\frac{\partial\boldsymbol{\zeta}_o}{\partial\xi}\cdot\mathbf{P}\dot{\boldsymbol{\zeta}}'\right)\Big|_{s=0}.\end{aligned} \tag{2.36}$$

Near the fold point, the eigenvector $\boldsymbol{\eta} \equiv \dot{\boldsymbol{\zeta}}$ and $\dot{\xi}(0) = 0$. For the function $\mathbf{P} = \mathcal{L}_{\zeta'\zeta'}$, which is a symmetric matrix, one can write

$$\begin{aligned}\dot{\boldsymbol{\zeta}}'\cdot\mathcal{L}_{\zeta'\zeta'}\frac{\partial^2\boldsymbol{\zeta}_o}{\partial\xi^2}\Big|_{s=0} &= \left(\dot{\boldsymbol{\zeta}}'\cdot\mathcal{L}_{\zeta'\zeta'}\frac{\partial\boldsymbol{\zeta}_o}{\partial\xi} + \mathcal{L}_{\zeta\zeta'}\frac{\partial\boldsymbol{\zeta}_o}{\partial\xi}\dot{\xi}\cdot\frac{\partial\boldsymbol{\zeta}_o}{\partial\xi}\right)\Big|_{s=0}, \\ &= \left(\mathcal{L}_{\zeta'\zeta'}\dot{\boldsymbol{\zeta}}'\cdot\frac{\partial\boldsymbol{\zeta}_o}{\partial\xi} + \mathcal{L}_{\zeta\zeta'}\frac{\partial\boldsymbol{\zeta}_o}{\partial\xi}\dot{\xi}\cdot\frac{\partial\boldsymbol{\zeta}_o}{\partial\xi}\right)\Big|_{s=0} = \frac{d}{d\tau}\left(\mathcal{L}_{\zeta'}\cdot\frac{\partial\boldsymbol{\zeta}_o}{\partial\xi}\right)\Big|_{s=0}.\end{aligned} \tag{2.37}$$

In the end, on substituting the relation (2.37) in (2.36), the expression for the $\dot{\mu}$ can be rewritten as

$$\dot{\mu} = \ddot{\xi}\frac{d}{d\tau}\left(\mathcal{L}_{\zeta'}\cdot\frac{\partial\boldsymbol{\zeta}_o}{\partial\xi}\right)\Big|_{s=0}. \tag{2.38}$$

We define the plot of $\left[\mathcal{L}_{\zeta'}\cdot\frac{\partial\boldsymbol{\zeta}_o}{\partial\xi}\right]$ vs. ξ as a *distinguished bifurcation diagram* for our ξ-dependent variational problem. The sign of $\ddot{\xi}$ determines if the fold is opening to the right or the left. The sign of $\left[\mathcal{L}_{\zeta'}\cdot\frac{\partial\boldsymbol{\zeta}_o}{\partial\xi}\right]$ gives the direction of traversal at the fold. This combined qualitative information predicts if $\dot{\mu}$ is increasing or decreasing as it crosses the fold point, as illustrated in Figure 2.2. In brief, in a *simple fold* opening to the left on the bifurcation diagram, the lower branch has its *index*, i.e., the number of *conjugate points* lower than that on the upper branch. Likewise, the number of *conjugate points* increases in the lower branch of the fold opening to the right.

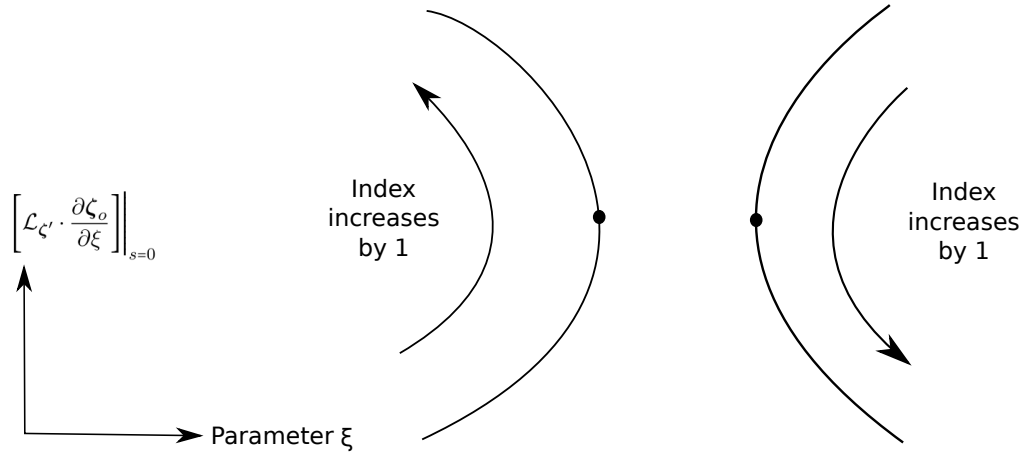

Fig. 2.2 The direction of *index* change in a *distinguished bifurcation diagram* for a parameter-dependent variational problem with one end fixed and the other end free.

In this chapter, we presented several mathematical tools, such as *conjugate points*, *Morse*

index, and *distinguished bifurcation diagrams* to analyze the stability of variational problems subject to fixed-free boundary conditions. Now, we shall use Kirchhoff elastic rods to put these techniques into practice in the real world. In the next chapter, we briefly present the Kirchhoff elastic rods and determine their equilibria along with their stability properties.

CHAPTER 3

Kirchhoff Elastic Theory of Rods

The formulation of elastic rods used in the examples is based on the *Kirchhoff rod theory*. In the *Special Cosserat rod theory* (Antman, 2006), the rod deforms such that the cross-sections remain planar throughout the process. These deformations may include flexure, torsion, axial tensions, and shear of the cross-section with respect to the axis. *Kirchhoff rod theory*, on the other hand, enables only flexure or torsion. In this chapter, we review the *Kirchhoff rod theory* commencing with kinematic equations.

3.1 Kinematics

An elastic rod is described as an orientable curve in 3D space using a centreline $\mathbf{r} : [0, l] \ni s \longrightarrow \mathbb{R}^3$ and an orientation frame spanned by the orthonormal unit vectors called directors $\mathbf{d}_i : s \longrightarrow \mathbb{R}^3, i = 1, 2, 3$. The independent variable s is the arc length of the unstressed rod. The centerline $\mathbf{r}(s)$ is often interpreted as the centroid of the material cross-section at s which is spanned by the directors $\mathbf{d}_1(s)$ and $\mathbf{d}_2(s)$ with $\mathbf{d}_3(s) = \mathbf{d}_1(s) \times \mathbf{d}_2(s)$ giving the normal of the cross-section. This director frame is connected to a fixed, right-handed laboratory, orthonormal frame with basis $\{\mathbf{e}_i\} \in \mathbb{R}^3$, $i = 1, 2, 3$ through a proper rotation matrix $\mathcal{R}(s) \in SO(3)$ by the relation

$$\mathbf{d}_i(s) = \mathcal{R}(s)\mathbf{e}_i, \qquad i = 1, 2, 3. \tag{3.1}$$

The rotation matrix $\mathcal{R}(s) \in SO(3)$ is given in terms of direction cosines of $\{\mathbf{d}_i(s)\}$ for $i = 1, 2, 3$ as

$$\mathcal{R}(s) = \begin{bmatrix} \mathbf{d}_1(s)\cdot\mathbf{e}_1 & \mathbf{d}_2(s)\cdot\mathbf{e}_1 & \mathbf{d}_3(s)\cdot\mathbf{e}_1 \\ \mathbf{d}_1(s)\cdot\mathbf{e}_2 & \mathbf{d}_2(s)\cdot\mathbf{e}_2 & \mathbf{d}_3(s)\cdot\mathbf{e}_2 \\ \mathbf{d}_1(s)\cdot\mathbf{e}_3 & \mathbf{d}_2(s)\cdot\mathbf{e}_3 & \mathbf{d}_3(s)\cdot\mathbf{e}_3 \end{bmatrix}. \tag{3.2}$$

The rate of change of $\mathbf{r}(s)$ with respect to s gives the stretch vector $\mathbf{v}(s) \in \mathbb{R}^3$ as

$$\mathbf{v}(s) = \mathbf{r}'(s),$$

where $()'$ denotes the differentiation with respect to arc length s. The first two components of $\mathbf{v}(s)$ with respect to the director frame, $v_1(s) \equiv \mathbf{v}(s)\cdot\mathbf{d}_1(s)$ and $v_2(s) \equiv \mathbf{v}(s)\cdot\mathbf{d}_2(s)$, correspond to transverse shearing, whereas the third component, $v_3(s) \equiv \mathbf{v}(s)\cdot\mathbf{d}_3(s)$, corresponds to stretching or compression of the rod.

The rate of change of the director frame $\{\mathbf{d}_1, \mathbf{d}_2, \mathbf{d}_3\}$ with respect to the arc length s is characterized through the Darboux vector $\mathbf{u} \in \mathbb{R}^3$ as

$$\mathbf{d}_i'(s) = \mathbf{u}(s) \times \mathbf{d}_i(s), \qquad i = 1, 2, 3.$$

Here, $\times$ denotes the cross product between two vectors. The vector $\mathbf{u}(s)$ is equivalent to the angular velocity of the director frames measured with respect to arc length s instead of time. The first two components of $\mathbf{u}(s)$ with respect to the director frame, $u_1(s) \equiv \mathbf{u}(s) \cdot \mathbf{d}_1(s)$ and $u_2(s) \equiv \mathbf{u}(s) \cdot \mathbf{d}_2(s)$, represent bending strains, whereas the third component, $u_3(s) \equiv \mathbf{u}(s) \cdot \mathbf{d}_3(s)$, represents twist (or torsion). Throughout this thesis, we are interested in strain components along the directors $\{\mathbf{d}_1, \mathbf{d}_2, \mathbf{d}_3\}$, and we will use $\mathtt{u}$ to denote the triad of components $[u_1, u_2, u_3]$.

3.2 Force and Moment Balance Laws

In rod mechanics, rod configurations under the action of loads are studied. These loads are transmitted along the rod cross-section as internal force $\mathbf{n}(s) \in \mathbb{R}^3$ and internal moment $\mathbf{m}(s) \in \mathbb{R}^3$ at $\mathbf{r}(s)$. The rod may be subject to an external distributed force $\mathbf{f}(s) \in \mathbb{R}^3$ and an external distributed moment $\mathbf{l}(s) \in \mathbb{R}^3$. Then the force and moment balance laws read

$$\mathbf{n}'(s) + \mathbf{f}(s) = \mathbf{0}, \tag{3.3a}$$

$$\mathbf{m}'(s) + \mathbf{r}'(s) \times \mathbf{n}(s) + \mathbf{l}(s) = \mathbf{0}. \tag{3.3b}$$

The local components $m_i(s) \equiv \mathbf{m}(s) \cdot \mathbf{d}_i(s)$, $i = 1, 2$ are called bending moments, and the component $m_3(s) \equiv \mathbf{m}(s) \cdot \mathbf{d}_3(s)$ is called twisting moment in the rod. We use $\mathtt{m}$ to denote the triad of these components $\mathtt{m} \equiv [m_1, m_2, m_3]$. Similarly, the first components of $n_i(s) \equiv \mathbf{n}(s) \cdot \mathbf{d}_i(s)$, $i = 1, 2$ are called shearing forces and $n_3(s) \equiv \mathbf{n}(s) \cdot \mathbf{d}_3(s)$ is called tension.

3.3 Constitutive Relations

Constitutive relations connect the kinematic variables $\mathbf{u}$(s) and $\mathbf{v}(s)$ along the rod with the transmitted forces $\mathbf{n}(s)$ and moments $\mathbf{m}(s)$. We are particularly interested in inextensible and unshearable cases, where the $\mathbf{d}_3$-axis is constrained to the tangent of the rod centerline $\mathbf{r}$(s) as shown in Figure (3.1), which is mathematically written as

$$\mathbf{r}'(s) = \mathbf{d}_3(s), \tag{3.4}$$

or equivalently

$$v_1(s) = v_2(s) = 0, \qquad v_3(s) = 1.$$

This restriction is to be satisfied no matter what load is applied to the rod, and the strain $\mathbf{v}(s)$ is no longer a variable and does not appear in the constitutive relations.

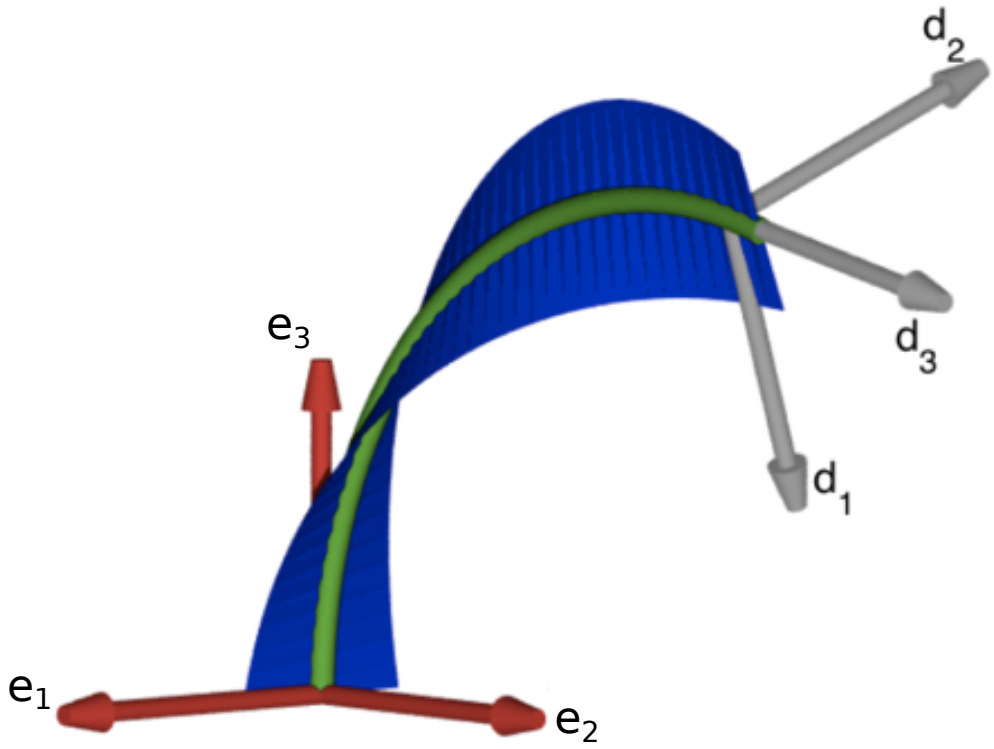

Fig. 3.1 Inextensibility and unshearability constrains the $\mathbf{d}_3-$axis to be the tangent of the position vector $\mathbf{r}$.

We consider the unstressed configuration or lowest energy configuration to be the reference state. Let $\hat{\mathfrak{u}} \equiv [\hat{u}_1(s), \hat{u}_2(s), \hat{u}_3(s)]$ be the triplet of strain components in its unstressed configuration. We also use the terms *intrinsic shape* or *precurvature* to denote this triad. The unstressed rod is straight when $\hat{u}_1(s) \equiv \hat{u}_2(s) \equiv 0$. In addition, it is untwisted if the component $\hat{u}_3(s) \equiv 0$. If the component $\hat{u}_i, i = 1, 2$ is independent of s and has a fixed non-zero value, and further, if the third component $\hat{u}_3 \equiv 0$, the rod's centreline is in the form of a circular arc. In this scenario, if the third component $\hat{u}_3$ is also independent of s and has a fixed non-zero value, then the rod's centerline is in the form of a helix.

We consider the rods that satisfy *hyperelastic* constitutive law. A convex strain energy density function $W : \{\mathbf{w}, s\} \to \mathbb{R}^+$, $\mathbf{w} = [w_1, w_2, w_3]$ exists such that it satisfies $\frac{\partial W(0,s)}{\partial w_i} = 0, i = 1, 2, 3, \forall s$, and the moment components are given by

$$m_i(s) = \frac{\partial}{\partial w_i} W(w_i, s), \quad i = 1, 2, 3, \tag{3.5}$$

where the shifted strain argument $w_i \equiv u_i - \hat{u}_i$ describe the deformation from intrinsic shape $\hat{u}_i$. For a simple linearly elastic constitutive model where the strain energy density function is given by

$$W\left(u_i - \hat{u}_i, s\right) = \sum_{i=1}^{3} \frac{1}{2} K_i(s) \left(u_i(s) - \hat{u}_i(s)\right)^2, \tag{3.6}$$

the moment components are

$$m_i = \frac{\partial W}{\partial w_i} = K_i(s)\left(u_i(s) - \hat{u}_i(s)\right), \qquad i = 1,2,3. \tag{3.7}$$

Here, $K_i : s \to \mathbb{R}$ for $i = 1,2$ are called bending stiffnesses and $K_3 : s \to \mathbb{R}$ is called torsional stiffness of the rod. If the material composing the rods is homogeneous and isotropic, then the constants in the stiffness are interpreted to be K_1=EI_1, K_2=EI_2 and K_3=GJ, where $I_i \in \mathbb{R}, i = 1,2$ is the area moment of inertia about $\mathbf{d}_i$- axis, $E \in \mathbb{R}$ is the Young's Modulus of the material, $J \in \mathbb{R}$ is area polar moment of inertia about the rod axis ($\mathbf{d}_3$-axis), $G = E/2(1+\nu)$ is the Shear modulus of the material, and ν is the Poisson's ratio.

In all examples presented in this thesis, we assume that the rods are uniform $K_i(s) = K_i$, $\hat{u}_i(s) = \hat{u}_i$, $i = 1,2,3$. If these uniform rods are intrinsically straight and are of circular cross-section, they follow a *transversely isotropic* constitutive law, and these tubes have equal bending stiffnesses $K_1 = K_2$. If the uniform rods have a non-zero intrinsic curvature and are of circular cross-section, they are assumed to follow a *constitutively transversely isotropic* constitutive law, and these tubes still have equal bending stiffnesses $K_1 = K_2$.

3.4 Euler Parameters or Quaternions

The director frame $\{\mathbf{d}_1, \mathbf{d}_2, \mathbf{d}_3\}$ is connected to the fixed frame $\{\mathbf{e}_1, \mathbf{e}_2, \mathbf{e}_3\}$ through a $SO(3)$ matrix (3.2). There are several choices to parameterize the matrices in $SO(3)$. The most common way is through a three-parameter representation of *Euler angles*. Due to the topology of $SO(3)$, a set of three parameters cannot provide a global representation. A polar singularity arises when working around certain values of these parameters. Furthermore, *Euler angles* also employ trigonometric functions, which are computationally expensive and slower. Alternatively, Quaternions also referred to as *Euler parameters*, can be employed, and they mitigate the mentioned issues. Quaternions $\mathbf{q} \in \mathbb{R}^4$ with unit norm constraint $|\mathbf{q}|^2 = 1$ characterize the orientation of the director frame in 3D space (Shuster, 1993). Its drawback is that the unit norm constraint must be maintained throughout the solution path, and therefore, it appears in the governing equations. According to Euler's theorem (Goldstein, 1951), any central orientation can be described as a simple rotation by an angle θ about a fixed axis. Let $\mathbf{a} = [a_1\mathbf{e}_1 + a_2\mathbf{e}_2 + a_3\mathbf{e}_3]$ be this fixed axis. Then, the component of the associated quadruplet of quaternions $\mathbf{q} = [q_1, q_2, q_3, q_4]^T$ are

$$q_1 = a_1 \sin(\theta/2), \tag{3.8a}$$

$$q_2 = a_2 \sin(\theta/2), \tag{3.8b}$$

$$q_3 = a_3 \sin(\theta/2), \tag{3.8c}$$

$$q_4 = \cos(\theta/2). \tag{3.8d}$$

The components of directors $\mathbf{d}_i \in \mathbb{R}^3, i = 1,2,3$ with respect to the fixed coordinate system $\{\mathbf{e}_1, \mathbf{e}_2, \mathbf{e}_3\}$ can be expressed in terms of the quaternions $\mathbf{q}$ as

$$\mathbf{d}_1 = \frac{1}{|\mathbf{q}|^2}\begin{bmatrix} q_1^2 - q_2^2 - q_3^2 + q_4^2 \\ 2(q_1q_2 + q_3q_4) \\ 2(q_1q_3 - q_2q_4) \end{bmatrix}, \tag{3.9a}$$

$$\mathbf{d}_2 = \frac{1}{|\mathbf{q}|^2}\begin{bmatrix} 2(q_1q_2 - q_3q_4) \\ -q_1^2 + q_2^2 - q_3^2 + q_4^2 \\ 2(q_2q_3 + q_1q_4) \end{bmatrix}, \tag{3.9b}$$

$$\mathbf{d}_3 = \frac{1}{|\mathbf{q}|^2}\begin{bmatrix} 2(q_1q_3 + q_2q_4) \\ 2(q_2q_3 - q_1q_4) \\ -q_1^2 - q_2^2 + q_3^2 + q_4^2 \end{bmatrix}. \tag{3.9c}$$

Thus, $\mathbf{q}$ as a function of s, gives the local frame $\{\mathbf{d}_1, \mathbf{d}_2, \mathbf{d}_3\}$ along its arc length s. As a result, the strain components $u_i(s)$, $i = 1,2,3$, are obtained in terms of the quaternions and their derivatives (Dichmann et al., 1996) as

$$u_i(s) = \frac{2}{|\mathbf{q}|^2}\mathbf{B}_i\mathbf{q} \cdot \mathbf{q}', \qquad i = 1,2,3, \tag{3.10}$$

where $\mathbf{B}_j$, $j = 1,2,3$ are 4×4 skew symmetric matrices given by

$$\mathbf{B}_1 = \begin{bmatrix} 0 & 0 & 0 & 1 \\ 0 & 0 & 1 & 0 \\ 0 & -1 & 0 & 0 \\ -1 & 0 & 0 & 0 \end{bmatrix}, \tag{3.11a}$$

$$\mathbf{B}_2 = \begin{bmatrix} 0 & 0 & -1 & 0 \\ 0 & 0 & 0 & 1 \\ 1 & 0 & 0 & 0 \\ 0 & -1 & 0 & 0 \end{bmatrix}, \tag{3.11b}$$

$$\mathbf{B}_3 = \begin{bmatrix} 0 & 1 & 0 & 0 \\ -1 & 0 & 0 & 0 \\ 0 & 0 & 0 & 1 \\ 0 & 0 & -1 & 0 \end{bmatrix}. \tag{3.11c}$$

These matrices, when applied on $\mathbf{q} \in \mathbb{R}^4$ yield vectors that are orthogonal to each other as well as orthogonal to $\mathbf{q}(s)$

$$\begin{aligned} &\mathbf{B}_i\mathbf{q} \cdot \mathbf{B}_j\mathbf{q} = 0, \quad i \neq j, \quad i = 1,2,3, \\ &\mathbf{B}_i\mathbf{q} \cdot \mathbf{B}_i\mathbf{q} = |\mathbf{q}|^2 = 1, \quad i = 1,2,3, \\ &\mathbf{B}_i\mathbf{q} \cdot \mathbf{q} = 0, \quad i = 1,2,3, \end{aligned}$$

3.5 Work done by External forces

We consider a problem where a massless elastic rod is clamped at one end, and a dead load is applied at the other end, as shown in Figure 3.2. The terminal load exerts a force $\mathbf{F} \in \mathbb{R}^3$ and a moment $\boldsymbol{\Upsilon}(\mathbf{q}(l)) \times \mathbf{F} \in \mathbb{R}^3$ at the tip $s = l$, where $\boldsymbol{\Upsilon}(\mathbf{q}(l))$ is the arm vector connecting the point of attachment at tip $s = l$ and point of application of the concentrated conservative force $\mathbf{F}$. This arm is tied to the director frame at the tip $s = l$ as

$$\boldsymbol{\Upsilon}(\mathbf{q}(l)) \equiv \Delta_1 \mathbf{d}_1(\mathbf{q}(l)) + \Delta_2 \mathbf{d}_2(\mathbf{q}(l)) + \Delta_3 \mathbf{d}_3(\mathbf{q}(l)), \tag{3.12}$$

where Δ_1, Δ_2 and Δ_3 are the scalar components of the arm in the payload's frame, and the vector $\Delta \equiv [\Delta_1, \Delta_2, \Delta_3]$ represents them. Subsequently, the stored potential energy resulting from this applied tip load $\mathbf{F}$ is given by

$$E_l = \mathbf{F} \cdot (\mathbf{r}(l) + \boldsymbol{\Upsilon}(\mathbf{q}(l))) \,. \tag{3.13}$$

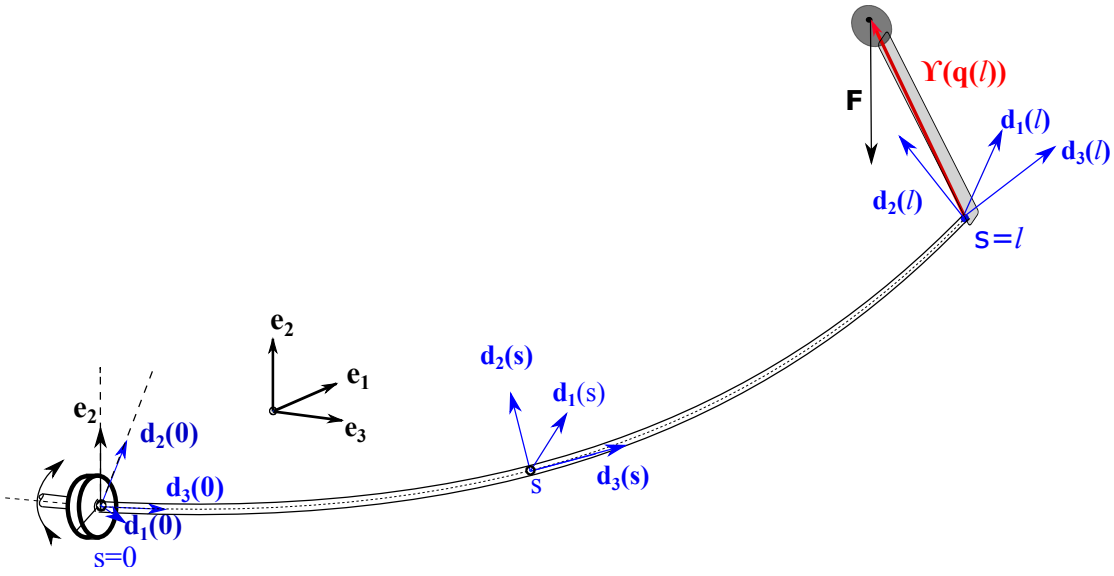

Fig. 3.2 Schematic showing an elastic rod with a tip load acting through a lever arm

3.6 Variational Problem

A variational principle is applied to determine the equilibrium configurations of the elastic rod for the specified boundary conditions. From now on, we write the strain components $\mathtt{u}$ in the energy density function W explicitly in terms of quaternions $\mathbf{q}(s)$ and their derivatives $\mathbf{q}'(s)$ using the relations (3.10) as

$$W\left(u_i - \hat{u}_i, s\right) = W\left(\frac{2}{|\mathbf{q}|^2}\mathbf{B}_i\mathbf{q} \cdot \mathbf{q}' - \hat{u}_i, s\right), \qquad i = 1, 2, 3.$$

The equilibrium configurations are the constrained critical points of the total energy functional, which is the sum of elastic strain energy and stored potential energy (3.13)

$$\int_0^l W\left(\frac{2}{|\mathbf{q}|^2}\mathbf{B}_i\mathbf{q}\cdot\mathbf{q}' - \hat{u}_i, s\right) ds + \mathbf{F}\cdot(\mathbf{r}(l) + \boldsymbol{\Upsilon}(\mathbf{q}(l)))\,, \tag{3.14}$$

subject to the pointwise inextensibility and unshearability constraint:

$$\mathbf{r}' - \mathbf{d}_3 = \mathbf{0}.$$

The fixed quaternion norm constraint can be implemented either as a holonomic constraint (only function of states)

$$\mathbf{q}\cdot\mathbf{q} - 1 = 0, \tag{3.15}$$

or as a non-holonomic constraint (function of states and their derivatives)

$$\mathbf{q}\cdot\mathbf{q}' = 0. \tag{3.16}$$

We proceed with the latter case which leads to *impetus-striction* treatment of the problem (Dichmann and Maddocks, 1996). The constraint (3.16) is equivalent to (3.15) if the boundary conditions are specified at any boundary. This constrained variational problem is formulated as an unconstrained variational problem using the Lagrange multipliers $\boldsymbol{\lambda} : s \to \mathbb{R}^3$, $\boldsymbol{\eta} : s \to \mathbb{R}$. We require that the functional

$$\begin{aligned} J &= \int_0^l L(\mathbf{r}, \mathbf{r}', \mathbf{q}, \mathbf{q}', s) ds, \\ &= \int_0^l W\left(\frac{2}{|\mathbf{q}|^2}\mathbf{B}_i\mathbf{q}\cdot\mathbf{q}' - \hat{u}_i, s\right) + \boldsymbol{\lambda}\cdot\left(\mathbf{r}' - \mathbf{d}_3\right) + \eta\mathbf{q}\cdot\mathbf{q}' ds + \mathbf{F}\cdot(\mathbf{r}(l) + \boldsymbol{\Upsilon}(\mathbf{q}(l))) \end{aligned} \tag{3.17}$$

is stationary for the equilibrium configurations. The integrand in this functional L is referred to as the *Augmented Lagrangian*.

3.7 Equilibrium Configurations

The application of *Euler-Lagrange equations* (2.2) on the *Augmented Lagrangian* functional L (3.17) gives the rod equilibria. In this section, we verify whether the equilibrium equations agree with the force-balance laws (3.3) (for e.g. see (Rogers, 1997)). The *Euler-Lagrange equations* with respect to the state $\mathbf{r}(s)$ lead to

$$\boldsymbol{\lambda}' = \mathbf{0}, \tag{3.18}$$

and the *Natural boundary condition* at the free end $s = l$ lead to

$$\boldsymbol{\lambda}(l) + \mathbf{F} = \mathbf{0}.$$

This is equivalent to the force-balance equations (3.18) with a zero distributed load $\mathbf{f}$, and the Lagrange multiplier $\boldsymbol{\lambda}(s)$ can be physically interpreted as the internal force $\mathbf{n}(s)$ described in (3.3a), and it maintains a constant value of $-\mathbf{F}$. Now consider the *Euler-Lagrange equations* with respect to the variable $\mathbf{q}(s)$:

$$-\left(W_u \frac{\partial \mathbf{u}}{\partial \mathbf{q}'} + \eta \mathbf{q}\right)' + W_u \frac{\partial \mathbf{u}}{\partial \mathbf{q}} + \eta \mathbf{q}' - \frac{\partial}{\partial \mathbf{q}} (\boldsymbol{\lambda} \cdot \mathbf{d}_3) = \mathbf{0}. \tag{3.19}$$

After writing the expressions for W_u and derivatives, the equation (3.19) becomes

$$\sum_{i=1}^{3} 2m_i' \frac{\mathbf{B}_i \mathbf{q}}{|\mathbf{q}|^2} = \sum_{i=1}^{3} -m_i \left(\frac{2\mathbf{B}_i \mathbf{q}'}{|\mathbf{q}|^2} + 2u_i \frac{\mathbf{q}}{|\mathbf{q}|^2} \right) + \eta' \mathbf{q} - \frac{\partial}{\partial \mathbf{q}} (\boldsymbol{\lambda} \cdot \mathbf{d}_3). \tag{3.20}$$

We project these equations onto $\mathbf{B}_j \mathbf{q}$-space $(j = 1, 2, 3)$ to recover the moment balance laws. Taking the inner product of (3.20) with $\mathbf{B}_j \mathbf{q}$ results in

$$2m_j' = \sum_{i=1}^{3} -2m_i u_k \epsilon_{ijk} - \frac{\partial}{\partial \mathbf{q}} (\boldsymbol{\lambda} \cdot \mathbf{d}_3) \cdot \mathbf{B}_j \mathbf{q}, \quad j = 1, 2, 3,$$

where ϵ_{ijk} is the standard permutation symbol. The last term can be rewritten as

$$\begin{aligned} \frac{\partial}{\partial \mathbf{q}} (\boldsymbol{\lambda} \cdot \mathbf{d}_3) \cdot \mathbf{B}_j \mathbf{q} &= \left(\frac{\partial \mathbf{d}_3}{\partial \mathbf{q}} \right)^T \lambda \cdot \mathbf{B}_j \mathbf{q} = \left(\frac{\partial \mathbf{d}_3}{\partial \mathbf{q}} \right) \mathbf{B}_j \mathbf{q} \cdot \boldsymbol{\lambda} \\ &= 2\epsilon_{j3k} \mathbf{d}_\mathbf{k} \cdot \boldsymbol{\lambda}, \end{aligned}$$

which leads to the equilibrium equations

$$m_j' = \sum_{i=1}^{3} -m_j u_k \epsilon_{ijk} - \epsilon_{j3k} \mathbf{d}_\mathbf{k} \cdot \boldsymbol{\lambda}, \quad j = 1, 2, 3.$$

This expression reduces to

$$m_1' = -u_2 m_3 + u_3 m_2 + \mathbf{d}_2 \cdot \boldsymbol{\lambda}, \tag{3.21a}$$

$$m_2' = u_1 m_3 - u_3 m_1 - \mathbf{d}_1 \cdot \boldsymbol{\lambda}, \tag{3.21b}$$

$$m_3' = -u_1 m_2 + u_2 m_1, \tag{3.21c}$$

which are equivalent to moment-balance laws (3.3b) in the fixed frame. So far, the stated results have been thoroughly established. However, the subsequent result on the *Natural Boundary condition* constitutes a novel contribution. The projection of the *Natural Boundary condition*

$$W_u \frac{\partial \mathbf{u}}{\partial \mathbf{q}'} + \eta \mathbf{q}(l) + \frac{\partial}{\partial \mathbf{q}} (\mathbf{F} \cdot \boldsymbol{\Upsilon}(\mathbf{q}(l))) = \mathbf{0}$$

onto $\mathbf{B}_i \mathbf{q}(l)/2, i = 1, 2, 3$ produces

$$\left(2W_{u_i} \mathbf{B}_i \mathbf{q}(l) + \eta \mathbf{q}(l) + \frac{\partial}{\partial \mathbf{q}} (\mathbf{F} \cdot \boldsymbol{\Upsilon}(\mathbf{q})) \right) \cdot \mathbf{B}_i \mathbf{q}(l)/2 = 0, \quad i = 1, 2, 3, \tag{3.22}$$

which further yields

$$m_i(l) + \left(\frac{\partial}{\partial \mathbf{q}} \left(\Delta_1 \mathbf{d}_1(l) + \Delta_2 \mathbf{d}_2(l) + \Delta_3 \mathbf{d}_3(l) \right) \cdot \mathbf{F} \right) \cdot \mathbf{B}_i \mathbf{q}(l) = 0, \quad i = 1, 2, 3.$$

We use the derivatives of the directors $\mathbf{d}_i(\mathbf{q})$ (Dichmann et al., 1996) (presented in Appendix B), and project them onto the $\mathbf{B}_i\mathbf{q}$-space to obtain the following expressions:

$$\begin{aligned}
&\frac{\partial \mathbf{d}_1}{\partial \mathbf{q}} \cdot \mathbf{B}_1\mathbf{q}/2 = \mathbf{0}, \quad \frac{\partial \mathbf{d}_1}{\partial \mathbf{q}} \cdot \mathbf{B}_2\mathbf{q}/2 = -\mathbf{d}_3, \quad \frac{\partial \mathbf{d}_1}{\partial \mathbf{q}} \cdot \mathbf{B}_3\mathbf{q}/2 = \mathbf{d}_2, \\
&\frac{\partial \mathbf{d}_2}{\partial \mathbf{q}} \cdot \mathbf{B}_1\mathbf{q}/2 = \mathbf{d}_3, \quad \frac{\partial \mathbf{d}_2}{\partial \mathbf{q}} \cdot \mathbf{B}_2\mathbf{q}/2 = \mathbf{0}, \quad \frac{\partial \mathbf{d}_2}{\partial \mathbf{q}} \cdot \mathbf{B}_3\mathbf{q}/2 = -\mathbf{d}_1, \\
&\frac{\partial \mathbf{d}_3}{\partial \mathbf{q}} \cdot \mathbf{B}_1\mathbf{q}/2 = -\mathbf{d}_2, \quad \frac{\partial \mathbf{d}_3}{\partial \mathbf{q}} \cdot \mathbf{B}_2\mathbf{q}/2 = \mathbf{d}_1, \quad \frac{\partial \mathbf{d}_3}{\partial \mathbf{q}} \cdot \mathbf{B}_3\mathbf{q}/2 = \mathbf{0}.
\end{aligned} \tag{3.23}$$

All the variables are evaluated at the end $s = l$. On substituting the terms from (3.23), we obtain

$$m_i(l) + \mathbf{F} \cdot \left(\epsilon_{ijk} \Delta_j \mathbf{d}_k(\mathbf{q}(l)) \right) = 0, \qquad i = 1, 2, 3.$$

The term inside the brackets can be written as a vector cross product $\boldsymbol{\Upsilon}(\mathbf{q}(l)) \times \mathbf{d}_i$ in the following manner

$$m_i(l) - \left(\mathbf{F} \cdot \left(\Delta_1 \mathbf{d}_1(l) + \Delta_2 \mathbf{d}_2(l) + \Delta_3 \mathbf{d}_3(l) \right) \times \mathbf{d}_i(l) \right) = 0, \qquad i = 1, 2, 3.$$

In the end, we obtain the balance of the moments along the directors $\mathbf{d}_i, i = 1, 2, 3$ at the tip $s = l$

$$m_i(l) + \left(\boldsymbol{\Upsilon}(\mathbf{q}(l)) \times \mathbf{F} \right) \cdot \mathbf{d}_i(l) = 0, \qquad i = 1, 2, 3.$$

3.8 Hamiltonian Formulation of Rods

The Hamiltonian form of the equilibria (Dichmann et al., 1996) provides the equilibria as a simple set of first-order ODEs. This form is convenient for both numerical computations and analysis. In addition, this formulation yields additional conserved quantities (also called integrals), which can serve as benchmarks for validating numerical computations. Consequently, this formulation is employed in this work to reap these benefits. We limit ourselves to the linear *hyperelastic* rods with a quadratic form of elastic energy density.

The Hamiltonian formulation involves the standard Legendre transform $W^*(\mathtt{m}, s)$ (Goldstein, 1951) of the constitutive function $W(\mathbf{w}, s)$, which is assumed to be strictly convex with respect to $\mathbf{w}$, where $\mathbf{w} = \mathtt{u} - \hat{\mathtt{u}}$ is the shifted strain argument. The variable conjugate to the $\mathbf{w}$ in case of *hyperelastic rods* is the triad of the components of the moment along the director frame $\mathtt{m}$

$$\mathtt{m} = \frac{d}{d\mathbf{w}} W(\mathbf{w}, s).$$

Owing to the strict convexity condition of W, this relation can be inverted to solve for $\mathbf{w}$

$$\mathbf{w} \equiv \mathtt{u} - \hat{\mathtt{u}} = \Phi(\mathtt{m}).$$

Then, the Legendre transform is then defined to be

$$W^*(\mathtt{m}) := \mathtt{m} \cdot \Phi(\mathtt{m}) - W(\Phi(\mathtt{m})).$$

For the simple case of quadratic strain energy function of the form

$$W\left(u_i - \hat{u}_i, s\right) = \sum_{i=1}^{3} \frac{1}{2} K_i(s) \left(u_i(s) - \hat{u}_i(s)\right)^2, \tag{3.24}$$

the Hamiltonian variables are given by

$$m_i = K_i \left(u_i(s) - \hat{u}_i(s)\right), \qquad \Phi(\mathtt{m}) \equiv u_i(s) - \hat{u}_i(s) = m_i/K_i,$$

and the associated Legendre transform reads

$$W^*(\mathtt{m}) = \sum_{i=1}^{3} m_i \hat{u}_i + m_i^2/2K_i.$$

Let us derive the Hamiltonian formulation of the equilibria for our current tip-loaded elastic rod system, which has the *Augmented Lagrangian* of the form

$$L(\mathbf{r}, \mathbf{r}', \mathbf{q}, \mathbf{q}', s) = W\left(\frac{2}{|\mathbf{q}|^2}\mathbf{B}_j\mathbf{q}\cdot\mathbf{q}' - \hat{u}_j, s\right) + \boldsymbol{\lambda}\cdot\left(\mathbf{r}' - \mathbf{d}_3\right) + \eta\mathbf{q}\cdot\mathbf{q}'.$$

The phase variables in this Hamiltonian formulation include the states $\mathbf{r}$ and $\mathbf{q}$, along with their corresponding conjugate momenta $\mathbf{n}$ and $\boldsymbol{\mu}$. The internal force $\mathbf{n}$ and the *impetus* $\boldsymbol{\mu}$ are defined using the *Augmented Lagrangian* L as

$$\mathbf{n} \equiv \frac{\partial L}{\partial \mathbf{r}'} = \boldsymbol{\lambda}, \tag{3.25a}$$

$$\boldsymbol{\mu} \equiv \frac{\partial L}{\partial \mathbf{q}'} = 2W_{u_i}\frac{\mathbf{B}_i\mathbf{q}}{|\mathbf{q}|^2} + \eta\mathbf{q}, \quad i = 1,2,3. \tag{3.25b}$$

The dot product of (3.25b) with $\mathbf{q}$ gives the expression for the Lagrange multiplier η

$$\boldsymbol{\mu}\cdot\mathbf{q} = \eta. \tag{3.26}$$

Similarly, the dot product of (3.25b) with $\mathbf{B}_i\mathbf{q}/2$ gives the components of the internal moment $\mathtt{m}$ in terms of Hamiltonian variables

$$\frac{\boldsymbol{\mu}\cdot\mathbf{B}_i\mathbf{q}}{2} = W_{u_i} \equiv m_i, \quad \text{for} \quad i = 1,2,3. \tag{3.27}$$

The Hamiltonian of the system is obtained after taking a Legendre transform of the *Augmented Lagrangian* L, which is obtained as

$$\begin{aligned} H(\mathbf{r},\mathbf{q},\mathbf{n},\boldsymbol{\mu},s) &= \mathbf{n}\cdot\mathbf{r}' + \boldsymbol{\mu}\cdot\mathbf{q}' - L(\mathbf{r},\mathbf{r}',\mathbf{q},\mathbf{q}',s) \\ &= \mathbf{n}\cdot\mathbf{r}' + \left(2W_{u_i}\frac{\mathbf{B}_i\mathbf{q}}{|\mathbf{q}|^2} + \eta\mathbf{q}\right)\cdot\mathbf{q}' - W\left(\frac{2}{|\mathbf{q}|^2}\mathbf{B}_j\mathbf{q}\cdot\mathbf{q}' - \hat{u}_j, s\right) \\ &\qquad - \mathbf{n}\cdot\left(\mathbf{r}' - \mathbf{d}_3\right) - \eta\mathbf{q}\cdot\mathbf{q}' \\ &= \mathbf{n}\cdot\mathbf{d}_3 + \sum_{i=1}^{i=3} m_i\hat{u}_i + \frac{1}{2}\mathtt{m}\cdot\mathbf{K}^{-1}\mathtt{m}. \end{aligned} \tag{3.28}$$

The system of equations that govern the equilibria are obtained from the Hamiltonian H with phase variables $\boldsymbol{\zeta}, \mathbf{p}$ as

$$\begin{bmatrix}\boldsymbol{\zeta}\\ \mathbf{p}\end{bmatrix}' = \begin{bmatrix}\mathbf{0} & \mathbf{I}\\ -\mathbf{I} & \mathbf{0}\end{bmatrix}\begin{bmatrix}H_{\boldsymbol{\zeta}}\\ H_{\mathbf{p}}\end{bmatrix}$$

which for the present context of elastic rods take the form

$$\mathbf{r}'(s) = \frac{\partial H}{\partial \mathbf{n}} = \mathbf{d}_3, \tag{3.29a}$$

$$\mathbf{n}'(s) = -\frac{\partial H}{\partial \mathbf{r}} = \mathbf{0}, \tag{3.29b}$$

$$\mathbf{q}'(s) = \frac{\partial H}{\partial \boldsymbol{\mu}} = \sum_{j=1}^{3}\left(K_{jj}^{-1}m_j + \hat{u}_j\right)\frac{1}{2}\mathbf{B}_j\mathbf{q}, \tag{3.29c}$$

$$\boldsymbol{\mu}'(s) = -\frac{\partial H}{\partial \mathbf{q}} = \sum_{j=1}^{3}\left(K_{jj}^{-1}m_j + \hat{u}_j\right)\frac{1}{2}\mathbf{B}_j\boldsymbol{\mu} - \frac{\partial \mathbf{d}_3}{\partial \mathbf{q}}^T\mathbf{n}, \tag{3.29d}$$

where the derivative $\frac{\partial \mathbf{d}_3}{\partial \mathbf{q}}$ is given by

$$\frac{\partial \mathbf{d}_3}{\partial \mathbf{q}} = 2\begin{bmatrix} q_3 & q_4 & q_1 & q_2\\ -q_4 & q_3 & q_2 & -q_1\\ -q_1 & -q_2 & q_3 & q_4\end{bmatrix}, \tag{3.30}$$

and the components $m_i, i = 1,2,3$ are written in terms of phase variables $\boldsymbol{\mu}$ and $\mathbf{q}$ using the relation (3.27).

3.9 Conserved Quantities

The three components of internal force $\mathbf{n}$ along the fixed frame are conserved due to the translational symmetry of the Hamiltonian system. Similarly, the three components of $\mathbf{m} + \mathbf{r}\times\mathbf{n}$ are conserved due to the rotational symmetry of the Hamiltonian system about the three fixed axes. The norm of the quaternion $\mathbf{q}$ is a conserved quantity by construction $(|\mathbf{q}| = 1)$. Moreover, the

quantity $\boldsymbol{\mu}\cdot\mathbf{q}+2\mathbf{r}\cdot\mathbf{n}$ is also conserved, as illustrated below

$$\begin{aligned}\frac{d}{ds}\left(\boldsymbol{\mu}\cdot\mathbf{q}+2\mathbf{r}\cdot\mathbf{n}\right) &= \boldsymbol{\mu}'\cdot\mathbf{q}+\boldsymbol{\mu}\cdot\mathbf{q}'+2\mathbf{n}\cdot\mathbf{r}'+2\mathbf{n}'\cdot\mathbf{r},\\ &= \sum_{j=1}^{3}\left(\mathbf{K^{-1}}_{jj}m_j+\hat{u}_j\right)\frac{1}{2}\mathbf{B}_j\boldsymbol{\mu}\cdot\mathbf{q}-\frac{\partial\mathbf{d}_3}{\partial\mathbf{q}}^T\mathbf{n}\cdot\mathbf{q}\\ &\qquad+\sum_{j=1}^{3}\left(\mathbf{K^{-1}}_{jj}m_j+\hat{u}_j\right)\frac{1}{2}\mathbf{B}_j\mathbf{q}\cdot\boldsymbol{\mu}+2\mathbf{n}\cdot\mathbf{d}_3,\\ &= -\mathbf{n}\cdot\frac{\partial\mathbf{d}_3}{\partial\mathbf{q}}\mathbf{q}+2\mathbf{n}\cdot\mathbf{d}_3=0.\end{aligned}$$

The expressions for the derivatives are used from (3.28). The skew-symmetric nature of $\mathbf{B}_i$ $(i=1,2,3)$ matrices is utilized in the second step. Euler's theorem for homogeneous functions gives the relation $\frac{\partial\mathbf{d}_3}{\partial\mathbf{q}}\mathbf{q}=2\mathbf{d}_3$, and is used in the last step. The quantity $\boldsymbol{\mu}\cdot\mathbf{q}$ is also an expression for the Lagrange multiplier η (3.26). Suppose the rod has translation symmetry along its arc length s. Its constitutive law has no explicit dependence on s. For a quadratic strain energy function, this condition is satisfied when the stiffnesses K_i $(i=1,2,3)$ and unstressed strains $\hat{u}_i$ $(i=1,2,3)$ are constant. Under these conditions, the Hamiltonian H is also a conserved quantity. We employ some of these conserved quantities to validate the accuracy of our numerical results.

3.10 Boundary Conditions

Here is a summary of the boundary conditions for an elastic rod clamped at the $s=0$ and free at the other end $s=l$. The fixed boundary conditions at the clamped end $s=0$ are

$$\begin{aligned}\mathbf{r}(0)&=[0,0,0]^T,\\ \mathbf{q}(0)&=\mathbf{q_0},\end{aligned}\tag{3.31}$$

and we have 7 *Natural boundary condition* at the free end $s=l$. Physically, six of these conditions pertain to force-moment balance at the tip $s=l$

$$\mathbf{n}(l)+\boldsymbol{F}=\mathbf{0},\tag{3.32a}$$

$$m_i(l)+\left(\boldsymbol{\Upsilon}(\mathbf{q}(l))\times\mathbf{F}\right)\cdot\mathbf{d}_i(\mathbf{q}(l))=0,\qquad i=1,2,3.\tag{3.32b}$$

The last three conditions (3.32b) are the resultant of the projection of 4-dimensional *Natural boundary condition* with respect to the variable $\mathbf{q}$ onto $\mathbf{B}_i\mathbf{q}(l)$- space, and the details are already presented in section 3.7. Its projection on the flat direction $\mathbf{q}(l)$ is implemented using the conserved quantity $\boldsymbol{\mu}\cdot\mathbf{q}+2\mathbf{r}\cdot\mathbf{n}$

$$\begin{aligned}\boldsymbol{\mu}(0)\cdot\mathbf{q}(0)+2\mathbf{r}(0)\cdot\mathbf{n}(0)&=\boldsymbol{\mu}(l)\cdot\mathbf{q}(l)+2\mathbf{r}(l)\cdot\mathbf{n}(l)\\ &\implies\boldsymbol{\mu}(0)\cdot\mathbf{q}(0)=\boldsymbol{\mu}(l)\cdot\mathbf{q}(l)+2\mathbf{r}(l)\cdot\mathbf{n}(l).\end{aligned}$$

The quantity $\boldsymbol{\mu}(0) \cdot \mathbf{q}(0) \equiv \eta(0)$ can be specified as any value, and its specification assigns a value to the Lagrange multiplier η and removes the gauge freedom in $\boldsymbol{\mu}$ (Li and Maddocks, 1996). So, we impose

$$\boldsymbol{\mu}(l) \cdot \mathbf{q}(l) + 2\mathbf{r}(l) \cdot \mathbf{n}(l) = 0. \tag{3.33}$$

in our numerical computations.

3.11 Hamiltonian Form of Jacobi Equations

The equilibria $\boldsymbol{\zeta}_o$ obtained as the solutions to the (3.29) with the boundary conditions (3.31),(3.32b) and (3.33) must satisfy the *Legendre's strengthened condition* (2.14) along with the *Jacobi condition* to represent the local minima of the functional

$$\int_0^l W\left(\frac{2}{|\mathbf{q}|^2}\mathbf{B}_j\mathbf{q}\cdot\mathbf{q}' - \hat{u}_j, s\right) ds + \mathbf{F}\cdot(\mathbf{r}(l) + \boldsymbol{\Upsilon}(\mathbf{q}(l))).$$

This requirement implies that the matrix $W_{\boldsymbol{\zeta}'\boldsymbol{\zeta}'}$ must be positive definite. However, in our current problem where $\boldsymbol{\zeta} \equiv \begin{bmatrix}\mathbf{r}\\ \mathbf{q}\end{bmatrix}$, the matrix $W_{\boldsymbol{\zeta}'\boldsymbol{\zeta}'}$ is of the form

$$W_{\boldsymbol{\zeta}'\boldsymbol{\zeta}'} = \begin{bmatrix} 0 & 0 & 0 & 0 & 0 & 0 & 0\\ 0 & 0 & 0 & 0 & 0 & 0 & 0\\ 0 & 0 & 0 & 0 & 0 & 0 & 0\\ 0 & 0 & 0 & K_{11} & 0 & 0 & 0\\ 0 & 0 & 0 & 0 & K_{22} & 0 & 0\\ 0 & 0 & 0 & 0 & 0 & K_{33} & 0\\ 0 & 0 & 0 & 0 & 0 & 0 & 0 \end{bmatrix},$$

and is only positive semi-definite. We avoid this problem by decoupling $\mathbf{r}$ from the variational problem for stability analysis. The state $\mathbf{r}$ has no explicit contribution in the elastic strain energy $W(\mathtt{u} - \hat{\mathtt{u}}, s)$, and it acts only through boundary conditions. It acts indirectly through $\mathbf{q}$ by inextensibility and unshearability constraint ($\mathbf{r}' = \mathbf{d}_3$). Its conjugate momentum $\mathbf{n}$ is a constant function $\mathbf{n}(s) = -\mathbf{F}$. We eliminate the variables $\mathbf{r}$ and $\mathbf{n}$ by substituting these relations in the functional

$$\int_0^l L ds = \int_0^l \mathbf{W}\left(\frac{2}{|\mathbf{q}|^2}\mathbf{B}_j\mathbf{q}\cdot\mathbf{q}' - \hat{u}_j, s\right) + \mathbf{F}\cdot\mathbf{d}_3 ds + \mathbf{F}\cdot\boldsymbol{\Upsilon}(\mathbf{q}(l)). \tag{3.34}$$

As a result, we have a new decoupled Hamiltonian function $\bar{H}$ for the functional, which depends only on $\mathbf{q}$ and $\boldsymbol{\mu}$ as the phase variables as

$$\bar{H}(\mathbf{q}, \boldsymbol{\mu}, s) = -\mathbf{F}\cdot\mathbf{d}_3 + \sum_{i=1}^{i=3} m_i\hat{u}_i + \frac{1}{2}\mathtt{m}\cdot\mathbf{K}^{-1}\mathtt{m}.$$

Even so, we have a semi-definite matrix $L_{\mathbf{q}'\mathbf{q}'}$

$$L_{\mathbf{q}'\mathbf{q}'} = \begin{bmatrix} K_{11} & 0 & 0 & 0 \\ 0 & K_{22} & 0 & 0 \\ 0 & 0 & K_{33} & 0 \\ 0 & 0 & 0 & 0 \end{bmatrix},$$

and it arises due to the limitation imposed on the norm of the quaternions $\mathbf{q}$. Rogers (1997) mitigated this problem by restricting the variations $\mathbf{h}_\mathbf{q}$, which ensures the unit-norm constraint: $\mathbf{q} \cdot \mathbf{q} = 1$. Subsequently, $\mathbf{h}_\mathbf{q}$ must satisfy

$$\mathbf{q} \cdot \mathbf{h}_\mathbf{q} = 0 \implies \mathbf{h}_\mathbf{q} \in \mathbf{q}^\perp.$$

There are many choices of the basis for $\mathbf{q}^\perp$, and we choose the basis $\{\mathbf{B}_1\mathbf{q}, \mathbf{B}_2\mathbf{q}, \mathbf{B}_3\mathbf{q}\}$ for our computations. Any arbitrary variation $\mathbf{h}_\mathbf{q} \in \mathbb{R}^4$ can be projected on to the $\mathbf{q}^\perp$ using the following Π matrix leading a projection in $\mathbb{R}^3$.

$$\Pi = \Big[\mathbf{B}_1\mathbf{q}, \mathbf{B}_2\mathbf{q}, \mathbf{B}_3\mathbf{q}\Big]^T \equiv \begin{bmatrix} q_4 & q_3 & -q_2 & -q_1 \\ -q_3 & q_4 & q_1 & -q_2 \\ q_2 & -q_1 & q_4 & -q_3 \end{bmatrix}, \tag{3.35}$$

The second variation along the projected space is obtained by substituting $\bar{\mathbf{h}} = \Pi^T\mathbf{h}$ in the second variation

$$\begin{aligned} \delta^2 J[\mathbf{h}] = \frac{1}{2}\int_0^l & \mathbf{h}' \cdot \Pi L_{\mathbf{q}'\mathbf{q}'}\Pi^T\mathbf{h}' + \mathbf{h}' \cdot \Big[\Pi L_{q'\mathbf{q}'}\Pi'^T + \Pi L_{\mathbf{q}'\mathbf{q}}\Pi^T\Big]\mathbf{h} \\ & + \mathbf{h} \cdot \Big[\Pi' L_{\mathbf{q}'\mathbf{q}'}\Pi^T + \Pi L_{\mathbf{q}'\mathbf{q}}\Pi^T\Big]\mathbf{h}' \\ & + \mathbf{h} \cdot \Big[\Pi' L_{\mathbf{q}'\mathbf{q}'}\Pi'^T + \Pi L_{\mathbf{q}\mathbf{q}}\Pi^T + \Pi L_{\mathbf{q}\mathbf{q}'}\Pi'^T + \Pi' L_{\mathbf{q}'\mathbf{q}}\Pi^T\Big]\mathbf{h}. \end{aligned}$$

The quadratic form of this expression can be rewritten in terms of the *Jacobi operator* as

$$\delta^2 J[\mathbf{h}] = \langle \mathbf{h}, \bar{\mathcal{S}}\mathbf{h} \rangle,$$

where $\bar{\mathcal{S}}$ is given by

$$\bar{\mathcal{S}}\mathbf{h} = -\frac{d}{ds}\Big[\bar{\mathbf{P}}\mathbf{h}' + \bar{\mathbf{C}}^T\mathbf{h}\Big] + \bar{\mathbf{C}}\mathbf{h} + \bar{\mathbf{Q}}\mathbf{h},$$

and

$$\begin{aligned} \bar{\mathbf{P}} &= \Pi L_{\mathbf{q}'\mathbf{q}'}\Pi^T, \\ \bar{\mathbf{Q}} &= \Pi' L_{\mathbf{q}'\mathbf{q}'}\Pi'^T + \Pi L_{\mathbf{q}\mathbf{q}}\Pi^T + \Pi L_{\mathbf{q}\mathbf{q}'}\Pi'^T + \Pi' L_{\mathbf{q}'\mathbf{q}}\Pi^T, \\ \bar{\mathbf{C}} &= \Pi' L_{\mathbf{q}'\mathbf{q}'}\Pi^T + \Pi L_{\mathbf{q}\mathbf{q}'}\Pi^T. \end{aligned}$$

Then, the projected matrix $L_{\mathbf{q}'\mathbf{q}'}$ on Π^T-space

$$\bar{\mathbf{P}} = \begin{pmatrix} K_{11} & 0 & 0 \\ 0 & K_{22} & 0 \\ 0 & 0 & K_{33} \end{pmatrix}, \tag{3.36}$$

is always positive definite. Therefore, the *Legendre's strengthened condition* is satisfied as long as the allowed variations are in $\mathbf{q}^{\perp}$ - space. Furthermore, this condition guarantees that the *weak minima* $\boldsymbol{\zeta}_o$ also qualifies as a *strong minima* (subsection 2.1.2). The linearization of the Hamiltonian form of the equilibria gives the Hamiltonian form of the *Jacobi operator* $\mathcal{S}$,

$$\begin{bmatrix} \mathbf{h_q} \\ \mathbf{h}_{\boldsymbol{\mu}} \end{bmatrix}' = \begin{bmatrix} H_{\mathbf{qq}} & H_{\mathbf{q}\boldsymbol{\mu}} \\ H_{\boldsymbol{\mu}\mathbf{q}} & H_{\boldsymbol{\mu}\boldsymbol{\mu}} \end{bmatrix} \begin{bmatrix} \mathbf{h_q} \\ \mathbf{h}_{\boldsymbol{\mu}} \end{bmatrix}, \tag{3.37}$$

where $\mathbf{h_q}$,$\mathbf{h}_{\mu}$ are the variations in the $\mathbf{q}$ and $\boldsymbol{\mu}$ respectively. The expressions for the Hessian matrices are detailed in Appendix C. When the variations $\mathbf{h_q}$ are restricted to $\mathbf{q}^{\perp}-$ space, (3.37) corresponds to the Hamiltonian form of the $\bar{\mathcal{S}}$.

Jacobi condition Given the positive definiteness of $\bar{\mathbf{P}}$, the absence of *conjugate points* in the interval $[0, l]$ is the sufficient condition for the equilibrium $\boldsymbol{\zeta}_o$ to be stable. We compute the *conjugate points* in the following manner. Firstly, the boundary with the *Natural boundary condition* $(s = l)$ is selected, and the *initial value problems* (IVP) are solved towards the other end $(s = 0)$ for a basis of initial values for $\mathbf{h_q}$ and a zero vector for $\mathbf{h}_{\boldsymbol{\mu}}$. Nevertheless, the flat direction of $\mathbf{h_q}$ is not of interest, and the basis is chosen in the $\mathbf{q}^{\perp}$- space. As a result, three sets of eight first-order IVPs are solved towards $s = 0$ with the following sets of initial values at $s = l$

$$\mathbf{h_q}(l) = \mathbf{B}_i\mathbf{q}(l), \quad i = 1, 2, 3.$$

and the $\mathbf{h}_{\boldsymbol{\mu}}(l)$ components satisfying the linearized boundary condition (3.32b)

$$\mathbf{h}_{\boldsymbol{\mu}}(l) \cdot \mathbf{B}_i\mathbf{q}(l) + \boldsymbol{\mu}(l) \cdot \mathbf{B}_i\mathbf{h_q}(l) + \left(\frac{\partial}{\partial \mathbf{q}}\boldsymbol{\Upsilon}(\mathbf{q}(l)) \times \mathbf{F} \cdot \mathbf{d}_i(l)\right) \cdot \mathbf{h_q}(l) = 0, \qquad i = 1, 2, 3, \tag{3.38}$$

and the linearized integral (3.33)

$$\boldsymbol{\mu}(l) \cdot \mathbf{h_q}(l) + \mathbf{q}(l) \cdot \mathbf{h}_{\boldsymbol{\mu}}(l) = 0. \tag{3.39}$$

The algebraic system (3.38) and (3.39) is solved to obtain the initial values for the components $\mathbf{h}_{\boldsymbol{\mu}}(l)$.

The components corresponding to the IVP solution $\mathbf{h_q}(s)$ for i th set of IVP are denoted as

$\mathbf{h_q}^{(j)}$ $(j = 1, 2, 3)$. These four components are arranged as rows in the 4×3 matrix along s as

$$\left[\mathbf{h_q}^{(1)}(s) \quad \mathbf{h_q}^{(2)}(s) \quad \mathbf{h_q}^{(3)}(s)\right].$$

This matrix is projected onto $\mathbf{q}^{\perp}$- space by left multiplying with the matrix Π^T (3.35) to give a 3×3 matrix:

$$\Pi^T\left[\mathbf{h_q}^{(1)}(s) \quad \mathbf{h_q}^{(2)}(s) \quad \mathbf{h_q}^{(3)}(s)\right].$$

We refer to this matrix as *stability matrix*. A point σ is called a *conjugate point* of l if the determinant of this 3×3 *stability matrix* vanishes for any $\sigma \in [0, l]$. To analyze the stability of the equilibria determined by the 14-dimensional Hamiltonian system, we need to solve a 24-dimensional IVP. One approach is to couple both systems, resulting in a $(24 + 14)$-dimensional BVP. Alternatively, one can first solve the 14-dimensional Hamiltonian system BVP and then address the 24-dimensional IVP separately. The second approach is more computationally efficient since the BVP is of smaller size, and IVPs can be solved more quickly compared to BVPs of the same size.

To sum up, we have presented the Hamiltonian form of equilibria for an elastic rod clamped at one end and attached to a dead load at the other end that exerts combined force and moment. The conserved quantities that arise out of this method are also presented. In addition, a numerical implementation for the *Jacobi condition* was also detailed. This machinery is helpful in numerically investigating the rod equilibria and their associated stability properties. The following chapter will delve into the details of the numerical computations utilized to investigate the elastic rods.

CHAPTER 4

Numerical Continuation

In this thesis, we compute rod equilibria while systematically varying parameters and investigate their behavior. These parameters describe either material properties, geometric properties, or boundary conditions. *Parameter continuation* software *AUTO-07p* (Doedel et al., 2007) is employed for this study. This *continuation* technique numerically solves the parameter-dependent *boundary value problems* (BVPs) that are reduced to nonlinear algebraic equations by discretization. As the parameter changes, nonlinear phenomena such as *folds* and *bifurcations* may arise, and this method can detect them. Previous versions of the software *AUTO-07p* have been successful in computing robust solutions for elastic rod models, and have been widely used in the field (Dichmann et al., 1996; Healey and Mehta, 2005). In this chapter, we briefly provide an overview of the *parameter continuation method* (Doedel et al., 1991a,b), and then provide some details of numerical computations utilizing *AUTO-07p*.

4.1 Parameter Continuation

Consider a nonlinear algebraic system of the form

$$\begin{aligned} \mathbf{g}(\mathbf{x},\gamma) = \mathbf{0}, \qquad & \mathbf{g} : \mathbb{R}^{N_d} \times \mathbb{R} \longrightarrow \mathbb{R}^{N_d}, \\ & \gamma \in \mathbb{R}, \end{aligned} \tag{4.1}$$

where γ is the system parameter, and N_d is the dimension of the given problem. *Parameter continuation* explores the solution space of (4.1) as the parameter γ is varied, and studies their dependence on the parameter. The system can have more than one parameter. Nevertheless, in numerics, only one parameter is varied at a time while maintaining others fixed. Infinite-dimensional problems like BVPs are converted to the finite-dimensional algebraic system of the form (4.1) after discretizing using orthogonal collocation (see later section (4.2)). In this scenario, the dimension of the problem N_d depends on the dimension of the state in the BVP, the number of discretization intervals, and the number of collocation points within each interval.

For simplicity, we take $\mathbf{y} = [\mathbf{x}, \gamma]$ and, then rewrite (4.1) as

$$\mathbf{g}(\mathbf{y}) = \mathbf{0}, \qquad \mathbf{g} : \mathbb{R}^{N_d+1} \longrightarrow \mathbb{R}^{N_d}. \tag{4.2}$$

A solution $\mathbf{y_o}$ of (4.2) is said to be *regular* if the Jacobian of the algebraic system $\mathbf{g_y}(\mathbf{y_o})$ is of rank N_d. Then it follows from the *Implicit Function Theorem* that a unique solution branch

$\mathbf{y} = [\mathbf{x}(\tau), \gamma(\tau)]$ passes through the regular solution $\mathbf{y_o}$, for some choice of parameterization τ of the branch. Along this solution branch, the components $\mathbf{x}$ can be expressed in terms of the other component γ, i.e., the state $\mathbf{x}$ can be expressed as $\mathbf{x}(\gamma)$.

The principle of *parameter continuation* is to start from a known initial regular solution $\mathbf{y_o}$ and compute a nearby solution on the solution branch through a perturbation in γ. This process is repeated multiple times until a full set of branched continued solutions is obtained. Let $\mathbf{p}(\mathbf{y}(\tau), \tau) = 0$ be the function of parameterization. Our goal is to determine the continuous curve of solutions satisfying

$$\begin{aligned} \mathbf{g}(\mathbf{y}(\tau)) &= \mathbf{0}, \\ \mathbf{p}(\mathbf{y}(\tau), \tau) &= 0, \end{aligned}$$

around a known solution $\mathbf{y_o} = [\mathbf{x}_o, \gamma_o]$. Suppose that the direction vector $\dot{\mathbf{y}}$ is known at $\mathbf{y_o}$, where $\dot{()}$ denotes the derivative with respect to τ. The next solution $\mathbf{y}(\tau_o + \Delta\tau)$ is obtained through the Newton iterative method which consists of solving $\Delta\mathbf{y}$ from

$$\begin{bmatrix} \mathbf{g_y}(\mathbf{y}^{(i)}) \\ \mathbf{p}_y(\mathbf{y}^{(i)}) \end{bmatrix} \Delta\mathbf{y} = \begin{bmatrix} \mathbf{g}(\mathbf{y}^{(i)}) \\ \mathbf{p}(\mathbf{y}^{(i)}) \end{bmatrix}, \tag{4.3}$$

followed by setting

$$\mathbf{y}^{(i+1)} = \mathbf{y}^{(i)} + \Delta\mathbf{y}.$$

These two steps are carried out iteratively until the solution converges. As an initial approximation,

$$\mathbf{y}^{(0)}(\tau_o + \Delta\tau) = \mathbf{y}_o + \dot{\mathbf{y}}\Delta\tau \tag{4.4}$$

is used. The direction vector at the new point $\dot{\mathbf{y}}_1$ is found after the convergence of Newton's iteration using the relation

$$\begin{bmatrix} \mathbf{g_y} \\ \mathbf{p}_y \end{bmatrix} \dot{\mathbf{y}}_1 = \begin{bmatrix} \mathbf{0} \\ \mathbf{p}_\tau \end{bmatrix}.$$

The vector is then normalized to the unit norm, i.e., $|\dot{\mathbf{y}}_1| = 1$. This procedure is applied in a similar manner to the next point and is run iteratively.

There are several choices of *parameterization* functions $\mathbf{p}(\mathbf{y}(\tau), \tau)$. *Natural parameter continuation* employs the simple choice of γ as a parameter, i.e., $\mathbf{p}(\mathbf{y}(\tau), \tau) = \gamma - \tau$. However, this method fails in the vicinity of the solutions where the Jacobian $\mathbf{g_y}$ becomes singular. We briefly discuss a simpler version of these singular points called *simple folds or simple limit points*, which are frequently encountered in the present investigation.

Simple Fold: A solution $(\mathbf{x_o}, \gamma_o)$ is called a *simple fold* (or *simple limit point*) if

$$\dim N(\mathbf{g}^{\mathbf{0}}_{\mathbf{x}}) = 1, \qquad \mathbf{g}^{\mathbf{0}}_{\gamma} \notin R(\mathbf{g}^{\mathbf{0}}_{\mathbf{x}}).$$

Here, $N(\mathbf{g_x^0})$ and $R(\mathbf{g_x^0})$ denote, respectively, the Null Space and the Range of $\mathbf{g_x^0}$. Differentiating $\mathbf{g}(\mathbf{x}(\tau), \gamma(\tau)) = 0$ with respect to τ gives the relation

$$\mathbf{g_x}\dot{\mathbf{x}} + \mathbf{g}_\gamma\dot{\gamma} = 0.$$

The parameterization is chosen such that

$$|\dot{\mathbf{x}}|^2 + \dot{\gamma}^2 = 1.$$

and, hence, at a *fold* $(\mathbf{x_0}, \gamma_0)$, $\dot{\gamma}_0 = 0$, and as $\dim N(\mathbf{g_x^0}) = 1$, we have $N(\mathbf{g_x^0}) = \text{span}\{\dot{\mathbf{x}}_\mathbf{0}\}$.

The Δy required for the Newton iterative procedure (4.3) is not available near the *fold point* due to the singular nature of the Jacobian matrix, and the *continuation* fails to proceed further. To compute past the fold, other methods like *Norm continuation* or *Pseudo-arclength continuation* can be chosen. In *Norm continuation*, parameterization function $\mathbf{p}(\mathbf{y}(\tau), \tau) = \langle \mathbf{y}(\tau), \mathbf{y}(\tau)\rangle - \tau^2$ is used. Even this method has some limitations and fails near higher-order fold points.

The popular *Pseudo-arclength continuation* (Keller, 1977) utilizes the parametrization function:

$$\mathbf{p}(\mathbf{y}(\tau), \tau) = |\dot{\mathbf{y}}|^2 - 1. \tag{4.5}$$

This theoretical tool is approximated for computations as

$$(\mathbf{y_1} - \mathbf{y_o})\,\dot{\mathbf{y}} - \Delta\tau = 0.$$

Geometrically, this method looks for a solution $\mathbf{y}_1$ to $\mathbf{g}(\mathbf{y})$ in a hyperplane perpendicular to a unit vector $\dot{\mathbf{y}}$, and that is at a distance $\Delta\tau$ from $\mathbf{y}_o$. This method works for every regular solution point $\mathbf{y}_o$ (including folds) provided that $\Delta\tau$ is sufficiently small.

The Newton iteration step for solving the equations now includes solving

$$\begin{bmatrix} \mathbf{g_x}(\mathbf{x}^i, \gamma^i) & \mathbf{g}_\gamma(\mathbf{x}^i, \gamma^i) \\ \mathbf{x_0}^* & \dot{\gamma} \end{bmatrix} \begin{bmatrix} \Delta\mathbf{x} \\ \Delta\gamma \end{bmatrix} = - \begin{bmatrix} \mathbf{g}(\mathbf{x}^i, \gamma^i) \\ (\mathbf{x}^i - \mathbf{x_o})^*\,\dot{\mathbf{x}}_o + (\gamma^i - \gamma_o)\,\dot{\gamma}_0 - \Delta\tau \end{bmatrix}.$$

The next direction vector $[\dot{\mathbf{x}}_\mathbf{1}, \dot{\gamma}]$ is defined by the equations

$$\mathbf{g_x}\dot{\mathbf{x}}_\mathbf{1} + \mathbf{g}_\gamma\dot{\gamma} = 0, \qquad (\dot{\mathbf{x}}_0)^*\,\dot{\mathbf{x}}_1 + \dot{\gamma}_o\dot{\gamma}_1 = 1.$$

Therefore, the direction vector $[\dot{\mathbf{x}}_\mathbf{1}, \dot{\gamma}]$ required for the next step is obtained by back substituting at the end of Newton iterations. This direction vector must then be normalized to a unit vector. This process is carried out iteratively along the τ and is capable of proceeding beyond the singular points such as *simple folds* without any issues.

4.2 Orthogonal Collocation

Collocation methods convert an infinite-dimensional problem into a finite-dimensional problem over a discretized space, facilitating the numerical computation of the solutions. Consider a system of first-order Ordinary Differential Equations (ODEs) of the form:

$$\begin{aligned} \frac{d}{ds}\mathbf{x}(s) = \mathbf{f}(\mathbf{x}(s), \gamma), \qquad & s \in [0,1], \\ & \mathbf{x}(\cdot,\cdot), \ \ \mathbf{f}(\cdot,\cdot) \in \mathbb{R}^{N_d}, \\ & \gamma \in \mathbb{R}, \end{aligned} \tag{4.6}$$

subject to the boundary conditions

$$\mathbf{b}(\mathbf{x}(0,\gamma), \mathbf{x}(1,\boldsymbol{\gamma}), \gamma) = \mathbf{0}, \qquad \mathbf{b}(\cdot,\cdot,\cdot) \in \mathbb{R}^{N_b}.$$

AUTO-07p solves BVPs using orthogonal collocation with piecewise continuous polynomial functions (Ascher et al., 1981). This means the unknown function is approximated as a polynomial of a specified degree in the given subintervals. The interval $[0,1]$ is discretized into n steps as

$$s_0 = 0 < s_1 < \ldots s_k < s_{k+1} < \ldots s_n = 1,$$

with the stepsize $h_k = s_k - s_{k-1}$ for $1 \leq k \leq n$. The collocation solution $P(\mathbf{x})$ is determined as a set of polynomial functions

$$P(\mathbf{x}) = (P_1^m, P_2^m, ..P_n^m),$$

where each term P_k^m is a polynomial $a_m s^m + a_{m-1}s^{m-1} + \cdots + a_o \ \forall s \in [s_{k-1}, s_k]$, $k = 1, 2, \ldots, n$ with the coefficients $a_0, a_1, \cdots a_m$ being N_d-dimensional vectors. Therefore, a m th degree collocation polynomial is described using $(m+1)nN_d$ scalar variables. These functions satisfy continuity at the mesh boundaries

$$P_k^m(x(t_k)) = P_{k+1}^m(x(t_{k+1})), \qquad k = 1, \ldots, n-1,$$

leading to $(n-1)N_d$ algebraic equations. The collocation solution $P(\mathbf{x})$ is required to satisfy the given differential equations at the *Gauss collocation points* within each interval $[s_{k-1}, s_k]$

$$P_k^{m\prime}(z_{j,i}) = \mathbf{f}(P_k^m(z_{j,i}), \gamma), \qquad j = 1, 2, \ldots, m.$$

The collocation points $z_{j,i}$ in each sub-interval are the roots of the mth degree *Legendre* polynomial (*Gauss points*). Table 4.1 presents collocation points for degrees from $m = 2$ to $m = 5$. These points provide the necessary algebraic equations to determine the collocation polynomials. This method is equivalent to using an *implicit Runga-Kutta method*. Additionally, the polynomials P_k^m meet the boundary conditions, and the $(m+1)nN$ variables are determined

No. of collocation points	Legendre Polynomial	Collocation points (zeros of the Legendre's polynomial translated from $[-1,1]$ to $[0,1]$)
2	$\frac{1}{2}(3x^2-1)$	$\frac{1}{2}-\frac{1}{2\sqrt{3}}, \quad \frac{1}{2}+\frac{1}{2\sqrt{3}}$
3	$\frac{1}{2}(5x^3-3x)$	$\frac{1}{2}-\frac{1}{2}\sqrt{\frac{3}{5}}, \quad \frac{1}{2}, \quad \frac{1}{2}+\frac{1}{2}\sqrt{\frac{3}{5}}$
4	$\frac{1}{8}(35x^4-30x^2+3)$	$\frac{1}{2}-\frac{1}{2}\sqrt{\frac{3}{7}+\frac{2}{7}\sqrt{\frac{6}{5}}}, \quad \frac{1}{2}-\frac{1}{2}\sqrt{\frac{3}{7}-\frac{2}{7}\sqrt{\frac{6}{5}}}, \quad \frac{1}{2}+\frac{1}{2}\sqrt{\frac{3}{7}-\frac{2}{7}\sqrt{\frac{6}{5}}}, \quad \frac{1}{2}+\frac{1}{2}\sqrt{\frac{3}{7}+\frac{2}{7}\sqrt{\frac{6}{5}}}$
5	$\frac{1}{8}(63x^5-70x^3+15x)$	$\frac{1}{2}-\frac{1}{6}\sqrt{5+2\sqrt{\frac{10}{7}}}, \quad \frac{1}{2}-\frac{1}{6}\sqrt{5+2\sqrt{\frac{10}{7}}}, \quad \frac{1}{2}, \quad \frac{1}{2}+\frac{1}{6}\sqrt{5-2\sqrt{\frac{10}{7}}}, \quad \frac{1}{2}+\frac{1}{6}\sqrt{5+2\sqrt{\frac{10}{7}}}$

Table 4.1 Collocation points in $[0,1]$

by the resulting set of algebraic equations:

$$\begin{aligned}&\text{Collocation}: mnN_d,\\ &\text{Continuity}: (n-1)N_d,\\ &\text{Boundary conditions}: N_b(=N_d).\end{aligned}$$

This method is implemented in *AUTO-07p* by introducing *Lagrange basis polynomials* in each subinterval $[s_{j-1}, s_j]$. For any given distinct m node points $s^{(1)}, \ldots s^{(m)}$ in the interval $[s_{j-1}, s_j]$, define

$$l_{j,i}(s), \quad j = 1, \ldots, n, \quad i = 0, 1, \ldots m,$$

by

$$l_{j,i}(s) = \prod_{k=1, k\neq i}^{m} \frac{s - s^{(i)}}{s^{(k)} - s^{(i)}}.$$

The local polynomial is then written in the form of a Lagrange interpolating polynomial as

$$\mathbf{p}_j(s) = \sum_{i=0}^{m} l_{j,i}\mathbf{x}_{j-1}^{(i)},$$

where $\mathbf{x}_{j-1}^{(i)}$ is the value of $\mathbf{x}$ at i th node point in the interval $[s_{j-1}, s_j]$. The nodes are chosen as the roots of the *orthogonal polynomials* (Table 4.1). If the m collocation points are chosen as the roots of m th order *Legendre orthogonal polynomial*, then the order of accuracy of the collocation method is m, i.e.,

$$\max_{[0,1]} |\mathbf{x}(s) - \mathbf{p}_j(s))| = \mathcal{O}(h^m),$$

and we have *superconvergence* at the meshpoints t_k (Doedel, 2007)

$$\max_k |\mathbf{x}(s_k) - \mathbf{p}_j(s_k))| = \mathcal{O}(h^{2m}).$$

Now, we require an additional pseudo-arclength parameterization equation to complete the *continuation* setup. The pseudo-arclength equation (4.5) used for computation purposes appears as

$$\int_0^1 (\mathbf{x}(s) - \mathbf{x_o}(\mathbf{s})) * \dot{\mathbf{x}}_o ds + (\gamma - \gamma_o) * \dot{\gamma} - \tau = 0,$$

where $(\mathbf{x}_o, \gamma)$, is the previously known computed point on the solution branch, and $(\dot{\mathbf{x}}_o, \dot{\gamma})$ is the normalized direction vector of the branch at that point. Then, the discretized pseudo-arclength equation is of the form

$$\sum_{j=1}^{n}\sum_{i=0}^{m} \omega_{j,i} \left(\mathbf{x}_{j-1}^{(i)} - (\mathbf{x_o})_{j-1}^{(i)}\right) * (\mathbf{x_o})_j^{(i)} + (\gamma - \gamma_o) * \dot{\gamma}_o - \tau = 0,$$

where $\omega_{j,i}$ are the Lagrange quadrature coefficients. The $(m+1)N$ algebraic equations from the discretized BVP are solved along with the discretized pseudo-arclength equation using a sufficiently small value of τ. Its value should not be too large so that some of the folds are undetected, nor too small so that it consumes more computational time and resources. *AUTO-07p* employs an efficient method to solve this linear system of equations (Doedel et al., 1991b). It condenses some parameters using Gauss elimination and separately solves the resultant decoupled system.

4.3 Solving a BVP using *AUTO-07p*

Now, we will provide a brief overview of the *AUTO-07p* software. This tool solves the parameter-dependent BVPs expressed in the ODEs of the form

$$\begin{aligned} \frac{d}{ds}\mathbf{x}(s,\gamma) = \mathbf{g}(\mathbf{x}(s,\boldsymbol{\gamma}),\boldsymbol{\gamma}), \qquad & s \in [0,1], \\ & \mathbf{x}(\cdot,\cdot),\ \ \mathbf{g}(\cdot,\cdot) \in \mathbb{R}^{N_d}, \\ & \boldsymbol{\gamma} \in \mathbb{R}^{N_p}, \end{aligned} \tag{4.7}$$

subject to boundary conditions

$$\mathbf{b}(\mathbf{x}(0,\boldsymbol{\gamma}),\mathbf{x}(1,\boldsymbol{\gamma}),\boldsymbol{\gamma}) = \mathbf{0}, \qquad \mathbf{b}(.,.,.) \in \mathbb{R}^{N_b}.$$

Here, we use $\boldsymbol{\gamma}$ to represent the vector of system parameters $[\gamma_1, \gamma_2, \ldots \gamma_{N_p}]$, N_d to denote the dimension of the problem, and N_b to indicate the number of boundary conditions. These parameters are included either through the algebraic system $\mathbf{g}(\cdot,\cdot)$, or through boundary conditions $\mathbf{b}(\cdot,\cdot,\cdot)$.

To solve a BVP, the user has to provide an ANSI-C ($filename.c$), or a FORTRAN source file ($filename.f90$) that gives the problem description (4.7). It includes the expressions for the right hand side $\mathbf{g}(.,.)$ of (4.7), the boundary conditions $\mathbf{b}(\cdot,\cdot,\cdot)$, and a known initial point $\mathbf{x}_o(.,.)$ for *continuation*. The dependence of the problem on the parameters $\boldsymbol{\gamma}$ is also included here. *Continuation* can be carried out in the system itself $\mathbf{g}(.,.)$, or in boundary conditions $\mathbf{b}(\cdot,\cdot,\cdot)$.

Continuation is executed with options provided in a constants file ($c.filename$), which controls all variables aspects of the run. The control aspects of a run, such as the number of discretization mesh intervals (NTST), the number of collocation points per interval (NCOL), solver precision, step size, the number of steps along a solution branch, choice of branch, selection of parameter γ_k for *continuation*, and so on, are regulated by this file. It also includes instructions to report the solution for a specific parameter value and to terminate the *continuation* at a certain parameter value. For each solution, the state variables $\mathbf{x}(\cdot,\cdot)$, and the vector of system parameters $\boldsymbol{\gamma}$ are printed out. By default, these solutions are printed in the file *fort.8*, and if specified, they are also printed in the file *s.filename*. Some examples of these auto-files are provided in the provided code (Appendix D).

CHAPTER 5

Hysteresis in Tip-Loaded Cantilevers: Equilibria and their Stability

In this chapter, we use the proposed machinery from Chapter 3 to determine the equilibria of tip-loaded cantilevers along with their stability properties. We incorporate a parameter in this system and formulate it as a parameter-dependent variational problem. Then, we investigate the parameter's influence on the equilibria with the aid of *distinguished bifurcation diagrams*. The parameter we have employed defines the rotation and induces the 2π - periodicity in the system. The primary focus is to understand the effect of intrinsic curvature on rod equilibria before exploring the more complex CTCR systems. To date, very few studies have been undertaken in the closely connected field of research. For instance, Armanini et al. (2017) investigated similar catapult behavior in tip-loaded intrinsically straight elastic rods.

5.1 Setup

An inextensible and unshearable massless elastic rod of circular cross-section is clamped at one end and connected to a dead load at the other, as shown in Figure 5.1. The dead load exerts a downward force $\mathbf{F} \equiv -F_2\mathbf{e_2}$ and a moment $\boldsymbol{\Upsilon}(\mathbf{q}(l)) \times \mathbf{F}$ due to an offset of the loading at the tip $s = l$. Just, recall that $\boldsymbol{\Upsilon}(\mathbf{q}(l))$ (3.12) is the lever arm of the load in the fixed frame and is given by $\Delta_1\mathbf{d}_1(\mathbf{q}(l)) + \Delta_2\mathbf{d}_2(\mathbf{q}(l)) + \Delta_3\mathbf{d}_3(\mathbf{q}(l))$, where Δ_1, Δ_2 and Δ_3 are the components of the arm in the $\{\mathbf{d}_1, \mathbf{d}_2, \mathbf{d}_3\}$ frame at the tip $s = l$. The clamped end is quasi-statically rotated about its horizontal tangent by an angle θ, and the rod response is examined. As a result, we have a parameter-dependent variational problem with the parameter being θ. We carry out numerical

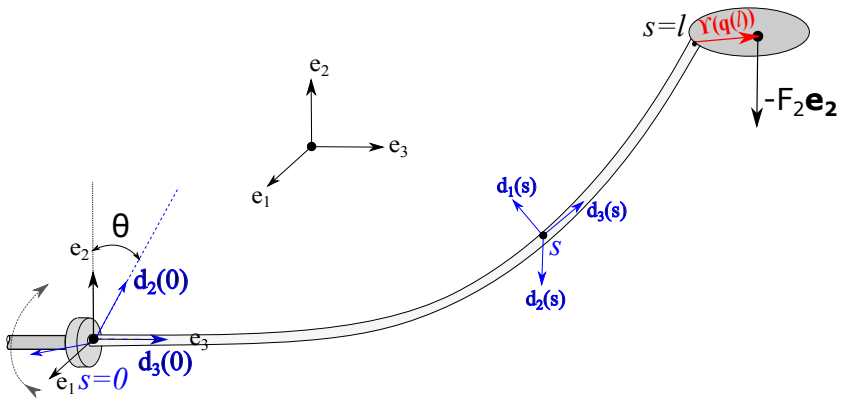

Fig. 5.1 Schematic of the setup

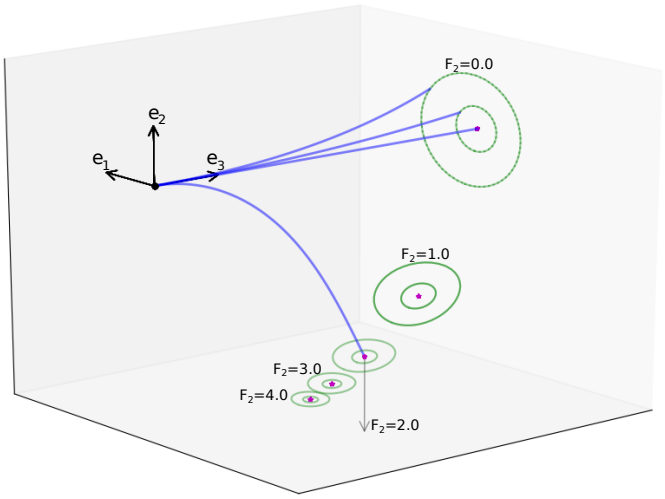

Fig. 5.2 Rods with small intrinsic curvature. The tip of an isotropic rod is a single point (purple), whereas the tips of rods with intrinsic curvature $\hat{u}_1 = 0.1$ and 0.2 trace closed smooth curves (in green for two intrinsic shaped rods at load F_2).

continuation along this parameter using *AUTO-07p*. The rod is assumed uniform with stiffnesses

$$K_1(s) = K_2(s) = 1.0, \quad K_3(s) = 1.0/1.3, \tag{5.1}$$

and a minimum energy intrinsic shape corresponding to the Darboux vector $\hat{\mathrm{u}}(s) = [\hat{u}_1, 0, \hat{u}_3]$.

This rod system is modeled using the Hamiltonian formulation of the rod equilibria (3.29), and the solutions are numerically continued along the parameter θ from a known initial solution using the following set of boundary conditions:

$$\begin{aligned}
&\mathbf{r}(0) = [0,0,0]^T, \qquad \mathbf{q}(0) = \left[0, 0, \sin\frac{\theta}{2}, \cos\frac{\theta}{2}\right]^T, \\
&\mathbf{n}(l) + \mathbf{F} = \mathbf{0}, \\
&m_i(l) + (\boldsymbol{\Upsilon}(\mathbf{q}(l)) \times \mathbf{F}) \cdot \mathbf{d}_i(\mathbf{q}(l)) = 0, \quad i = 1,2,3, \\
&\boldsymbol{\mu}(0) \cdot \mathbf{q}(0) = 0.
\end{aligned} \tag{5.2}$$

The simple, known, straight solution is initially taken as an initial guess. *Parameter continuation* is carried out sequentially to the required system parameters such as $\hat{u}_1$, $\hat{u}_3$, length l, arm Δ and tip load F_2. In the final step, solutions are continued along θ, fixing the values of the remaining parameters.

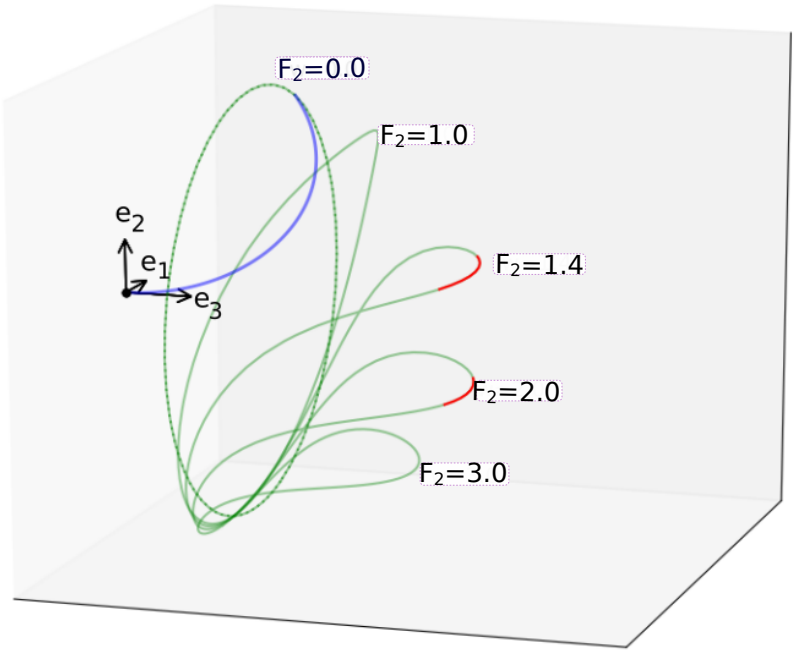

Fig. 5.3 Rod with higher intrinsic curvature. High intrinsic curvatures lead to unstable equilibria (red segments) for intermediate loads F_2.

For isotropic rods subjected to a pure concentrated tip loading ($\Delta = [0, 0, 0]$) (no moment corresponding to an offset load); there is a unique equilibrium with a planar centerline for different rotations of the clamped end θ. The rod centerlines depend only on the magnitude of tip load $\mathbf{F}$ and are independent of θ. Meanwhile, when the intrinsic curvature and twist of the rod are varied to non-zero values, distinct equilibrium centerlines are obtained for different values of θ. Lower intrinsic curvatures $\hat{u}_1$ and twists $\hat{u}_3$ result in equilibria consisting of smooth, continuously varying centerlines with their tip tracing closed curves, as shown in Figure 5.2. With increasing tip loads, these traces get smaller and eventually converge to a point. Further increase in the intrinsic curvatures results in the equilibrium solution sets with folds. Multiple equilibria exist for certain values of θ, and some of these are unstable. Traditionally, the folds are known to be associated with the presence of snap-back instability, where the rod snaps to the adjacent stable equilibrium. Since the equilibria depend on their history, the term hysteresis is used interchangeably to refer to this phenomenon. We examine the stability of the equilibria in the subsequent analysis and determine if the rod snaps. In Figure 5.3, the trace shown in red corresponds to unstable equilibria, and the rod would snap to the nearest stable configuration. Figure 5.4 shows the planar projections of rod configuration as the clamped end is rotated in the clockwise direction as seen towards $-\mathbf{e_3}$ direction. The snap motion occurs around $\theta = \pi$ where the rod centerline appears curving upwards. The red tip trace depicts the snap motion. Interestingly, this snapping behavior vanishes for higher tip loads such as $F_2 = 3.0$. In the following sections of this chapter, we will show a comprehensive description and analysis of this behavior, exploring its dependence on system parameters such as rod length, tip load, torsion, and arm.

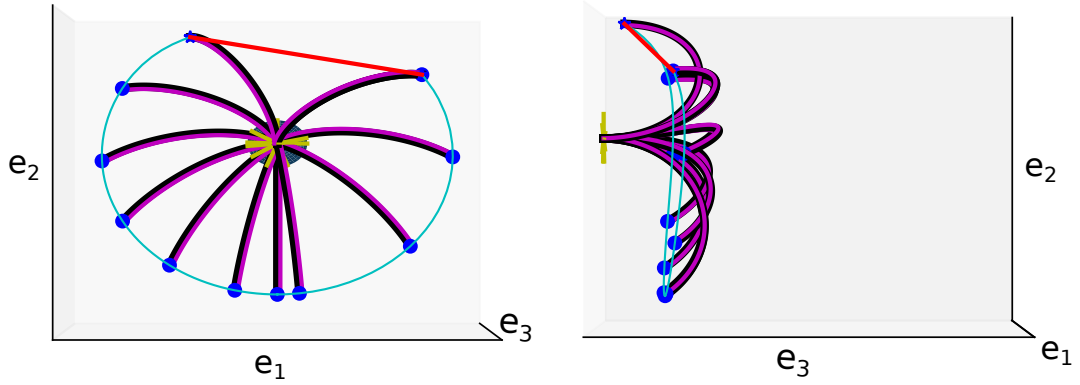

(a) $\mathbf{e}_1 - \mathbf{e}_2$ plane as seen in -$\mathbf{e}_3$ direction **(b)** $\mathbf{e}_2 - \mathbf{e}_3$ plane as seen in -$\mathbf{e}_1$ direction

Fig. 5.4 Planar projections of the rod centerlines with the tip trace as its clamped end is rotated about the horizontal tangent $F_2 = 1.0$ and $l = 1.75$. The trace represented in cyan corresponds to a smooth motion whereas that of red corresponds to an assumed snapping displacement.

5.2 Distinguished Bifurcation Diagram

As described in Chapter 2 (section 2.4), the qualitative information about the stability exchange near the folds can be deduced from the *distinguished bifurcation diagrams*. The ordinate in these diagrams is given by

$$\mathcal{L}_{\zeta'} \cdot \frac{\partial \boldsymbol{\zeta}_o}{\partial \xi}\bigg|_{s=0}.$$

In the present case, the parameter $\xi \equiv \theta$ acts at the boundary $s = 0$ through the boundary condition $\zeta_o \equiv \mathbf{q_o}(\theta) = [0, 0, \sin\theta/2, \cos\theta/2]^T$. Subsequently, the expression for the ordinate in this θ-dependent variational problem is then evaluated as

$$\begin{aligned}\mathcal{L}_{\mathbf{q}'} \cdot \frac{1}{2}\left[0, 0, -\cos\frac{\theta}{2}, \sin\frac{\theta}{2}\right]^T /2 &= \boldsymbol{\mu} \cdot \frac{1}{2}\left[0, 0, -\cos\frac{\theta}{2}, \sin\frac{\theta}{2}\right]^T, \\ &= \boldsymbol{\mu} \cdot \mathbf{B}_3\mathbf{q}(0)/2 \equiv m_3(0).\end{aligned} \tag{5.3}$$

The tangential component of the internal moment $m_3(\equiv \mathbf{m} \cdot \mathbf{d}_3)$ at $s = 0$ plotted against the parameter θ serves as the corresponding *distinguished bifurcation diagram*.

5.3 Numerical Examples

Hysteresis in the angle θ occurs under specific conditions of length, load, and intrinsic curvatures. In the current study, we examine the dependence of this hysteresis on system parameters by analyzing bifurcation diagrams for three possible scenarios: 1) varying force at a fixed length, 2) varying length at a fixed load, and 3) varying the intrinsic torsion component or the lever arm of the load. By investigating these factors, a better understanding on the effect of intrinsic curvature on hysteresis behavior can be gained.

5.3.1 Fixed Length and Varying Load

Consider an elastic rod with parameters $\hat{\mathbf{u}} = [1.5, 0, 0]$, length $l = 1.7$, and $\Delta = [0, 0, 0]$. *Parameter continuation* is performed along the clamp angle θ by increasing the value of F_2 in steps from 0 to 5.1. The value of $m_3(0)$ is evaluated from the computed solutions and plotted as a function of θ for different values of F_2 to give the corresponding *distinguished bifurcation diagrams*. The diagrams for the cases of $F_2 = 0.8, 2.0$ and 3.5 are presented in Figure 5.5. The curves corresponding to $F_2 = 0.8$ and $F_2 = 3.5$ have no folds, and the equilibria are stable for all values of θ. The stability is verified through *Jacobi condition* by showing that these equilibria have no *conjugate points*, as depicted in Figures 5.6a, 5.6b. Note that the *strengthened Legendre's condition* (3.36) is always satisfied. *Conjugate points* are computed as described in the section 3.11 for the equilibria denoted as 'o' in Figure 5.5. On the other hand, the diagram for $F_2 = 2.0$ consists of two folds. The equilibria corresponding to the θ in the region between the folds are unstable, as verified by the presence of *conjugate points* as shown in Figure 5.6c. It indicates an exchange of stability and the presence of a hysteresis region. The *distinguished bifurcation diagram* (Figure 2.2 in Chapter 2) predicts that the upper branch in the fold opening left side and the lower branch in the fold opening right side are unstable. In our situation, the region between the folds tallies with these unstable branches.

Bifurcation diagrams are obtained for a range of values of tip load F_2 from 0 to 5.0 and plotted as a contour surface, as shown in Figure 5.7. We refer to this plot as a *bifurcation surface*. This surface is sliced by the planes $F_2 = 0.8, 2.0$ and 3.5, which gives the planar bifurcation diagrams already displayed in Figure 5.5. Another orthogonal plane $\theta = \pi$ cuts the surface, resulting in a curve that can be interpreted as a bifurcation diagram when the parameter F_2 is varied at a fixed θ. It demonstrates how an intrinsically curved rod with the clamped end at $\theta = \pi$ behaves with the increasing tip load F_2. Typically, the rod equilibria are planar for $\theta = 0$ and $\theta = \pi$ under vertical tip load. In the former case, the rod centerline curves downwards, and in the latter case, it curves upwards. We draw some preliminary conclusions through *Bifurcation theory* (Golubitsky and Schaeffer, 2014), relying primarily on the plots and without extensive analysis. As the tip load F_2 increases, the planar equilibria of the rod experience two pitchfork bifurcations, one being supercritical at F_{super} and the other being subcritical at F_{sub}. Bifurca-

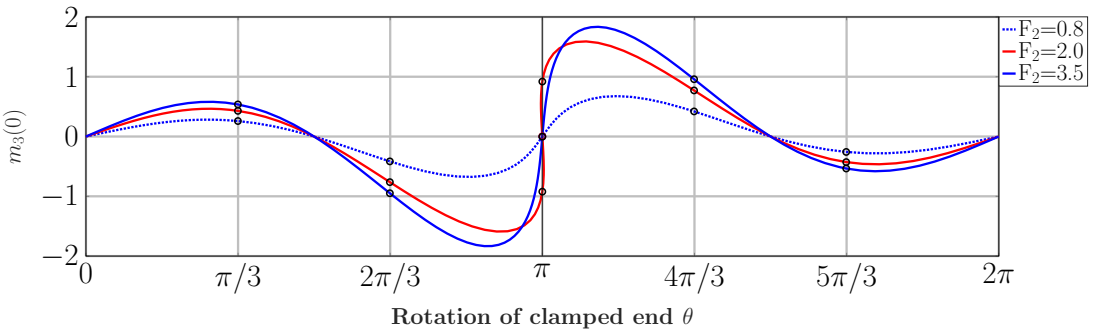

Fig. 5.5 The *distinguished bifurcation diagram* for tip loads $F_2 = 0.8, 2.0$ and 3.5. The points on the curve at intervals of $\pi/3$ are chosen for computing *conjugate points*(in Figure 5.6).

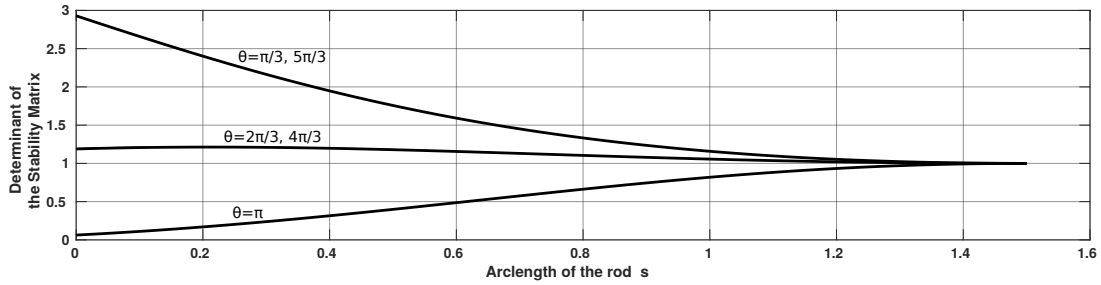

(a) $F_2 = 0.8$

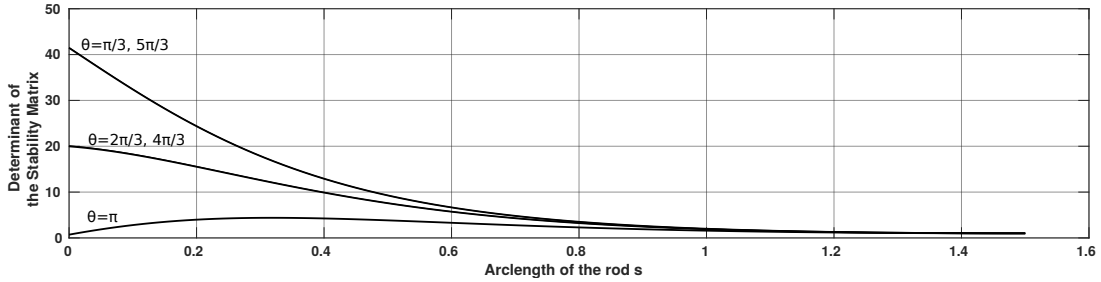

(b) $F_2 = 3.5$

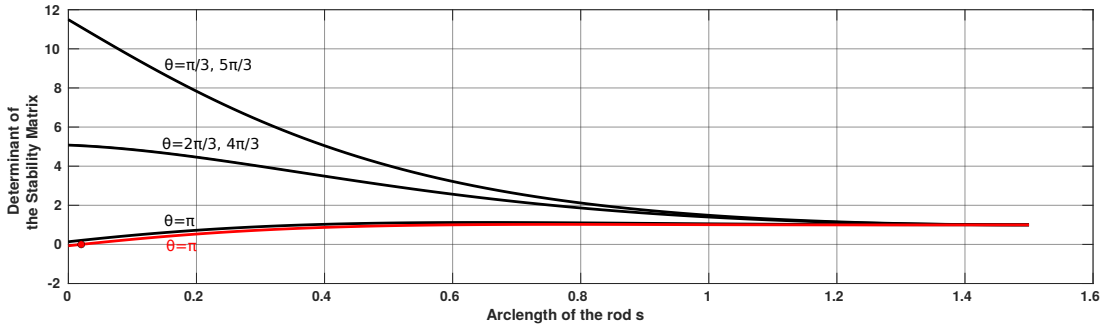

(c) $F_2 = 2.0$

Fig. 5.6 The computation of *conjugate points* for the equilibria corresponding to $\theta = k\pi/3$ $k = 1, \ldots, 5$ indicated in Figure 5.5. For the cases of $F_2 = 0.8$ and $F_2 = 3.5$, there are no *conjugate points*, and the equilibria are stable for all θ. On the other end, the diagram for $F_2 = 2.0$ has two folds. The equilibria for $\theta = \pi$ corresponding to the region between the folds have a conjugate point (indicated by the red point) and are unstable. The remaining equilibria do not have any *conjugate points* and are stable.

tion theory predicts that the trivial solution loses its stability at supercritical pitchfork bifurcation F_{super}, and gains stability at the subcritical pitchfork bifurcation F_{sub}. That is planar configuration (straight black line) loses its stability at F_{super} and assumes stable non-planar configuration (indicated by the black curved portion). On further increasing F_2, the planar configuration becomes stable at F_{sub}. Therefore, the equilibria along the trivial line segment connecting F_{super} and F_{sub} are unstable. This is in agreement with our prediction as the straight line corresponds to $\theta = \pi$ lies in the unstable region between the folds. We observe snapping behavior if the tip load F_2 satisfies $F_{super} < F_2 < F_{sub}$.

The *bifurcation surfaces* are plotted for different values of l, for a fixed $\hat{\mathrm{u}}$ and Δ in Figure 5.8. The surfaces corresponding to lower values of l have no folds, and the plane $\theta = \pi$ cuts the surface, resulting in a straight line as shown in Figure 5.8a. The snap-free solution paths are

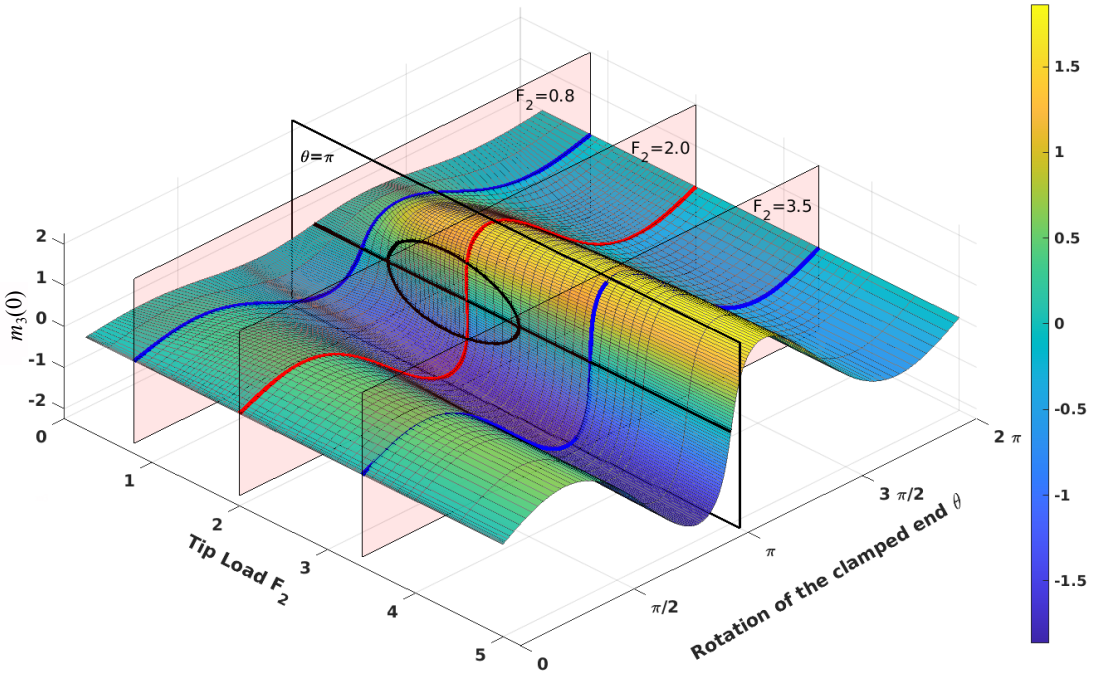

Fig. 5.7 The surface plot of the response $m_3(0)$ for continued solutions for an intrinsic curvature $\hat{\mathbf{u}} = [1.5, 0, 0]$ and length l as a function of parameter θ and tip load F_2. The planes $F_2 = 0.8, 2.0$ and 3.5 cut the surface resulting in smooth $m_3(0)$ vs. θ curves.

obtained for any tip load F_2 for this value of l. When the value of l exceeds a critical value, folded surfaces start appearing and are demonstrated by planar bifurcation curves on the plane $\theta = \pi$ as shown in Figure 5.8b,5.8c,5.8d. The values of F_{super} and F_{sub} are dependent on l, and consequently, the functions $F_{super}(l)$ and $F_{sub}(l)$ are used. As the value of l is increased, the distance between the bifurcation points, i.e., $F_{super}(l)$ and $F_{sub}(l)$, increases. Let us say we have a tip load F_2^o at length l_1 such that $F_2^o > F_{sub}(l_1)$. In this case, snapping does not occur as θ is varied. If the length is increased to l_2, the value of $F_{sub}(l_2)$ also increases. It can be raised to l_2 such that $F_2^o < F_{sub}(l_2)$. Then, with the same tip load of F_2^o but with a longer rod l_2, snapping can be witnessed.

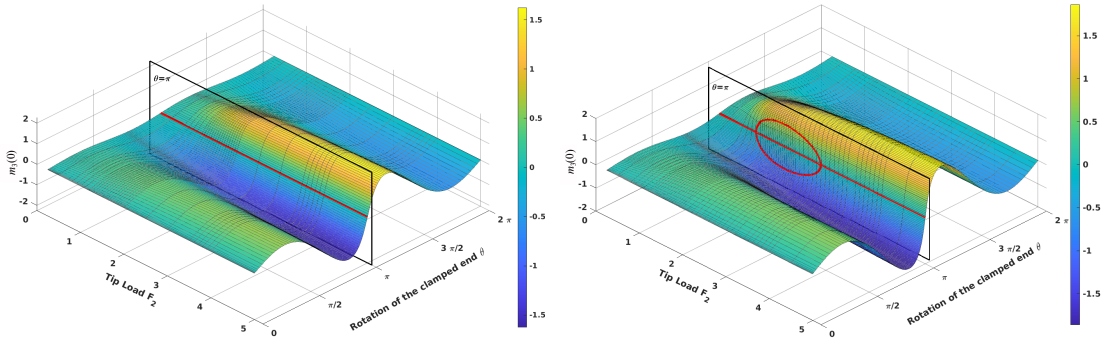

(a) $l = 1.2$ **(b)** $l = 1.5$

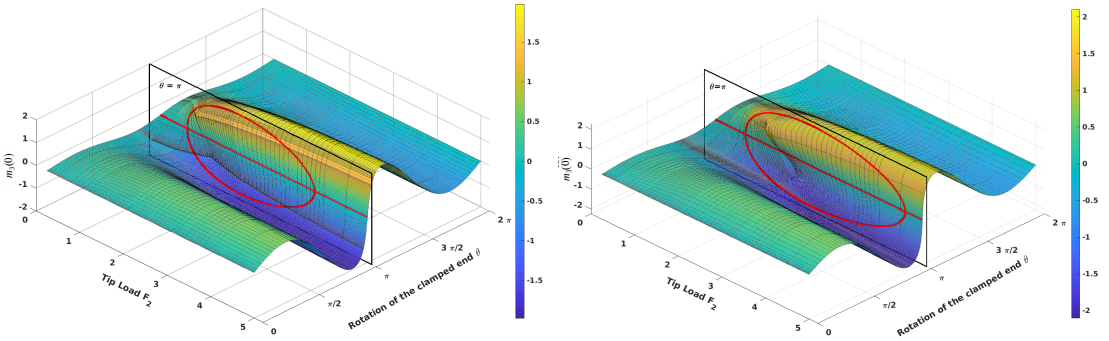

(c) $l = 1.7$ **(d)** $l = 2.0$

Fig. 5.8 The surface plot of $m_3(0)$ for *continuation* solutions as a function of input angle θ and tip load F_2 for four different values of l. The contours obtained as the plane $\theta = \pi$ cuts the surface are also portrayed.

5.3.2 Fixed Load and Varying Length

Now, we slightly modify the prior scenario, in which the tip load F_2 is held constant, and the rod length l is varied. The value of l is varied in increments from 0 to 3.5 for fixed values of F_2, and the *continuation* solutions along θ are obtained for each of the length steps. The value of $m_3(0)$ is evaluated for the computed solutions, and a *bifurcation surface* as a function of l and θ is plotted. The *bifurcation surfaces* obtained for different values of F_2 are depicted in Figure 5.10. The stability information embedded in these surface plots is the same as that in the prior case. The plane $\theta = \pi$ cuts the surface and gives a bifurcation diagram. Here, it can be interpreted as the bifurcation diagram when length l is varied at a fixed tip load F_2 with the clamped end held at $\theta = \pi$. The straight line (in red) corresponds to a trivial solution: the rod's planar configuration at $\theta = \pi$ curving upwards. The planar configuration at $\theta = \pi$ loses its stability at l_{super} and buckles into a non-planar equilibrium as the value of l increases. The planar configuration restabilizes when the value of l is increased past l_{sub}. Here, the snapping behavior is observed as the clamped angle θ is varied for values of l that satisfy $l_{super} < l < l_{sub}$. The evolution of the rod's centerline as the clamped end is rotated about the horizontal tangent for $F_2 = 1.0$ and $l = 2.5$ is shown in Figure 5.9. On comparing it with the snapping case of $F_2 = 1.0$ and $l = 1.7$ presented in Figure 5.4, we can observe that an increase in the value of l causes the rod to bend inwards and guide around the snapping region.

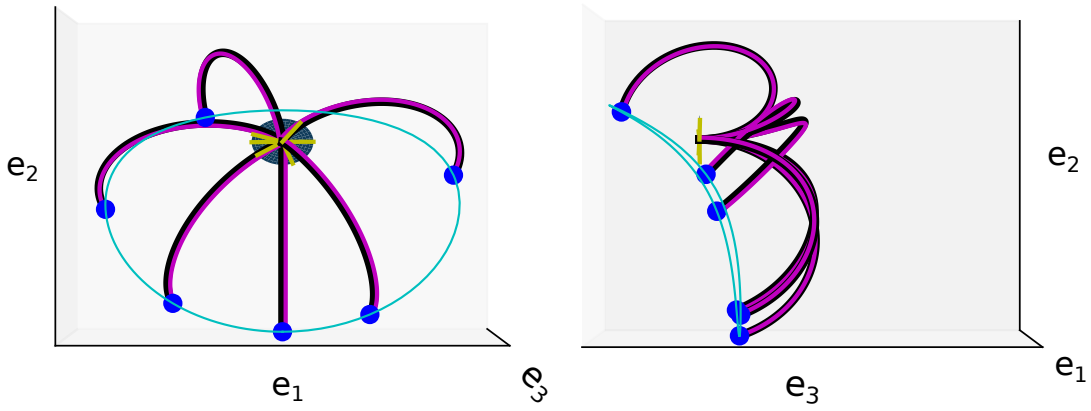

(a) $\mathbf{e_1} - \mathbf{e_2}$ plane as seen in $-\mathbf{e_3}$ direction **(b)** $\mathbf{e_2} - \mathbf{e_3}$ plane as seen in -$\mathbf{e_1}$ direction

Fig. 5.9 Planar projections of the rod centerlines with the tip trace as its clamped end is rotated about the horizontal tangent with a tip load $F_2 = 1.0$ and length $l = 2.5$. The tip trace is displayed in cyan.

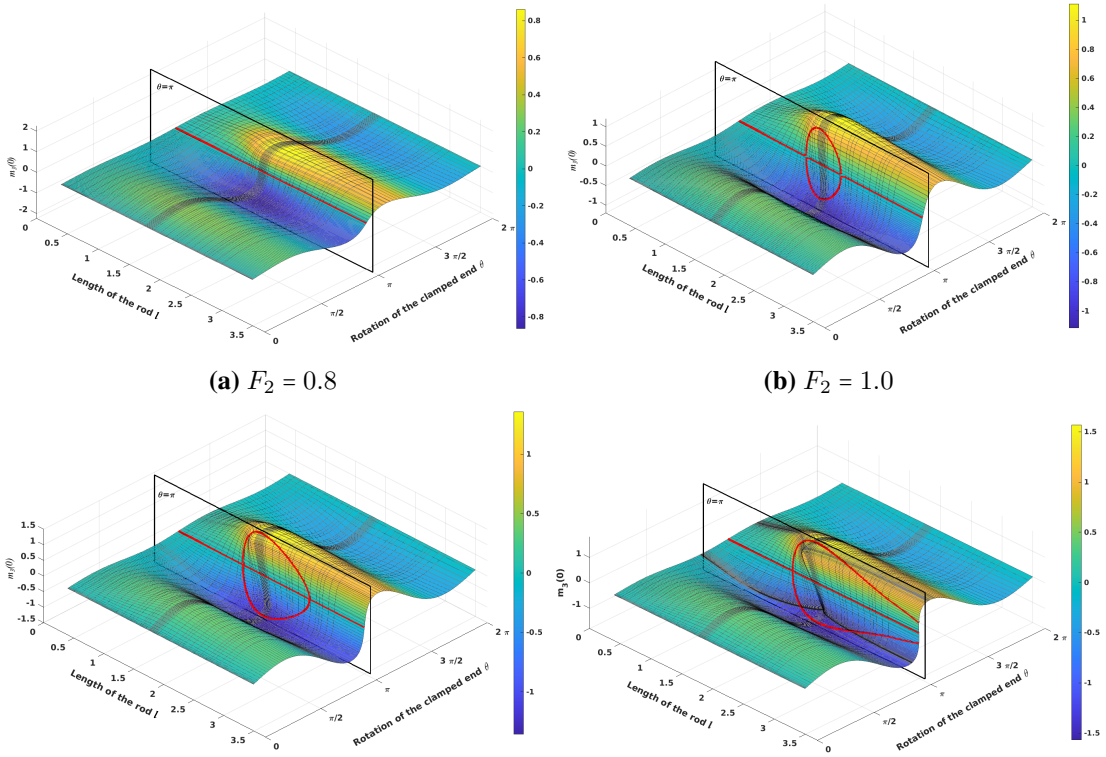

(a) $F_2 = 0.8$ **(b)** $F_2 = 1.0$

(c) $F_2 = 1.2$ **(d)** $F_2 = 1.4$

Fig. 5.10 The surface plot of the ordinate $m_3(0)$ for continued solutions as a function of the parameter θ and length of the rod l for different values of tip load F_2. The contour plots obtained as the $\theta = \pi$ plane slices the surface are shown in red.

5.3.3 Varying Intrinsic Torsion Component or Arm of the load

In the section, we slightly vary the torsion component to a non-zero value and examine its influence on the *bifurcation surfaces* depicted in Figure 5.8c and Figure 5.10c from previous examples. We consider the torsion $\hat{u}_3 = 0.01$ and carry out the *continuation* at a fixed load $F_2 = 1.2$, and for a range of l in $[0, 3.1]$. The *bifurcation surface* for the solutions is plotted as shown in Figure 5.11a. The symmetric surface for the case of $\hat{u}_3 = 0$ in Figure 5.10c transformed into a non-symmetric surface, as illustrated in Figure 5.11a and is more evident when

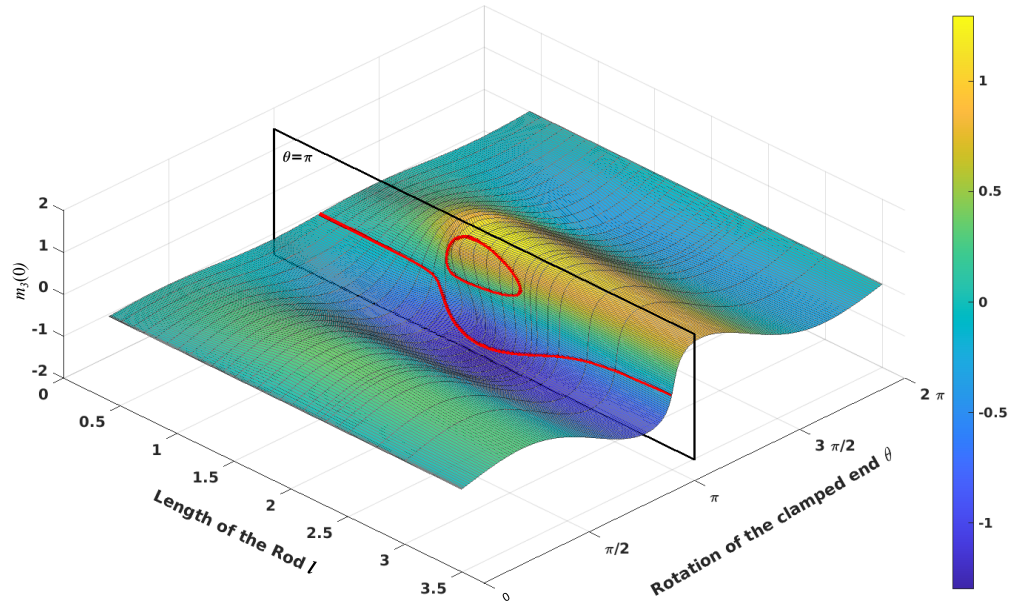

(a) Fixed $F_2 = 1.2$ and varying length l

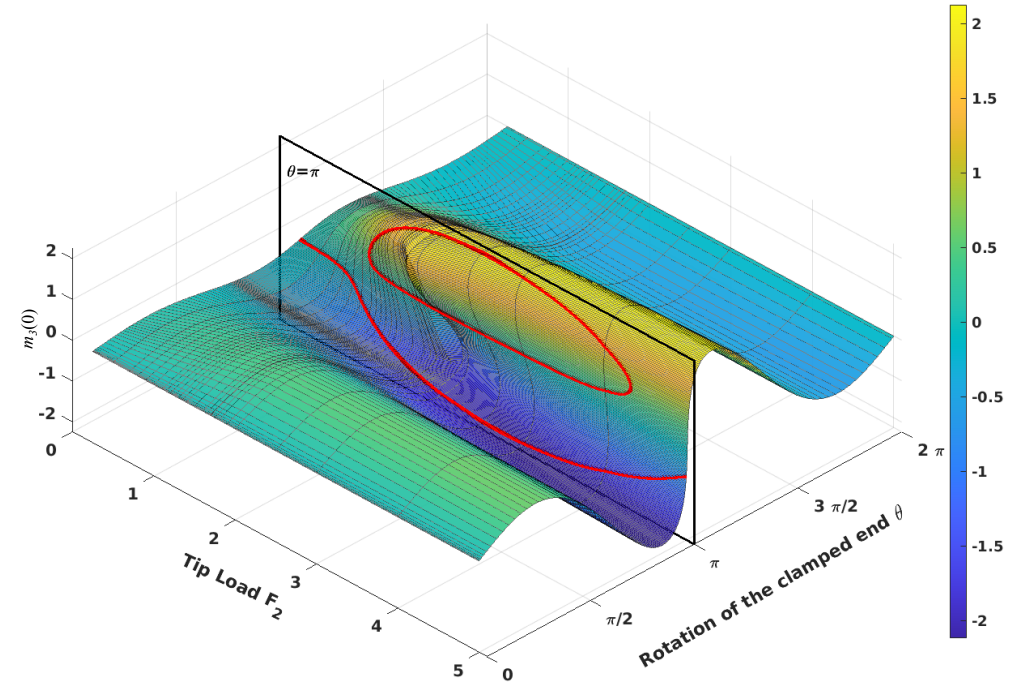

(b) Fixed $l = 1.7$ and varying load F_2

Fig. 5.11 The torsion $\hat{u}_3$ acts as a symmetry-breaking parameter.

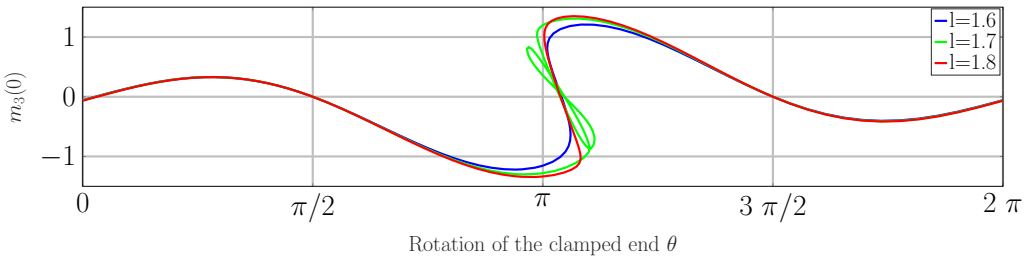

(a) Bifurcation diagrams for different values of l.

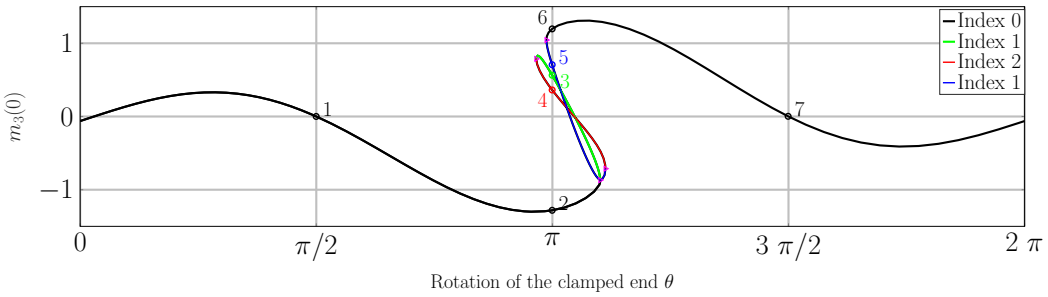

(b) The regions of the bifurcation diagram corresponding to $l = 1.7$ based on the *index*.

Fig. 5.12 Bifurcation diagram for fixed $F_2 = 1.2$, and $\hat{u} = [1.5, 0, 0.1]$.

the plane $\theta = \pi$ bisects it to fetch two disconnecting, non-symmetric curves (in red). Likewise, *continuation* solutions are obtained for load $l = 1.2$, and a range of tip load F_2 in $[0, 5.1]$, and the *bifurcation surface* is plotted. Here, the symmetric surface in Figure 5.8c also transformed to an asymmetric surface, as depicted in Figure 5.11b, and the bifurcation curve on the plane $\theta = \pi$ separates into two disconnecting curves. Both of these findings lead to the conclusion that the torsion $\hat{u}_3$ acts as an imperfect bifurcation parameter, breaking the symmetry in the system about $\theta = \pi$.

The bifurcation diagram on the $\theta = \pi$ plane in Figure 5.11a depicts the response of the elastic rod when its length l is varied while maintaining constant F_2 at constant $\theta = \pi$. If the rod equilibrium lies on the lower curve, it just stays on it when l is varied. However, if the equilibrium lies on the upper closed curve, it snaps to the lower curve when the value of l is varied past the folds. For $\hat{u}_3 = 0$, these curves are connected, and the equilibrium varies smoothly along the upper or lower pitchfork curve as the value of l is varied. Moreover, when $\hat{u}_3$ is non-zero, it imparts a preferred direction to these equilibria, i.e., the lower curve in this case. The same arguments apply to the bifurcation plot in Figure 5.11b, where the value of F_2 is varied at a fixed l of 1.7.

Let us further increase the value of $\hat{u}_3$ to 0.1 and conduct the *continuation* along θ maintaining the tip load constant $F_2 = 1.2$ for different values of $l \in [0, 3.1]$. Surprisingly, we obtained the bifurcation diagrams with four folds for intermediate values of l, as depicted in Figure 5.12. We observe that the number of folds rose from two to four as the value of l increased from 1.6 to 1.7. Further, an increase in the value of l to 1.8 decreased the folds back to two. The bifurcation diagram with four folds corresponding to $l = 1.7$ is shown in Figure 5.12b, where the folds di-

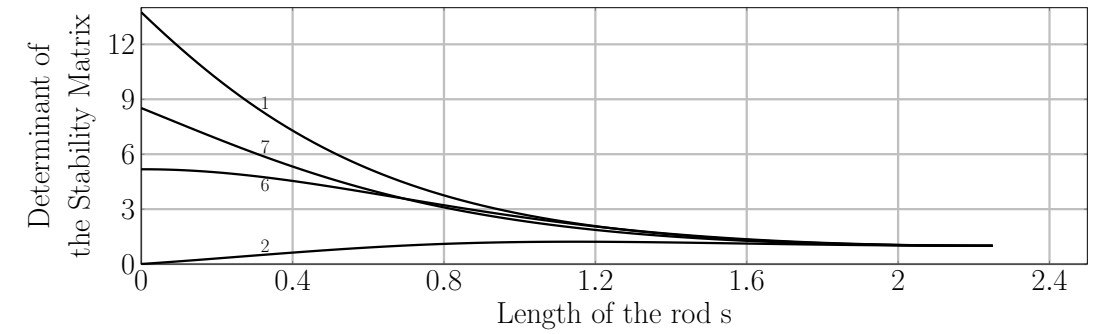

(a) No *conjugate points* exists for the equilibria labelled $1, 2, 6, 7$

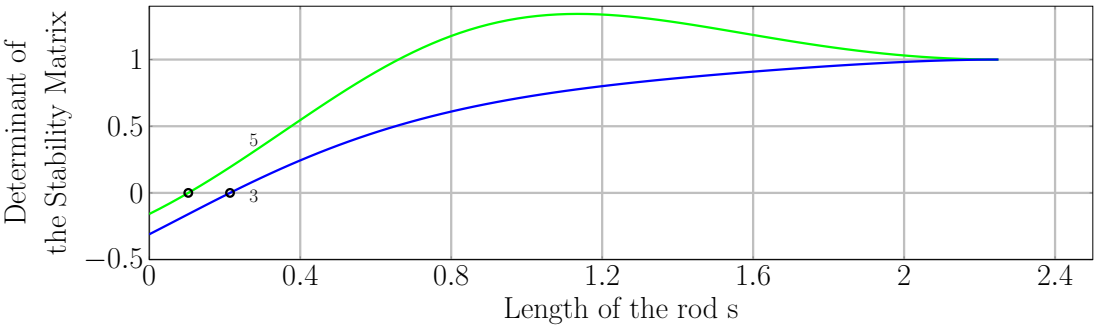

(b) One *conjugate point* (denoted in 'o') exists for the equilibria labelled 3 and 5.

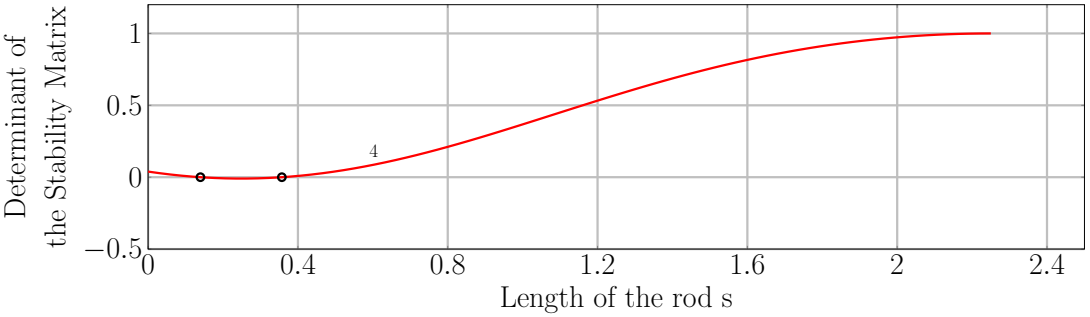

(c) Two *conjugate points* (denoted in 'o') exist for the equilibria labelled 4.

Fig. 5.13 Computation of *conjugate points* for the equilibria labeled in Figure 5.12b.

vide the diagram into different regions. The *Morse index* (section 2.3) is assigned to each region after computing the *conjugate points* for equilibria as illustrated in Figures 5.13a,5.13b,5.13c. The *index* in the upper branch increases by one if the fold opens to the left and decreases by one if it opens to the right. Therefore, it agrees with the prediction of *distinguished bifurcation diagrams* (Figure 2.2 in section 2.4). The planar views of rod centerlines for some values of θ along the bifurcation diagram are displayed in Figure 5.14. The five equilibria corresponding to $\theta = \pi$ are also illustrated in this figure along with their *index*. The only configurations with *index* 0 are stable and can realistically exist.

Now, we turn our attention to the effect of the load arm $\Delta = [\Delta_1, \Delta_2, \Delta_3]$ on the hysteresis behavior of the current clamped-rod setup. We study its impact on the *bifurcation surfaces* obtained for the case of $\Delta = [0, 0, 0]$ in Figure 5.8c and Figure 5.10c (from previous subsections 5.3.1 and 5.3.2). The centerlines of an unstressed uniform rod with intrinsic curvature

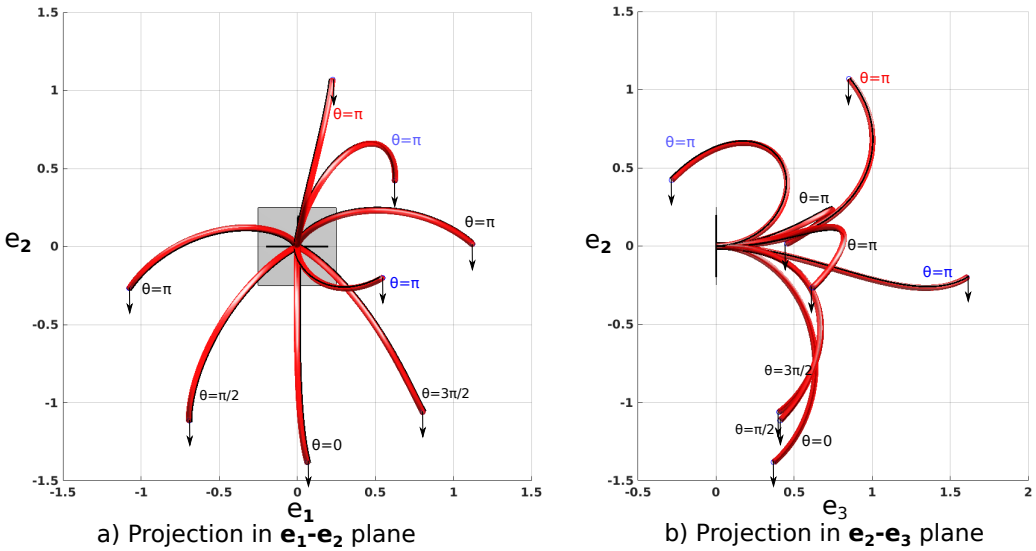

Fig. 5.14 Planar views of the equilibria for the given values of θ. The parameter $\theta = \pi$ corresponds to five equilibria. The red colored label corresponds to *index* 2, the blue corresponds to *index* 1, and the black to *index* 0.

$\hat{\mathrm{u}} = [\hat{u}_1, 0, 0]$ are planar and lie in the fixed $\mathbf{d}_2 - \mathbf{d}_3$. Therefore, non-zero value of the components Δ_2 or Δ_3 gives the arm which lies in this fixed $\mathbf{d}_2 - \mathbf{d}_3$ plane. Figure 5.15 shows the *bifurcation surfaces* obtained for these in-plane components $\Delta \equiv [0, 0.01, 0.0]$ and $\Delta = [0, 0.0, 0.01]$. No qualitative difference is visible in these plots in comparison with that in Figure 5.10c. Now consider the other component $\Delta = [0.01, 0.0, 0.0]$, which gives the arm non-planar with the plane of an unstressed elastic rod. The *bifurcation surface* for $F_2 = 1.2$, $\hat{\mathrm{u}} = [1.5, 0, 0]$ is obtained as shown in Figure 5.16, and it looks qualitatively similar to the *bifurcation surface*s in Figure 5.11. The symmetry in the surface is lost, and the bifurcation diagram along the plane $\theta = \pi$ separates into two disconnecting curves. Here, the component of the arm Δ_1 acts as a symmetry-breaking agent in a similar manner as the torsion component $\hat{u}_3$.

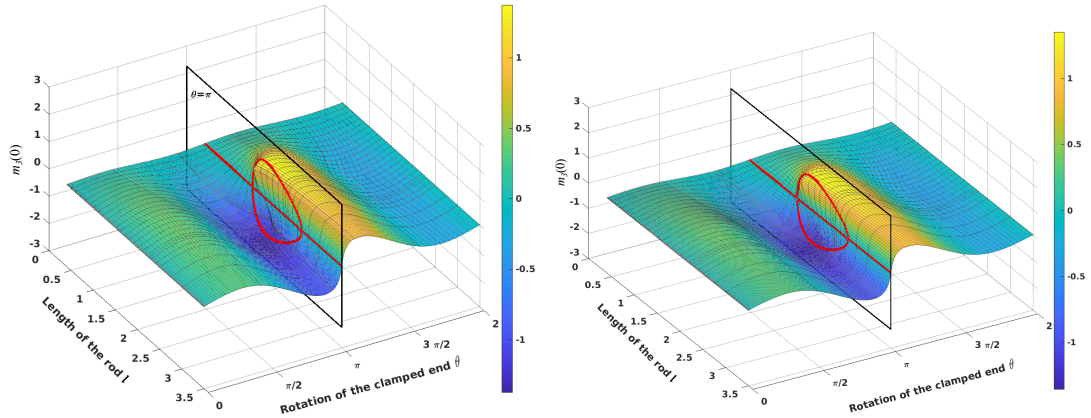

(a) $\Delta = [0, 0.01, 0]$. **(b)** $\Delta = [0, 0.0, 0.01]$.

Fig. 5.15 The effect of in-plane arm on the *bifurcation surface* of fixed $F_2 = 1.2$ and varying length l.

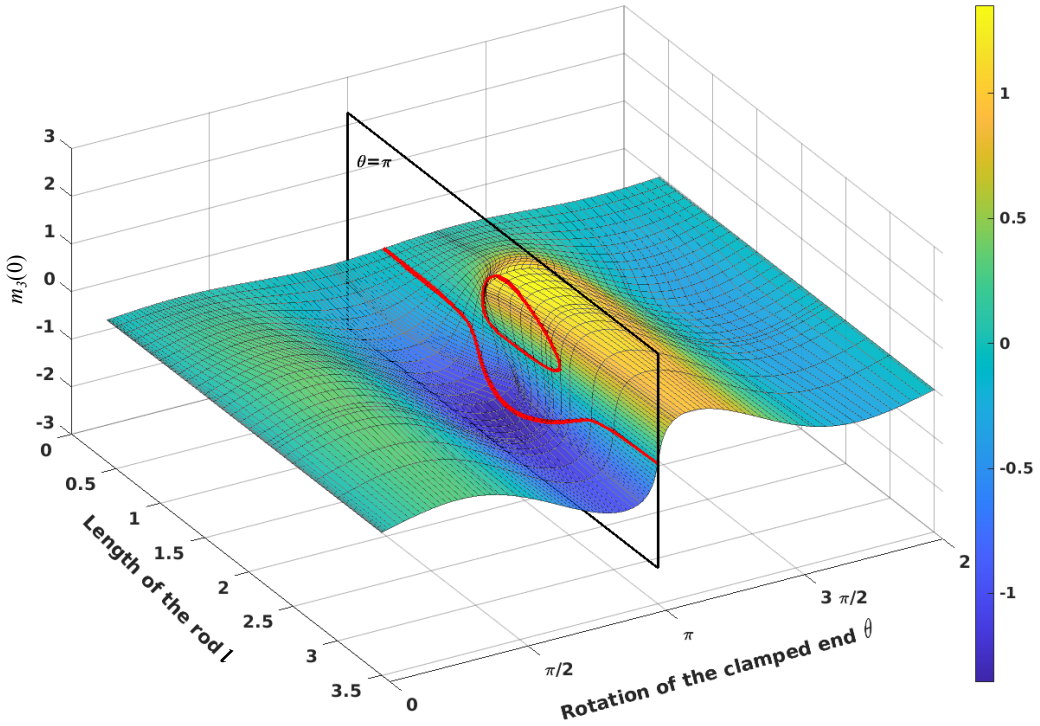

(a) Fixed $F_2 = 1.2$ and varying length l

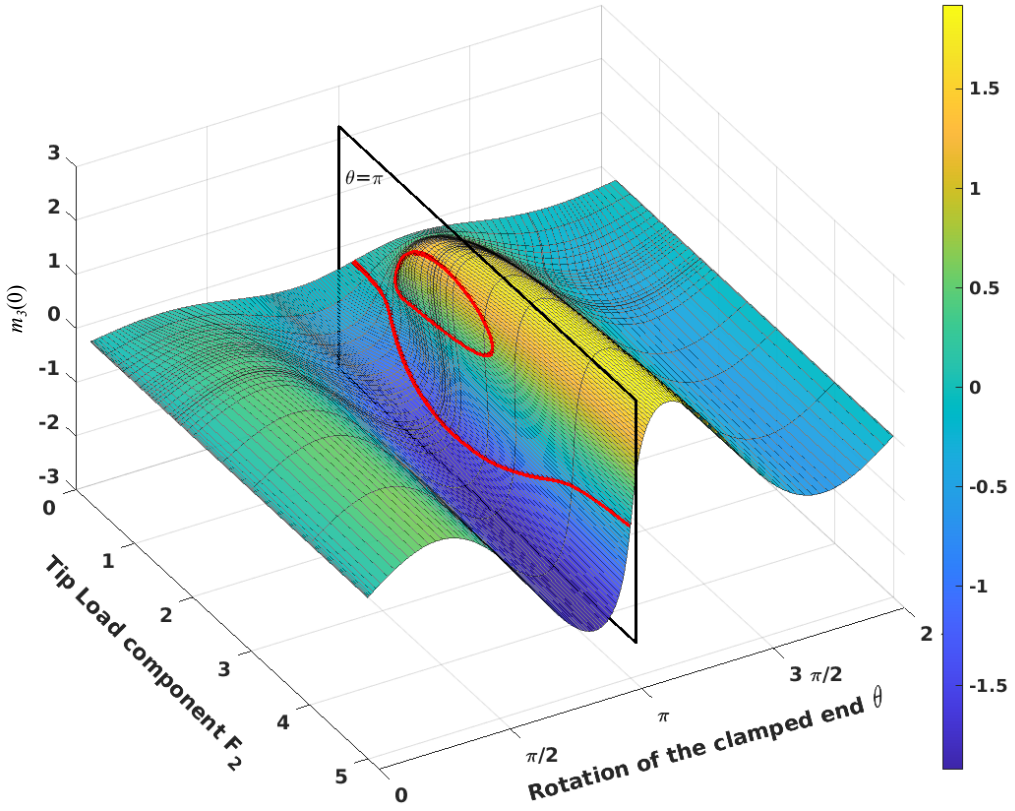

(b) Fixed $l = 1.7$ and varying load F_2

Fig. 5.16 The out-of-plane component of the load arm Δ_1 acts as a symmetry-breaking agent.

We further increase the value of Δ_1 to 0.1 and carry out the *continuation*. The length of the rod is fixed at l = 1.6, and the magnitude of tip load F_2 is varied. In this numerical experiment, we notice that bifurcation diagrams with four folds emerge for intermediate values of F_2, as shown in Figure 5.17. As the value of F_2 is increased from 1.3 to 1.4, the number of folds increases from two to four. Further, an increase in the value of F_2 from 1.4 to 1.7, led to a decrease in the folds to two. The regions in the bifurcation diagrams are assigned the *Morse index*,

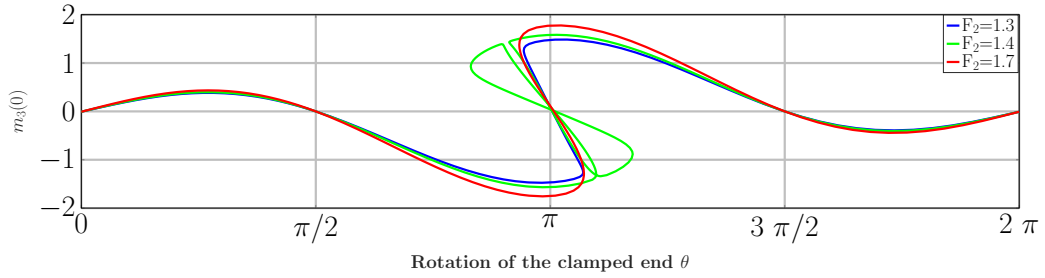

(a) Bifurcation diagrams for and l = 1.6 and three different values of F_2.

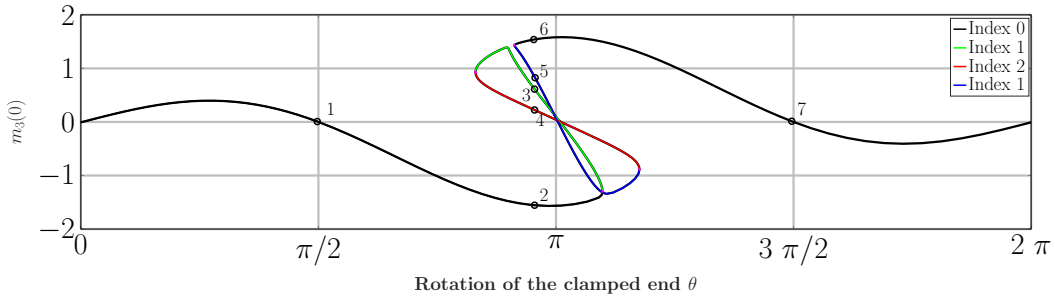

(b) Bifurcation diagrams for F_2 = 1.2. The plot consists of different regions separated by folds. Each region is assigned an *index* equal to the number of *conjugate points* the equilibrium in that region possesses.

Fig. 5.17 Bifurcation diagrams for the arm of the load $\Delta = [0.1, 0, 0]$.

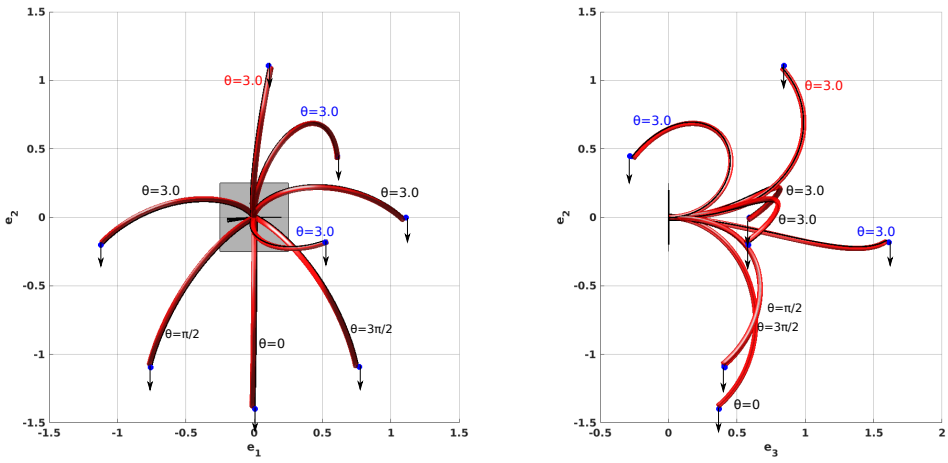

a) Projection in $\mathbf{e_1}$-$\mathbf{e_2}$ plane

b) Projection in $\mathbf{e_2}$-$\mathbf{e_3}$ plane

Fig. 5.18 Planar views of the rod centerlines for different values of θ. The parameter θ=3.0 corresponds to five rod equilibria. The color of the label is based on the *index*. The red color corresponds to *index* 2, blue corresponds to *index* 1, and black to *index* 0.

after computing the *conjugate points* for the equilibria. Their computations for some equilibria are shown in Figures 5.19a,5.19b,5.19c. The planar projections of centerlines of the equilibria in different regions along this curve are displayed in Figure 5.18. In summary, it can be deduced that the torsion component $\hat{u}_3$ and the arm component Δ_1 have a similar qualitative effect on the hysteresis behavior on the current clamped rod system. They induced symmetry-breaking and also resulted in the emergence of *index* 2 equilibria.

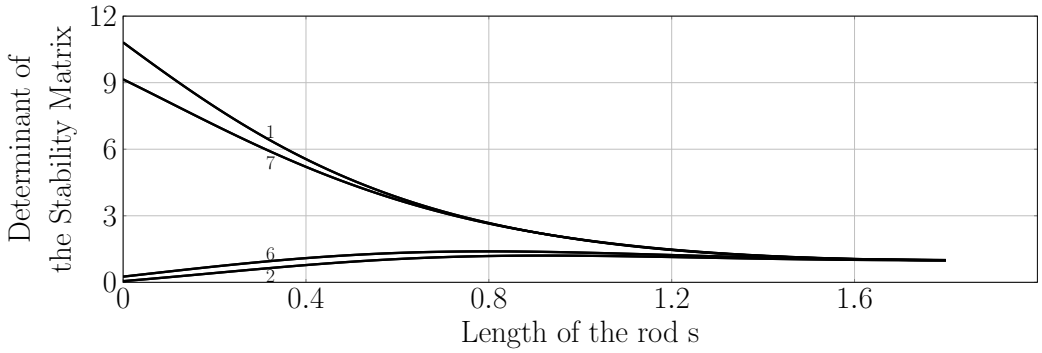

(a) No *conjugate point* exists for the equilibria labelled $1, 2, 6, 7$.

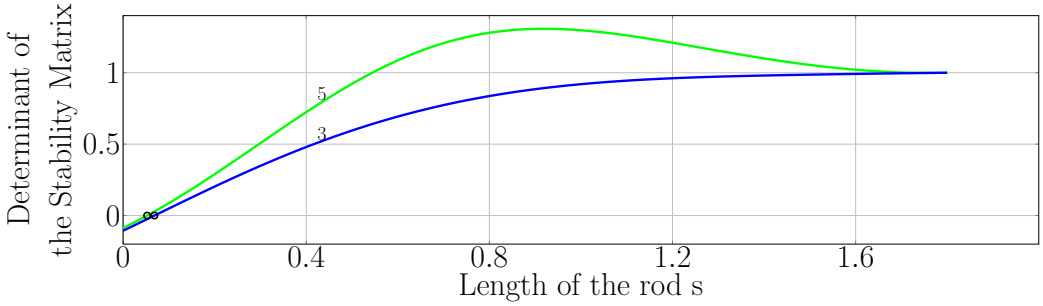

(b) One *conjugate point* (denoted in o) exists for the equilibria labelled $3, 4$ and therefore have *index* 1.

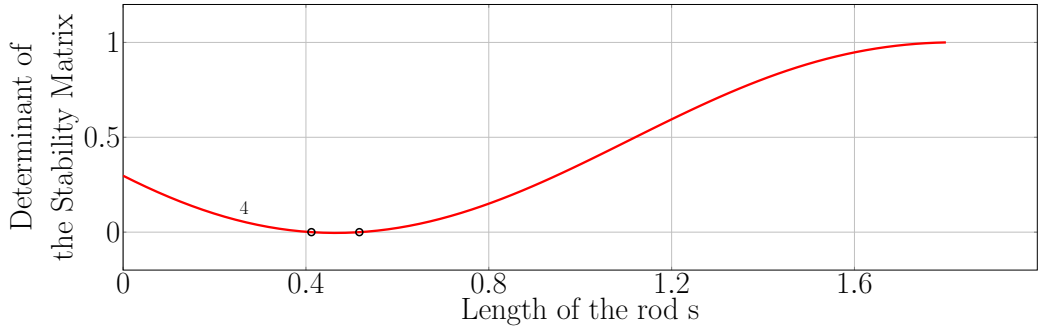

(c) Two *conjugate points* (denoted in o) exist for the equilibria labelled $3, 4$ and therefore have *index* 2.

Fig. 5.19 The *conjugate points* for the equilibria for the labels given along the bifurcation diagram in Figure 5.18

5.4 Conserved Quantities: Benchmark for Numerical Solutions

While performing numerical computation, one must ensure that the solutions converge and depict the actual system. We utilize the conserved quantities arising out of the Hamiltonian formulation 3.9 as benchmarks for verifying both the convergence and accuracy of the numerical solutions. The convergence is indirectly verified by considering the conserved quantities instead of comparing states at each discretization. We utilize the quantities $\mathbf{q} \cdot \mathbf{q} - 1$, $\boldsymbol{\mu} \cdot \mathbf{q} + 2\mathbf{r} \cdot \mathbf{n}$ and Hamiltonian H for this purpose. The elastic rod under consideration is uniform (constant stiffnesses K_1, K_3 and intrinsic shape $\hat{u}$), and as a consequence, the Hamiltonian H is conserved along the arc length s. We generate various *continuation* solutions using different numbers of mesh intervals and different numbers of *Gauss* collocation points and plot the corresponding conserved quantities, as given in Figures 5.20, 5.21 and 5.22. NTST denotes the number of mesh intervals, and NCOL denotes the number of *Gauss* collocation points. For this analysis, we consider the rod equilibrium pertaining to the parameters $\hat{\mathrm{u}} = [1.5, 0, 0]$, $L = 1.7$, $F_2 = 1.15$, $\Delta = [0.02, 0, 0]$ and $\theta = \frac{\pi}{2}$.

The spikes in the plots correspond to the discretized time steps, and they increase with the increase in NTST and NCOL. The quantities $\mathbf{q} \cdot \mathbf{q} - 1$, $\boldsymbol{\mu} \cdot \mathbf{q} + 2\mathbf{r} \cdot \mathbf{n}$ and H were found to be constant with an order of error depending on the mesh size and collocation. For instance, when using a lower mesh interval of 10 and collocation points of 2, these quantities were constant with an error of order $10^{-6} - 10^{-5}$. Doubling the number of mesh intervals to 20 reduced the error to the order 10^{-7} for all three quantities. Similarly, doubling the collocation points to 4 further reduced the error from a order of 10^{-7} to 10^{-9}. So, it can be inferred that the solutions

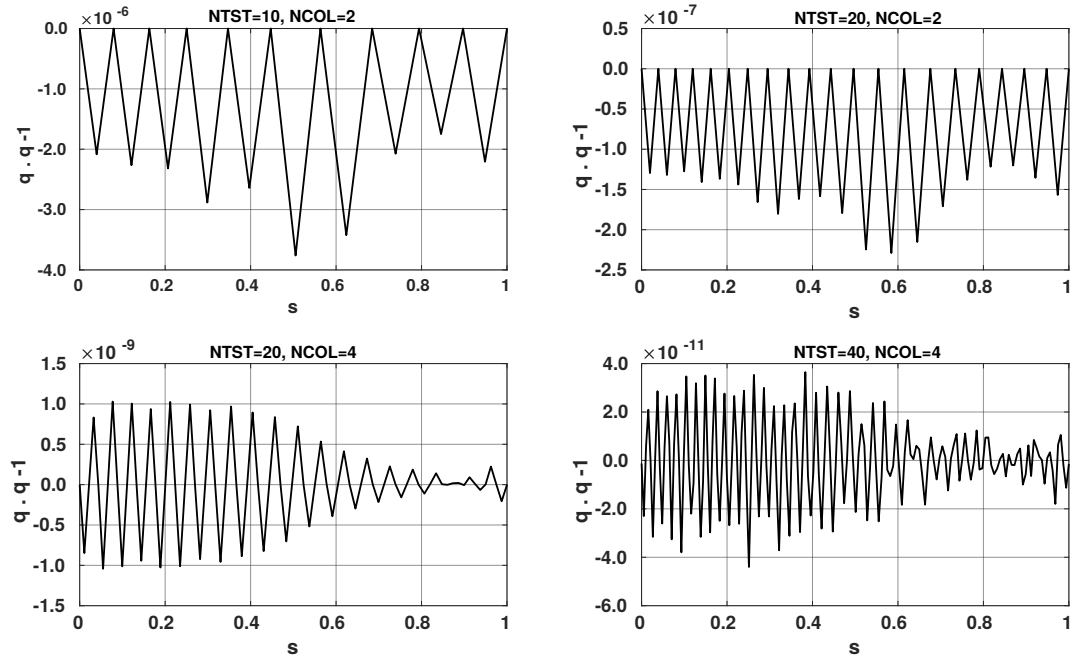

Fig. 5.20 Plot of the norm of the quaternions $\mathbf{q} \cdot \mathbf{q} - 1$ for a computed equilibrium where the interval has been discretized into NTST steps, and NCOL collocation points have been used.

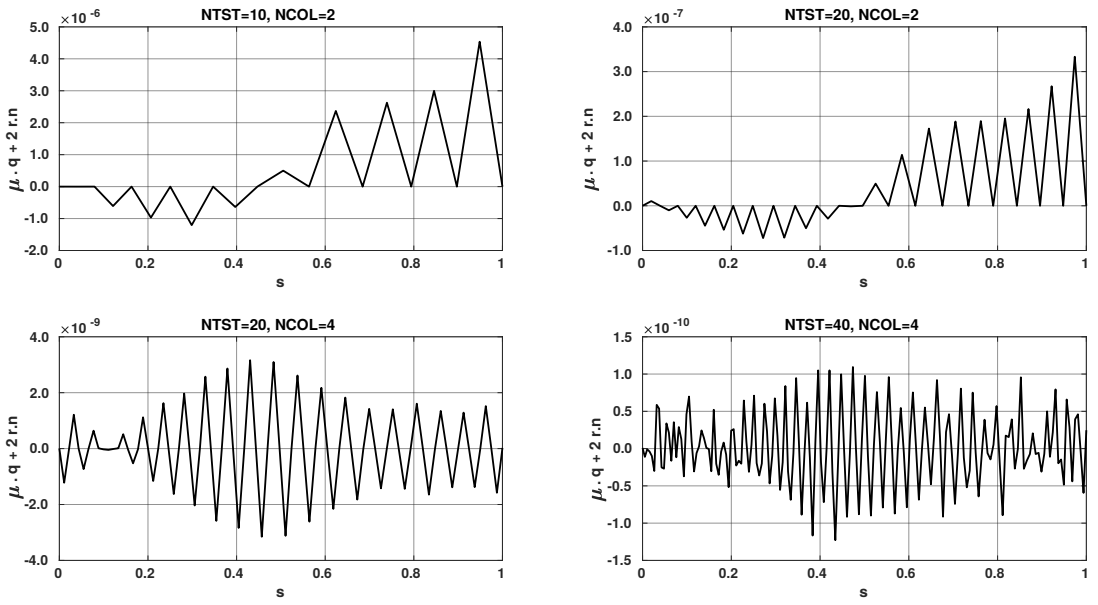

Fig. 5.21 Plot of the integral $\boldsymbol{\mu} \cdot \mathbf{q} + 2\mathbf{r} \cdot \mathbf{n}$ for a computed equilibrium where the interval has been discretized into NTST steps, and NCOL collocation points have been used.

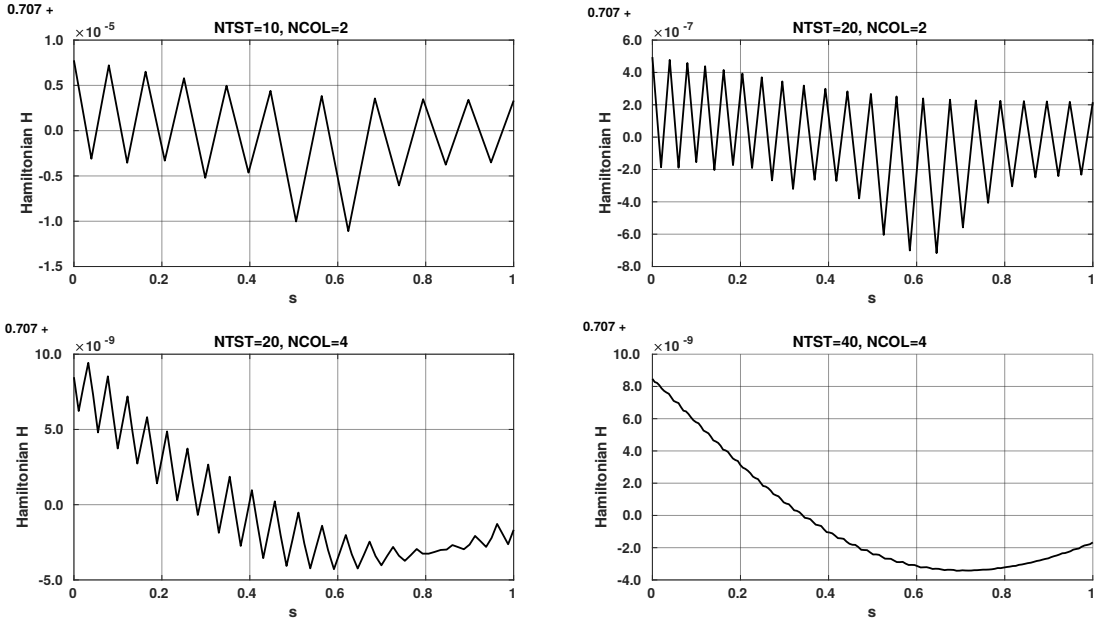

Fig. 5.22 Plot of the Hamiltonian H for a computed equilibrium where the interval has been discretized into NTST steps, and NCOL collocation points have been used.

converge with increasing mesh size and collocation points. In most of our computations in this chapter, we used 20 mesh intervals and 4 collocation points. Smaller mesh sizes and a higher number of collocation points give accurate results. But, they take longer computational time, and the solution files require larger computer storage.

5.5 Outlook

The impact of intrinsic curvature on the behavior of elastic rods subjected to tip loads was explored in this chapter. Emphasis was laid on studying the hysteresis phenomenon that arises when the clamp end is rotated. *Bifurcation surface*s were utilized to study their relationship with the rod length and tip load. The main finding of this chapter is that an initial increase in parameters such as rod length or tip load leads to the appearance of hysteresis behavior. Nevertheless, as the parameters continue to increase further, this hysteresis behavior disappears. Another takeaway is that the impact of the non-zero lever arm of the tip load, or torsion components of the intrinsic curvature, was found to have a symmetry-breaking effect on the rod equilibria. In addition, these system parameters also led to equilibria with an *index* of two. In these situations, *distinguished bifurcation diagrams* accurately predicted the change in the *index* near folds. Therefore, they can be employed in determining the stability of the equilibria without actually resorting to the computation of *conjugate points*. Nonetheless, the *index* for at least one equilibrium along the solution path must be determined by *conjugate point* computation to employ these diagrams. The next part will focus on the hysteresis behavior in a more complex elastic rod system of CTCR, which behaves as an elastic rod with intrinsic curvature with slightly complicated physics. In CTCRs, we have multiple sections with various intrinsic curvatures. As a result, they resemble elastic rods with piecewise intrinsic curvatures.

Part II

Concentric Tube Continuum Robots

CHAPTER 6

Concentric Tube Continuum Robot

6.1 Introduction

A Concentric Tube Continuum Robot (CTCR) is a system of two or more concentrically arranged elastic tubes of different stiffnesses and precurvatures (Rucker et al., 2010). Figure 6.1 displays its prototype, while Figure 6.2 displays its schematic. Each tube's end is connected to an actuator in the control unit at the base. The actuators mechanically control the tubes by relatively sliding and rotating the tubes one inside the other. The tubes are made of *Nitinol*, a shape memory alloy that undergoes large elastic deformations without any plasticity. The constituent tubes of the robot are restricted to take the shape of a common centerline referred to as the *backbone*. This *backbone* describes a smooth curve in the space, which depends on the imposed slides and rotations of the tubes by the control unit. An instrument such as a cutting tool, a needle, or a probe can be mounted at the robot's tip and maneuvered for several tasks. Because of their thin size and dexterity, these devices are useful for applications in confined spaces, such as minimally invasive surgeries. The spatial deformation of these continuum robots depends on the stiffnesses and the precurvatures of the constituent tubes, external loading, relative sliding, and twisting of the tubes at the base.

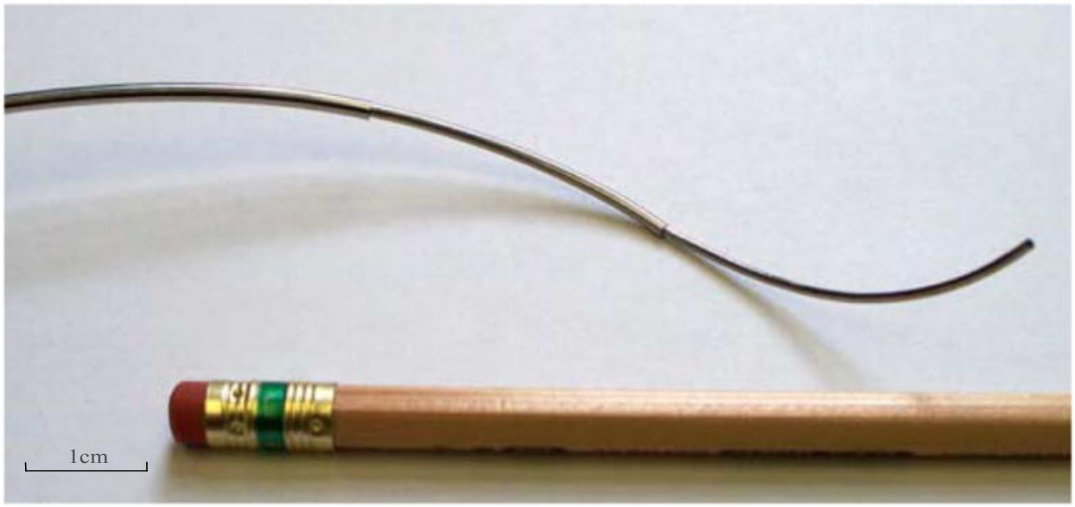

Fig. 6.1 A CTCR prototype consisting of three telescopic *Nitinol* tubes (adapted from (Rucker et al., 2010)).

The mechanical model for CTCRs (Rucker et al., 2010), which determines the equilibrium configurations for imposed lengths and the rotations of the tubes at the base, was developed using *Kirchhoff Rod theory*. This model incorporated the torsional compliance of the tubes but did not account for external loads. Geometric exact model (Rucker et al., 2010) was employed to model the CTCRs under the influence of external loads where force and moment balance on the constituent tubes is performed to obtain CTCR equilibria. However, the information about the stability of the equilibrium was not provided here. Ha et al. (2015) cast the problem of CTCR subjected to external loads as an *optimal control problem* and examined the stability properties of the resulting equilibria. In the current work, we consider a CTCR with a payload such as an instrument that exerts a tip load, and formulate it as a variational problem. The equilibria are determined by the stationary points of this variational problem, and their stability is determined by analyzing the second variation of the functional. These CTCRs consist of different sections, namely N-tube overlap, $N-1$ tube overlap, and so on, up to 1-tube overlap. As a result, the variational problem exhibits discontinuities in its integrand. We provide the required matching conditions at these points of discontinuity and analyze their stability properties. Furthermore, we generalize the notion of the index and *distinguished bifurcation diagrams* to CTCRs, as described for elastic rods in the previous part.

6.2 Variational Formulation

In this section, we discuss the kinematic model of the CTCR (Rucker et al., 2010), which is based on the *Kirchhoff Rod theory*. Consider a CTCR system consisting of N concentric tubes of different stiffnesses, precurvatures, and lengths. These tubes are identified with integers from 1 to N, with the innermost tube being 1 and the outermost being N. The notations and the properties used for elastic rods in Chapter 3 are utilized in the present context as well. The CTCR centerline is regarded as an elastic rod and a similar modelling approach is employed. The centerline $\mathbf{r}$ and local orientation frame $\{\mathbf{d}_1, \mathbf{d}_2, \mathbf{d}_3\}$ are described in terms of an independent parameter s, which is the arc length of the undeformed CTCR centerline. We impose hard loading at $s = 0$ for mathematical simplicity, i.e., the rotations of tubes directly at $s = 0$ are specified instead of at the actuators in the control unit. Let $l_1, l_2, \ldots, l_N$ be the lengths of the tubes with the property $l_1 \geq \ldots l_N$ and the innermost tube being the longest, and a schematic for the case of $N = 3$ is shown in Figure 6.2. The properties associated with i th tube are denoted using the superscript $[i]$. Each tube is modelled as a *Kirchhoff Rod*, and therefore, consists of its own centerline $\mathbf{r}^{[i]}(s)$ and a local frame $\{\mathbf{d}_1^{[i]}(s), \mathbf{d}_2^{[i]}(s), \mathbf{d}_3^{[i]}(s)\}$. The tubes are considered to be massless, unshearable, inextensible, linearly elastic, and have a stiffness $\mathbf{K}^{[\mathbf{i}]}$

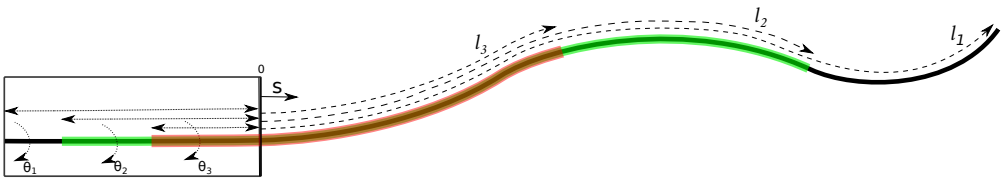

Fig. 6.2 Schematic of a three-tube CTCR with tubes of lengths l_1, l_2 and l_3 rotated by θ_1, θ_2 and θ_3 respectively

of the form $diag(K_{11}^{[i]}, K_{11}^{[i]}, K_{33}^{[i]})$ and precurvature $\hat{\mathfrak{u}}^{[i]} \in \mathbb{R}^3$ defined in its *material frame* $\{\mathbf{d}_1^{[i]}, \mathbf{d}_2^{[i]}, \mathbf{d}_3^{[i]}\}$. The different lengths l_k partition the total length into N segments S_k of length $L_k = l_k - l_{k+1} \geq 0$ such that S_k consists of k concentric tubes for $k = 1, \ldots, N$, as shown in Figure 6.2. The section S_N is located at the proximal end, whereas the section S_1 is located at the distal end. The constituent tubes of the CTCR deform while being constrained to share a common centerline curve in 3D space referred to as the *backbone*, and hence, the tangents of all the tubes, i.e., their $\mathbf{d}_3^{[i]}$-axes coincide. As these tubes are torsionally compliant, torsional displacement exists. Subsequently, the relative rotation of the tubes leads to different orientations of the director frames $\mathbf{d}_1^{[i]}(s)$ and $\mathbf{d}_2^{[i]}(s)$. We consider the *material frame* attached to the innermost tube (labelled $i = 1$) in its reference unstressed state as *backbone* reference for our formulations and computations. The relative rotation of the constituent tubes about the common tangent is evaluated with respect to this reference frame.

As a notational convenience, we use a specific step function $\tilde{\mathbf{K}}^{[k]}(s)$ to extend the tubes to a zero function beyond its length l_k as

$$\tilde{\mathbf{K}}^{[k]}(s) = \begin{cases} \mathbf{K}^{[k]}(s), & s \in [0, l_k], \\ 0, & s \in (l_k, l_1]. \end{cases} \tag{6.1}$$

Here, l_k is the length of the k-th tube calculated from $s = 0$ and is related to the lengths of the overlapping regions L_i as $l_k = \sum_{i=k}^{N} L_i$.

The *backbone* reference tube is described similarly to the previous part (Chapter3), employing a centerline $\mathbf{r} : s \to \mathbb{R}^3$ and an orientation frame $\{\mathbf{d}_1, \mathbf{d}_2, \mathbf{d}_3\}$ characterized by quaternions $\mathbf{q} : s \to \mathbb{R}^4$. Let $\mathtt{u}(s) = [u_1, u_2, u_3]$ be the triad of components of the Darboux vector of *backbone* defined in its *material frame* $\{\mathbf{d}_1, \mathbf{d}_2, \mathbf{d}_3\}$ i.e., $u_i \equiv \mathbf{u} \cdot \mathbf{d}_i$ for $i = 1, 2, 3$ and is expressed in terms of $\mathbf{q}(s)$ as

$$u_i(s) = \frac{2}{|\mathbf{q}|^2} \mathbf{B}_i \mathbf{q} \cdot \mathbf{q}', \qquad i = 1, 2, 3, \tag{6.2}$$

where $\mathbf{B}_i, i = 1, 2, 3$ are the same 4×4 matrices (3.11) defined in the section 3.4. Let $\alpha^{[i]} : s \to \mathbb{R}$ be the relative angle between the director frames of ith tube and that of the reference (tube 1) about the common tangent $\mathbf{d}_3(s)$. In a k-tube overlap portion, there are $k - 1$ relative angle functions $\alpha^{[i]}(s)$ where $2 \leq i \leq k$. These relative angle functions are represented in a column vector form $\boldsymbol{\alpha}(s) \in \mathbb{R}^{k-1} \equiv \left[\alpha^{[2]}(s) .... \alpha^{[k]}(s)\right]^T$. By definition, $\alpha^{[1]}(s) \equiv 0$, and therefore, is not included in $\boldsymbol{\alpha}$. For mathematical convenience, we consider the triad $\mathtt{u}$ as a column vector.

The Darboux vector $\mathtt{u}(s)$, defined within a director frame $\{\mathbf{d}_1, \mathbf{d}_2, \mathbf{d}_3\}$, is related to another director frame $\{\mathbf{D}_1, \mathbf{D}_2, \mathbf{D}_3\}$, which is rotated by a smoothly varying angle $\Theta : s \to \mathbb{R}$ about the common $\mathbf{d}_3$-axis through the relation

$$\mathbf{U}(\Theta, s) = \mathbf{R}(\Theta(s))\mathtt{u}(s) + [0 \quad 0 \quad \Theta'(s)]^T, \tag{6.3}$$

where $\mathbf{R}(\Theta(s)) \in SO(3)$ is a rotation matrix about $\mathbf{d}_3$-axis given by

$$\mathbf{R}(\Theta) = \begin{bmatrix} \cos\Theta & \sin\Theta & 0 \\ -\sin\Theta & \cos\Theta & 0 \\ 0 & 0 & 1 \end{bmatrix}.$$

Then, the elastic strain energy density of a i th tube defined in terms of the Darboux vector of the reference tube $\mathtt{u}$ and the angle between the frames $\alpha^{[i]}$ reads

$$\begin{aligned} E^{[i]}_{str}(\mathtt{u}, \alpha^{[i]}, \alpha^{[i]\prime}, s) &= \frac{1}{2}\left(\mathbf{U}(\alpha^{[i]}, s) - \hat{\mathtt{u}}^{[\mathtt{i}]}\right) \cdot \tilde{\mathbf{K}}^{[i]}(s) \left(\mathbf{U}(\alpha^{[i]}, s) - \hat{\mathtt{u}}^{[\mathtt{i}]}\right), \\ &= \frac{1}{2}\left(\mathtt{u} + \begin{bmatrix} 0 \\ 0 \\ \alpha^{[i]\prime} \end{bmatrix} - \mathbf{R}^T(\alpha^{[i]})\hat{\mathtt{u}}^{[\mathtt{i}]}\right) \cdot \tilde{\mathbf{K}}^{[i]}(s) \left(\mathtt{u} + \begin{bmatrix} 0 \\ 0 \\ \alpha^{[i]\prime} \end{bmatrix} - \mathbf{R}^T(\alpha^{[i]})\hat{\mathtt{u}}^{[\mathtt{i}]}\right). \end{aligned} \tag{6.4}$$

The orthogonality property of $\mathbf{R}(\alpha^{[i]})$ matrix and the diagonal nature of the stiffness matrix $\mathbf{K}^{[\mathtt{i}]}$ results in the relation

$$\mathbf{R}(\alpha^{[i]})^T \tilde{\mathbf{K}}^{[i]}(s) \mathbf{R}(\alpha^{[i]}) = \tilde{\mathbf{K}}^{[i]}(s).$$

Then, the strain energy density of i th tube (6.4) becomes

$$E^{[i]}_{str}(\mathtt{u}, \alpha^{[i]}, \alpha^{[i]\prime}, s) = \frac{1}{2}\left(\mathtt{u} + \begin{bmatrix} 0 \\ 0 \\ \alpha^{[i]\prime} \end{bmatrix} - \mathbf{R}^T(\alpha^{[i]})\hat{\mathtt{u}}^{[\mathtt{i}]}\right) \cdot \tilde{\mathbf{K}}^{[i]}(s) \left(\mathtt{u} + \begin{bmatrix} 0 \\ 0 \\ \alpha^{[i]\prime} \end{bmatrix} - \mathbf{R}^T(\alpha^{[i]})\hat{\mathtt{u}}^{[\mathtt{i}]}\right).$$

The function $E^{[i]}_{str}(\mathbf{u}, \alpha^{[i]}, \alpha^{[i]\prime}, s)$ is quadratic and convex with respect to $\mathtt{u}$ as well as $\alpha^{[i]\prime}$. Consequently, the following inverse relations can be obtained

$$\begin{aligned} \frac{\partial}{\partial \mathtt{u}} E^{[i]}_{str} \equiv \mathtt{m}^{[i]} &= \tilde{\mathbf{K}}^{[i]}(s) \left(\mathtt{u} + \begin{bmatrix} 0 \\ 0 \\ \alpha^{[i]\prime} \end{bmatrix} - \mathbf{R}(\alpha^{[i]})\hat{\mathtt{u}}^{[i]}\right), \\ \implies \mathtt{u} + \begin{bmatrix} 0 \\ 0 \\ \alpha^{[i]\prime} \end{bmatrix} - \mathbf{R}(\alpha^{[i]})\hat{\mathtt{u}}^{[i]} &= \tilde{\mathbf{K}}^{[\mathtt{i}]}(s)^{-1}\mathtt{m}^{[i]}, \\ \frac{\partial}{\partial \alpha^{[i]\prime}} E^{[i]}_{str} \equiv \beta^{[i]} = K^{[i]}_3(u_3 + \alpha^{[i]\prime} - \hat{u}^{[i]}_3) \implies \alpha^{[i]\prime} &= \frac{\beta^{[i]}}{K^{[i]}_3} - u_3 + \hat{u}^{[i]}_3. \end{aligned}$$

Each tube has an internal force $\mathbf{n}^{[\mathtt{i}]}$ and a moment $\mathbf{m}^{[\mathtt{i}]}$ transmitted along its length, and these vectors satisfy the force-moment balance equations (3.3). As each tube is considered to be *hyperelastic*, the term $\frac{\partial}{\partial \mathtt{u}} E^{[i]}_{str}$ gives the triad of components of the internal moment in the i th tube $\mathbf{m}^{[i]}$ along the *backbone* frame $\{\mathbf{d}_1, \mathbf{d}_2, \mathbf{d}_3\}$ frame, represented as $\mathtt{m}^{[i]} \equiv [m^{[i]}_1, m^{[i]}_2, m^{[i]}_3]$. Here, $m^{[i]}_k = \mathbf{m}^{[i]} \cdot \mathbf{d}_k$, for $k = 1, 2, 3$. This moment $\mathbf{m}^{[\mathtt{i}]}$ vanishes when the strain satisfies $\mathtt{u} = \mathbf{R}(\alpha^{[i]})\hat{\mathtt{u}} - \left[0, 0, \alpha^{[i]\prime}\right]^T$, where $\alpha^{[i]}$ is the stationary point of the functional $\int_0^{l_1} E^{[i]}_{str} ds$. The

term $\beta^{[i]}$ can be interpreted as a twist moment in the i th tube, i.e., $\mathbf{m}^{[\mathtt{i}]} \cdot \mathbf{d}_3$. We assume that no other interactions other than the mechanical contact occur between the tubes. For simplification, we use $[0 \quad 0 \quad \alpha^{[i]\prime}(s)]^T = \bar{\alpha}^{[i]\prime}$. Then, the total elastic strain energy stored in the system of N perfectly concentric tubes is just the sum of strain energies of its constituent tubes given by

$$
\begin{aligned}
&E_{str}(\mathtt{u}, \boldsymbol{\alpha}, \boldsymbol{\alpha}', s) \\
&\quad = \frac{1}{2} \int_0^{l_1} \sum_{i=1}^{N} \left(\mathbf{U}(\alpha^{[i]}, s) - \hat{\mathtt{u}}^{[\mathtt{i}]} \right) \cdot \tilde{\mathbf{K}}^{[i]}(s) \left(\mathbf{U}(\alpha^{[i]}, s) - \hat{\mathtt{u}}^{[\mathtt{i}]} \right) ds, \\
&\quad = \frac{1}{2} \int_0^{l_1} \sum_{i=1}^{N} \left(\mathtt{u}(s) + \bar{\alpha}^{[i]\prime} - \mathbf{R}(\alpha^{[i]})^T \hat{\mathtt{u}}^{[\mathtt{i}]} \right) \cdot \tilde{\mathbf{K}}^{[i]}(s) \left(\mathtt{u}(s) + \bar{\alpha}^{[i]\prime} - \mathbf{R}(\alpha^{[i]})^T \hat{\mathtt{u}}^{[\mathtt{i}]} \right) ds, \\
&\quad = \frac{1}{2} \int_0^{l_1} \mathtt{u}(s) \cdot \sum_{i=1}^{N} \tilde{\mathbf{K}}^{[i]}(s) \mathtt{u}(s) - 2\mathtt{u} \cdot \sum_{i=1}^{N} \tilde{\mathbf{K}}^{[i]}(s) \left(\mathbf{R}^T(\alpha^{[i]}) \hat{\mathtt{u}}^{[\mathtt{i}]} - \bar{\alpha}^{[i]\prime} \right) \\
&\qquad + \sum_{i=1}^{N} \left(\hat{\mathtt{u}}^{[\mathtt{i}]} - \bar{\alpha}^{[i]\prime} \right) \cdot \tilde{\mathbf{K}}^{[i]}(s) \left(\hat{\mathtt{u}}^{[\mathtt{i}]} - \bar{\alpha}^{[i]\prime} \right) ds.
\end{aligned}
$$

After adding and subtracting the following term to the integrand

$$
\frac{1}{2} \left(\mathbf{R}^T(\alpha^{[i]}) \hat{\mathtt{u}}^{[\mathtt{i}]} - \bar{\alpha}^{[i]\prime} \right) \cdot \sum_{i=1}^{N} \tilde{\mathbf{K}}^{[i]}(s) \left(\mathbf{R}^T(\alpha^{[i]}) \hat{\mathtt{u}}^{[\mathtt{i}]} - \bar{\alpha}^{[i]\prime} \right),
$$

we obtain

$$
\begin{aligned}
E_{str}(\mathtt{u}, \boldsymbol{\alpha}, \boldsymbol{\alpha}', s) = \frac{1}{2} \int_0^{l_1} &\mathtt{u}(s) \cdot \sum_{i=1}^{N} \tilde{\mathbf{K}}^{[i]}(s) \mathtt{u}(s) - 2\mathtt{u} \cdot \sum_{i=1}^{N} \tilde{\mathbf{K}}^{[i]}(s) \left(\mathbf{R}^T(\alpha^{[i]}) \hat{\mathtt{u}}^{[\mathtt{i}]} - \bar{\alpha}^{[i]\prime} \right) \\
&+ \left(\mathbf{R}^T(\alpha^{[i]}) \hat{\mathtt{u}}^{[\mathtt{i}]} - \bar{\alpha}^{[i]\prime} \right) \cdot \sum_{i=1}^{N} \tilde{\mathbf{K}}^{[i]}(s) \left(\mathbf{R}^T(\alpha^{[i]}) \hat{\mathtt{u}}^{[\mathtt{i}]} - \bar{\alpha}^{[i]\prime} \right) \\
&+ \sum_{i=1}^{N} \left(\hat{\mathtt{u}}^{[\mathtt{i}]} - \bar{\alpha}^{[i]\prime} \right) \cdot \tilde{\mathbf{K}}^{[i]}(s) \left(\hat{\mathtt{u}}^{[\mathtt{i}]} - \bar{\alpha}^{[i]\prime} \right) \\
&- \left(\mathbf{R}^T(\alpha^{[i]}) \hat{\mathtt{u}}^{[\mathtt{i}]} - \bar{\alpha}^{[i]\prime} \right) \cdot \sum_{i=1}^{N} \tilde{\mathbf{K}}^{[i]}(s) \left(\mathbf{R}^T(\alpha^{[i]}) \hat{\mathtt{u}}^{[\mathtt{i}]} - \bar{\alpha}^{[i]\prime} \right) ds.
\end{aligned}
$$

This expression can be written as a strain energy of a single-composite elastic rod (Rucker et al., 2010) as

$$
\begin{aligned}
E_{str}(\mathtt{u}, \boldsymbol{\alpha}, \boldsymbol{\alpha}', s) &= \int_0^{l_1} \mathcal{W}(\mathtt{u}, \boldsymbol{\alpha}, \boldsymbol{\alpha}') ds, \\
&= \int_0^{l_1} \frac{1}{2} (\mathtt{u} - \tilde{\mathtt{u}}) \cdot \mathbf{K}_{\mathbf{eff}} (\mathtt{u} - \tilde{\mathtt{u}}) + C(\alpha, \alpha') ds,
\end{aligned}
\tag{6.5}
$$

where

$$\mathbf{K_{eff}} = \sum_{i=1}^{N} \tilde{\mathbf{K}}^{[i]}(s), \tag{6.6a}$$

$$\tilde{\mathtt{u}}(\boldsymbol{\alpha}, \boldsymbol{\alpha}') = \mathbf{K_{eff}}^{-1} \sum_{i=1}^{N} \tilde{\mathbf{K}}^{[\mathtt{i}]}(s) \left(\mathbf{R}^T(\alpha^{[i]}) \hat{\mathtt{u}}^{[\mathtt{i}]} - \begin{bmatrix} 0 \\ 0 \\ \alpha^{[i]\prime} \end{bmatrix} \right), \tag{6.6b}$$

$$C(\boldsymbol{\alpha}, \boldsymbol{\alpha}') = \frac{1}{2} \sum_{i=1}^{N} \left(\hat{\mathtt{u}}^{[\mathtt{i}]} - \begin{bmatrix} 0 \\ 0 \\ \alpha^{[i]\prime} \end{bmatrix} \right) \cdot \tilde{\mathbf{K}}^{[i]}(s) \left(\hat{\mathtt{u}}^{[\mathtt{i}]} - \begin{bmatrix} 0 \\ 0 \\ \alpha^{[i]\prime} \end{bmatrix} \right) - \frac{1}{2} \tilde{\mathtt{u}} \cdot \mathbf{K_{eff}} \tilde{\mathtt{u}}. \tag{6.6c}$$

The integrand $\mathcal{W}$ is stationary when $\mathtt{u} = \tilde{\mathtt{u}}(\boldsymbol{\alpha}, \boldsymbol{\alpha}')$, and $\boldsymbol{\alpha}(s)$ is the extremal of the functional $\int_0^{l_1} C(\boldsymbol{\alpha}, \boldsymbol{\alpha}') ds$. The function $\mathcal{W}(\mathtt{u}, \boldsymbol{\alpha}, \boldsymbol{\alpha}')$ resembles an energy density function of an elastic rod with a stiffness $\mathbf{K_{eff}}$ and unstressed Darboux vector $\tilde{\mathtt{u}}$. The strain energy function $\mathcal{W}$ is the sum of convex functions of $\mathtt{u}$ and $\alpha^{[i]\prime}$, and therefore, is also convex with respect to $\mathtt{u}$ and $\alpha^{[i]\prime}$. Thus, the internal moment in the composite rod, which is the sum of internal moments in its constituent tubes $\mathtt{m}^{[\mathtt{i}]}$ $(i = 1, \ldots, N)$, is related to the $\mathtt{u}$ in the similar fashion as that of *hyperelastic rods* ((3.5) in section 3.3) and is given by

$$\mathtt{m}(s) = \sum_{i=1}^{N} \mathtt{m}^{[\mathtt{i}]} = \frac{\partial}{\partial \mathtt{u}} \mathcal{W}(\mathtt{u}, \boldsymbol{\alpha}, \boldsymbol{\alpha}', s) = \mathbf{K_{eff}}(s) \left(\mathtt{u} - \tilde{\mathtt{u}}(\boldsymbol{\alpha}, \boldsymbol{\alpha}', s) \right). \tag{6.7}$$

Essentially, the unloaded CTCR *backbone* behaves as a *hyperelastic rod* which assumes minimum energy at $\mathtt{u} = \tilde{\mathtt{u}}(\boldsymbol{\alpha}, \boldsymbol{\alpha}', s)$, where $\boldsymbol{\alpha}(s)$ simultaneously satisfies the extremum condition of the functional $\int_0^{l_1} C(\boldsymbol{\alpha}, \boldsymbol{\alpha}') ds$.

The CTCR structures are very thin, extremely flexible, and highly sensitive to external loads. Different scenarios of loading are possible during their operation. For instance, in applications like surgeries, tissues exert cutting forces as well as contact forces. These scenarios are challenging to model; therefore, we study these structures by restricting ourselves to the simple setting of a conservative tip load. Consider a CTCR system carrying a small payload like a surgical instrument at its tip $s = l_1$, as shown in Figure 6.3. Recall from section 3.5 that the payload exerts a constant force $\mathbf{F}$ and a moment $\boldsymbol{\Upsilon}(\mathbf{q}(l_1)) \times \mathbf{F}$ at the end $s = l$ and increases the

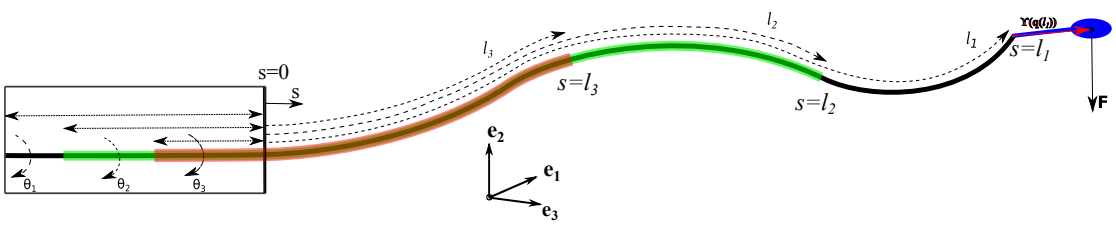

Fig. 6.3 Schematic showing a CTCR with a tip load $\mathbf{F}$ through a lever arm $\boldsymbol{\Upsilon}(\mathbf{q}(l))$.

potential energy of the system by

$$E_{load} = \mathbf{F} \cdot (\mathbf{r}(l_1) + \boldsymbol{\Upsilon}(\mathbf{q}(l_1))),$$

for an arm of the load in the fixed laboratory frame $\boldsymbol{\Upsilon}(\mathbf{q}(l_1))$, which in terms of local director frame at $s = l$ reads

$$\boldsymbol{\Upsilon}(\mathbf{q}(l_1)) = \Delta_1 \mathbf{d}_1(\mathbf{q}(l_1)) + \Delta_2 \mathbf{d}_2(\mathbf{q}(l_1)) + \Delta_3 \mathbf{d}_3(\mathbf{q}(l_1)).$$

The tip-loaded CTCR equilibria are determined by employing a similar methodology as that of elastic rods presented in Chapter 3 (Section3.5). We have a system of perfectly concentric unshearable, and inextensible tubes. As a consequence, the resulting composite rod system also behaves with the same property. First, we explicitly write u in terms of $\mathbf{q}$ and $\mathbf{q}'$ and later determine the stationary points of the total energy

$$\int_0^{l_1} \mathcal{W}\left(\frac{2\mathbf{B}_j \mathbf{q} \cdot \mathbf{q}'}{|\mathbf{q}|^2}, \boldsymbol{\alpha}, \boldsymbol{\alpha}', s\right) + \mathbf{F} \cdot (\mathbf{r}(l_1) + \boldsymbol{\Upsilon}(\mathbf{q}(l_1))), \tag{6.8}$$

adhering to the constraints of pointwise inextensibility and unshearability and the unit-norm of the quaternions $\mathbf{q}$:

$$\mathbf{r}'(s) - \mathbf{d}_3(s) = \mathbf{0}, \qquad \mathbf{q}(s) \cdot \mathbf{q}'(s) = 0. \tag{6.9}$$

So, we consider the minimization of the following associated functional $J \in \mathbb{R}$

$$\begin{aligned} J(\mathbf{r}, \mathbf{q}, \boldsymbol{\alpha}) &= \int_0^{l_1} \mathcal{W}\left(\frac{2\mathbf{B}_j \mathbf{q} \cdot \mathbf{q}'}{|\mathbf{q}|^2}, \boldsymbol{\alpha}, \boldsymbol{\alpha}', s\right) + \eta \mathbf{q} \cdot \mathbf{q}' + \boldsymbol{\lambda} \cdot \left(\mathbf{r}' - \mathbf{d}_3\right) ds \\ &\quad + \mathbf{F} \cdot (\mathbf{r}(l_1) + \boldsymbol{\Upsilon}(\mathbf{q}(l_1))), \\ &= \int_0^{l_1} \mathcal{L}\left(\mathbf{q}, \boldsymbol{\alpha}, \mathbf{q}', \boldsymbol{\alpha}', s\right) ds + \mathbf{F} \cdot (\mathbf{r}(l_1) + \boldsymbol{\Upsilon}(\mathbf{q}(l_1))), \end{aligned}$$

where $\boldsymbol{\lambda} \in \mathbb{R}^3$ and $\eta \in \mathbb{R}$ are the Lagrange multipliers associated with the pointwise constraints (6.9). The integrand, referred to as *Augmented Lagrangian* $\mathcal{L} : s \to \mathbb{R}$ reads

$$\mathcal{L}\left(\mathbf{r}, \mathbf{q}, \boldsymbol{\alpha}, \mathbf{r}', \mathbf{q}', \boldsymbol{\alpha}', s\right) = \mathcal{W}\left(\frac{2\mathbf{B}_j \mathbf{q} \cdot \mathbf{q}'}{|\mathbf{q}|^2}, \boldsymbol{\alpha}, \boldsymbol{\alpha}', s\right) + \eta \mathbf{q} \cdot \mathbf{q}' + \boldsymbol{\lambda} \cdot \left(\mathbf{r}' - \mathbf{d}_3\right). \tag{6.10}$$

The strain energy $\mathcal{W}$, as depicted in (6.5) depends on the stiffness matrix $\tilde{\mathbf{K}}^{[k]}(s)$, which is discontinuous at the boundary of the sections $s = l_k$ for $k = 2, \ldots, N$; consequently, the *Augmented Lagrangian* $\mathcal{L}$ is also discontinuous at these points.

6.3 Discontinuous Integrand

In the variational problems with discontinuous coefficients, additional matching conditions must be incorporated to determine the equilibria and their stability properties. Just recall that the

stationary points are the extremals of the *calculus of variations* problem

$$J(\boldsymbol{\zeta}) = \int_0^{l_1} \mathcal{L}(\boldsymbol{\zeta}, \boldsymbol{\zeta}', s) ds,$$

with both the ends, $s = 0$ and $s = l_1$, subject to either fixed or free boundary conditions. Suppose the integrand function $\mathcal{L}(\boldsymbol{\zeta}, \boldsymbol{\zeta}', s)$ is discontinuous at a known point $l_c \in [0, l_1]$. In the current scenario of CTCR, the point l_c corresponds to $l_k, k = 2, 3, \ldots, N-1$, i.e., the boundary between the sections. For the sake of simplicity, we discuss the system with just one point of discontinuity here. Nevertheless, these conditions are still applicable in cases with more than one point of discontinuity. The function $\boldsymbol{\zeta}(s)$ is continuous within the interval $[0, l_1]$, and we determine the essential conditions on its derivative $\boldsymbol{\zeta}'(s)$ for $\boldsymbol{\zeta}(s)$ to qualify as an extremal. The functional $\mathcal{L}$ can be decomposed about the discontinuous point l_c as

$$J(\boldsymbol{\zeta}) = \int_0^{l_1} \mathcal{L}(s) ds = \int_0^{l_c} \mathcal{L}_1(\boldsymbol{\zeta}, \boldsymbol{\zeta}', s) + \int_{l_c}^{l_1} \mathcal{L}_2(\boldsymbol{\zeta}, \boldsymbol{\zeta}', s) ds. \tag{6.11}$$

On applying the first-order necessary condition for the stationary points on $J(\boldsymbol{\zeta})$, we obtain

$$\begin{aligned}\delta J(\boldsymbol{\zeta})[\mathbf{h}] = \int_0^{l_c} \left(\left(-\frac{\partial \mathcal{L}_1}{\partial \boldsymbol{\zeta}'} \right)' + \frac{\partial \mathcal{L}_1}{\partial \boldsymbol{\zeta}} \right) \cdot \mathbf{h} + \left[\frac{\partial \mathcal{L}_1}{\partial \boldsymbol{\zeta}'} \cdot \mathbf{h} \right]_0^{l_c} \\ + \int_{l_c}^{l_1} \left(\left(-\frac{\partial \mathcal{L}_2}{\partial \boldsymbol{\zeta}'} \right)' + \frac{\partial \mathcal{L}_2}{\partial \boldsymbol{\zeta}} \right) \cdot \mathbf{h} + \left[\frac{\partial \mathcal{L}_2}{\partial \boldsymbol{\zeta}'} \cdot \mathbf{h} \right]_{l_c}^{l_1} = 0.\end{aligned}$$

This condition is satisfied for the critical points which are the solutions of *Euler-Lagrange* equations in each section

$$\begin{aligned}\left(-\frac{\partial \mathcal{L}_1}{\partial \boldsymbol{\zeta}'} \right)' + \frac{\partial \mathcal{L}_1}{\partial \boldsymbol{\zeta}} = \mathbf{0}, \quad \forall s \in [0, l_c], \\ \left(-\frac{\partial \mathcal{L}_2}{\partial \boldsymbol{\zeta}'} \right)' + \frac{\partial \mathcal{L}_2}{\partial \boldsymbol{\zeta}} = \mathbf{0}, \quad \forall s \in [l_c, l_1],\end{aligned} \tag{6.12}$$

along with the boundary conditions

$$\frac{\partial \mathcal{L}_1}{\partial \boldsymbol{\zeta}'} \cdot \mathbf{h} \Big|_{s=0} = 0, \qquad \frac{\partial \mathcal{L}_1}{\partial \boldsymbol{\zeta}'} \cdot \mathbf{h} \Big|_{s=l_1} = 0, \tag{6.13}$$

and the matching conditions

$$\frac{\partial \mathcal{L}_1}{\partial \boldsymbol{\zeta}'} \Big|_{s=l_c^-} = \frac{\partial \mathcal{L}_2}{\partial \boldsymbol{\zeta}'} \Big|_{s=l_c^+}. \tag{6.14}$$

In other words, the state $\boldsymbol{\zeta}$ and the term $\frac{\partial \mathcal{L}}{\partial \boldsymbol{\zeta}'}$ are continuous across the boundaries of point of discontinuity $s = l_c$, and these are termed as *matching conditions*. In terms of the Hamiltonian terminology, the phase variables $\boldsymbol{\zeta}$ and $\mathbf{p}$ are continuous across the point of discontinuity $s = l_c$. And if the functions $\mathcal{L}_1$ and $\mathcal{L}_2$ are convex in $\boldsymbol{\zeta}'$, then the derivative $\boldsymbol{\zeta}'$ is continuous across the point $s = l_c$. The extremal solutions do not possess *corner points*, even when the integrand $\mathcal{L}(\boldsymbol{\zeta}, \boldsymbol{\zeta}', s)$ exhibits discontinuities as a function of s.

Let us now verify whether these first-order conditions are consistent with Force-balance equations. The first-order conditions (6.12), (6.13) with respect to the state $\mathbf{r}$ yield

$$\begin{aligned}\boldsymbol{\lambda}'(s) &= \mathbf{0},\\ \boldsymbol{\lambda}(l_1) + \mathbf{F} &= \mathbf{0}.\end{aligned}$$

The Lagrange multiplier $\boldsymbol{\lambda}(s) \in \mathbb{R}^3$ which enforces the inextensibility and unshearability constraint, corresponds to the internal force vector $\mathbf{n}$ acting along the *backbone* composite rod. This internal force is the sum of the internal forces along the constituent tubes

$$\mathbf{n}(s) = \mathbf{n}^{[1]}(s) + \mathbf{n}^{[2]}(s) + \cdots + \mathbf{n}^{[N]}(s),$$

and satisfies the force balance law (3.3a). Here, $\mathbf{n}^{[k]}(s), k = 1, 2, \ldots, N$ is the internal force vector along the k th tube. Because of the contact forces with the other tubes, $\mathbf{n}^{[k]}$ is not constant along the length of the tube. However, their total sum $\mathbf{n}(s)$ remains conserved. The contact forces between the tubes collectively result in a net force of zero in the entire system of tubes. The corresponding matching condition: (6.14)

$$\mathbf{n}(l_k^-) = \mathbf{n}(l_k^+), \quad k = 2, \ldots, N,$$

denotes the balance of the internal forces at the boundary between the sections.

Similarly, the *Euler-Lagrange equations* and the *Natural boundary Conditions* with respect to the variable $\mathbf{q}$ give

$$\begin{aligned}-\left(\mathcal{W}_u \frac{\partial \mathbf{u}}{\partial \mathbf{q}'} + \eta \mathbf{q}\right)' + \mathcal{W}_u \frac{\partial \mathbf{u}}{\partial \mathbf{q}} + \eta \mathbf{q}' - \frac{\partial}{\partial \mathbf{q}} (\boldsymbol{\lambda} \cdot \mathbf{d}_3) &= 0,\\ \mathcal{W}_u \frac{\partial \mathbf{u}}{\partial \mathbf{q}'} + \eta \mathbf{q}(l_1) + \frac{\partial}{\partial \mathbf{q}} (\mathbf{F} \cdot \boldsymbol{\Upsilon}(\mathbf{q}(l_1))) &= \mathbf{0},\end{aligned} \tag{6.15}$$

respectively. Projecting these equations onto $\left[\mathbf{B}_1\mathbf{q}, \mathbf{B}_2\mathbf{q}, \mathbf{B}_3\mathbf{q}\right]$-space and then carrying out the similar calculations as in the section 3.7, we obtain the balance of the internal moment $\mathtt{m}$ along the *backbone* and at the tip $s = l$. The internal moment along the *backbone* $\mathtt{m}$ is the sum of internal moments along each tube

$$\mathtt{m}(s) = \mathtt{m}^{[1]}(s) + \mathtt{m}^{[2]}(s) + \cdots + \mathtt{m}^{[N]}(s).$$

The matching conditions (6.14) with respect to $\mathbf{q}$ projected on $[\mathbf{B}_1\mathbf{q}, \mathbf{B}_2\mathbf{q}, \mathbf{B}_3\mathbf{q}]$- space:

$$\mathtt{m}(l_k^-) = \mathtt{m}(l_k^+), \quad k = 2, \ldots, N,$$

leads to the balance of moments across the boundary between the sections. The *Natural boundary conditions* with respect to $\mathbf{q}$ at the tip $s = l$ can be physically interpreted as the balance of moments as shown for the case of elastic rods (section (3.27)).

When we get to the final term $\alpha^{[k]}$, the associated *Euler-Lagrange equations* gives

$$-\left(K_{33}^{[k]}\left(u_3+\alpha^{[k]\prime}-\hat{u}_3\right)\right)' = K_{11}^{[k]}\left(u_1\cos\alpha^{[k]}+u_2\sin\alpha^{[k]}-\hat{u}_1^{[k]}\right)\left(u_1\sin\alpha^{[k]}-u_2\cos\alpha^{[k]}\right) - K_{11}^{[k]}\left(u_1\sin\alpha^{[k]}-u_2\cos\alpha^{[k]}-\hat{u}_2^{[k]}\right)\left(u_1\cos\alpha^{[k]}+u_2\sin\alpha^{[k]}\right).$$

From now on, we use $\mathbf{K}$ instead of $\tilde{\mathbf{K}}$ as we consider only CTCR tube sections. After rewriting the expression in terms of Darboux vector components in k th tube's frame $\mathbf{U}(\alpha^{[k]}, s)$ using the relation 6.3, we obtain

$$-\left(K_{33}^{[k]}\left(U_3-\hat{u}_3^{[k]}\right)\right)' = -K_{11}^{[k]}\left(U_1-\hat{u}_1^{[k]}\right)U_2+K_{11}^{[k]}\left(U_2-\hat{u}_2^{[k]}\right)U_1.$$

The term $\mathbf{K}^{[\mathbf{k}]}\left(\mathbf{U}-\hat{\mathbf{u}}^{[\mathbf{k}]}\right)$ gives the components of moment along the k th tube *material frame* $(\bar{m}_1, \bar{m}_2, \bar{m}_3)$. Note, that m_p, $p = 1, 2, 3$ denotes component with respect to CTCR *backbone* (inner tube *material frame*). As a consequence, we obtain

$$\bar{m}_3^{[k]\prime} = \bar{m}_1^{[k]}U_2 - \bar{m}_2^{[k]}U_1,$$

which is equivalent to a component of the balance law of k th tube 3.3b in the fixed laboratory frame. The *Natural boundary condition* at the free end $s = l_k$ is

$$\left.\frac{\partial\mathcal{L}}{\partial\alpha^{[k]\prime}}\right|_{s=l_k} \equiv \bar{m}_3^{[k]}(l_k) = 0, \quad k = 2,\ldots,N,$$

and it corresponds to the zero-twisting moment of each tube at the end. The remaining boundary terms on $\alpha^{[k]}$ are coupled from its neighboring section. The matching conditions

$$\bar{m}_3^{[i]}(l_k^-) = \bar{m}_3^{[i]}(l_k^+), \quad i < k, \quad k = 2,\ldots,N,$$

gives the balance of twist moment $\bar{m}_3^{[i]}$ in i th tube across the boundary between the sections.

6.4 Hamiltonian Formulation of Equilibria

Now, we shall represent the CTCR equilibria described as the second-order *Euler-Lagrange equations* in the Hamiltonian form. As already pointed out, this form has the advantage of representing the equilibria in the compact form of first-order ODEs, which are easy to implement in numerical packages such as *AUTO-07p*, Python, and *matlab*. Furthermore, the additional conserved quantities resulting from this formulation can be employed for testing the accuracy and convergence of the numerical methods.

In this formulation, the Hamiltonian phase variables are $\mathbf{r}$, $\mathbf{q}$, $\alpha^{[i]}$, $i = 2, 3, \ldots, N$ and their

corresponding momenta $\mathbf{n}$, $\boldsymbol{\mu}$, $\beta^{[i]}$, $i = 2, 3, \ldots, N$, where the momenta are defined as

$$\mathbf{n} = \frac{\partial \mathcal{L}}{\partial \mathbf{r}'} = \boldsymbol{\lambda}, \tag{6.16a}$$

$$\boldsymbol{\mu} = \frac{\partial \mathcal{L}}{\partial \mathbf{q}'} = \mathcal{W}_{u_j} \frac{2\mathbf{B}_j \mathbf{q}}{|\mathbf{q}|^2} + \eta \mathbf{q}, \quad j = 1, 2, 3. \tag{6.16b}$$

$$\beta^{[i]} = \frac{\partial \mathcal{L}}{\partial \alpha^{[i]\prime}} = \frac{m_3 K_{33}^{[i]} + K_{33}^{[i]} \left(\sum_{j=1}^{N} K_{33}^{[j]} \left(\hat{u}_3^{[j]} - \alpha^{[j]\prime} \right) \right)}{\sum_{j=1}^{N} K_{33}^{[j]}} - K_{33}^{[i]} \left(\hat{u}_3^{[i]} - \alpha^{[i]\prime} \right), \quad i = 2, \ldots, N. \tag{6.16c}$$

The variables associated with relative twisting angles $\alpha^{[i]}$ are denoted as a column vector in $\mathbb{R}^{k-1}$ space using bold symbols and by dropping the superscript $[i]$. For example,

$$\boldsymbol{\beta} = \left[\beta^{[2]}, \beta^{[3]}, \ldots, \beta^{[N]} \right]^T, \qquad \boldsymbol{\alpha}' = \left[\alpha^{[2]\prime}, \alpha^{[3]\prime}, \ldots, \alpha^{[N]\prime} \right]^T.$$

By definition, $\alpha^{[i]}$ is the relative angle of orientation between ith tube and innermost tube 1st tube, so $\alpha^{[1]}$ and its conjugate momentum $\beta^{[1]}$ are identically zero and not included in $\boldsymbol{\alpha}$ and $\boldsymbol{\beta}$. The energy function $\mathcal{W}$ is convex with respect to $\alpha^{[i]\prime}$, and so is the function $\mathcal{L}$. Hence, the relation (6.16c) can be inverted to obtain $\alpha^{[i]\prime}$ as a function $\phi^{[i]} \in \mathbb{R}$ in terms of system variables and the momenta as

$$\begin{aligned} \alpha^{[i]\prime} &= \phi^{[i]} \left(\mathbf{r}, \mathbf{q}, \boldsymbol{\alpha}, \mathbf{n}, \boldsymbol{\mu}, \boldsymbol{\beta}, s \right), \\ &= \frac{\sum_{i=2}^{N} \beta^{[i]}}{K_{33}^{[1]}} + \frac{\beta^{[i]}}{K_{33}^{[i]}} - \frac{m_3}{K_{33}^{[1]}} + \hat{u}_3^{[i]} - \hat{u}_3^{[1]}. \end{aligned} \tag{6.17}$$

The dot product of $\boldsymbol{\mu}$ with $\mathbf{B}_i \mathbf{q}/2$ results in the component of the internal moment along the robot *backbone*'s director frame.

$$\boldsymbol{\mu} \cdot \mathbf{B}_i \mathbf{q}/2 = \mathcal{W}_{u_i} \equiv m_i \quad \equiv \mathbf{m} \cdot \mathbf{d}_i, \quad i = 1, 2, 3. \tag{6.18}$$

The Legendre transformation of the *Lagrangian* function $\mathcal{L}$ gives the Hamiltonian function of the CTCR system

$$H \left(\mathbf{r}, \mathbf{q}, \boldsymbol{\alpha}, \mathbf{n}, \boldsymbol{\mu}, \boldsymbol{\beta}, s \right) = \begin{bmatrix} \mathbf{r} \\ \mathbf{q} \\ \boldsymbol{\alpha} \end{bmatrix}' \cdot \begin{bmatrix} \mathbf{n} \\ \boldsymbol{\mu} \\ \boldsymbol{\beta} \end{bmatrix} - \mathcal{L}(\mathbf{r}, \mathbf{r}', \mathbf{q}, \mathbf{q}', \boldsymbol{\alpha}, \boldsymbol{\alpha}', s),$$

After expressing the variables in terms of the Hamiltonian variables, we obtain the Hamiltonian H as

$$H(\mathbf{r}, \mathbf{q}, \boldsymbol{\alpha}, \mathbf{n}, \boldsymbol{\mu}, \boldsymbol{\beta}, s) = \mathbf{n} \cdot \mathbf{d}_3 + \mathtt{m} \cdot \tilde{\mathtt{u}} + \boldsymbol{\beta} \cdot \boldsymbol{\phi} + \frac{1}{2} \mathtt{m} \cdot \mathbf{K_{eff}}^{-1} \mathtt{m} - \mathbf{C}(\boldsymbol{\alpha}, \boldsymbol{\phi}), \tag{6.19}$$

where the terms $\tilde{\mathtt{u}}, \mathbf{K_{eff}}$ and $\mathbf{C}\left(\boldsymbol{\alpha}, \boldsymbol{\phi}\right)$ are defined in (6.6). Then, the associated Hamiltonian system of equations governing the equilibria of an N-tube CTCR section can be derived from

the Hamiltonian 6.19 as

$$\mathbf{r}' = \frac{\partial H}{\partial \mathbf{n}} = \mathbf{d}_3, \tag{6.20a}$$

$$\mathbf{n}' = -\frac{\partial H}{\partial \mathbf{r}} = \mathbf{0}, \tag{6.20b}$$

$$\mathbf{q}' = \frac{\partial H}{\partial \boldsymbol{\mu}} = \sum_{j=1}^{3} \left(\mathbf{K}^{-1}_{\mathbf{eff}_{jj}} m_j + \tilde{u}_j\right) \frac{1}{2}\mathbf{B}_j \mathbf{q}, \tag{6.20c}$$

$$\boldsymbol{\mu}' = -\frac{\partial H}{\partial \mathbf{q}} = \sum_{j=1}^{3} \left(\mathbf{K}^{-1}_{\mathbf{eff}_{jj}} m_j + \tilde{u}_j\right) \frac{1}{2}\mathbf{B}_j \boldsymbol{\mu} - \frac{\partial \mathbf{d}_3(\mathbf{q})}{\partial \mathbf{q}}^T \mathbf{n}, \tag{6.20d}$$

$$\begin{aligned} \alpha^{[i]\prime} &= \frac{\partial H}{\partial \beta^{[i]}} \\ &= \frac{\sum_{j=2}^{N} \beta^{[j]}}{K_{33}^{[1]}} - \frac{m_3}{K_{33}^{[1]}} + \frac{\beta^{[i]}}{K_{33}^{[i]}} + \hat{u}_3^{[i]} - \hat{u}_3^{[1]}, \qquad i = 2, 3, \ldots, N. \end{aligned} \tag{6.20e}$$

$$\begin{aligned} \beta^{[i]\prime} &= -\frac{\partial H}{\partial \alpha^{[i]}} \\ &= \frac{K_{11}^{[i]} \hat{u}_1^{[i]}}{\sum_{j=1}^{N} K_{11}^{[j]}} \sum_{j=1}^{N} K_{11}^{[j]} \hat{u}_1^{[j]} \sin\left(\alpha^{[i]} - \alpha^{[j]}\right) + \frac{K_{11}^{[i]} \hat{u}_1^{[i]}}{\sum_{j=1}^{N} K_{11}^{[j]}} \left(m_1 \sin\alpha^{[i]} - m_2 \cos\alpha^{[i]}\right) \\ &+ \frac{K_{11}^{[i]} \hat{u}_1^{[i]}}{\sum_{j=1}^{N} K_{11}^{[j]}} \sum_{j=1}^{N} K_{11}^{[j]} \hat{u}_2^{[j]} \cos\left(\alpha^{[i]} - \alpha^{[j]}\right) - \frac{K_{11}^{[i]} \hat{u}_2^{[i]}}{\sum_{j=1}^{N} K_{11}^{[j]}} \left(m_1 \cos\alpha^{[i]} + m_2 \sin\alpha^{[i]}\right), \\ & \qquad i = 2, 3, \ldots, N. \end{aligned} \tag{6.20f}$$

The components $m_i, i = 1, 2, 3$ are obtained using the relation (6.18) and the derivative $\frac{\partial \mathbf{d}_3}{\partial \mathbf{q}}$ is same as that for the case of elastic rods (3.30).

6.5 Conserved Quantities

The Hamiltonian system 6.20 has a close resemblance with that of the elastic rod system 3.29, and as a consequence, inherits some of the conserved quantities. The three components of internal force $\mathbf{n}$ and $\mathbf{m} + \mathbf{r} \times \mathbf{n}$ along the fixed frame are conserved. However, these quantities are not conserved along the constituent tubes ($\mathbf{n}^{[i]}$ and $\mathbf{m}^{[i]}$). The quantity $\mathbf{q} \cdot \mathbf{q}$ is a conserved quantity by construction. In addition, the quantity $\boldsymbol{\mu} \cdot \mathbf{q} + 2\mathbf{r} \cdot \mathbf{n}$ also remains conserved, and its proof is the same as that presented in section 3.9. Suppose the CTCR exhibits translation symmetry along its arc length s. In that instance, the constitutive law has no explicit dependence on s. For a quadratic strain energy function, this condition is satisfied when the stiffnesses $\mathbf{K}^{[i]}$ and unstressed strains $\hat{u}_i$ are constant functions of s. The Hamiltonian H of each section is thus a conserved quantity.

6.6 Boundary Conditions and Matching Conditions

The equilibria of the CTCR system clamped at one end $s = 0$ attached to a dead load at the other end $s = l$ are obtained after solving the Hamiltonian system (6.20) employing the appropriate

boundary conditions. The *Dirichlet* boundary conditions at $s = 0$ read

$$\begin{aligned} \mathbf{r}(0) &= [0,0,0]^T, \qquad \mathbf{q}(0) = \mathbf{q}_o, \\ \alpha^{[i]}(0) &= \alpha_o^{[i]}, \quad i = 2,3,\ldots,N. \end{aligned} \tag{6.21}$$

where $\mathbf{q}_o, \alpha_o^{[i]}$ are some parameters, and the *Natural* boundary conditions at the other end $s = l$ in terms of physical quantities read

$$\begin{aligned} &\mathbf{n}(l_1) + \mathbf{F} = \mathbf{0}, \\ &m_i(l_1) + \boldsymbol{\Upsilon}(\mathbf{q}(l_1)) \times \mathbf{F}) \cdot \mathbf{d}_i = 0, \qquad i = 1,2,3, \\ &\boldsymbol{\beta}^{[j]}(l_j) = 0, \qquad j = 2,3,\ldots,N. \end{aligned} \tag{6.22}$$

We are short of a boundary condition to complete the system and solve it. The conserved quantity

$$\boldsymbol{\mu} \cdot \mathbf{q} + 2\mathbf{r} \cdot \mathbf{n} \tag{6.23}$$

is utilized to account for the additional boundary condition. So, we use

$$\boldsymbol{\mu}(0) \cdot \mathbf{q}(0) = \boldsymbol{\mu}(l_1) \cdot \mathbf{q}(l_1) + 2\mathbf{r}(l_1) \cdot \mathbf{n}(l_1) = 0. \tag{6.24}$$

We are free to choose any value for this quantity (Dichmann et al., 1996). In addition, the following matching conditions are imposed at the boundary between the k- tube section and the $(k-1)$- tube section

$$\begin{aligned} &\mathbf{r}(l_{k-}) = \mathbf{r}(l_{k+}), \quad \mathbf{q}(l_{k-}) = \mathbf{q}(l_{k+}), \quad \alpha^{[i]}(l_{k-}) = \alpha^{[i]}(l_{k+}) \text{ for } k-1 < i < N, \\ &\mathbf{n}(l_{k-}) = \mathbf{n}(l_{k+}), \quad \boldsymbol{\mu}(l_{k-}) = \boldsymbol{\mu}(l_{k+}), \quad \beta^{[i]}(l_{k-}) = \beta^{[i]}(l_{k+}) \text{ for } k-1 < i < N. \end{aligned} \tag{6.25}$$

6.7 Second-Order Conditions

The critical points $\boldsymbol{\zeta}_o$ obtained as solutions to the *Euler-Lagrange equations* (6.12), along with boundary conditions (6.13) and matching conditions (6.14), represent local minimum of the functional (6.11) with a point of discontinuity at $s = l_c$, if they satisfy the second-order condition

$$\delta^2 J(\boldsymbol{\zeta}_o)[\mathbf{h}] = \frac{1}{2}\int_0^{l_1} \left(\mathbf{h}' \cdot \mathbf{P}\mathbf{h}' + \mathbf{h} \cdot \mathbf{C}\mathbf{h}' + \mathbf{h}' \cdot \mathbf{C}^T\mathbf{h} + \mathbf{h} \cdot \mathbf{Q}\mathbf{h}\right) ds \geq 0. \tag{6.26}$$

Just recall that $\mathbf{P}, \mathbf{C}$ and $\mathbf{Q}$ are $p \times p$ Hessian matrices evaluated at the extremal $\boldsymbol{\zeta}_o$ given by

$$\begin{aligned} \mathbf{P} &= \frac{\partial^2}{\partial \boldsymbol{\zeta}'^2}\mathcal{L}(\zeta_o, \boldsymbol{\zeta}'_o, s) \equiv \mathcal{L}_{\boldsymbol{\zeta}'\boldsymbol{\zeta}'}(\boldsymbol{\zeta}_o, \zeta'_o, s), \\ \mathbf{C} &= \frac{\partial^2}{\partial \boldsymbol{\zeta}' \partial \boldsymbol{\zeta}}\mathcal{L}(\boldsymbol{\zeta}_o, \zeta'_o, s) \equiv \mathcal{L}_{\boldsymbol{\zeta}\boldsymbol{\zeta}'}(\boldsymbol{\zeta}_o, \boldsymbol{\zeta}'_o, s), \\ \mathbf{Q} &= \frac{\partial^2}{\partial \boldsymbol{\zeta}^2}\mathcal{L}(\boldsymbol{\zeta}_o, \boldsymbol{\zeta}'_o, s) \equiv \mathcal{L}_{\boldsymbol{\zeta}\boldsymbol{\zeta}}(\boldsymbol{\zeta}_o, \boldsymbol{\zeta}'_o, s), \end{aligned} \tag{6.27}$$

and the matrices $\mathbf{P}$ and $\mathbf{Q}$ are symmetric, whereas the matrix $\mathbf{C}$ may not be. Followed by the integration by parts and substitution of boundary conditions, this second-order condition (6.26) can be alternatively written as

$$\delta^2 J(\zeta_o)[\mathbf{h}] = \frac{1}{2}\langle \mathcal{S}\mathbf{h}, \mathbf{h}\rangle = \frac{1}{2}\langle \mathcal{S}\mathbf{h}, \mathbf{h}\rangle_1 + \frac{1}{2}\langle \mathcal{S}\mathbf{h}, \mathbf{h}\rangle_2 + \Big(\big(\mathbf{P}'\mathbf{h} + \mathbf{C}^T\mathbf{h}\big)\cdot\mathbf{h}\Big)_{l_{c-}} - \Big(\Big(\mathbf{P}\mathbf{h}' + \mathbf{C}^T\mathbf{h}\Big)\cdot\mathbf{h}\Big)_{l_{c+}} \geq 0,$$

where $\langle\cdot,\cdot\rangle_1$,$\langle\cdot,\cdot\rangle_2$ are the standard L^2-inner product in $[0, l_c]$ and $[l_c, l_1]$ respectively. The boundary term is the linearized matching condition. We postulate that the variations $\mathbf{h}$ must satisfy

$$\Big(\mathbf{P}\mathbf{h}' + \mathbf{C}^T\mathbf{h}\Big)\Big|_{l_{c-}} = \Big(\mathbf{P}\mathbf{h}' + \mathbf{C}^T\mathbf{h}\Big)\Big|_{l_{c+}}, \tag{6.28}$$

and refer to them as *secondary matching conditions*. Accordingly, we have a new set of admissible variations as

$$\mathcal{B}_{dis} \equiv \{\mathbf{h}(s) \in \mathcal{C}^0[0, l_1] : \mathbf{h}(0) = \mathbf{0}, \mathbf{P}\mathbf{h}'(l_1) + \mathbf{C}^T\mathbf{h}(l_1) = 0, \mathbf{P}\mathbf{h}'(l_{c-}) + \mathbf{C}^T\mathbf{h}(l_{c-}) = \mathbf{P}\mathbf{h}'(l_{c+}) + \mathbf{C}^T\mathbf{h}(l_{c+})\}. \tag{6.29}$$

For simplicity, the Hessian matrix due to the boundary term $\mathbf{B}$ (section 2.3) is omitted here and in subsequent results. However, the findings can be easily extended to incorporate them. Our claim (6.28) would support the self-adjointness property of the $\mathcal{S}$ operator as shown below.

Corollary 6.7.1. *The Jacobi operator is self-adjoint along the* $\mathbf{h} \in \mathcal{B}_{dis}$*, i.e.,* $\langle \mathcal{S}\mathbf{h_a}, \mathbf{h_b}\rangle = \langle \mathcal{S}\mathbf{h_b}, \mathbf{h_a}\rangle \ \forall \mathbf{h_a}, \mathbf{h_b} \in \mathcal{B}_{dis}$.

Proof. We use the results from Lemma (2.13) and write the L.H.S as

$$\begin{aligned}\langle \mathcal{S}\mathbf{h_a}, \mathbf{h_b}\rangle &= \langle \mathcal{S}\mathbf{h}_a, \mathbf{h_b}\rangle_1 + \langle \mathcal{S}\mathbf{h_a}, \mathbf{h_b}\rangle_2, \\ &= \langle \mathcal{S}\mathbf{h_b}, \mathbf{h_a}\rangle_1 + \langle \mathcal{S}\mathbf{h_b}, \mathbf{h_a}\rangle_2 + \Big[\big(\mathbf{P}\mathbf{h_b}' + \mathbf{C}^T\mathbf{h_b}\big)\cdot\mathbf{h_a}\Big]_{l_{c-}}^{l_1} + \Big[\big(\mathbf{P}\mathbf{h_b}' + \mathbf{C}^T\mathbf{h_b}\big)\cdot\mathbf{h_a}\Big]_0^{l_{c+}} \\ &\quad + \Big[\big(\mathbf{P}\mathbf{h_b}' + \mathbf{C}^T\mathbf{h_b}\big)\cdot\mathbf{h_a}\Big]_{l_{c-}}^{l_1} + \Big[\big(\mathbf{P}\mathbf{h_b}' + \mathbf{C}^T\mathbf{h_b}\big)\cdot\mathbf{h_a}\Big]_0^{l_{c+}}.\end{aligned}$$

The variables $\mathbf{h_a}, \mathbf{h_b}$ satisfy the conditions (6.29), and therefore the boundary terms vanish, leading to the self-adjointness property of $\mathcal{S}$ operator

$$\langle \mathcal{S}\mathbf{h_a}, \mathbf{h_b}\rangle = \langle \mathcal{S}\mathbf{h_b}, \mathbf{h_a}\rangle_1 + \langle \mathcal{S}\mathbf{h_b}, \mathbf{h_a}\rangle_2 = \langle \mathcal{S}\mathbf{h_b}, \mathbf{h_a}\rangle. \tag{6.30}$$

□

The conditions for second-order variations in variational problems with discontinuous integrands have been derived by various authors in the past (Bliss and Mason, 1906; Graves, 1930; Cole, 1940). In the words of Hamiltonian formalism, the variations in conjugate momenta $\mathbf{p}$ are continuous across the point of discontinuity $s = l_c$. Using these new matching conditions, we present a revised definition of the *conjugate point* as

Definition 6.7.4. *A point $l^* \in [0, l_1]$ is conjugate to the point l_1, if there is a nontrivial solution to*

$$\mathcal{S}\mathbf{h} = \mathbf{0}, \quad \mathbf{P}\mathbf{h}'(l_1) + \mathbf{C}^T\mathbf{h}(l_1) = \mathbf{0}, \quad \mathbf{h}(l^*) = \mathbf{0},$$

satisfying

$$\left(\mathbf{P}\mathbf{h}' + \mathbf{C}^T\mathbf{h}\right)\Big|_{l_{c-}} = \left(\mathbf{P}\mathbf{h}' + \mathbf{C}^T\mathbf{h}\right)\Big|_{l_{c+}} \tag{6.31}$$

at the point of discontinuity $s = l_c$.

The calculation methodology of the *conjugate point* is the same as that described in the 2.3.3 in the previous part, augmented by an additional matching condition 6.31.

Theorem 6.7.3. *If $\mathbf{P}$ is positive definite throughout the interval $[0, l]$, and the interval contains no point conjugate to l, then the functional is positive for all variations $\mathbf{h} \in C^1[0, l_1]$ satisfying $\mathbf{h}(0) = \mathbf{0}$, $\mathbf{P}\mathbf{h}'(l_1) + \mathbf{C}^T\mathbf{h}(l_1) = \mathbf{0}$ and $\left(\mathbf{P}\mathbf{h}' + \mathbf{C}^T\mathbf{h}\right)\Big|_{l_{c-}} = \left(\mathbf{P}\mathbf{h}' + \mathbf{C}^T\mathbf{h}\right)\Big|_{l_{c+}}$.*

Proof. The proof of this theorem is identical to that of the previous theorem (2.3.1) and is slightly modified to include the matching conditions. Let $\mathbf{W} : s \longrightarrow \mathbb{R}^{p\times p}$ be an arbitrary differentiable symmetric matrix. Without affecting the values of the integral (6.26), we can add the following term

$$\begin{aligned}
0 &= \int_0^{l_1} \frac{d}{ds}\left(\mathbf{W}\mathbf{h}\cdot\mathbf{h}\right) ds - \Big[\mathbf{W}\mathbf{h}\cdot\mathbf{h}\Big]_0^{l_1}, \\
0 &= \int_0^{l_1} \mathbf{W}'\mathbf{h}\cdot\mathbf{h} + \mathbf{W}\mathbf{h}'\cdot\mathbf{h} + \mathbf{W}\mathbf{h}\cdot\mathbf{h}' ds + \left(\mathbf{W}(l_1)\mathbf{h}(l_1)\cdot\mathbf{h}(l_1) - \mathbf{W}(0)\mathbf{h}(0)\cdot\mathbf{h}(0)\right) \\
&\quad + \Big[\mathbf{W}(l_{c+})\mathbf{h}(l_{c+})\cdot\mathbf{h}(l_{c+}) - \mathbf{W}(l_{c+})\mathbf{h}(l_{c+})\cdot\mathbf{h}(l_{c+})\Big],
\end{aligned}$$

The boundary term $\mathbf{h}(0)$ vanishes, and the matrix $\mathbf{W}(l_1)$ is chosen as a zero matrix such that the boundary term $\mathbf{W}(l_1)\mathbf{h}(l_1)\cdot\mathbf{h}(l_1)$ is zero for any $\mathbf{h}(l_1)$. The last term does not contribute to the integrand as long as

$$\begin{aligned}
\mathbf{W}(l_{c-})\mathbf{h}(l_{c-})\cdot\mathbf{h}(l_{c-}) &= \mathbf{W}(l_{c+})\mathbf{h}(l_{c+})\cdot\mathbf{h}(l_{c+}) \\
\implies \mathbf{W}(l_{c-})\mathbf{h}(l_{c-}) &= \mathbf{W}(l_{c+})\mathbf{h}(l_{c}+),
\end{aligned} \tag{6.32}$$

is satisfied. Then the second variation becomes

$$\begin{aligned}
\delta^2 J(\boldsymbol{\zeta}_o)[\mathbf{h}] &= \int_0^{l_1} \mathbf{P}\mathbf{h}'\cdot\mathbf{h}' + \mathbf{C}\mathbf{h}'\cdot\mathbf{h} + \mathbf{C}^T\mathbf{h}\cdot\mathbf{h}' + \mathbf{Q}\mathbf{h}\cdot\mathbf{h} + \mathbf{W}'\mathbf{h}\cdot\mathbf{h} + \mathbf{W}\mathbf{h}\cdot\mathbf{h}' + \mathbf{W}\mathbf{h}'\cdot\mathbf{h} ds, \\
&\quad + \Big[\mathbf{W}(l_{c+})\mathbf{h}(l_{c+})\cdot\mathbf{h}(l_{c+}) - \mathbf{W}(l_{c+})\mathbf{h}(l_{c+})\cdot\mathbf{h}(l_{c+})\Big], \\
&= \int_0^{l_c} \mathbf{P}\mathbf{h}'\cdot\mathbf{h}' + \left(\mathbf{C}+\mathbf{W}\right)\mathbf{h}\cdot\mathbf{h}' + \left(\mathbf{C}+\mathbf{W}\right)^T\mathbf{h}'\cdot\mathbf{h} + \left(\mathbf{Q}+\mathbf{W}'\right)\mathbf{h}\cdot\mathbf{h} ds \\
&\quad + \int_{l_c}^{l_1} \mathbf{P}\mathbf{h}'\cdot\mathbf{h}' + \left(\mathbf{C}+\mathbf{W}\right)\mathbf{h}\cdot\mathbf{h}' + \left(\mathbf{C}+\mathbf{W}\right)^T\mathbf{h}'\cdot\mathbf{h} + \left(\mathbf{Q}+\mathbf{W}'\right)\mathbf{h}\cdot\mathbf{h} ds.
\end{aligned}$$

If the $\mathbf{W}(s)$ is chosen to be the solution of

$$\begin{aligned}&\mathbf{P}^{1/2}\left(\mathbf{Q}+\mathbf{W}'\right)^{1/2}=\left(\mathbf{C}+\mathbf{W}\right)^{T},\\&\implies \mathbf{Q}+\mathbf{W}'=\left(\mathbf{C}+\mathbf{W}\right)\mathbf{P}^{-1}\left(\mathbf{C}^{T}+\mathbf{W}\right),\end{aligned}$$

then the integrand can be written a sum of perfect squares

$$\begin{aligned}&\int_0^{l_c}\mathbf{P}\left(\mathbf{h}'+\mathbf{P}^{-1/2}\left(\mathbf{Q}+\mathbf{W}\right)\mathbf{Q}^{-1/2}\mathbf{h}\right)\cdot\left(\mathbf{h}'+\mathbf{P}^{-1/2}\left(\mathbf{Q}+\mathbf{W}\right)\mathbf{Q}^{-1/2}\mathbf{h}\right)ds\\+&\int_{l_c}^{l_1}\mathbf{P}\left(\mathbf{h}'+\mathbf{P}^{-1/2}\left(\mathbf{Q}+\mathbf{W}\right)\mathbf{Q}^{-1/2}\mathbf{h}\right)\cdot\left(\mathbf{h}'+\mathbf{P}^{-1/2}\left(\mathbf{Q}+\mathbf{W}\right)\mathbf{Q}^{-1/2}\mathbf{h}\right)ds.\end{aligned}$$

Here, the integrand is always non-negative and is zero only when $\mathbf{h}(s)\equiv\mathbf{0}$. On substituting

$$\mathbf{C}^{T}+\mathbf{W}=-\mathbf{P}\mathbf{U}'\mathbf{U}^{-1},$$

where $\mathbf{U}$ is a new unknown matrix, we obtain the matrix form of the *Jacobi equations*

$$-\frac{d}{ds}\left(\mathbf{P}\mathbf{U}'+\mathbf{C}^{T}\mathbf{U}\right)+\left(\mathbf{C}\mathbf{U}'+\mathbf{Q}\mathbf{U}\right)=\mathbf{0}, \tag{6.33}$$

The matrix $\mathbf{W}(s)$ satisfies the boundary conditions as well as the matching conditions (6.32)

$$\mathbf{P}\mathbf{U}'(l_c-)+\mathbf{C}^{T}\mathbf{U}(l_c-)=\mathbf{P}\mathbf{U}'(l_c+)+\mathbf{C}^{T}\mathbf{U}(l_c+).$$

The matrix $\mathbf{U}$ is invertible, if the interval $[0,l_1]$ contains no *conjugate point*. Then, a solution to *Matrix Ricatti equations* $\mathbf{W}(s)$ exists which satisfies the boundary conditions and matching conditions. Therefore, a matrix $\mathbf{W}(s)$ which can convert the integrand to a perfect square (always non-negative) exists.

□

Theorem 6.7.4. *If* $\mathbf{P}$ *is positive definite throughout the interval* $[0,l_1]$*, and this interval contains point conjugate to* l_1*, then the second variation quadratic functional is not necessarily positive for all* $\mathbf{h}\in\mathcal{B}_{dis}$.

Proof. Suppose there exists a point $s=l_1^*$ *conjugate* to $s=l_1$ on $0<s<l_1$. Then, there exists a non-null accessory extremal $\mathbf{h}(s)$ satisfying $\mathbf{h}(l_1^*)=\mathbf{0}$ and $\mathbf{P}\mathbf{h}'(l_1)+\mathbf{C}^{T}\mathbf{h}(l_1)=\mathbf{0}$. Let $\boldsymbol{\gamma}(s)$ be a continuous arc defined as

$$\boldsymbol{\gamma}(s)=\begin{cases}\mathbf{0}, & 0<s<l_1^*,\\ \mathbf{h}(s), & l_1^*<s<l_1.\end{cases}$$

Two cases are possible as depicted in Figure (6.4). In the first case $l_1^*<l_c$, the second variation

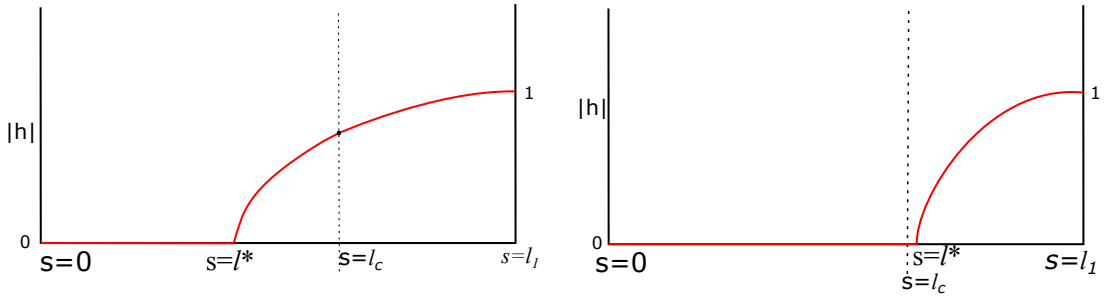

Fig. 6.4 The broken accessory extremal $\gamma(s) \in \mathcal{B}$ with a point of discontinuity integrand at $s = l_c$

$\delta^2 J(\zeta_o)$ along the arc $\boldsymbol{\gamma}$ takes the value of zero as

$$\begin{aligned}
\delta^2 J(\zeta_o)[\boldsymbol{\gamma}] &= \frac{1}{2}\langle \mathcal{S}\gamma(s), \gamma(s)\rangle \\
&= \frac{1}{2}\langle \mathcal{S}\gamma(s), \gamma(s)\rangle_1 + \frac{1}{2}\langle \mathcal{S}\gamma(s), \gamma(s)\rangle_2, \\
&= \frac{1}{2}\Big[\big(\mathbf{P}(s)\mathbf{h}'(s) + \mathbf{C}^T(s)\mathbf{h}(s)\big)\cdot \mathbf{h}(s)\Big]_{l_1^*}^{l_c-} \\
&\qquad + \frac{1}{2}\Big[\big(\mathbf{P}(s)\mathbf{h}'(s) + \mathbf{C}^T(s)\mathbf{h}(s)\big)\cdot \mathbf{h}(s)\Big]_{l_{c+}}^{l_1}, \\
&= 0.
\end{aligned}$$

The value of the integral is zero along the non-trivial $\mathbf{h}(s)$, as it is the solution of $\mathcal{S}\mathbf{h} = 0$ satisfying the matching conditions. In the second case $l_1^* > l_c$, the value of the integral is also zero, and the solution satisfies the matching conditions at trivial solution $\mathbf{h}(s) = \mathbf{0}$. If $\mathbf{P}(s)$ is positive definite, then by *Weierstrass-Erdmann conditions* (2.6a), the arc $\gamma(s)$ with a corner point cannot be the local minimizer. However, the functional $\delta^2 J$ is zero along this curve. Therefore, another minimizing arc may exist that further reduces the value of the second variation $\delta^2 J < 0$, proving the theorem.

□

Jacobi operator of discontinuous systems $\mathcal{S}$ with the *secondary matching conditions* is self-adjoint and regular, and therefore, it has the same spectral properties as that of the continuous systems. The set of properties defined in the previous part for the variational problems with fixed-free ends (section 2.3) can be adapted to these problems with discontinuous integrand by including the matching conditions. Likewise, the notion of *Morse index* can be extended to the problems with discontinuous integrand as

Definition 6.7.5. *Morse index of a variational problem with discontinuous integrand is equal to the number of* conjugate points *given as per the definition* (6.7.4).

6.8 Distinguished Bifurcation Diagram

We already verified in section 2.4 if the *distinguished bifurcation diagrams* are consistent with the variational problems, where one end is fixed and the other end is free. Let us investigate if they also align with problems having discontinuous integrand. Consider a parameter-dependent

variational problem of the form

$$J(\boldsymbol{\zeta}, \xi) = \int_0^{l_1} \mathcal{L}(\boldsymbol{\zeta}, \boldsymbol{\zeta}', \xi, s) ds, \tag{6.34}$$

with a known point of discontinuity at $s = l_c$ subject to a parameter-dependent fixed boundary conditions at $s = 0$ and free boundary conditions at $s = l$. The critical points $(\boldsymbol{\zeta}(s, \tau), \xi(\tau))$ obtained as a solution of the *Euler-Lagrange equations*

$$-\mathcal{L}'_{\boldsymbol{\zeta}'} + \mathcal{L}_{\boldsymbol{\zeta}} = \mathbf{0}, \qquad \boldsymbol{\zeta}(0) = \boldsymbol{\zeta}_o(\xi), \quad \mathbf{p}(l_1) = \mathbf{0}, \tag{6.35}$$

and the matching conditions:

$$\boldsymbol{\zeta}(l_{c-}) = \boldsymbol{\zeta}(l_{c+}), \qquad \mathbf{p}(l_{c-}) = \mathbf{p}(l_{c+}), \tag{6.36}$$

minimizes the functional (6.34) if they satisfy the second-order condition

$$\delta^2 J(\boldsymbol{\zeta})[\mathbf{h}] \geq 0, \quad \forall \mathbf{h} \in \mathcal{B}_{dis}. \tag{6.37}$$

Here, τ is some parameterization along the family of equilibria and $\mathcal{B}_{dis}$ is the set of admissible variations (6.29). Applying the same approach elucidated in the section 2.4, a linear eigenvalue problem can be embedded in the *Jacobi condition* as

$$\begin{aligned} &\mathcal{S}\boldsymbol{\eta} = \mu\boldsymbol{\eta}, \\ &\boldsymbol{\eta}(0) = \mathbf{0}, \qquad \mathbf{P}\boldsymbol{\eta}'(l_1) + \mathbf{C}^T\boldsymbol{\eta}(l_1) = \mathbf{0}, \\ &\mathbf{P}\boldsymbol{\eta}'(l_{c-}) + \mathbf{C}^T\boldsymbol{\eta}(l_{c-}) = \mathbf{P}\boldsymbol{\eta}'(l_{c+}) + \mathbf{C}^T\boldsymbol{\eta}(l_{c+}), \end{aligned} \tag{6.38}$$

and this problem must have only non-negative eigenvalues μ to satisfy the second-order condition (6.37). At the fold point, the eigenvalues change sign. Differentiating the *Euler-Lagrange equations*, nonlinear boundary conditions (6.35) and the matching conditions (6.36) with respect to pseudo-arclength τ results in the BVP

$$\begin{aligned} &\mathcal{S}\dot{\boldsymbol{\zeta}} = \mathbf{0}, \\ &\dot{\boldsymbol{\zeta}}(0) = \frac{d\boldsymbol{\zeta}_o}{d\xi}\dot{\xi}, \qquad \dot{\mathbf{p}}(l_1) \equiv \mathbf{P}\dot{\boldsymbol{\zeta}}'(l_1) + \mathbf{C}^T\dot{\boldsymbol{\zeta}}(l_1) = \mathbf{0}, \\ &\mathbf{P}\dot{\boldsymbol{\zeta}}'(l_c-) + \mathbf{C}^T\dot{\boldsymbol{\zeta}}(l_c-) = \mathbf{P}\dot{\boldsymbol{\zeta}}'(l_c+) + \mathbf{C}^T\dot{\boldsymbol{\zeta}}(l_c+). \end{aligned} \tag{6.39}$$

This BVP coincides with the eigenvalue problem with zero eigenvalue $\mu = 0$ when $\dot{\xi} = 0$. We also assume that $\mu = 0$ is the simple eigenvalue at the fold, and $\dot{\boldsymbol{\zeta}}$ is the corresponding eigenvector. Then, the expression for $\dot{\mu}$ is evaluated by differentiating the eigenvalue problem (6.38)

with respect to pseudo-arclength τ as

$$\begin{aligned}
&\mathcal{S}\dot{\boldsymbol{\eta}} + \dot{\mathcal{S}}\boldsymbol{\eta} = \dot{\mu}\boldsymbol{\eta} + \mu\dot{\boldsymbol{\eta}},\\
&\dot{\boldsymbol{\eta}}(0) = \mathbf{0}, \qquad \dot{\mathbf{p}}(l_1) \equiv \mathbf{P}\dot{\boldsymbol{\eta}}'(l_1) + \mathbf{C}^T\dot{\boldsymbol{\eta}}'(l_1) + \dot{\mathbf{P}}\boldsymbol{\eta}(l_1) + \dot{\mathbf{C}}^T\boldsymbol{\eta}(l_1) = \mathbf{0},\\
&\mathbf{P}\dot{\boldsymbol{\eta}}'(l_c-) + \mathbf{C}^T\dot{\boldsymbol{\eta}}'(l_c-) + \dot{\mathbf{P}}\boldsymbol{\eta}(l_c-) + \dot{\mathbf{C}}^T\boldsymbol{\eta}(l_c-)\\
&\qquad\qquad = \mathbf{P}\dot{\boldsymbol{\eta}}'(l_c+) + \mathbf{C}^T\dot{\boldsymbol{\eta}}'(l_c+) + \dot{\mathbf{P}}\boldsymbol{\eta}(l_c+) + \dot{\mathbf{C}}^T\boldsymbol{\eta}(l_c+),
\end{aligned} \tag{6.40}$$

where the notation $\dot{\mathcal{S}}$ is defined same as in (2.33). Taking the L^2-inner-product of the equation (6.40) with $\dot{\boldsymbol{\zeta}}$ and bearing in mind that $\boldsymbol{\eta} \equiv \dot{\boldsymbol{\zeta}}$ near the fold yields the expression for $\dot{\mu}$ as

$$\dot{\mu}\langle\dot{\boldsymbol{\zeta}}, \dot{\boldsymbol{\zeta}}\rangle = \langle\mathcal{S}\dot{\boldsymbol{\eta}}, \dot{\boldsymbol{\zeta}}\rangle + \langle\dot{\mathcal{S}}\dot{\boldsymbol{\zeta}}, \dot{\boldsymbol{\zeta}}\rangle. \tag{6.41}$$

The first term $\langle\mathcal{S}\dot{\boldsymbol{\eta}}, \dot{\boldsymbol{\zeta}}\rangle$ simplifies after integrating by parts (Lemma (2.13)) with the given boundary conditions and matching conditions.

$$\langle\mathcal{S}\dot{\boldsymbol{\eta}}, \dot{\boldsymbol{\zeta}}\rangle = \langle\mathcal{S}\dot{\boldsymbol{\zeta}}, \dot{\boldsymbol{\eta}}\rangle + \left(\mathbf{P}\dot{\boldsymbol{\eta}}' + \mathbf{C}^T\boldsymbol{\eta}\right)\cdot\dot{\boldsymbol{\zeta}}\Big|_{s=l_c-} + \left[\left(\mathbf{P}\dot{\boldsymbol{\eta}}' + \mathbf{C}^T\boldsymbol{\eta}\right)\cdot\dot{\boldsymbol{\zeta}}\right]_{l_c+}^{l_1}.$$

Subsequently, we utilize the fact that $\dot{\boldsymbol{\zeta}}$ is the zero eigenvector of $\mathcal{S}$, and eliminate the $\dot{\boldsymbol{\eta}}$ terms using the relations (6.40) to get

$$\langle\mathcal{S}\dot{\boldsymbol{\eta}}, \dot{\boldsymbol{\zeta}}\rangle = -\left(\dot{\mathbf{P}}\boldsymbol{\eta}' + \dot{\mathbf{C}}^T\boldsymbol{\eta}\right)\cdot\dot{\boldsymbol{\zeta}}\Big|_{s=l_c-} - \left[\left(\dot{\mathbf{P}}\boldsymbol{\eta}' + \dot{\mathbf{C}}^T\boldsymbol{\eta}\right)\cdot\dot{\boldsymbol{\zeta}}\right]_{l_c+}^{l_1}. \tag{6.42}$$

The differentiation of (6.39) with respect to pseudo-arclength τ enables $\langle\dot{\mathcal{S}}\dot{\boldsymbol{\zeta}}, \dot{\boldsymbol{\zeta}}\rangle = -\langle\mathcal{S}\ddot{\boldsymbol{\zeta}}, \dot{\boldsymbol{\zeta}}\rangle$. Furthermore, we derive the following results on the boundary conditions and matching conditions at the fold by differentiating (6.39) with respect to τ

$$\begin{aligned}
&\ddot{\boldsymbol{\zeta}}(0) = \frac{\partial^2\boldsymbol{\zeta}_o}{\partial\xi^{22}}\dot{\xi}^2 + \frac{\partial\boldsymbol{\zeta}_o}{\partial\xi}\ddot{\xi} = \frac{\partial\boldsymbol{\zeta}_o}{\partial\xi}\ddot{\xi},\\
&\ddot{\boldsymbol{\zeta}}(l_1) \equiv \mathbf{P}\ddot{\boldsymbol{\zeta}}' + \mathbf{C}^{\mathbf{T}}\ddot{\boldsymbol{\zeta}} + \dot{\mathbf{P}}\dot{\boldsymbol{\zeta}}' + \dot{\mathbf{C}}^T\dot{\boldsymbol{\zeta}}' = \mathbf{0},\\
&\mathbf{P}\ddot{\boldsymbol{\zeta}}'(l_{c-}) + \mathbf{C}^{\mathbf{T}}\ddot{\boldsymbol{\zeta}}(l_{c-}) + \dot{\mathbf{P}}\dot{\boldsymbol{\zeta}}'(l_{c-}) + \dot{\mathbf{C}}^T\dot{\boldsymbol{\zeta}}(l_{c-})\\
&\qquad\qquad = \mathbf{P}\ddot{\boldsymbol{\zeta}}'(l_{c+}) + \mathbf{C}^{\mathbf{T}}\ddot{\boldsymbol{\zeta}}(l_{c+}) + \dot{\mathbf{P}}\dot{\boldsymbol{\zeta}}'(l_{c+}) + \dot{\mathbf{C}}^{\mathbf{T}}\dot{\boldsymbol{\zeta}}(l_{c+}).
\end{aligned} \tag{6.43}$$

The application of lemma (2.13) with boundary conditions and matching conditions, and recalling that $\dot{\boldsymbol{\zeta}}$ is the zero eigenvector of $\mathcal{S}$ at the fold, we obtain

$$\begin{aligned}
-\langle\mathcal{S}\ddot{\boldsymbol{\zeta}}, \dot{\boldsymbol{\zeta}}\rangle = -\langle\ddot{\boldsymbol{\zeta}}, \mathcal{S}\dot{\boldsymbol{\zeta}}\rangle &+ \left[\left(\mathbf{P}\ddot{\boldsymbol{\zeta}}' + \mathbf{C}^T\ddot{\boldsymbol{\zeta}}\right)\cdot\dot{\boldsymbol{\zeta}}\right]_0^{l_c-} - \left[\left(\mathbf{P}\dot{\boldsymbol{\zeta}}' + \mathbf{C}^T\dot{\boldsymbol{\zeta}}\right)\cdot\ddot{\boldsymbol{\zeta}}\right]_0^{l_c-}\\
&+ \left[\left(\mathbf{P}\ddot{\boldsymbol{\zeta}}' + \mathbf{C}^T\ddot{\boldsymbol{\zeta}}\right)\cdot\dot{\boldsymbol{\zeta}}\right]_{l_c+}^{l_1} - \left[\left(\mathbf{P}\dot{\boldsymbol{\zeta}}' + \mathbf{C}^T\dot{\boldsymbol{\zeta}}\right)\cdot\ddot{\boldsymbol{\zeta}}\right]_{l_c+}^{l_1},\\
= \ddot{\xi}\left(\frac{\partial\boldsymbol{\zeta}_o}{\partial\xi}\cdot\mathbf{P}\dot{\boldsymbol{\zeta}}'\right)\Big|_{s=0} &+ \left(\dot{\mathbf{P}}\dot{\boldsymbol{\zeta}}' + \dot{\mathbf{C}}^T\dot{\boldsymbol{\zeta}}\right)\cdot\dot{\boldsymbol{\zeta}}\Big|_{s=l_c-} + \left[\left(\dot{\mathbf{P}}\dot{\boldsymbol{\zeta}}' + \dot{\mathbf{C}}^T\dot{\boldsymbol{\zeta}}\right)\cdot\dot{\boldsymbol{\zeta}}\right]_{l_c}^{l_1}.
\end{aligned} \tag{6.44}$$

If we assume that $\langle \dot{\boldsymbol{\zeta}}, \dot{\boldsymbol{\zeta}} \rangle = 1$ and on substituting (6.42), (6.44) in (6.41), the expression for $\dot{\mu}$ becomes

$$\begin{aligned}\dot{\mu} = \ddot{\xi}\left(\frac{\partial \boldsymbol{\zeta}_o}{\partial \xi} \cdot \mathbf{P}\dot{\boldsymbol{\zeta}}'\right)\Big|_{s=0} + \left(\dot{\mathbf{P}}\dot{\boldsymbol{\zeta}}' + \dot{\mathbf{C}}^T\dot{\boldsymbol{\zeta}}\right)\cdot\dot{\boldsymbol{\zeta}}\Big|_{s=l_{c-}} + \left[\left(\dot{\mathbf{P}}\dot{\boldsymbol{\zeta}}' + \dot{\mathbf{C}}^T\dot{\boldsymbol{\zeta}}\right)\cdot\dot{\boldsymbol{\zeta}}\right]_{l_c}^{l_1} \\ - \left(\dot{\mathbf{P}}\boldsymbol{\eta}' + \dot{\mathbf{C}}^T\boldsymbol{\eta}\right)\cdot\dot{\boldsymbol{\zeta}}\Big|_{s=l_{c-}} - \left[\left(\dot{\mathbf{P}}\boldsymbol{\eta}' + \dot{\mathbf{C}}^T\boldsymbol{\eta}\right)\cdot\dot{\boldsymbol{\zeta}}\right]_{l_{c+}}^{l_1}, \\ = \ddot{\xi}\left(\frac{\partial \boldsymbol{\zeta}_o}{\partial \xi} \cdot \mathbf{P}\dot{\boldsymbol{\zeta}}'\right)\Big|_{s=0}.\end{aligned}$$

The term $\left(\frac{\partial \boldsymbol{\zeta}_o}{\partial \tau} \cdot \mathbf{P}\dot{\boldsymbol{\zeta}}'\right)$ can be modified and written as $\frac{d}{d\tau}\left(\mathcal{L}_{\boldsymbol{\zeta}'} \cdot \frac{\partial \boldsymbol{\zeta}_o}{\partial \xi}\right)$ as previously illustrated (2.37) in section 2.4 . Ultimately, we get the expression for $\dot{\mu}$ as

$$\dot{\mu} = \ddot{\xi}\frac{d}{d\tau}\left(\mathcal{L}_{\boldsymbol{\zeta}'} \cdot \frac{\partial \boldsymbol{\zeta}_o}{\partial \xi}\right)\Big|_{s=0}, \tag{6.45}$$

which is the same expression as (2.38) in section 2.4, we derived for a variational problem with continuous coefficients. The qualitative information predicting if $\dot{\mu}$ is increasing or decreasing as it traverses the fold point is identical to that illustrated in Figure (2.2) for a ξ vs $\left(\mathcal{L}_{\boldsymbol{\zeta}'} \cdot \frac{\partial \boldsymbol{\zeta}_o}{\partial \xi}\right)$ plot.

6.9 Stability of the Hamiltonian System of CTCR

6.9.1 CTCR with a Single section

The CTCR equilibria $\boldsymbol{\zeta}_o$ obtained as a stationary point of the energy functional 6.8 is minimum only if its second variation is non-negative along the variations satisfying linearized boundary conditions. Proceeding with the similar reasoning presented in the section 3.11, we eliminate the variables $\mathbf{r}$ and $\mathbf{n}$ in the functional. They have no explicit contribution to the elastic-tube system, and they act indirectly through $\mathbf{q}$ by inextensibility and unshearability constraint $(\mathbf{r}' - \mathbf{d}_3) = \mathbf{0}$. The energy functional

$$\int_0^{l_1} \mathcal{W}\left(\mathbf{u}, \boldsymbol{\alpha}, \boldsymbol{\alpha}', s\right) ds + \mathbf{F} \cdot \left(\mathbf{r}(l_1) + \boldsymbol{\Upsilon}(\mathbf{q}(l_1))\right),$$

is reformulated such that its dependence on $\mathbf{r}$ is eliminated in the following manner

$$\begin{aligned}&\int_0^{l_1} \mathcal{W}\left(\mathbf{u}, \boldsymbol{\alpha}, \boldsymbol{\alpha}', s\right) + \mathbf{F} \cdot \mathbf{r}' ds + + \mathbf{F} \cdot \boldsymbol{\Upsilon}(\mathbf{q}(l_1)) + \mathbf{F} \cdot \mathbf{r}(0), \\ &= \int_0^{l_1} \mathcal{W}\left(\mathbf{u}, \boldsymbol{\alpha}, \boldsymbol{\alpha}', s\right) + \mathbf{F} \cdot \mathbf{d}_3(\mathbf{q}) ds + \mathbf{F} \cdot \boldsymbol{\Upsilon}(\mathbf{q}(l_1)) + \text{constant}.\end{aligned}$$

Henceforth, the energy density $\bar{\mathcal{W}} \equiv \mathcal{W} + \mathbf{F} \cdot \mathbf{d}_3$ explicitly depends only on the variables $\mathbf{q}, \boldsymbol{\alpha}$. The *strengthened Legendre's condition* (3.36) requires the positive definiteness of the

$\bar{\mathcal{W}}_{\boldsymbol{\zeta}'\boldsymbol{\zeta}'}$ matrix for any k-tube section where $\boldsymbol{\zeta} \equiv \begin{bmatrix} \mathbf{q} \\ \boldsymbol{\alpha} \end{bmatrix}$. However, the matrix

$$\mathbf{P} \equiv \bar{\mathcal{W}}_{\boldsymbol{\zeta}'\boldsymbol{\zeta}'} = \begin{bmatrix} \mathbf{K_{eff}}_{11} & 0 & 0 & 0 & 0 & . & . \\ 0 & \mathbf{K_{eff}}_{22} & 0 & 0 & 0 & . & . \\ 0 & 0 & \mathbf{K_{eff}}_{33} & 0 & 0 & . & . \\ 0 & 0 & 0 & 0 & 0 & . & . \\ 0 & 0 & 0 & 0 & K_{33}^{[2]} & . & . \\ . & . & . & . & . & . & . \\ . & . & . & . & . & . & K_{33}^{[k]} \end{bmatrix}$$

is only positive semi-definite owing to the degeneracy of the state $\mathbf{q}$. As already pointed out in section 3.11, this degeneracy arises due to the four-dimensional $\mathbf{q}$ representation of the three-dimensional subspace of directors $\in SO(3)$, and we apply the same approach to mitigate it. The variations orthogonal to $\mathbf{q}$ at s which spans $\{\mathbf{B}_1\mathbf{q}(s), \mathbf{B}_2\mathbf{q}(s), \mathbf{B_3q(s)}\}$ are considered. Hence, $\mathbf{h_q} = \psi_1\mathbf{B}_1\mathbf{q} + \psi_2\mathbf{B}_2\mathbf{q} + \psi_3\mathbf{B}_3\mathbf{q}$ for some scalars ψ_1, ψ_2 and ψ_3. After performing the identical calculations as in section 3.11 for this change of variables, the matrix $\mathbf{P}$ transforms to

$$\bar{\mathbf{P}} \equiv \bar{\mathcal{W}}_{\boldsymbol{\zeta}'\boldsymbol{\zeta}'} = \begin{bmatrix} \mathbf{K_{eff}}_{11} & 0 & 0 & 0 & 0 & . \\ 0 & \mathbf{K_{eff}}_{22} & 0 & 0 & 0 & . \\ 0 & 0 & \mathbf{K_{eff}}_{33} & 0 & 0 & . \\ 0 & 0 & 0 & K_{33}^{[2]} & . & . \\ . & . & . & . & . & . \\ . & . & . & . & . & K_{33}^{[k]} \end{bmatrix},$$

which is positive definite for each k-tube section. Then, it is required to demonstrate the absence of *conjugate points* in order for the equilibria to be local minima. As the matrix $\bar{\mathbf{P}}$ is positive definite, this resulting *weak* minima also qualifies as a *strong* minima (subsection 2.1.2).

The equilibrium equations (6.20c-f) are linearized to give the following Hamiltonian form of the *Jacobi equations*:

$$\begin{aligned} \mathbf{h_q}' &= \left[\frac{\partial^2 H}{\partial \mathbf{q}\partial\boldsymbol{\mu}}\right]\mathbf{h_q} + \left[\frac{\partial^2 H}{\partial\boldsymbol{\mu}\partial\boldsymbol{\mu}}\right]\mathbf{h}_\mu + \left[\frac{\partial^2 H}{\partial\boldsymbol{\alpha}\partial\boldsymbol{\mu}}\right]\mathbf{h}_\alpha + \left[\frac{\partial^2 H}{\partial\boldsymbol{\beta}\partial\boldsymbol{\mu}}\right]\mathbf{h}_{\boldsymbol{\beta}}, \\ \mathbf{h}_\mu' &= \left[\frac{-\partial^2 H}{\partial \mathbf{q}\partial\mathbf{q}}\right]\mathbf{h_q} + \left[\frac{-\partial^2 H}{\partial\boldsymbol{\mu}\partial\mathbf{q}}\right]\mathbf{h}_\mu + \left[\frac{-\partial^2 H}{\partial\boldsymbol{\alpha}\partial\mathbf{q}}\right]\mathbf{h}_\alpha + \left[\frac{-\partial^2 H}{\partial\boldsymbol{\beta}\partial\mathbf{q}}\right]\mathbf{h}_{\boldsymbol{\beta}}, \\ \mathbf{h}_{\boldsymbol{\alpha}}' &= \left[\frac{\partial^2 H}{\partial \mathbf{q}\partial\boldsymbol{\beta}}\right]\mathbf{h_q} + \left[\frac{\partial^2 H}{\partial\boldsymbol{\mu}\partial\boldsymbol{\beta}}\right]\mathbf{h}_{\boldsymbol{\mu}} + \left[\frac{\partial^2 H}{\partial\boldsymbol{\alpha}\partial\boldsymbol{\beta}}\right]\mathbf{h}_\alpha + \left[\frac{\partial^2 H}{\partial\boldsymbol{\beta}\partial\boldsymbol{\beta}}\right]\mathbf{h}_{\boldsymbol{\beta}}, \\ \mathbf{h}_{\boldsymbol{\beta}}' &= \left[\frac{-\partial^2 H}{\partial \mathbf{q}\partial\boldsymbol{\alpha}}\right]\mathbf{h_q} + \left[\frac{-\partial^2 H}{\partial\boldsymbol{\mu}\partial\boldsymbol{\alpha}}\right]\mathbf{h}_{\boldsymbol{\mu}} + \left[\frac{-\partial^2 H}{\partial\boldsymbol{\alpha}\partial\boldsymbol{\alpha}}\right]\mathbf{h}_\alpha + \left[\frac{-\partial^2 H}{\partial\boldsymbol{\beta}\partial\boldsymbol{\alpha}}\right]\mathbf{h}_{\boldsymbol{\beta}}. \end{aligned} \tag{6.46}$$

The expressions for these *Hessian* matrices for the cases of the three-tube section, two-tube section, and one-tube section are given in Appendix C. The equations corresponding to $\mathbf{r}$ and its conjugate momentum $\mathbf{n}$ are not included here since the energy functional no longer depends

on these states. The value of $\mathbf{n}(s)$ is replaced with the constant $-\mathbf{F}$ vector. The absence of *conjugate points* is the requirement for an equilibrium to be stable (*Jacobi condition*). The computation of *conjugate points* is already shown in Chapter 3 (section 3.11). First, consider the case where the robot has only a single section with N tubes, which has a fixed end at $s = 0$ and a free end at $s = l_N$. Later, we extend it to CTCRs with multiple sections.

The *Jacobi equations* (6.46) are solved as an IVP with a basis of initial conditions at the free end $s = l_N$ towards the fixed end $s = 0$. The basis for $\mathbf{h_q}$ is chosen to be the basis of $\mathbf{q}^\perp$-space. For a section with N tubes, $(N-1)+3$ sets of IVPs are solved with the following sets of initial conditions on $\mathbf{h_q}$ and $\mathbf{h_\alpha}$

$$\begin{aligned}
&\mathbf{h_q}(l_N) = [\mathbf{B}_1\mathbf{q}], \quad \mathbf{h_\alpha}(l_N) = [0,\ldots,0]^T,\\
&\mathbf{h_q}(l_N) = [\mathbf{B}_2\mathbf{q}], \quad \mathbf{h_\alpha}(l_N) = [0,\ldots,0]^T,\\
&\mathbf{h_q}(l_N) = [\mathbf{B}_3\mathbf{q}], \quad \mathbf{h_\alpha}(l_N) = [0,\ldots,0]^T,\\
&\mathbf{h_q}(l_N) = [\mathbf{0}], \qquad \mathbf{h_\alpha}(l_N) = [1,\ldots,0]^T,\\
&\qquad\ldots,\\
&\mathbf{h_q}(l_N) = [\mathbf{0}], \qquad \mathbf{h_\alpha}(l_N) = [0,\ldots,1]^T.
\end{aligned}$$

The value of $\mathbf{h}_\beta(l_N)$ is taken as zero vector for all these sets of IVPs, whereas the value of $\mathbf{h_\mu}(l_N)$ is an algebraic system satisfying the linearized boundary conditions

$$\mathbf{h_\mu}(l_N)\cdot\mathbf{B}_i\mathbf{q}(l_N) + \boldsymbol{\mu}(l_N)\cdot\mathbf{B}_i\mathbf{h_q}(l_N) + \left(\frac{\partial}{\partial\mathbf{q}}\left(\Upsilon(l_N)\times\mathbf{F}\right)\cdot\mathbf{d}_i(l_N)\right)\cdot\mathbf{h_q}(l_N) = 0, \quad i = 1,2,3, \tag{6.47}$$

and the linearized integral 6.23

$$\boldsymbol{\mu}(l_N)\cdot\mathbf{h_q}(l_N) + \mathbf{q}(l_N)\cdot\mathbf{h_\mu}(l_N) = 0. \tag{6.48}$$

The solutions $\mathbf{h_q}(s)$ and $\mathbf{h_\alpha}(s)$ are collected, and the components of the solutions corresponding to $\mathbf{h_q}(s)$ are projected onto the $\mathbf{q}^\perp$-space by multiplying with $[\mathbf{B}_1\mathbf{q}(s), \mathbf{B}_2\mathbf{q}(s), \mathbf{B}_3\mathbf{q}(s)]^T$ matrix to give a three-dimensional projected components. This projected $\mathbf{h_q}(s)$ and $\mathbf{h_\alpha}(s)$ for each given set of initial values are arranged as the rows in the matrix along the arc length s of the CTCR. We call this matrix *stability matrix*. A point σ is called the *conjugate point* to l_N if the determinant of this *stability matrix* vanishes for any $\sigma \in [0, l_N]$.

6.9.2 CTCR with Multiple sections

Now, let us extend the *conjugate point* computations to the CTCRs that consist of multiple sections using matching conditions. Consider the CTCR consisting of N-sections, each section S_k consists of $k-$ tube overlap and is represented along arc length as $s \in [l_{k+1}, l_k]$. Each section has a different number of variables i.e., the section S_k has $\mathbf{q}, \alpha^{[2]}, \alpha^{[3]}, \ldots, \alpha^{[k]}$. We know that as the number of tubes k increases, the dimension of the equilibrium equations increases. Similarly, the dimension of the *Jacobi equations* also increases with the number of tubes k. The

Jacobi equations are solved from the free end as an IVP from $s = l_1$ towards the end $s = 0$. The *Jacobi equations* of a one-tube section, i.e., that of a rod with a basis of initial values on $\mathbf{h_q}$ are solved in the same manner as elucidated in the section 3.11. The following matching conditions are imposed near the boundaries between the sections S_k and S_{k-1}:

$$\mathbf{h_q}\Big|_{s=l_{k_-}} = \mathbf{h_q}\Big|_{s=l_{k_+}}, \quad \mathbf{h_\mu}\Big|_{s=l_{k_-}} = \mathbf{h_\mu}\Big|_{s=l_{k_+}},$$
$$\mathbf{h_{\alpha^{[j]}}}\Big|_{s=l_{k_-}} = \mathbf{h_{\alpha^{[j]}}}\Big|_{s=l_{k_+}}, \quad \mathbf{h_{\beta^{[j]}}}\Big|_{s=l_{k_-}} = \mathbf{h_{\beta^{[j]}}}\Big|_{s=l_{k_+}}, \quad 2 < j < k, \quad \text{for } k = 2, 3, \ldots, N.$$

The initial conditions for the states $\mathbf{h_\mu}$ and $\mathbf{h_\beta}$ are same as presented (6.47),(6.48) in previous subsection 6.9.1. The $(N-1)+3$ sets of IVPs are solved using the following sets of initial conditions

$$\begin{aligned}
&\mathbf{h_q}(l_1) = [\mathbf{B}_1\mathbf{q}], \quad \mathbf{h}_{\alpha^{[2]}}(l_2) = 0, \mathbf{h}_{\alpha^{[3]}}(l_3) = 0, \ldots, \mathbf{h}_{\alpha^{[N-1]}}(l_{N-1}) = 0,\\
&\mathbf{h_q}(l_1) = [\mathbf{B}_2\mathbf{q}], \quad \mathbf{h}_{\alpha^{[2]}}(l_2) = 0, \mathbf{h}_{\alpha^{[3]}}(l_3) = 0, \ldots, \mathbf{h}_{\alpha^{[N-1]}}(l_{N-1}) = 0,\\
&\mathbf{h_q}(l_1) = [\mathbf{B}_3\mathbf{q}], \quad \mathbf{h}_{\alpha^{[2]}}(l_2) = 0, \mathbf{h}_{\alpha^{[3]}}(l_3) = 0, \ldots, \mathbf{h}_{\alpha^{[N-1]}}(l_{N-1}) = 0,\\
&\mathbf{h_q}(l_1) = [\mathbf{0}], \quad \mathbf{h}_{\alpha^{[2]}}(l_2) = 1, \mathbf{h}_{\alpha^{[3]}}(l_3) = 0, \ldots, \mathbf{h}_{\alpha^{[N-1]}}(l_{N-1}) = 0,\\
&\mathbf{h_q}(l_1) = [\mathbf{0}], \quad \mathbf{h}_{\alpha^{[2]}}(l_2) = 0, \mathbf{h}_{\alpha^{[3]}}(l_3) = 1, \ldots, \mathbf{h}_{\alpha^{[N-1]}}(l_{N-1}) = 0,\\
&\ldots\ldots\ldots\ldots\ldots\ldots\ldots\\
&\mathbf{h_q}(l_1) = [\mathbf{0}], \quad \mathbf{h}_{\alpha^{[2]}}(l_2) = 0, \mathbf{h}_{\alpha^{[3]}}(l_3) = 0, \ldots, \mathbf{h}_{\alpha^{[N-1]}}(l_{N-1}) = 1.
\end{aligned}$$

The solutions $\mathbf{h_q}$ and $\mathbf{h_\alpha}$ are collected, and the $\mathbf{h_q}$ components are projected on to $\mathbf{q}^\perp$-space. This projected $\mathbf{h_q}(s)$ and $\mathbf{h_\alpha}(s)$ for each given set of initial values are arranged as rows of the matrix along the arc length s of the CTCR, leading to the *stability matrix* along the length of each section of the CTCR. Now, the *conjugate point* is defined as the point l_1^* for which the determinant of this matrix vanishes for any $l_1^* \in [0, l_1]$.

6.10 Summary

We reviewed the kinematic model of CTCR and presented the Hamiltonian formulation of the CTCR equilibria. *Conjugate points* were employed for assessing the stability properties of the resulting equilibria. The cases of CTCRs with multiple sections can also be included in this analysis. A numerical implementation for the corresponding computation has also been presented. The concept of *distinguished bifurcation diagrams* was also extended to these problems for stability determination. In the next part, we apply these concepts to CTCR with multiple sections and study the effect of tip load on the CTCR equilibria and resulting hysteresis behavior.

CHAPTER 7

Numerical Examples: Hysteresis in CTCRs

This chapter presents a few numerical examples illustrating the hysteresis behavior in CTCRs. We leverage the framework developed in the previous chapter for this demonstration. We model the CTCR as a parameter-dependent variational problem where the parameter describes the boundary conditions at the root $s = 0$. Typically, the system is 2π- periodic about this parameter. By numerically continuing in this parameter, we obtain a family of equilibria; sometimes, these solutions are characterized by folds. These folds represent the region of hysteresis. The stability properties of the equilibria are determined with the aid of *conjugate points*. The *distinguished bifurcation diagrams* can also employed to determine the direction of stability near these folds. First, we present examples of simple cases of Two-Tube CTCR. Subsequently, we extend the discussion to a more complex Three-Tube CTCR.

7.1 Two-Tube CTCR

Consider an example consisting of a two-tube robot. It has two sections: a section with two-tube overlap (of length L_2) and a section with one tube (of length L_1). The properties of the constituent tubes of the CTCR (Burgner-Kahrs et al., 2014) used for our numerical experiments are listed in Table 7.1. The governing equations describing the equilibria of the two-tube section of the CTCR (6.20) read

$$\mathbf{r}' = \mathbf{d}_3, \tag{7.1a}$$

$$\mathbf{n}' = \mathbf{0}, \tag{7.1b}$$

$$\mathbf{q}' = \sum_{j=1}^{3} \left(\mathbf{K}_{\mathbf{eff}}^{-\mathbf{1}}{}_{jj} m_j + \tilde{u}_j\right) \frac{1}{2}\mathbf{B}_j \mathbf{q}, \tag{7.1c}$$

$$\boldsymbol{\mu}' = \sum_{j=1}^{3} \left(\mathbf{K}_{\mathbf{eff}}^{-\mathbf{1}}{}_{jj} m_j + \tilde{u}_j\right) \frac{1}{2}\mathbf{B}_j \boldsymbol{\mu} - \frac{\partial \mathbf{d}_3}{\partial \mathbf{q}}^T \mathbf{n}, \tag{7.1d}$$

$$\alpha^{[2]\prime} = \frac{K_{33}^{[1]} + K_{33}^{[2]}}{K_{33}^{[1]} K_{33}^{[2]}} \beta^{[2]} - \frac{m_3}{K_{33}^{[1]}} + \hat{u}_3^{[2]} - \hat{u}_3^{[1]}, \tag{7.1e}$$

$$\beta^{[2]\prime} = \frac{K_{11}^{[1]} K_{11}^{[2]}}{K_{11}^{[1]} + K_{11}^{[2]}} \hat{u}_1^{[1]} \hat{u}_1^{[2]} \sin\alpha^{[2]} + \frac{K_{11}^{[2]} \hat{u}_1^{[2]}}{K_{11}^{[1]} + K_{11}^{[2]}} (m_1 \sin\alpha^{[2]} - m_2 \cos\alpha^{[2]}), \tag{7.1f}$$

Option	Tube 1	Tube 2
Bending Stiffness $K_{11}^{[i]}$ ($\times 10^4\,\mathrm{N.mm^2}$)	0.009	0.102
Torsion Stiffness $K_{33}^{[i]}$ ($\times 10^4\,\mathrm{N.mm^2}$)	0.009/1.3	0.102/1.3
Precurvature vector ($\mathrm{mm^{-1}}$)	[1/35,0,0]	[1/70,0,0]
Maximum Length (mm)	220	110

Table 7.1 Parameters of the two-tube CTCR .

where the vector $\tilde{\mathbf{u}} \equiv [\tilde{u}_1, \tilde{u}_2, \tilde{u}_3]^T$ is given by

$$\tilde{\mathbf{u}} = \begin{bmatrix} \left(K_{11}^{[1]}\hat{u}_1^{[1]} + K_{11}^{[2]}\left(\hat{u}_1^{[2]}\cos\alpha^{[2]} - \hat{u}_2^{[2]}\sin\alpha^{[2]}\right)\right)/(K_{11}^{[1]} + K_{11}^{[2]}) \\ \left(K_{11}^{[1]}\hat{u}_1^{[1]} + K_{11}^{[2]}\left(\hat{u}_1^{[2]}\sin\alpha^{[2]} + \hat{u}_2^{[2]}\cos\alpha^{[2]}\right)\right)/(K_{11}^{[1]} + K_{11}^{[2]}) \\ \left(K_{33}^{[1]}\left(\hat{u}_3^{[1]}\right) + K_{33}^{[2]}\left(\hat{u}_3^{[2]} - \alpha^{[2]\prime}\right)\right)/(K_{33}^{[1]} + K_{33}^{[2]}) \end{bmatrix}. \tag{7.2}$$

The ODEs are solved with the following set of boundary conditions (as described in section 6.6).

$$\begin{aligned} &\mathbf{r}(0) = [0,0,0]^T, \qquad \mathbf{q}(0) = \mathbf{q}_o, \qquad \alpha^{[2]}(0) = \alpha_o^{[2]}, \\ &\mathbf{n}(l_1) + \mathbf{F} = 0, \\ &\boldsymbol{\mu}(l_1)\cdot\mathbf{B}_i\mathbf{q}(l_1)/2 + (\boldsymbol{\Upsilon}(\mathbf{q}(l_1))\times\mathbf{F})\cdot\mathbf{d}_i(l_1), \quad i = 1,2,3. \\ &\boldsymbol{\mu}(l_1)\cdot\mathbf{q}(l_1) + 2\mathbf{r}(l_1)\cdot\mathbf{n}(l_1) = 0, \\ &\beta^{[2]}(l_2) = 0 \end{aligned}$$

Generally, this BVP can be solved in $[0, l_1]$ as a 16- dimensional problem using step function for $\mathbf{K}^{[2]}(s)$. Nevertheless, the majority of the numerical methods cannot handle discontinuous function solutions and pose severe challenges due to convergence issues. So, we employ the alternative method of coupled boundary conditions where the BVP for the two-tube overlap is solved for $s \in [0, l_2]$ and that of the one-tube overlap for $s \in [l_2, l_1]$, where $l_2 = L_2$ and $l_1 = L_1 + L_2$. And the boundary conditions are coupled at the boundary between the section $s = l_2$ as

$$\begin{aligned} \mathbf{r}\big|_{s=l_2^-} &= \mathbf{r}\big|_{s=l_2^+}, \quad \mathbf{q}\big|_{s=l_2^-} = \mathbf{q}\big|_{s=l_2^+}, \\ \mathbf{n}\big|_{s=l_2^-} &= \mathbf{n}\big|_{s=l_2^+}, \quad \boldsymbol{\mu}\big|_{s=l_2^-} = \boldsymbol{\mu}\big|_{s=l_2^+}. \end{aligned}$$

Thus, a BVP with 16 first-order ODEs corresponding to the two-tube overlap section and 14 first-order ODEs corresponding to the one-tube section must be solved numerically. The disadvantage of this approach is the increased dimension of the problem.

In our numerical experiments, we consider only varying orientations of the CTCR backbone about the tangent at the root $s = 0$. The CTCR is positioned so that the tangent of its backbone $\mathbf{d}_3$ at the proximal end $s = 0$ is aligned along the fixed $\mathbf{e}_3$- axis. If θ is the angle between the

$\mathbf{d}_1$-axis of the backbone with the fixed $\mathbf{e}_1$- axis, the quaternion $\mathbf{q}$ at the root $s = 0$ reads

$$\mathbf{q}(0) \equiv \mathbf{q}_o = \left[0, 0, \sin\frac{\theta}{2}, \cos\frac{\theta}{2}\right]^T. \tag{7.3}$$

7.1.1 Distinguished Bifurcation Diagram

We employ the *distinguished bifurcation diagrams* (section 6.8) to analyze the stability characteristics of the robot configurations. In the current problem, the varying parameter is either the relative angle between the tubes at the root $\alpha_o^{[2]}$ or the rotation of the CTCR backbone at the root $s = 0$ (θ in $\mathbf{q}(0) \equiv \left[0, 0, \sin\frac{\theta}{2}, \cos\frac{\theta}{2}\right]$). In the former case, the ordinate in these bifurcation diagrams (2.38) is given by

$$\left(\mathcal{L}_{\alpha^{[2]\prime}} \cdot \frac{\partial \alpha^{[2]}(0)}{\partial \alpha_o^{[2]}}\right)\Bigg|_{s=0} = \beta^{[2]}(0).$$

In the latter case, where θ serves as the varying parameter, the ordinate is

$$\begin{aligned}\left(\mathcal{L}_{\mathbf{q}'} \cdot \frac{\partial}{\partial\theta}\mathbf{q}\right)\Big|_{s=0} &= \boldsymbol{\mu}(0) \cdot \frac{\partial}{\partial\theta}\mathbf{q}(0),\\ &= \boldsymbol{\mu}(0) \cdot \frac{1}{2}\left[0, 0, \cos\frac{\theta}{2}, -\sin\frac{\theta}{2}\right]^T,\\ &= \boldsymbol{\mu}(0) \cdot \mathbf{B}_3\mathbf{q}(0)/2 \equiv m_3(0),\end{aligned} \tag{7.4}$$

which is a tangential component of the bending moment at $s = 0$ and is the same as that for the elastic rod (5.3).

7.1.2 Hysteresis in an Unloaded CTCR

We begin by discussing about a well-known snapping phenomenon (Gilbert et al., 2016) that occurs in the unloaded CTCRs when the relative angle between the tubes at the root $s = 0$ $\alpha^{[2]}(0)$ ($= \alpha_o^{[2]}$) is varied. The operator controls the CTCR by altering the rotation of the tubes at the root $s = 0$ and the lengths of sections L_1 and L_2. For the current numerical experiment, the orientation of the backbone, i.e., the reference inner tube at root $s = 0$ is fixed at $\theta = 0$, while the parameter $\alpha_o^{[2]}$ is varied. As no load is attached to the tip, the one-tube section behaves as a rigid rod, and its length L_1 does not affect the equilibrium of the two-tube section. *Continuation* is performed in the parameter $\alpha_0^{[2]}$ from 0 to 2π, while considering different values of L_2 within the interval $[0, 1.8]$. The CTCR backbone, when $\alpha_o^{[2]} = 0$ consists of piecewise circular arcs, and the corresponding state is supplied as an initial guess to initiate the *continuation*. The ordinate $\beta^{[2]}(0)$ is plotted from the continued solutions in terms of the control parameters $\alpha_o^{[2]}$ and L_2 to yield the *bifurcation surface* as shown in Figure 7.1. Also, the $\beta^{[2]}(0)$ vs. $\alpha_o^{[2]}$ bifurcation diagrams for $L_2 = 0.6$ and $L_2 = 0.75$ are shown by the corresponding planes bisecting the surface, and their planar versions are displayed in Figure 7.2a. The folded region appears symmetric about the plane $\alpha_o^{[2]} = \pi$. The stability exchange information near the folds is ver-

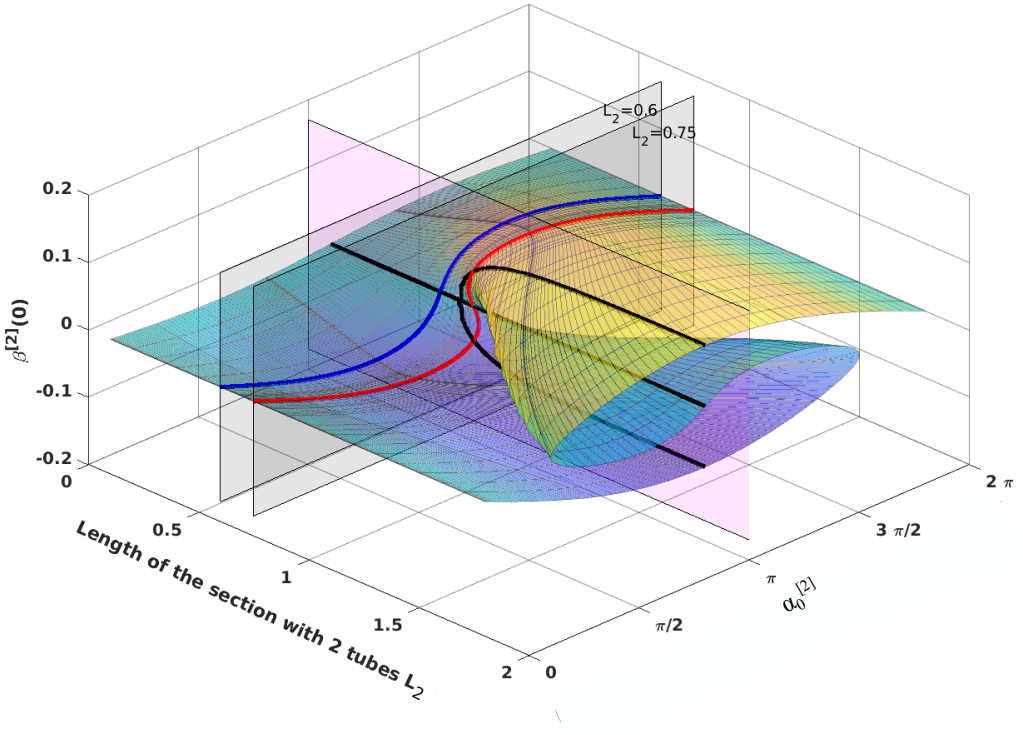

Fig. 7.1 The surface plot of ordinate $\beta^{[2]}(0)$ as a function of $\alpha_o^{[2]}$ and L_2.

ified by computing the *conjugate point* for certain equilibria along the diagram, following the procedure described in section 6.9 and is depicted in Figure 7.2b. The equilibrium labelled as 3 at $\alpha_o^{[2]}$, located between the folds has one *conjugate point* (*index* 1), whereas the equilibria with the remaining labels have zero *conjugate points* (*index* 0). The change in *index* at the folds concurs with the prediction of the theory of *distinguished bifurcation diagrams* (section 2.4), which suggests that the *index* increase in the upper part of the fold opening to the left and vice versa. The region between the folds is unstable, leading to a discontinuous curve of stable equilibria. Consequently, the unstable equilibrium snaps to the adjacent stable equilibrium when operated through this parameter space.

The system exhibits symmetry about the $\alpha_o^{[2]} = \pi$ plane, and the solutions of *Jacobi equations* are identical for $\alpha_o^{[2]} = \pi - b$ and $\alpha_o^{[2]} = \pi + b$ for any $b \in [0, \pi]$. This is why the determinant of the *stability matrix* vs. arc length plots in Figure 7.2b coincide for $\alpha_o^{[2]} = \pi/2$ and $\alpha_o^{[2]} = 3\pi/2$. Moreover, it's worth noting that the determinant has a constant value of one along the one-tube section. In this section, there are no elastic deformations and, consequently, the *stability matrix* remains unchanged and retains its identity matrix form.

Figures 7.1 and 7.2 indicate that when the length of the section, L_2 exceeds a critical value L_{crit}, folds emerge in the bifurcation diagrams, implying a hysteresis behavior. From the perspective of physics, the hysteresis region can be interpreted as the region in which the accumulated elastic strain energy in the tubes is released abruptly. As a result, the CTCR backbone moves from a stable configuration to an adjacent stable one resulting in a snapping motion. This motion is not desired during the operations and must be avoided. On the other hand, there

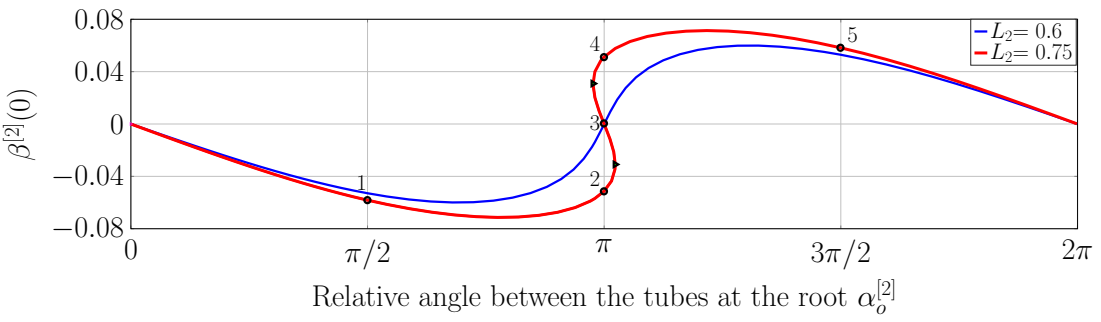

(a)

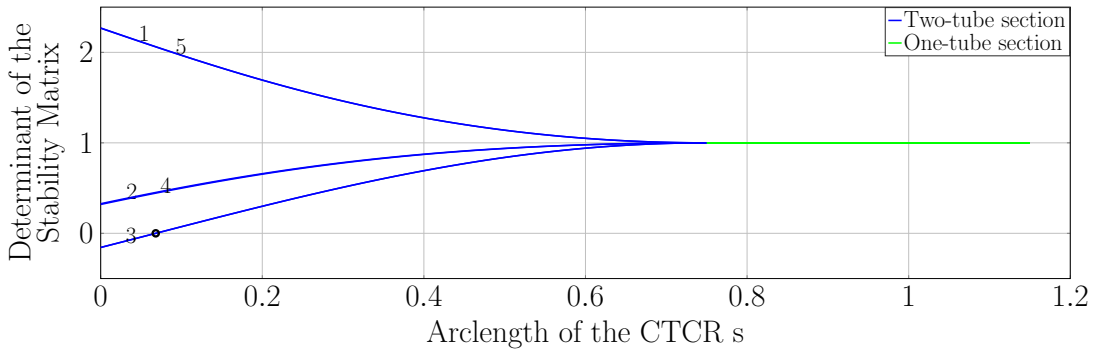

(b)

Fig. 7.2 a) The *distinguished bifurcation diagrams* on the planes L_2 = 0.6 and L_2 = 0.75. The folds are denoted by Δ. Some equilibria along the curve are chosen to determine their stability and labelled with integers. b) The determinant of the *stability matrix* along different sections is shown in different colors. The equilibrium corresponding to label 3 has a *conjugate point* (marked as "o") and is unstable. The remaining equilibria have no conjugate points and are stable.

has been a growing interest in utilizing the elastic instability phenomena in CTCRs for harnessing applications. For instance, researchers are exploring the use of snapping for ablation purposes (Alfalahi et al., 2021) or cutting and suturing procedures (Riojas et al., 2018). In any case, the study of the snapping behavior and its dependence on the parameters helps for the efficient utilization of CTCRs.

Figure 7.1 also reveals an intriguing observation when the plane $\alpha_o^{[2]} = \pi$ intersects the surface, yielding a plot containing a pitchfork. This plot can be interpreted as a pitchfork bifurcation diagram when L_2 is varied while keeping $\alpha_o^{[2]}$ fixed at π. It exhibits characteristics of a *supercritical pitchfork bifurcation* at L_{crit} which leads to an unstable trivial solution and a stable non-trivial solution. In this diagram, the straight line represents the trivial solution, whereas the curved parts of the pitchfork correspond to the non-trivial solutions. The $\beta^{[2]}(0)$ vs. $\alpha_o^{[2]}$ bifurcation diagram for $L_2 > L_{crit}$ features folds, whereas the diagram for $L_2 < L_{crit}$ have no folds. The value of L_{crit} denotes the pitchfork bifurcation point and can be evaluated by carrying out the bifurcation analysis (Gilbert et al., 2016) on the equations governing $\alpha^{[2]}(s)$. For unloaded robots, the equations governing the $\alpha^{[2]}(s)$ can be decoupled from the system resulting in the

following second-order equations

$$\alpha^{[2]\prime\prime} - \frac{(K_{33}^{[1]} + K_{33}^{[2]})K_{11}^{[1]}K_{11}^{[2]}}{(K_{11}^{[1]} + K_{11}^{[2]})K_{33}^{[1]}K_{33}^{[2]}}\hat{u}_1^{[1]}\hat{u}_1^{[2]}\sin\alpha^{[2]} = 0,$$
$$\alpha^{[2]}(0) = \alpha_o^{[2]} \qquad \alpha^{[2]\prime}(l_2) = 0,$$

which have a trivial solution of $\alpha^{[2]}(s) = \pi$ when $\alpha_o^{[2]} = \pi$. This system of equations is analogous to *Euler's elastica* with its coordinate offset by a value of π. The solutions bifurcate when the linearized equations are non-invertible, which arises when

$$L_{crit} = \frac{2k-1}{2}\frac{\pi}{\sqrt{\sigma}}, \quad k = 1, 2\ldots, \qquad \text{where } \sigma = \frac{(K_{33}^{[1]} + K_{33}^{[2]})K_{11}^{[1]}K_{11}^{[2]}}{(K_{11}^{[1]} + K_{11}^{[2]})K_{33}^{[1]}K_{33}^{[2]}}\hat{u}_1^{[1]}\hat{u}_1^{[2]}. \tag{7.5}$$

The first bifurcation mode with $k = 1$ gives the value of L_{crit}, which has a value of 0.682 for the parameters in Table 7.1.

7.1.3 Effect of Tip Load

Let us now investigate the effect of tip load on the hysteresis region. We apply a concentrated tip load $\mathbf{F} = f\mathbf{e}_1 + f\mathbf{e}_2$ ($\boldsymbol{\Delta} = [0, 0, 0]$) at the tip of a one-tube section of length $L_1 = 0.5$. *Parameter continuation* is carried out for a load value of $f = 0.003$ along the parameter $\alpha_o^{[2]}$ for

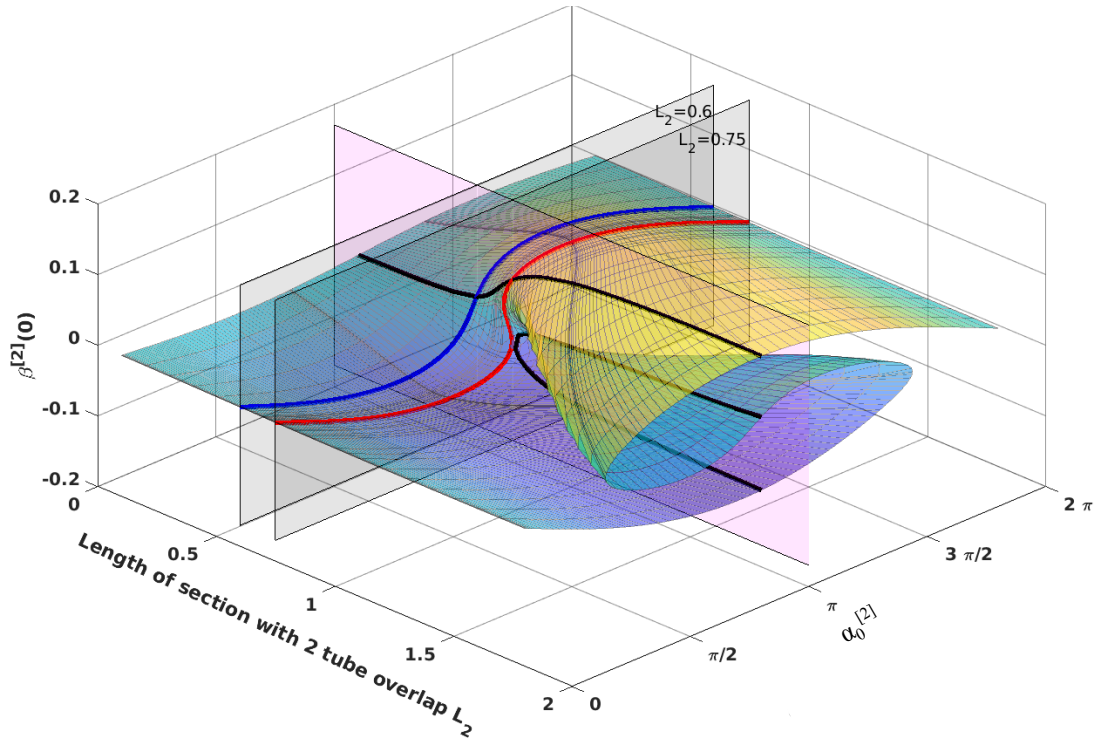

Fig. 7.3 The plot of $\beta^{[2]}(0)$ obtained from the continued solutions with a tip load $F = f\mathbf{e}_1 + f\mathbf{e}_2$ for $f = 0.003$ in terms of control parameters $\alpha_o^{[2]}$ and L_2. The planes $L_2 = 0.6$ and $L_2 = 0.75$ cut the surface resulting in *distinguished bifurcation diagrams*. Another orthogonal plane $\alpha_o^{[2]} = \pi$ intersects the surface and gives two curves (in black).

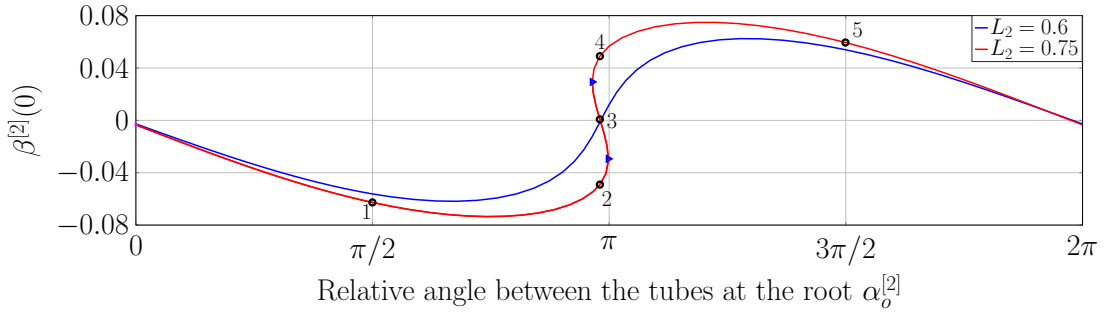

(a) Distinguished bifurcation diagram

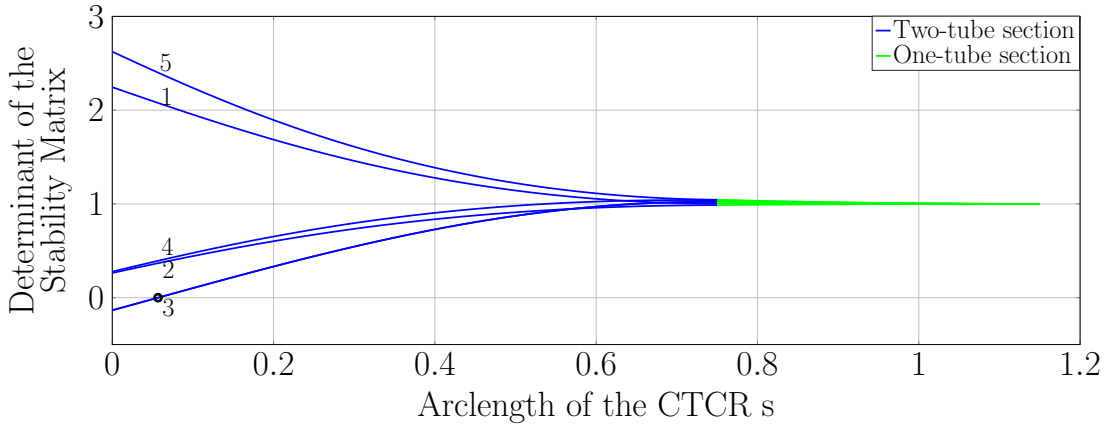

(b) Computation of *conjugate points*

Fig. 7.4 a) The *distinguished bifurcation diagrams* when a CTCR with sections $L_2 = 0.6$ and $L_2 = 0.75$ and a tip load $f\mathbf{e}_1 + f\mathbf{e}_2$ for $f = 0.003$. The fold points are shown in Δ. b) The equilibrium corresponding to label 3 has a *conjugate point* (in "o") and is unstable. The remaining equilibria have no conjugate points and are stable.

different values of L_2. The resulting *bifurcation surface* is illustrated in Figure 7.3. Unlike the previous case, the *bifurcation surface* is not symmetric, and the pitchfork bifurcation diagram appearing on the plane $\alpha_o^{[2]} = \pi$ (in Figure 7.1) is now separated into two disconnected curves as shown in Figure 7.3. This finding implies that the tip load acts as an imperfect bifurcation parameter, breaking the system's symmetry. We also observe that the location of the fold in Figure 7.4a shifted slightly left of π compared to the unloaded case depicted in Figure 7.2a. Some points along the bifurcation diagram in Figure 7.4a are chosen for stability determination and are labelled. Figure 7.4b illustrates the computation of *conjugate points* for these equilibria. In the earlier case, when $\alpha_o^{[2]} = \pi$, there are three equilibria, one of which is unstable. In the current case, there is only one stable equilibrium. On comparing the determinant of the *stability matrix* vs. arc length s plots (Figure 7.4a and Figure 7.4b), we notice a significant difference between the cases of $\alpha_o^{[2]} = \pi/2$ and $\alpha_o^{[2]} = 3\pi/2$. These plots no longer coincide as the system lost its symmetry about $\alpha_o^{[2]} = \pi$ plane. Additionally, we notice in Figure 7.4b that the determinant of the *stability matrix* along the one-tube section is not constant, in contrast to the preceding example without a tip load. The one-tube section experiences elastic deformations due to the tip load, varying the *stability matrix* along its arc length.

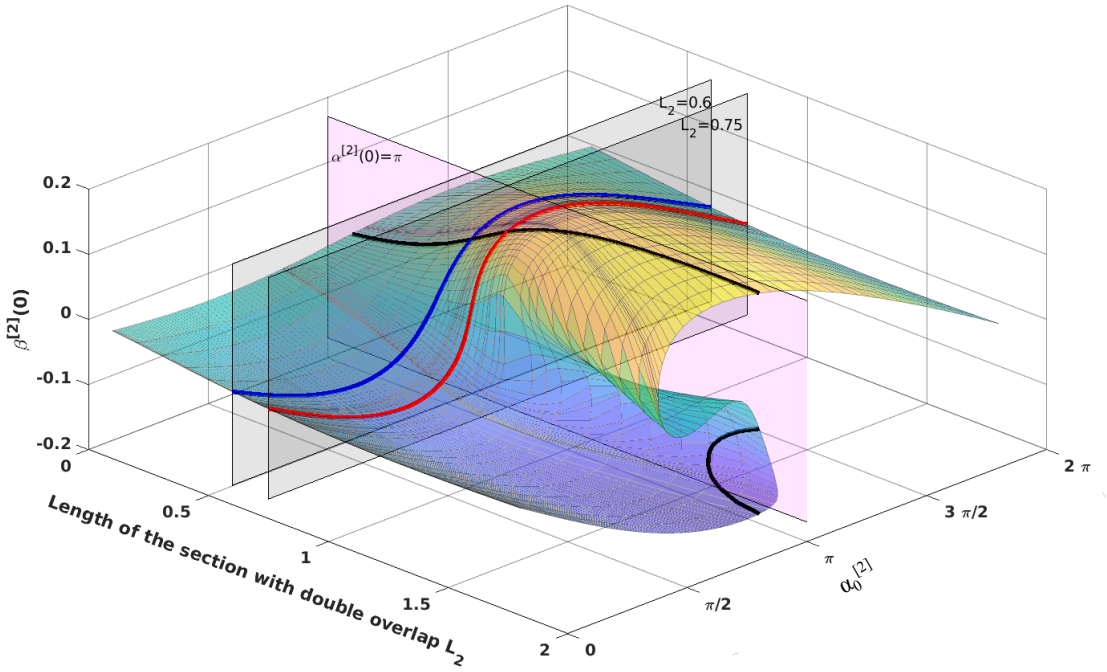

(a) *Bifurcation surface*

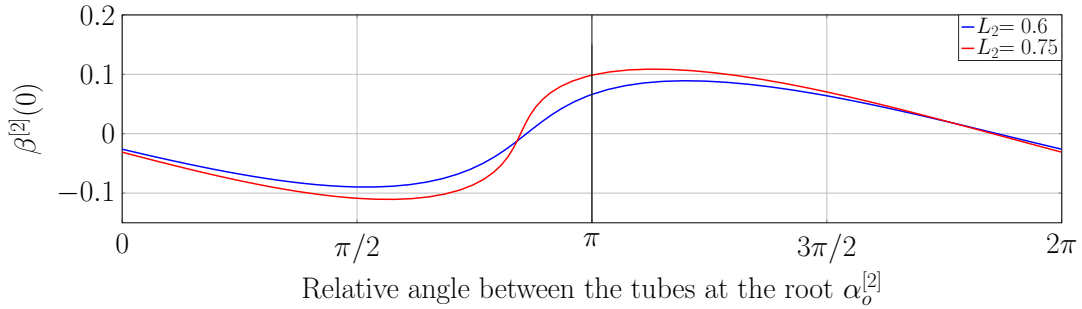

(b) *Distinguished bifurcation diagrams* for $L_2 = 0.6$ and 0.75.

Fig. 7.5 a) The plot of ordinate $\beta^{[2]}(0)$ for the continued solutions as a function of L_2 and $\alpha_o^{[2]}$ with a tip load $f\mathbf{e}_1 + f\mathbf{e}_2$ for $f = 0.01$. The *distinguished bifurcation diagrams* on the planes $L_2 = 0.6$ and $L_2 = 0.75$ are shown. b) The corresponding bifurcation diagrams have no folds.

The presence of the tip load not only shifts the location of the fold in the diagram but also alters its characteristics. For instance, consider the bifurcation diagram at $L_2 = 0.75$. This diagram exhibits folds for both cases of $f = 0$ (Figure 7.1) and $f = 0.003$ (Figure 7.3). When the load is increased to $f = 0.01$, the *bifurcation surface* changes gradually with the cusp piercing out of the plane of $L_2 = 0.75$ in Figure 7.5a. As a result, we obtain the foldless path for $L_2 = 0.75$ as shown in Figure 7.5b. The plane $\alpha_o^{[2]} = \pi$ cuts the bifurcation surface and gives imperfect pitchfork curves. These curves are more separated compared to the previous case of $f = 0.003$ given in Figure 7.3. In summary, the tip load acts as a stabilizing agent for certain unstable equilibria, or conversely, destabilizes some stable equilibria. Moreover, it results in the asymmetrical behavior of the CTCR system with respect to the rotation parameter $\alpha_o^{[2]}$.

7.2 Three-tube CTCR

In this example, we consider a three-tube CTCR, which consists of three sections. The governing equations describing the relative rotation of the tubes in the three-tube section are given by

$$\alpha^{[2]\prime} = \frac{\beta^{[2]} + \beta^{[3]}}{K_{33}^{[1]}} - \frac{m_3}{K_{33}^{[1]}} + \frac{\beta^{[2]}}{K_{33}^{[2]}} + \hat{u}_3^{[2]} - \hat{u}_3^{[1]}, \tag{7.6a}$$

$$\alpha^{[3]\prime} = \frac{\beta^{[2]} + \beta^{[3]}}{K_{33}^{[1]}} - \frac{m_3}{K_{33}^{[1]}} + \frac{\beta^{[3]}}{K_{33}^{[3]}} + \hat{u}_3^{[3]} - \hat{u}_3^{[1]}, \tag{7.6b}$$

$$\begin{aligned}\beta^{[2]\prime} = \frac{K_{11}^{[2]}\hat{u}_1^{[2]}}{K_{11}^{[1]} + K_{11}^{[2]} + K_{11}^{[3]}}\Big(&K_{11}^{[1]}\hat{u}_1^{[1]}\sin\alpha^{[2]} + K_{11}^{[3]}\hat{u}_1^{[3]}\sin\left(\alpha^{[2]} - \alpha^{[3]}\right) \\ &+ m_1\sin\alpha^{[2]} - m_2\cos\alpha^{[2]}\Big),\end{aligned} \tag{7.6c}$$

$$\begin{aligned}\beta^{[3]\prime} = \frac{K_{11}^{[3]}\hat{u}_1^{[3]}}{K_{11}^{[1]} + K_{11}^{[2]} + K_{11}^{[3]}}\Big(&K_{11}^{[1]}\hat{u}_1^{[1]}\sin\alpha^{[3]} + K_{11}^{[2]}\hat{u}_1^{[2]}\sin\left(\alpha^{[3]} - \alpha^{[2]}\right) \\ &+ m_1\sin\alpha^{[3]} - m_2\cos\alpha^{[3]}\Big),\end{aligned} \tag{7.6d}$$

and the governing equations for the remaining state variables $\mathbf{r}, \mathbf{n}, \mathbf{q}$ and $\boldsymbol{\mu}$ are same as that of previous example 7.1 with the vector $\tilde{\mathbf{u}}$ taking the form

$$\tilde{\mathbf{u}} = \begin{bmatrix} \frac{K_{11}^{[1]}\hat{u}_1^{[1]} + K_{11}^{[2]}\left(\hat{u}_1^{[2]}\cos\alpha^{[2]} - \hat{u}_2^{[2]}\sin\alpha^{[2]}\right) + K_{11}^{[3]}\left(\hat{u}_1^{[3]}\cos\alpha^{[3]} - \hat{u}_2^{[3]}\sin\alpha^{[3]}\right)}{K_{11}^{[1]} + K_{11}^{[2]} + K_{11}^{[3]}} \\ \frac{K_{11}^{[1]}\hat{u}_2^{[1]} + K_{11}^{[2]}\left(\hat{u}_1^{[2]}\sin\alpha^{[2]} + \hat{u}_2^{[2]}\cos\alpha^{[2]}\right) + K_{11}^{[3]}\left(\hat{u}_1^{[3]}\sin\alpha^{[3]} + \hat{u}_2^{[3]}\cos\alpha^{[3]}\right)}{K_{11}^{[1]} + K_{11}^{[2]} + K_{11}^{[3]}} \\ \frac{K_{33}^{[1]}\hat{u}_3^{[1]} + K_{33}^{[2]}\left(\hat{u}_3^{[2]} - \alpha^{[2]\prime}\right) + K_{33}^{[3]}\left(\hat{u}_3^{[3]} - \alpha^{[3]\prime}\right)}{K_{33}^{[1]} + K_{33}^{[2]} + K_{33}^{[3]}} \end{bmatrix}$$

The corresponding boundary conditions are

$$\begin{aligned} \alpha^{[2]}(0) &= \alpha_o^{[2]}, \quad & \alpha^{[3]}(0) &= \alpha_o^{[3]}, \\ \beta^{[2]}(l_2) &= 0, & \beta^{[3]}(l_3) &= 0, \end{aligned}$$

At the end $s = l_3$, all state variables except $\alpha^{[3]}(s)$ and $\beta^{[3]}(s)$ are coupled to those of the two-tube section which has the governing equations of the form (7.1). The states are coupled to the one-tube section in the same way as that of the previous problem. As a result, we have a 48-dimensional first-order ODE system. The properties of the CTCR (Burgner-Kahrs et al., 2014) used for the numerical experiment are given in Table 7.2.

For three-tube CTCRs, three rotation parameters can be varied, namely the relative angle between the tubes at the root $\alpha_o^{[2]}$, $\alpha_o^{[3]}$ and the rotation of the CTCR backbone at the root θ. If

Table 7.2 Parameters of the CTCR used in the examples.

Option	Tube 1	Tube 2	Tube 3
Bending Stiffness $K_{11}^{[i]}$ $(\times 10^4 N.mm^2)$	0.009	0.102	0.733
Torsion Stiffness $K_{33}^{[i]}$ $(\times 10^4 N.mm^2)$	0.009/1.3	0.102/1.3	0.733/1.3
Precurvature vector (mm^{-1})	[1/35,0,0]	[1/70,0,0]	[1/160,0,0]
Maximum Length (mm)	330	220	110

the parameter $\alpha_o^{[k]}$, $k = 1, 2$ is varied, the ordinate of *distinguished bifurcation diagram* is

$$\left(\mathcal{L}_{\alpha^{[k]\prime}} \cdot \frac{\partial \alpha^{[k]}(0)}{\partial \alpha_o^{[k]}}\right)\Big|_{s=0} = \beta^{[k]}(0), \quad k = 1, 2.$$

When the orientation of the CTCR backbone about the $\mathbf{e}_3$- axis θ is varied, the ordinate remains the same as in the previous case (section 7.1.1(7.4)), which is $m_3(0)$.

7.2.1 Hysteresis in an Unloaded CTCR

Hysteresis behavior in an unloaded two-tube CTCR has been extensively studied (Gilbert et al., 2016), and some details are already provided in the previous section 7.1. Analytical formulae for critical section lengths are available (7.5). However, when the robot consists of multiple sections, the relative angles function $\alpha^{[k]}(s)$, $k = 2, \ldots, N$ couple across the sections, and the determination of the hysteresis region becomes increasingly difficult. We illustrate this effect through a numerical example using a three-tube CTCR. Figure 7.6 depicts the schematic of a three-tube CTCR .

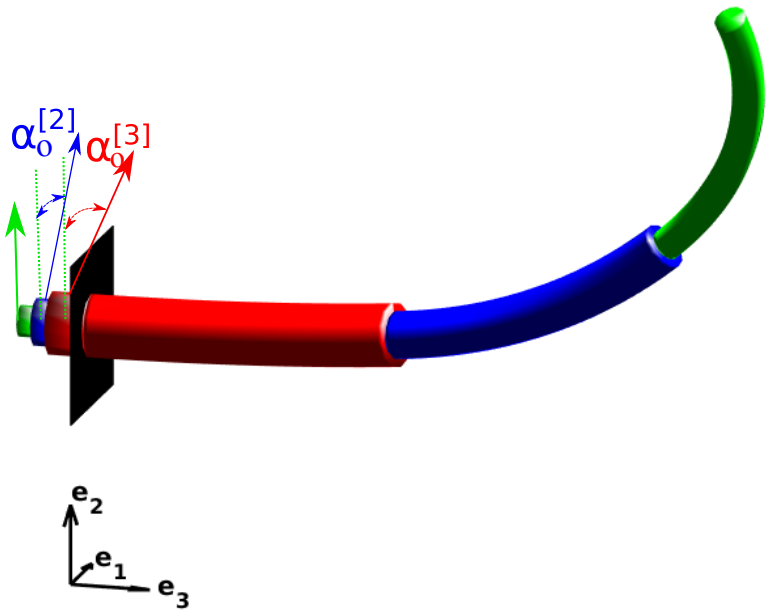

Fig. 7.6 The schematic of the three-tube CTCR. Tubes 1,2 and 3 are shown in green, blue, and red, respectively. The user varies the relative angle between the material frame of the tubes at the root $s = 0$, i.e., $\alpha_o^{[2]}$ and $\alpha_o^{[3]}$.

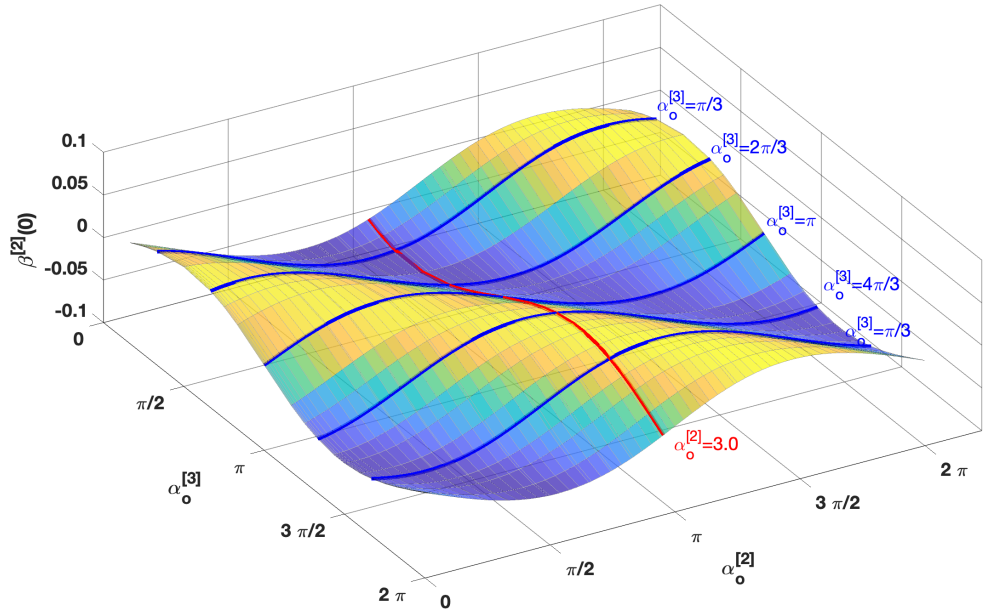

Fig. 7.7 *Bifurcation surface* of a CTCR with only a three-tube section $L_3 = 0.5, L_2 = 0$. The bifurcation diagrams at $\alpha_o^{[3]} = k\frac{\pi}{3}$, $k = 1, \ldots, 5$ and $\alpha_o^{[2]} = 3.0$ are indicated by the corresponding planes bisecting the surface.

Consider an unloaded three-tube CTCR with sections $L_3 = 0.5$ and $L_2 = 0.3$. The two-tube section length L_2 is lower than the critical length for snap-back instability ($L_2 < L_{2,crit} \equiv 0.692$) evaluated in the preceding example). Here, $L_{k,crit}$ denotes the critical length of the k th tube section for snap-back instability in an unloaded CTCR. If a section-length is higher than $L_{k,crit}$, snapping occurs in this system as the values of $\alpha^{[k]}(0), k = 2, 3$ are varied in $[0, 2\pi]$. We prove that the section length L_3 is lower than the $L_{3,crit}$ by numerical *continuation* followed by plotting a *bifurcation surface*, as depicted in Figure 7.7. For plotting this surface, *continuation* is first carried out along the parameter $\alpha_o^{[3]}$ from 0 to 2π. For each of these equilibria, solutions are then continued along $\alpha_o^{[2]}$ from 0 to 2π. The value of $\beta^{[2]}(0)$ is plotted against the parameters $\alpha_o^{[2]}$ and $\alpha_o^{[3]}$ to give a surface plot. Since no folds appear in any fixed planes of $\alpha_o^{[2]}$, $\alpha_o^{[3]}$, or on the surface, it can be concluded that the length $L_3 < L_{3,crit}$. In other words, if only a single three-tube section or a two-tube section of these lengths exists, snapping does not occur when the tubes are relatively rotated from 0 to 2π. As no tip load is considered, the single-rod section has no effect on the equilibria, and its length L_1 is irrelevant in the present context.

The *bifurcation surface* for section-lengths $L_3 = 0.5$ and $L_2 = 0.3$ is shown in Figure 7.8. In this analysis, $\alpha_o^{[2]}$ is the varying parameter, and $\beta^{[2]}(0)$ is the ordinate in the *distinguished bifurcation diagram*. The top view of the surface illustrates how the hysteresis region varies in the plane of parameters $\alpha_o^{[2]}$ and $\alpha_o^{[3]}$. The bifurcation diagrams for a fixed value of $\alpha_o^{[3]}$ at regular intervals of $\pi/3$ are shown on their respective planes. Their planar versions are presented in Figure 7.8c. We notice that only the bifurcation diagram for the plane $\alpha_o^{[3]} = \pi$ exhibits folds, while the remaining do not. Furthermore, another plane $\alpha_o^{[3]} = 3.0$ intersects the *bifurcation*

surface and results in a plot of $\beta^{[2]}(0)$ vs. $\alpha_o^{[3]}$ (in red) that has a fold. However, this plot is not the *distinguished bifurcation diagram* since the ordinate should be $\beta^{[3]}(0)$ instead of $\beta^{[2]}(0)$.

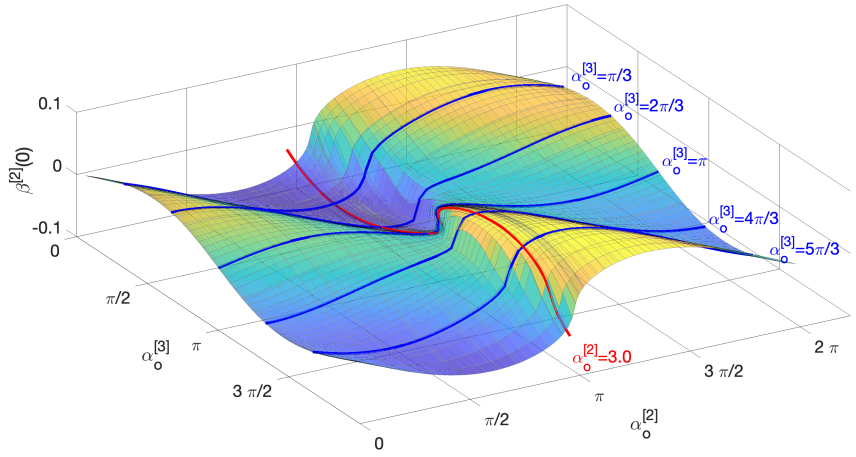

(a) The *bifurcation surface*.

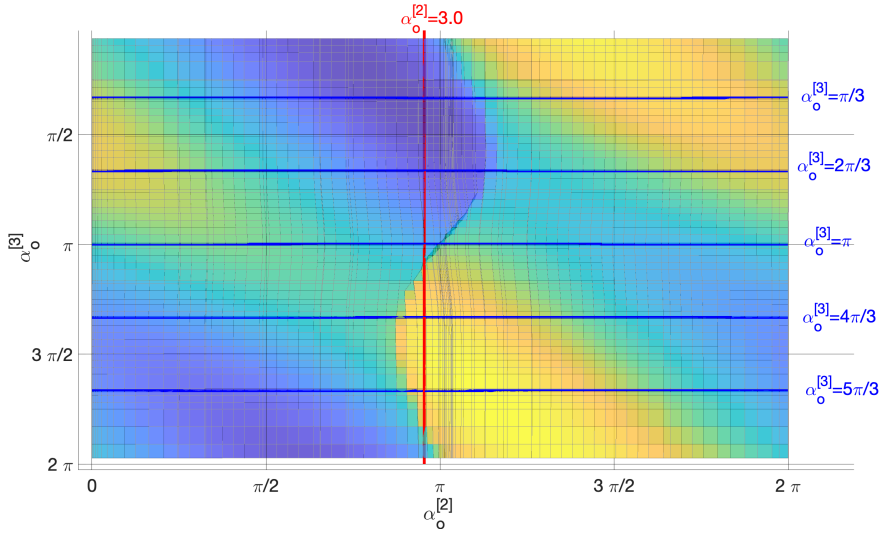

(b) Top view of the *bifurcation surface*.

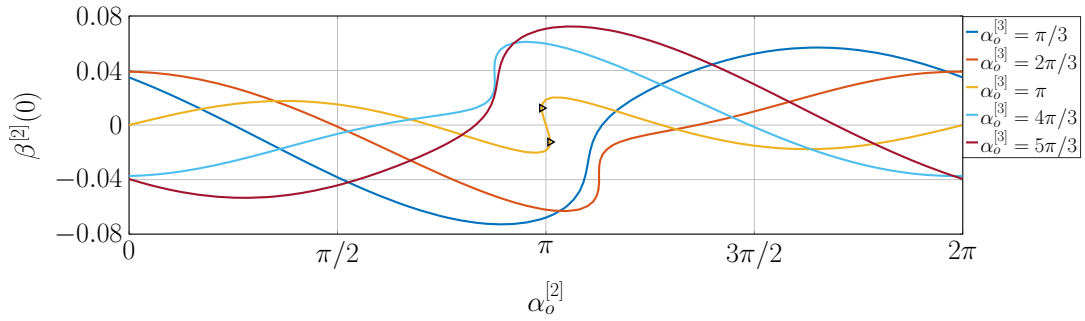

(c) Bifurcation diagrams along the planes $\alpha_o^{[3]} = \frac{\pi}{3}, \frac{2\pi}{3}, \pi, \frac{4\pi}{3}$ and $\frac{5\pi}{3}$

Fig. 7.8 The *bifurcation surface* plot of $\beta^{[2]}(0)$ in terms of $\alpha_o^{[2]}$ and $\alpha_o^{[3]}$ for the sections $L_3 = 0.5$ and $L_2 = 0.3$. The bifurcation diagrams at $\alpha_o^{[3]} = k\frac{\pi}{3}$, $k = 1, \ldots, 5$ (in blue) and $\alpha_o^{[2]} = 3.0$ (in red) are indicated by the corresponding planes bisecting the surface, and their planar versions are presented in (c).

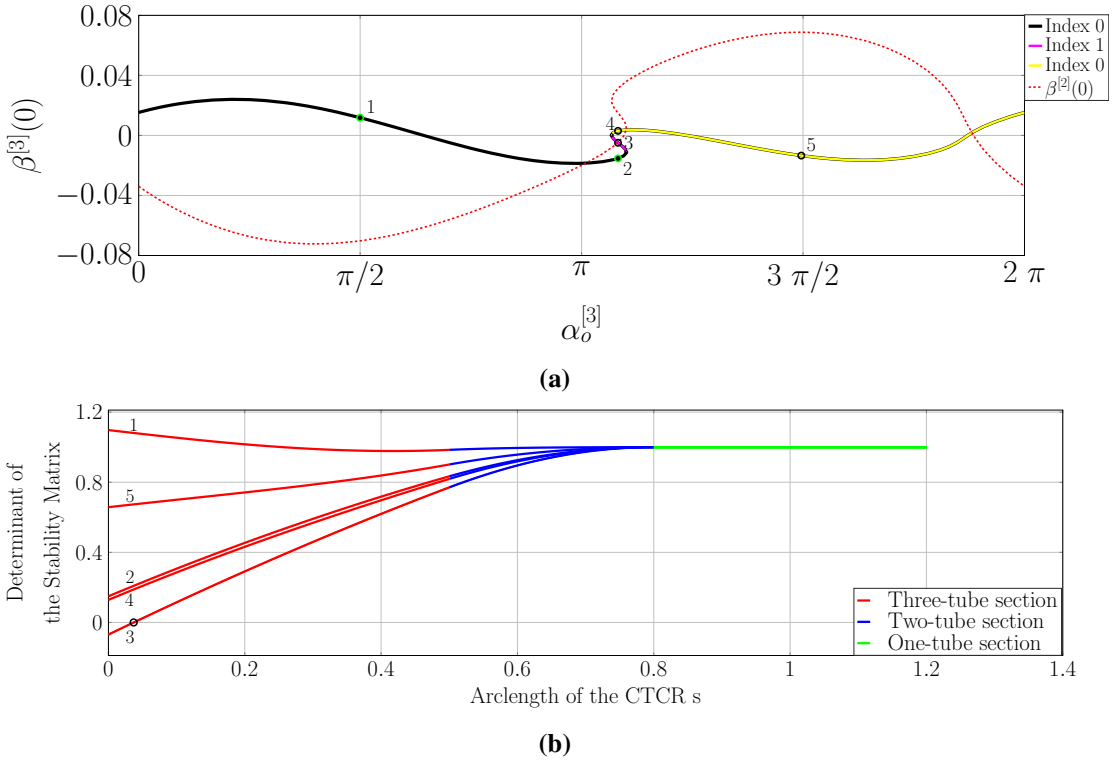

(a)

(b)

Fig. 7.9 a) The *distinguished bifurcation diagram* along the plane $\alpha_o^{[2]} = 3.0$ in Figure 7.8a (Red dotted curve is shown as a solid curve in the Figure 7.8a). b) The *conjugate point* computation for the equilibria in different regions of the diagram shown in (a). The determinant of the *stability matrix* along different sections is shown in different colors.

The value of $\beta^{[3]}(0)$ is plotted to give the correct bifurcation diagram as shown in Figure 7.9a. We have two sets of bifurcation diagrams, namely $\beta^{[2]}(0)$ vs. $\alpha_o^{[2]}$ plot and $\beta^{[3]}(0)$ vs. $\alpha_o^{[3]}$ plot. The stability properties of the equilibria in the latter plot are determined using *conjugate points* as shown in Figure 7.9b. The branches of the curve are represented using the *indices* based on the number of *conjugate points* they possess. It is also worth noting that the CTCR system is 2π periodic in $\alpha_o^{[i]}$, $i = 2, 3$. As a result, the left and right branches of the diagram have the same *index* of 0. Then, the *index* value alternates between 1 and 0 in successive folds as the *index* cannot be negative. In both the plots of $\beta^{[2]}(0)$ vs. $\alpha_o^{[2]}$ and $\beta^{[3]}(0)$ vs. $\alpha_o^{[3]}$, the *index* increased in the upper branch of the fold opening left as predicted. Therefore, we have a region between the folds corresponding to *index* 1, which is unstable equilibria. The CTCR snaps between either side of this region when operated in this regime.

Now, let us consider a scenario where the lengths of the sections L_2 and L_3 are varied such that their sum, $L_2 + L_3$, is maintained at a constant value of 0.8. Consider sections with lengths $L_2 = 0.4$ and $L_3 = 0.4$. *Continuation* is performed along the parameter $\alpha_o^{[2]}$ for different values of $\alpha_o^{[3]}$ within $[0, 2\pi]$ interval. Figure 7.10 shows the corresponding *bifurcation surface* consisting of ordinate $\beta^{[2]}(0)$ plotted against the parameters $\alpha_o^{[2]}$ and $\alpha_o^{[3]}$. The difference between the color contrasts in Figure 7.10 illustrates the inverted S-shaped hysteresis region. This contrast is not so pronounced in the previous case (Figure 7.8b). Additionally, the planes of constant $\alpha_o^{[3]}$ at regular intervals of $\pi/3$ slice the surface resulting in bifurcation plots, and their planar

versions are presented in Figure 7.10c. All these diagrams have S-shaped folds, indicating that the snapping occurs when $\alpha_o^{[2]}$ is varied from 0 to 2π for any fixed value of $\alpha_o^{[3]} \in [0, 2\pi]$. However, in the previous case, snapping occurs only within a band of values of $\alpha_o^{[3]}$ around π when

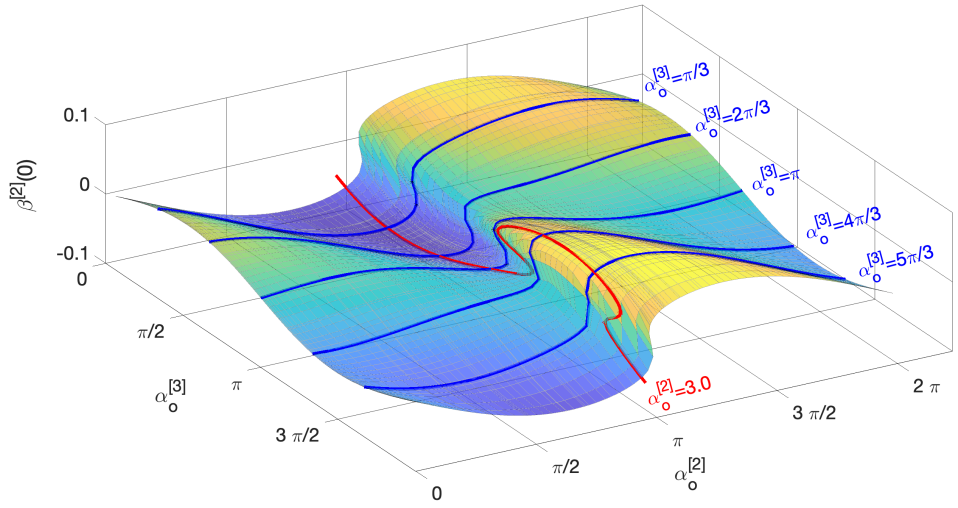

(a) The *bifurcation surface*.

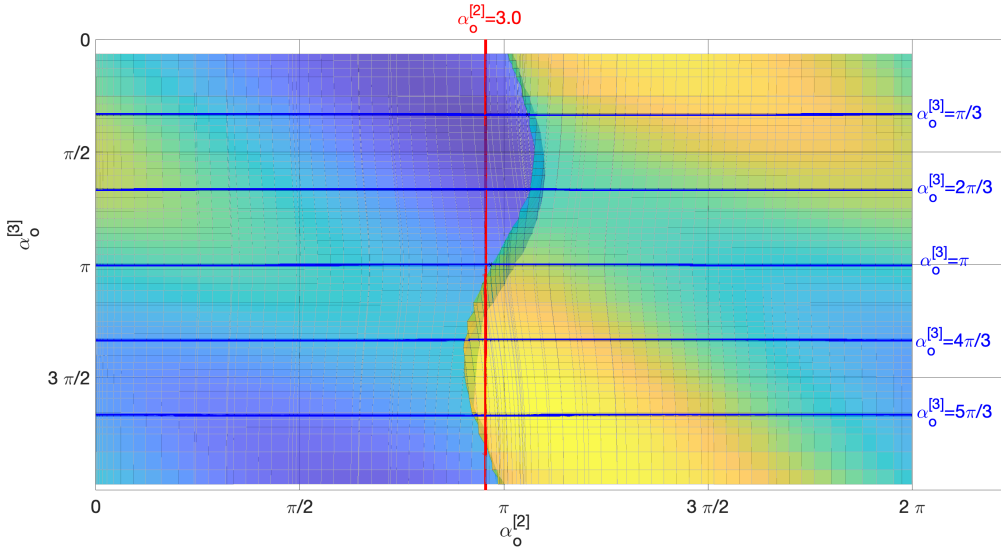

(b) Top view of the *bifurcation surface*.

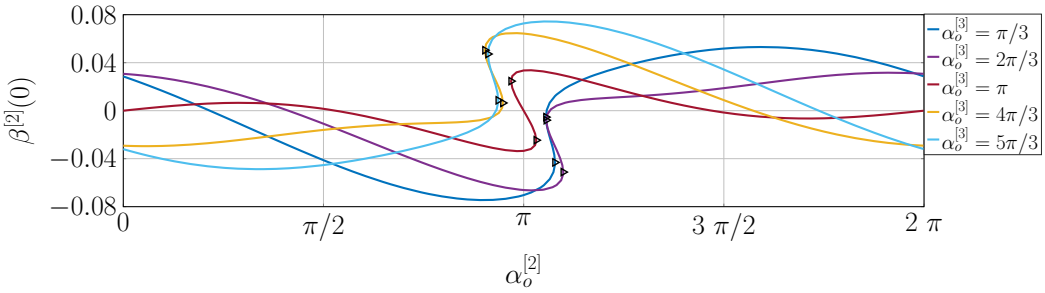

(c) Bifurcation diagrams along the planes $\alpha_o^{[3]} = \frac{\pi}{3}, \frac{2\pi}{3}, \pi, \frac{4\pi}{3}$ and $\frac{5\pi}{3}$.

Fig. 7.10 a) The *bifurcation surface* for the sections $L_3 = 0.4$ and $L_2 = 0.4$. The bifurcation diagrams at $\alpha_o^{[3]} = k\frac{\pi}{3}$, $k = 1, \ldots, 5$ (in blue) and $\alpha_o^{[2]} = 3.0$ (in red) are indicated by the corresponding planes bisecting the surface. The planar diagrams are displayed in (c).

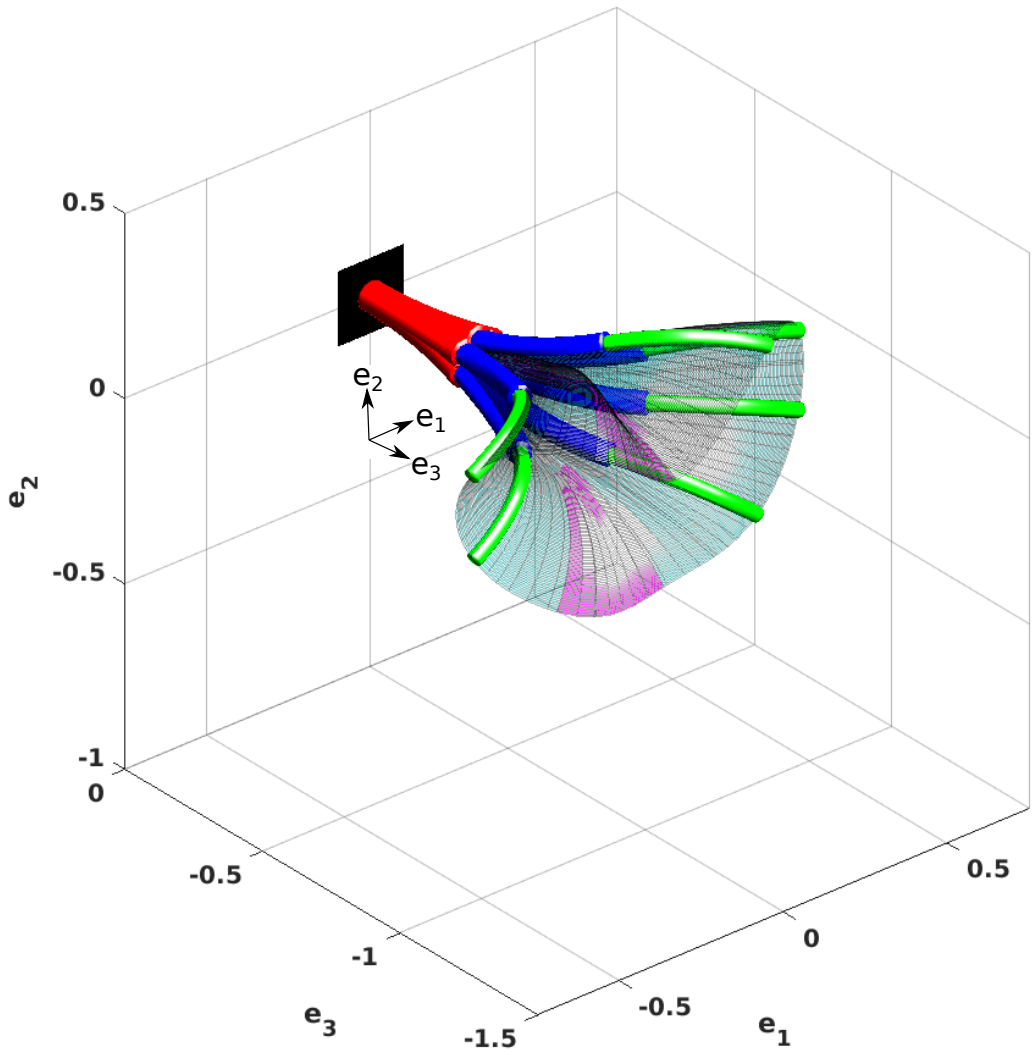

Fig. 7.11 The surface traced by the CTCR when $\alpha_o^{[3]}$ is varied from 0 to 2π at a fixed $\alpha_o^{[2]} = 3.0$ for $L_2 = 0.5$ and $L_3 = 0.3$. The surface corresponding to the unstable equilibria is indicated in magenta. The CTCR configurations for $\alpha_o^{[3]} = 0, \pi/3, 2\pi/3, \pi, 4\pi/3$ and $5\pi/3$ are also shown.

$\alpha_o^{[2]}$ is varied from 0 to 2π. In addition, the plane $\alpha_o^{[2]} = 3.0$ intersects the surface and yields a $\beta^{[2]}(0)$ vs. $\alpha_o^{[3]}$ plot with four folds. The ordinate $\beta^{[3]}(0)$ is plotted to generate the bifurcation diagram as shown in Figure 7.12a. Figure 7.12b and 7.12c illustrate the computation of *conjugate points* for the equilibria in different regions of the bifurcation diagram, and the branches are assigned an *index*. The *index* oscillates between 0 and 1 across the four folds. Hence, the CTCR snaps twice when $\alpha_o^{[3]}$ is varied from 0 to 2π while keeping $\alpha_o^{[2]}$ fixed at the value of 3.0. Figure 7.11 shows a visual representation of the surface traced by the CTCR and some of its configurations during this process. The surface shown in magenta corresponds to the unstable equilibria, and these equilibria jump to the closest stable equilibrium located on the cyan surface.

Now, we further investigate the system by varying the lengths of the sections to $L_3 = 0.3$ and $L_2 = 0.5$. Figure 7.13 displays the *bifurcation surface* for these section lengths. There are S-shaped folds on constant $\alpha_o^{[3]}$ planes, and their planar versions are shown in Figure 7.13c.

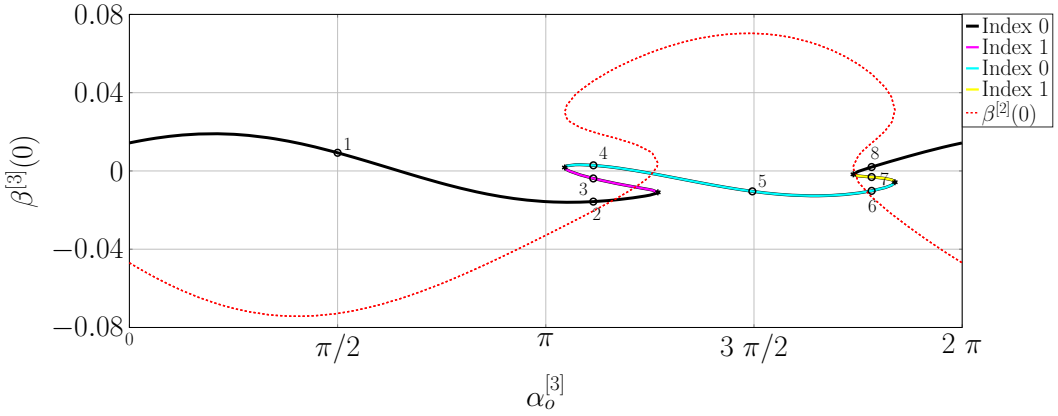

(a) *Distinguished bifurcation diagram* when $\alpha_o^{[3]}$ is varied at a fixed $\alpha_o^{[2]}$ of 3.0.

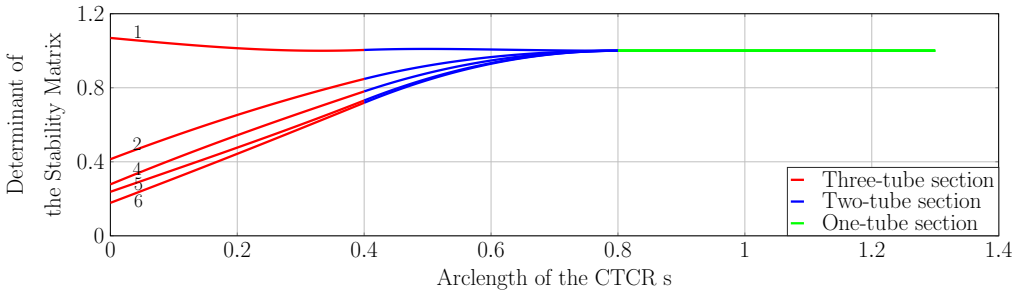

(b) Computation of*conjugate points* for equilibria labelled $1, 2, 4, 5, 6$ and 8.

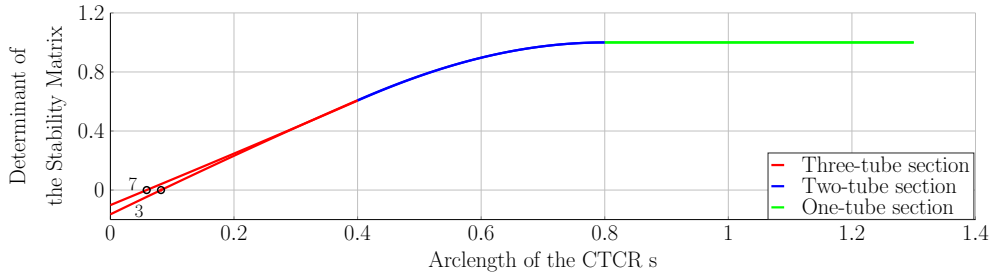

(c) Computation of *conjugate points* for equilibria labelled 3 and 7.

Fig. 7.12 a) The *distinguished bifurcation curve* along the plane $\alpha_o^{[2]} = 3.0$ in Figure 7.10a (red dotted curve represents the solid red curve in the Figure 7.10a). Equilibria from different regions of the curve are chosen for stability determination. The equilibrium in the pink and yellow regions is unstable as they have a *conjugate point* (shown in red dot). The remaining equilibria have no conjugate points and are stable

On comparing with Figure 7.10c, we observe that the unstable region (the distance between the folds) widens from the first case to the third case. Additionally, the strong S-shaped contrasting border between the surfaces in the top view in Figure 7.13 emphasizes the presence of hysteresis in the system. The plane $\alpha_o^{[3]} = 3.0$ slices the surface and gives rise to two non-connecting curves (in red). Thus, a continuous folded curve on the plane in the previous cases (red curves in Figure 7.8a and Figure 7.10a) separated into two disconnected curves. Specifically, in this situation, the lower curve has no folds, whereas the upper curve forms a closed curve with two folds. The stability exchange along the closed curve is analyzed by plotting the $\beta^{[3]}(0)$ vs. $\alpha_o^{[3]}$ plot as shown in Figure 7.14. It can be inferred that a closed bifurcation diagram must be in the 8-shaped curve as given to account for the increase in the *index* at one fold and the decrease

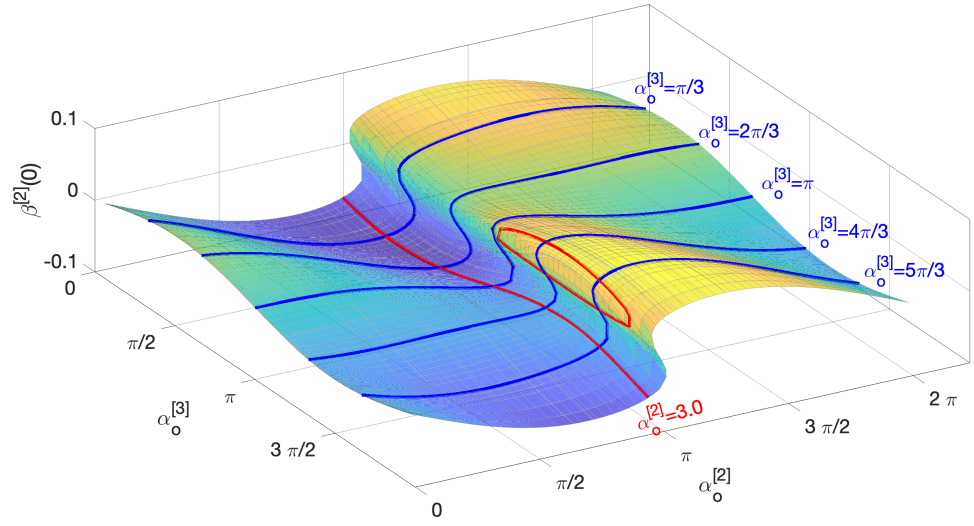

(a) The *bifurcation surface*

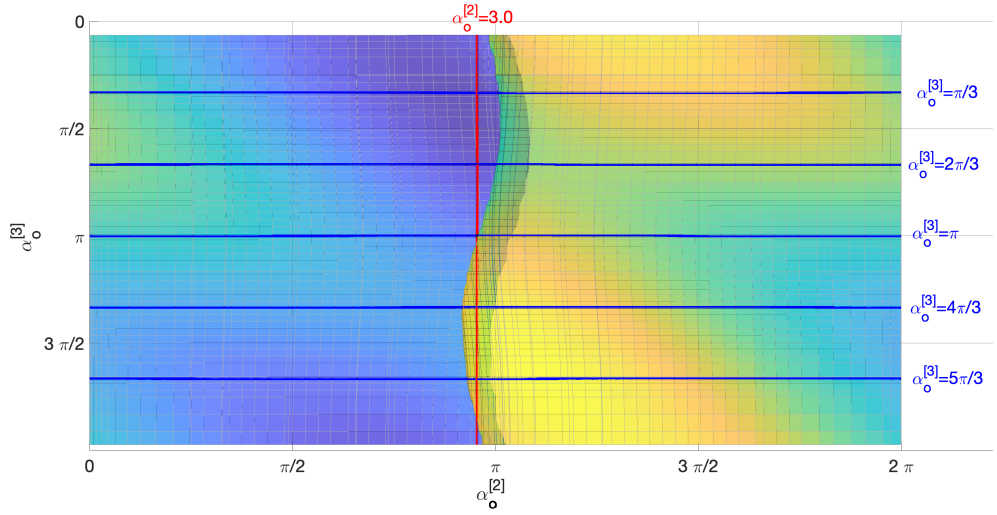

(b) Top view of *bifurcation surface*

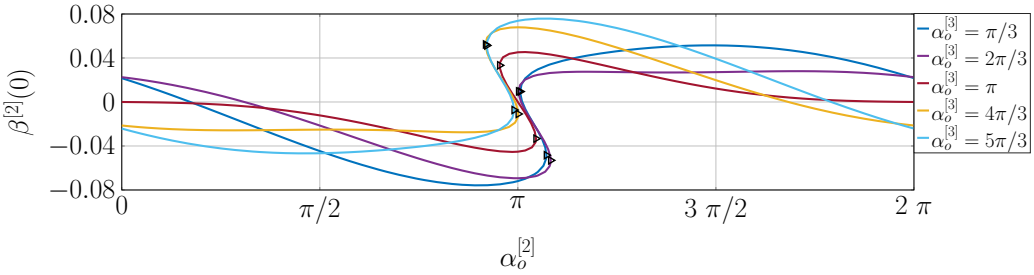

(c) *Distinguished bifurcation diagrams* along the planes

Fig. 7.13 The *bifurcation surface* for the sections of $L_3 = 0.4$ and $L_2 = 0.4$. The bifurcation diagrams at $\alpha_o^{[3]} = k\frac{\pi}{3}$, $k = 1, \ldots, 5$(in blue) and $\alpha_o^{[2]} = 3.0$ (in red) are indicated by the corresponding planes bisecting the surface. The planar views of these plots are shown in (c). The plane $\alpha_o^{[2]} = 3.0$ cuts the surface yielding two disconnected curves.

in the *index* at the other. There are two possibilities for CTCR behavior on this plane. If the equilibrium lies on the lower curve, it remains on this lower curve without any snap motion as the parameter $\alpha_o^{[3]}$ is varied in $[0, 2\pi]$. On the other hand, if the CTCR equilibria lie on the

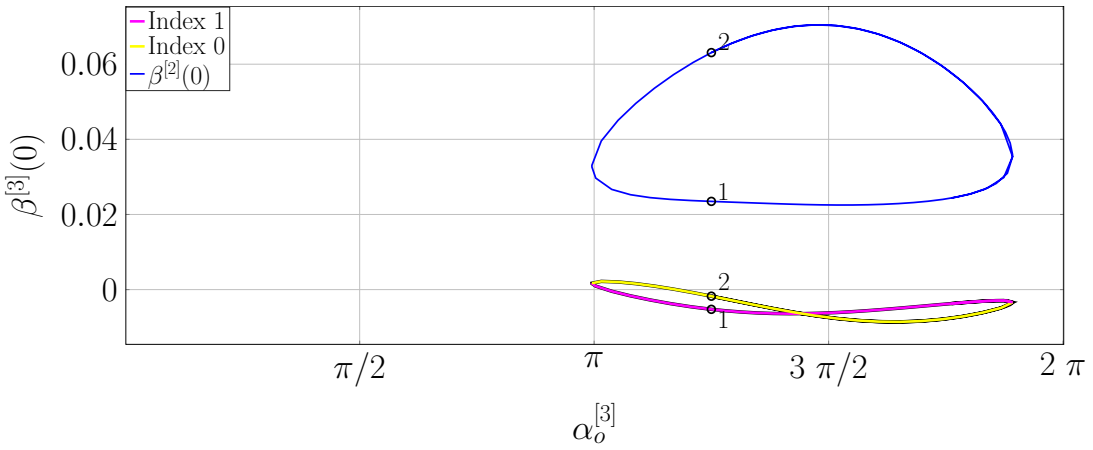

(a) *Distinguished bifurcation diagram* for the closed curve traced on the plane $\alpha_o^{[2]} = 3.0$ in Figure 7.13

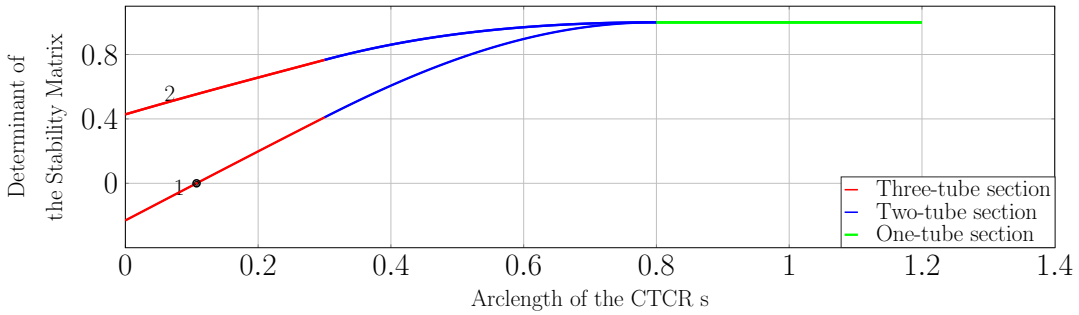

(b) *Conjugate points* for the equilibria at the labels

Fig. 7.14 a) The *distinguished bifurcation diagram* for the closed loop along the plane $\alpha_o^{[2]} = 3.0$ in Figure 7.13a. (The red closed curve in 7.13a is shown as a blue curve here). b) The stability of equilibria separated by the folds is determined through *conjugate points*.

upper curve, the CTCR snaps to the lower curve when the parameter $\alpha_o^{[3]}$ is varied beyond the folds.

From the findings in these three cases, we conclude that the section lengths affect the snapping behavior of the CTCR. The coupling across the sections leads to an unpredictable snapping behavior. The hysteresis region is commonly circumvented by shortening the section lengths and navigating around this region. However, the current examples infer that the individual section lengths can be varied without altering the total length to evade or induce hysteresis in the CTCR system.

7.2.2 Effect of Tip Load and its Direction on the Hysteresis Behavior

In the third case, we study the influence of tip load and its direction on the hysteresis behavior of the three-tube CTCRs. The snapping behavior of a tip-loaded intrinsically curved elastic rod when its clamped end is rotated has been already reported in Chapter 5. CTCR backbone behaves as an intrinsically curved elastic structure for any fixed relative angle parameters $\alpha_o^{[2]}$ and $\alpha_o^{[3]}$. Hence, CTCRs subject to rotating tip loads may exhibit hysteresis behavior. Moreover, the CTCR consists of piecewise spatially curved elastic rod structures. A combination of these effects, along with the additional player, relative rotation between the tubes, further increases the complexity of the system. For the current numerical experiment, we consider the three-tube CTCR with properties given in Table 7.2. The response of the CTCR under a rotating tip load can be studied either by fixing the CTCR orientation at $s = 0$ and varying the load direction or by fixing the load direction and varying the CTCR's orientation at $s = 0$. Both approaches are equivalent, but the latter is chosen as it mimics the many realistic scenarios where the loads such as gravity are in a fixed direction, and the robot's orientation varies. The tangent of the CTCR backbone is aligned along the fixed $\mathbf{e}_3$- axis and is rotated by angle θ about it.

A wide range of parameter space and loading cases is possible. However, this example's primary objective is to illustrate potential hysteresis created by rotating tip loads. Therefore, we have chosen to focus on a specific case with predefined parameters. We consider section lengths of $L_1 = 0.6$, $L_2 = 0.45$ and $L_3 = 0.45$ and fix the relative angle between the tubes at the root: $\alpha_o^{[2]} = \frac{5\pi}{6}$ and $\alpha_o^{[3]} = \frac{7\pi}{6}$. A tip load $\mathbf{F} = -F_2\mathbf{e}_2$ with a lever arm $\Delta = [0, 0.1, 0]$) is applied. First, the CTCR equilibrium for a zero tip load for the given control parameters is obtained through *continuation*. Subsequently, the solutions are continued along the load parameter F_2 from 0 to 0.13. For each of these intermediate solutions, *continuation* is again performed along the angle

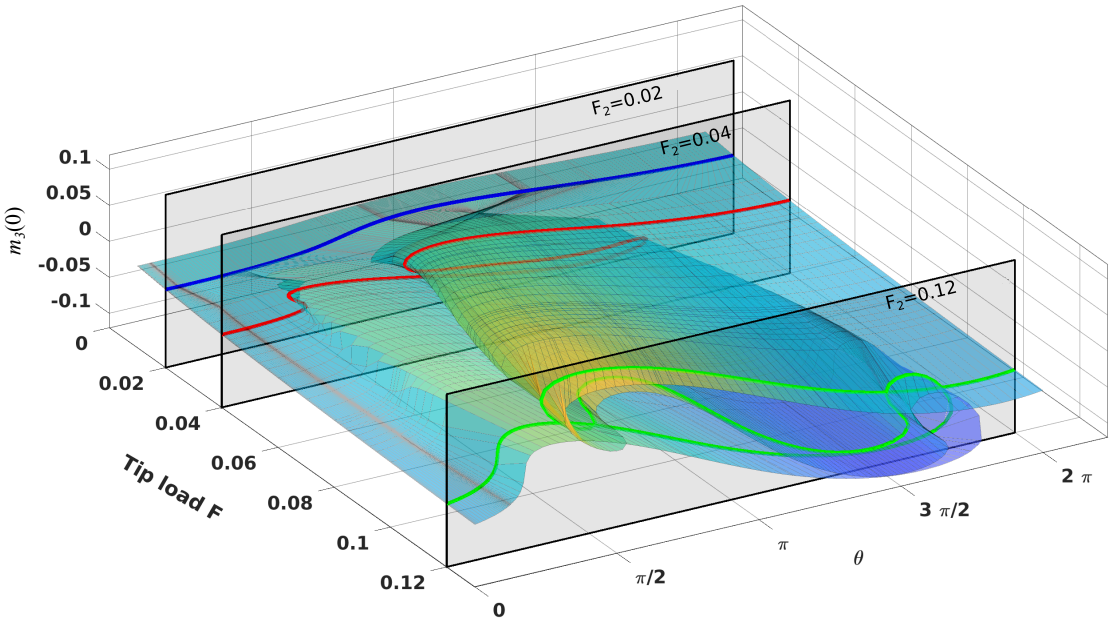

Fig. 7.15 The plot of ordinate $m_3(0)$ for continued solutions along θ for F_2. The *distinguished bifurcation diagrams* for $F_2 = 0.02$, $F_2 = 0.04$ and $F_2 = 0.12$ are shown.

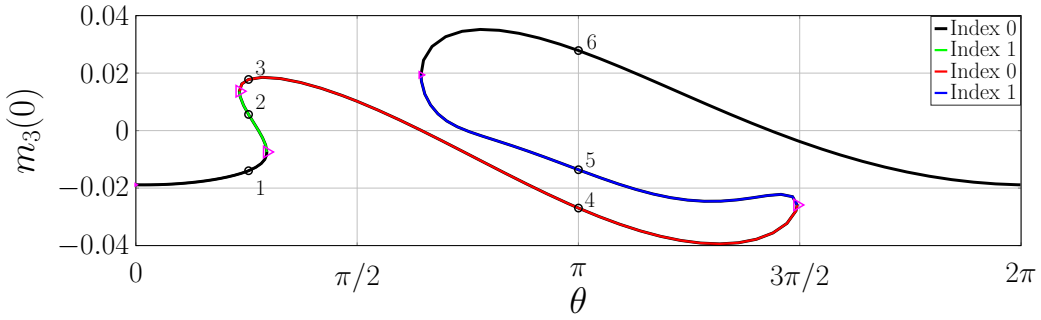

(a) Distinguished bifurcation diagram for the load $F_2 = 0.04$

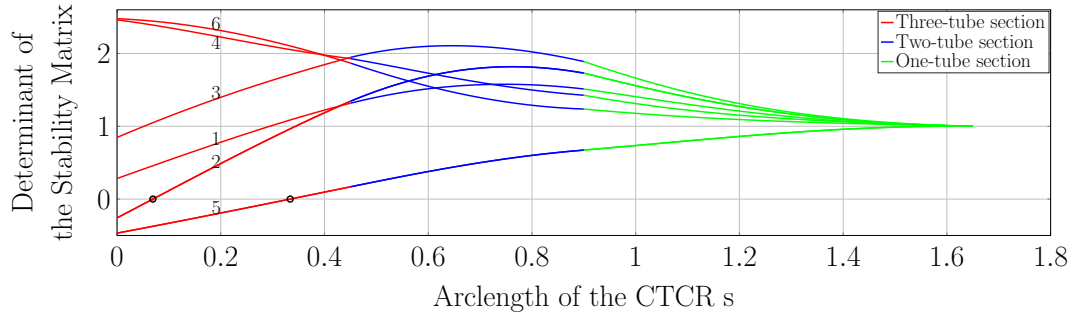

(b) The equilibria with labels 2 and 5 in the above figure have one *conjugate point* whereas those with remaining labels have no *conjugate points*.

Fig. 7.16 *Distinguished bifurcation diagram* for a case with the tip load $F_2 = 0.04$ and the *conjugate point* computations for the labelled equilibria.

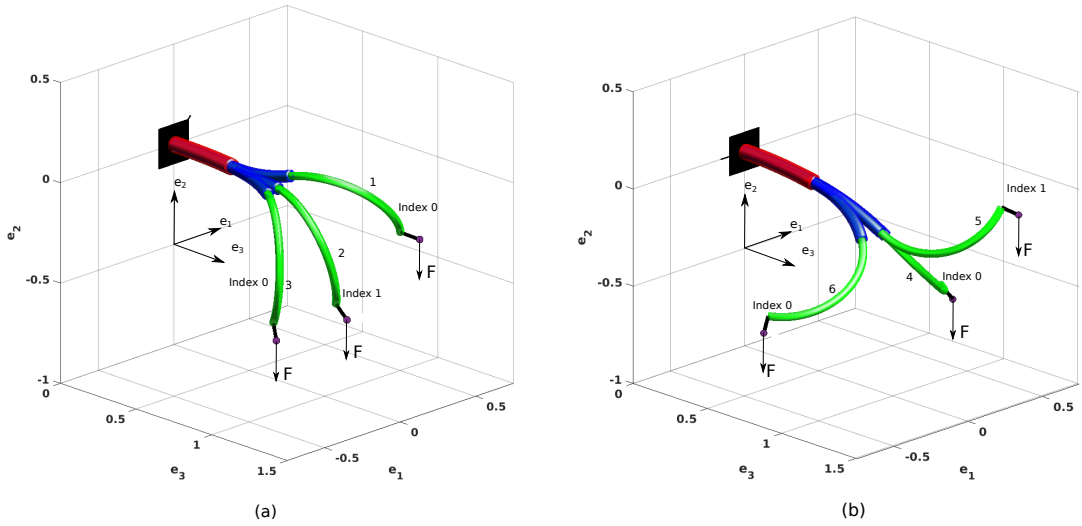

Fig. 7.17 The robot centerlines for the equilibria with labels in the Figure 7.16a.

parameter θ from 0 to 2π. The ordinate $m_3(0)$ is evaluated from the computed solutions and is plotted as a function of F_2 and θ to obtain a *bifurcation surface* as shown in Figure 7.15. The bifurcation diagrams for the loads $F_2 = 0.02, 0.04$ and 0.12 are also shown on their respective planes. At lower loads, such as $F_2 = 0.02$, there are no folds, and therefore, there is no sign of hysteresis, and the robot's tip moves smoothly tracing a closed continuous curve. With a slightly higher load of 0.04, hysteresis suddenly appears in the system. Interestingly, the bifurcation di-

agram for this case, as shown in Figure 7.16a has more than two folds. The four folds divide the diagram into five distinct regions. An equilibrium from each region is picked, labelled, and the *index* is assigned after computing the *conjugate points* as illustrated in Figure 7.16b. The CTCR snaps twice as its backbone is completely rotated about the horizontal tangent. The centerlines of the CTCR backbone for the labelled points in Figure 7.16a are shown in Figure 7.17.

We now turn to the case of higher tip load $F_2 = 0.12$. In this case, the bifurcation diagram shown in Figure 7.18a exhibits more than four folds. The stability of the equilibria in these different regions is analyzed by computing the *conjugate points*, as depicted in Figures 7.18b,7.18c. In comparison to the bifurcation diagram of $F_2 = 0.04$ (Figure 7.16a), we observe that only one hysteresis region exists here. As the load is increased, the first hysteresis region diminishes (left

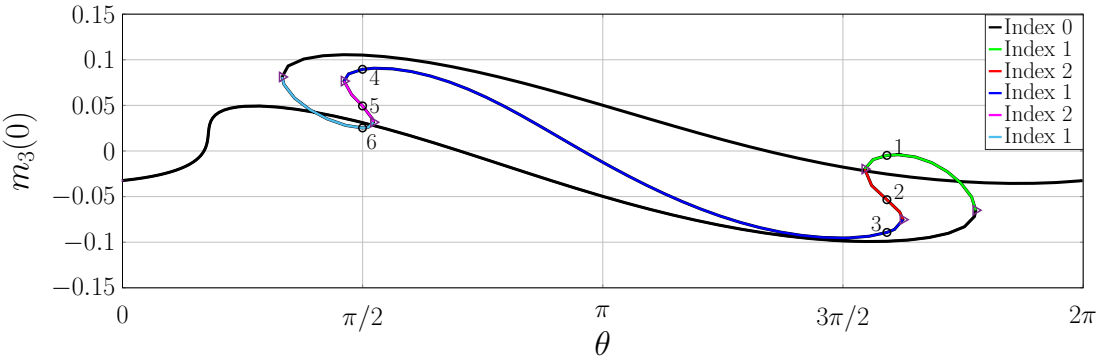

(a) Distinguished bifurcation diagram.

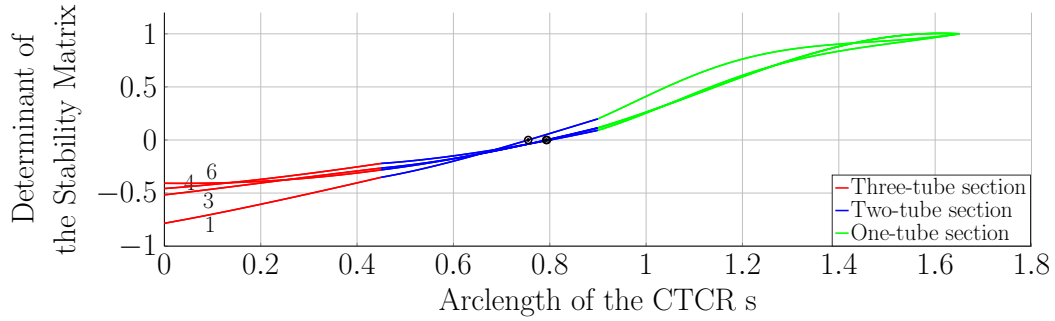

(b) The equilibria labelled $1, 3, 4$ and 6 have one *conjugate point*.

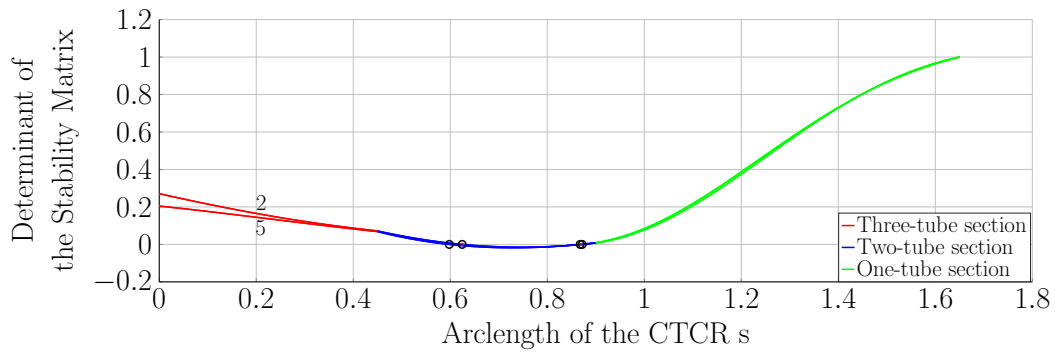

(c) The equilibria labelled 2 and 5 have two conjugate points.

Fig. 7.18 *Distinguished bifurcation diagram* for a case with the tip load $F_2 = 0.12$ and the *conjugate point* computations for the labelled equilibria.

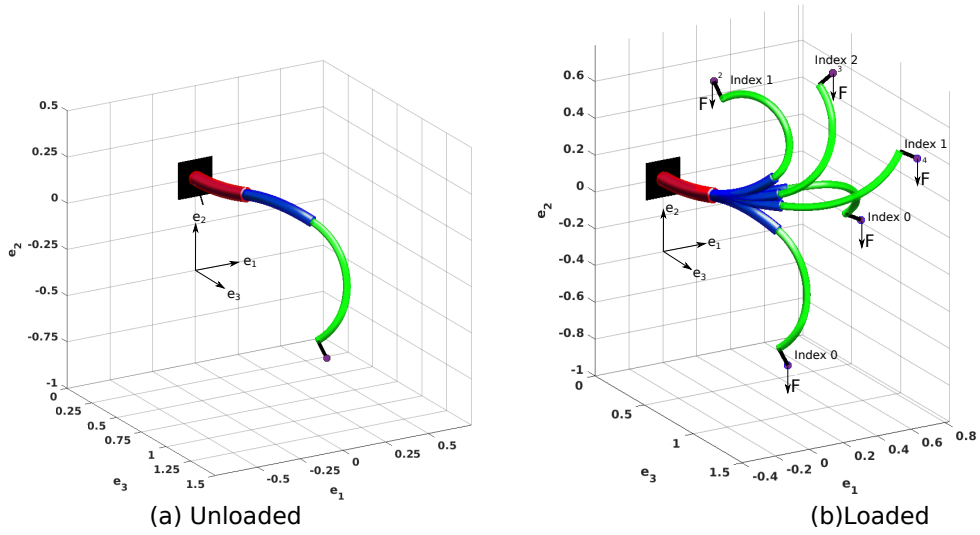

(a)

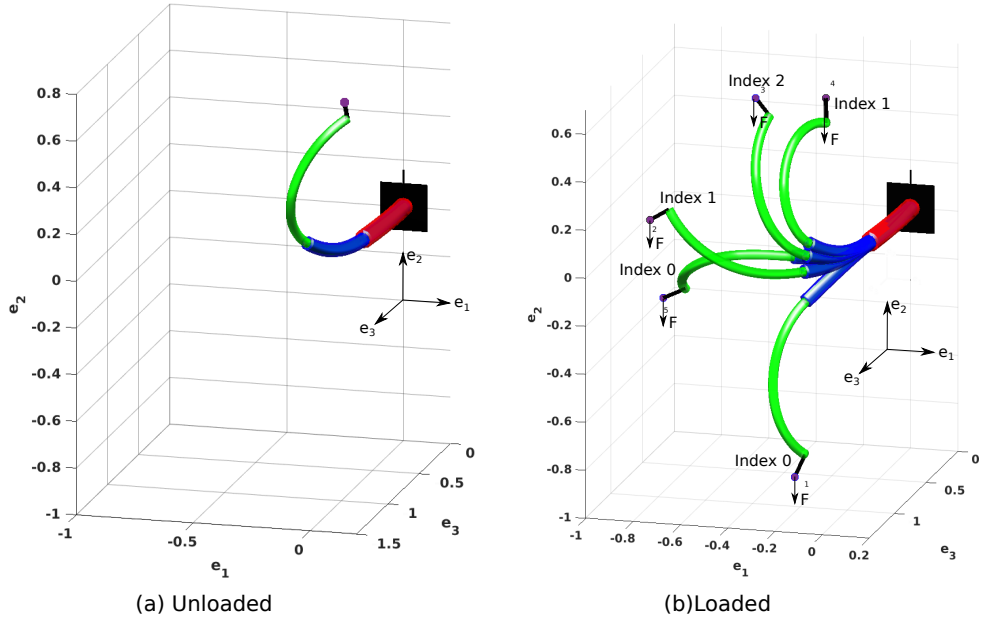

(b)

Fig. 7.19 a) The CTCR configurations corresponding to the points 1,2 and 3 ($\alpha_o^{[2]}$ = 3.0, $\alpha_o^{[2]}$ = 0.8, F_2 = 0.04) from Figure 7.16a. b) The CTCR configurations corresponding to points 4,5 and 6 ($\alpha_o^{[2]}$ = 3.0, $\alpha_o^{[2]}$ = π, F_2 = 0.04) from Figure 7.16a. CTCR configurations with zero tip load for the same control parameters are also displayed for comparison.

folded region in Figure 7.16a), eventually vanishing completely when F_2 = 0.12. In addition, multiple unstable equilibria appear for the current load case as presented in Figure 7.19. The significant aspect of this example is the emergence of equilibria with an *index* of 2. There is an increase in the *index* in the upper branch of the fold opening left and the lower branch of the fold opening right, which aligns with the predictions of *distinguished bifurcation diagram* (discussed in Figure 2.2).

Summarizing the findings, we conclude that the CTCR inherits the hysteresis characteristics from intrinsically curved elastic structures. The piecewise spatially curved elastic structures of CTCR increase the complexity of the problem, and the behavior is non-intuitive. Lower loads resulted in two hysteresis regions which were reduced to one region for higher loads. This study holds the potential to explore the utilization of CTCR as a catapult in surgical procedures, where an instrument or manipulator applies the tip load and cuts the tissue during the snap motion. We determined the stability properties of various equilibria using *conjugate points* and also established a correlation with the shape of *distinguished bifurcation diagrams* in parallel. So, one can just employ these diagrams to determine the stability properties of equilibria without resorting to *conjugate point* computation. Nonetheless, the *index* for one equilibrium along the path must be evaluated to utilize these diagrams.

7.3 Convergence Studies

As the tubes of the CTCR under consideration are uniform in arc length s, the Hamiltonian of each CTCR section H remains constant. In addition to the Hamiltonian H, conserved quantities discussed in the section 6.5 such as $\boldsymbol{\mu}\cdot\mathbf{q}+2\mathbf{r}\cdot\mathbf{n}$, $\mathbf{q}\cdot\mathbf{q}$ can be utilized to test the numerical accuracy and convergence of the solutions. We consider an equilibrium corresponding to the parameters $\theta = 2\pi/3, \alpha_o^{[2]} = 5\pi/6, \alpha_o^{[3]} = 7\pi/6, L_1 = 0.75, L_2 = 0.45, L_3 = 0.45$ and evaluate the three conserved quantities for different number of mesh intervals (NTST) and collocation points (NCOL). Figures 7.20, 7.21 and 7.22 show, respectively, the evaluated Hamiltonian H, $\boldsymbol{\mu}\cdot\mathbf{q}+2\mathbf{r}\cdot\mathbf{n}$ and $\mathbf{q}\cdot\mathbf{q}-1$ along three sections for different values of NTST and NCOL. The Hamiltonian H is conserved along each section within an order of accuracy, as shown in Figure 7.20. Clearly, the accuracy is dependent on the number of mesh intervals and the number of collocation points. The accuracy is in the order of 10^{-6} – 10^{-5} during *continuation* with 5 mesh intervals and 2 collocation points, which is further enhanced by reducing the step size and increasing the number of collocation points, or by using a combination of both. It improved to an order of 10^{-9}

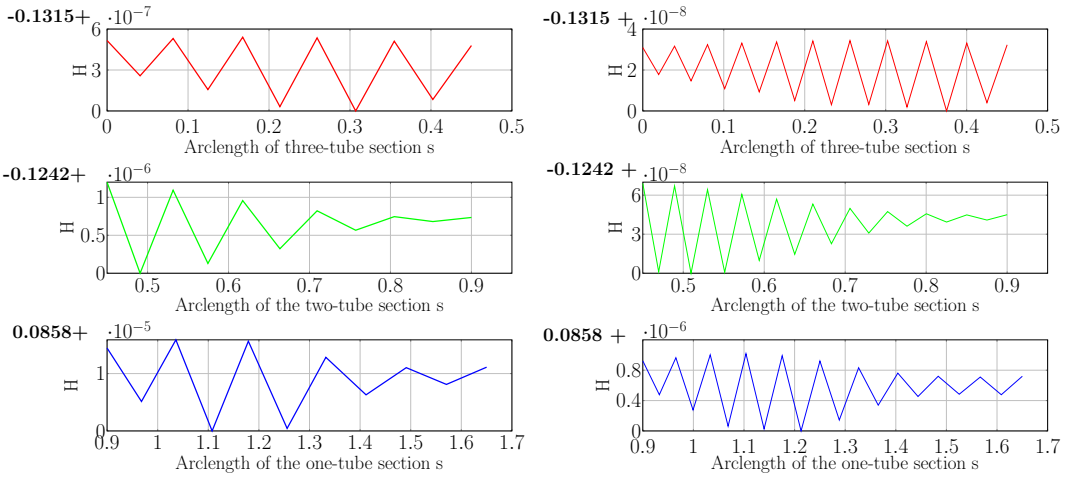

(a) NTST=5, NCOL=2

(b) NTST=10, NCOL=2

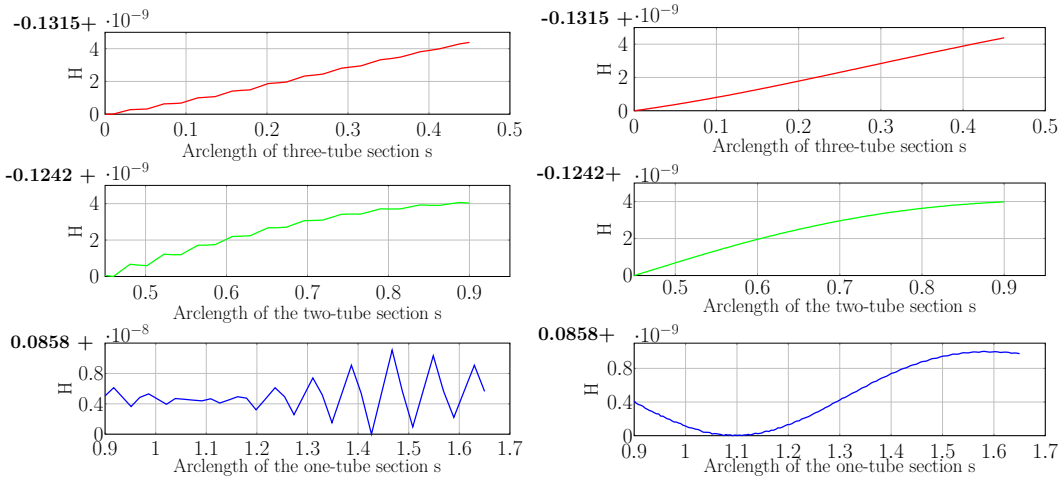

(c) NTST=10, NCOL=4

(d) NTST=40, NCOL=4

Fig. 7.20 The plot of Hamiltonian H along each section for different numerical parameters.

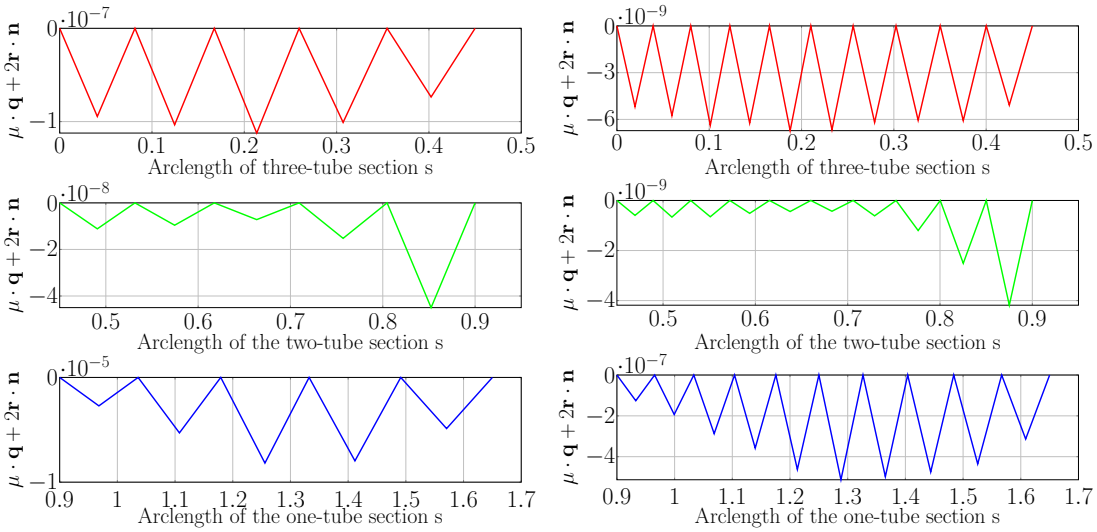

(a) NTST=5, NCOL=2 **(b)** NTST=10, NCOL=2

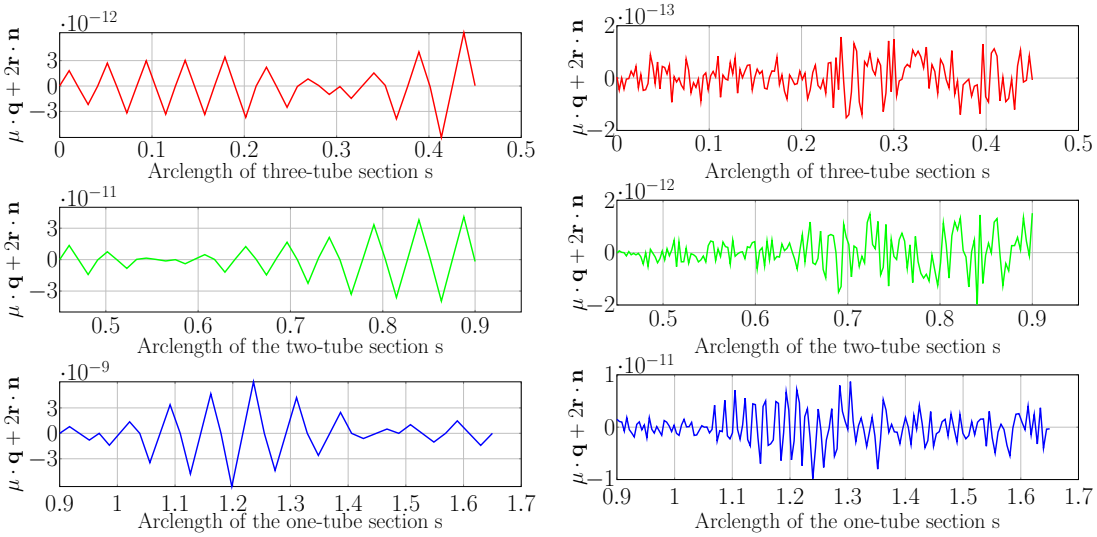

(c) NTST=10, NCOL=4 **(d)** NTST=40, NCOL=4

Fig. 7.21 The plot of $\boldsymbol{\mu} \cdot \mathbf{q} + 2\mathbf{r} \cdot \mathbf{n}$ along each section for different numerical parameters.

for NTST=40 and NCOL=4. Likewise, the values of the remaining quantities $\boldsymbol{\mu} \cdot \mathbf{q} + 2\mathbf{r} \cdot \mathbf{n}$ and $\mathbf{q} \cdot \mathbf{q} - 1$ remained close to zero, and their accuracy also improved with the decreasing stepsize or the increasing number of collocation points. For NTST=40 and NCOL=4, the accuracy of these quantities improved to even finer values of 10^{-13} – 10^{-11}. This improvement in accuracy with decreasing stepsize indirectly indicates the convergence of numerical solutions. If the solutions are converging, the numerical solution of the state approaches the actual state with decreasing stepsize, resulting in a more accurate evaluation of the conserved quantities.

Figures 7.20, 7.21 and 7.22 also point out that the order of accuracy varies between different sections of the CTCR. Higher accuracy is observed in the three-tube section, whereas lower accuracy is observed in the one-tube section for any discretization (NTST and NCOL). Furthermore, when comparing the results with those of the elastic rod problem in Figure 5.21 and Figure 5.22 (in Chapter 5), it is evident that higher accuracy is observed for smaller mesh sizes

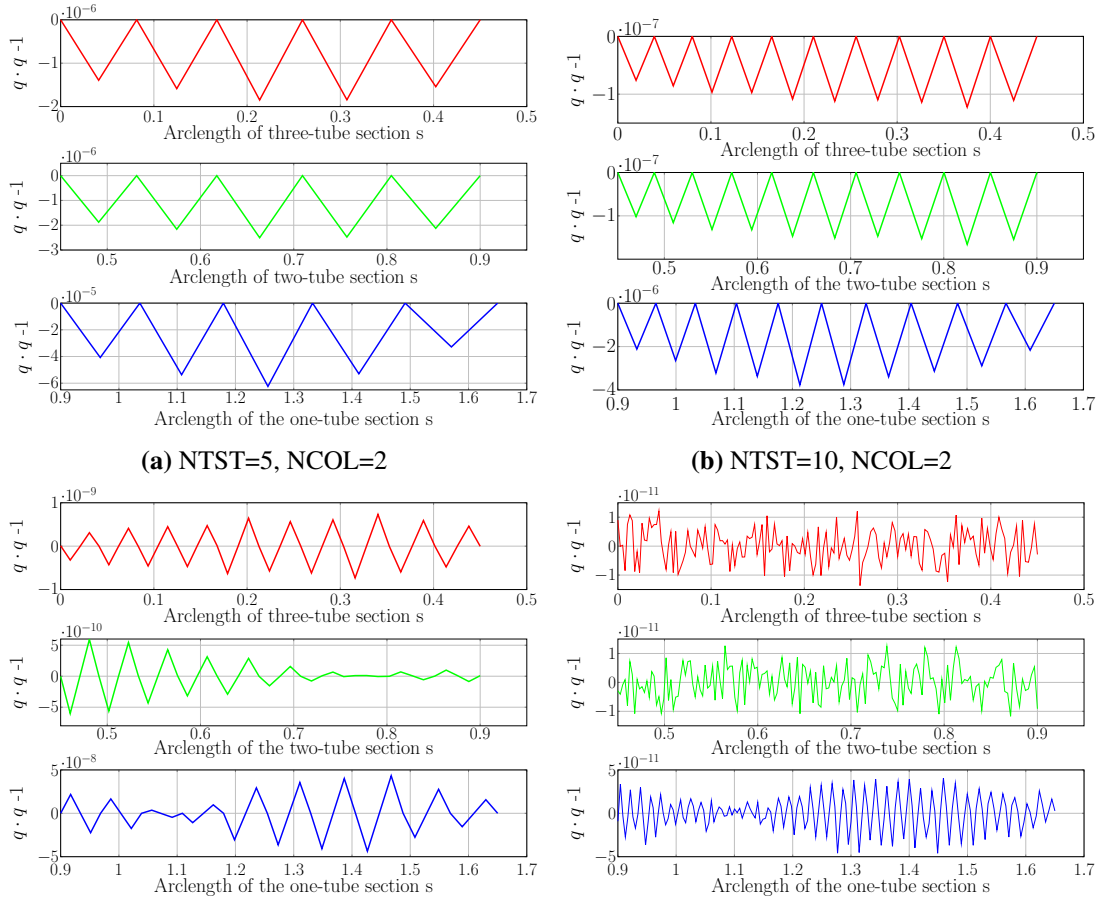

(a) NTST=5, NCOL=2

(b) NTST=10, NCOL=2

(c) NTST=10, NCOL=4

(d) NTST=40, NCOL=4

Fig. 7.22 The plot of the quantity $\mathbf{q}\cdot\mathbf{q}-1$ along each section for different numerical parameters.

and fewer collocation points for higher-dimensional CTCR problem. For example, an accuracy of order 10^{-9} is obtained for 40 mesh intervals and 4 collocation points (in Figure 5.22), while similar accuracy is obtained in the current CTCR case with only 10 mesh intervals and 4 collocation points(in Figure 7.20c). The *continuation* method of current 48-dimensional BVP with NTST mesh points and NCOL collocation points includes solving a $48\times(\text{NCOL}+1)\times\text{NTST}+1$-dimensional algebraic system using Newton iteration (section 4.2). In the case of elastic rods, this algebraic system is $14\times(\text{NCOL}+1)\times\text{NTST}+1$, which is nearly $1/4$ the size of the CTCR. Therefore, if the stopping criteria on the error usually given by the sum of the squares of the residuals, is the same for both cases, the elastic rod with 4 times the mesh intervals as that of CTCR would fetch comparable algebraic systems and yield results with the same order of accuracy. This finding suggests that using smaller mesh sizes and fewer collocation points can provide relatively accurate results for problems with larger dimensions, which saves computational time and storage.

7.4 Outlook

We have explored the hysteresis behavior exhibited by the tip-loaded CTCRs. The stability of the CTCR equilibria has been examined through computation of the *conjugate points* and

distinguished bifurcation diagrams. The effect of section lengths of CTCR on its hysteresis behavior has been examined using *bifurcation surfaces*. It is useful in designing tasks in which the robot maintains a constant total length while strategically adjusting its section lengths to either approach or evade the hysteresis region. The impact of the tip load and its direction have also been highlighted. This study is also instrumental in devising tasks that either evade or exploit snapping phenomena for more advantageous applications. The conserved quantities were employed to verify the accuracy and convergence of the numerical solutions.

Part III

Optimal Control of Concentric Tube Continuum Robots

CHAPTER 8

Optimal Control Problem

8.1 Introduction

Significant research has been conducted on employing the CTCRs in minimally invasive surgeries (Burgner et al., 2011; Burgner et al., 2013; Burgner-Kahrs et al., 2014; Swaney et al., 2014; Mitros et al., 2021). Suitable control strategies and accurate mechanical models are crucial for performing these surgical tasks with great accuracy and precision. The previous parts have focused on developing the mechanical model of CTCRs and analyzing the stability properties of the resulting equilibria. In this part of the thesis, we take a step further by deploying optimal control techniques to model the maneuvering task of these robots. We conceptualize robot navigation as an open-loop gradient-based optimization problem, leveraging the mechanical model established in the previous part.

In this chapter, we offer concise overviews of *optimal control problem*, Non-Linear programming (NLP), and a few NLP algorithms. These concepts are key for establishing the robot navigation setup. More comprehensive details can be found in the standard textbooks Nocedal and Wright (2006); Betts (2010); Bryson and Ho (2018).

Consider a system with a set of state variables $\mathbf{x} : t \to \mathbb{R}^n$, where time t is an independent parameter. A set of control variables $\mathbf{c} : t \to \mathbb{R}^m$ drives the system from a specified initial state $t = 0$ to a desired final state $t = t_F$. These state and control variables are governed by the system of first-order Ordinary Differential Equations (ODEs), referred to as *state* or *system* equations

$$\frac{d}{dt}\mathbf{x}(t) \equiv \dot{\mathbf{x}}(t) = f(\mathbf{x}(t), \mathbf{c}(t)), \tag{8.1}$$

with the initial conditions

$$\mathbf{x}(0) = \mathbf{x_o}. \tag{8.2}$$

The goal of *optimal control problem* is to find a suitable trajectory for the control variables $\mathbf{c}(t)$ that enhances the system's performance over the time interval $[0, t_F]$. This task is accomplished by expressing the performance in sets of objective functions and minimizing them. The objective function is often characterized by the state at the final time t_F (known as *Mayer term*)

$$\mathbf{M} = \phi\left(\mathbf{x}(t_F), t_F\right), \tag{8.3}$$

or, in terms of the state trajectory $\mathbf{x}(t)$ and control trajectory $\mathbf{c}(t)$ (known as *Lagrange term*)

$$\mathbf{L} = \int_0^{t_F} \Psi\left(\mathbf{x}(t), \mathbf{c}(t), t\right) dt, \tag{8.4}$$

where ϕ is the scalar function of the state $\mathbf{x}$ at final time t_F, and Ψ is the scalar function of the state $\mathbf{x}$ and control variables $\mathbf{c}$ at time t. In some problems, the final time t_F is specified; in other problems, it is a variable. We consider only the cases where the final time t_F is known.

The solution to this *optimal control problem* is approached by writing the augmented performance index by adjoining the *system dynamics* using the Lagrange multiplier $\mathbf{\Lambda} \in \mathbb{R}^n$ as

$$\bar{J} = \phi(\mathbf{x}(t_F), t_F) + \int_0^{t_F} \Psi\left(\mathbf{x}(t), \mathbf{c}(t)\right) + \mathbf{\Lambda} \cdot \left(f(\mathbf{x}(t), \mathbf{c}(t)) - \dot{\mathbf{x}}(t)\right) dt. \tag{8.5}$$

The Lagrange multiplier $\mathbf{\Lambda}$ is also referred to as *costates* or *adjoint variables* in *optimal control* terminology. The stationary point of this functional is obtained by imposing the condition that the first variation vanishes (i.e., $\delta\bar{J} = 0$). Consequently, the following necessary conditions for the stationary points (or extremum) are obtained:

$$\dot{\mathbf{x}}(t) = \mathcal{H}_\Lambda, \tag{8.6a}$$

$$\dot{\mathbf{\Lambda}}(t) = -\mathcal{H}_x, \tag{8.6b}$$

$$\mathcal{H}_c = 0, \tag{8.6c}$$

where $\mathcal{H}$ is the Hamiltonian function given by

$$\mathcal{H}(\mathbf{x}, \mathbf{\Lambda}, \mathbf{c}, t) = \Psi\left(\mathbf{x}(t), \mathbf{c}(t)\right) + \mathbf{\Lambda} \cdot f(\mathbf{x}(t), \mathbf{c}(t)). \tag{8.7}$$

The subscripts denote the partial derivative of $\mathcal{H}$ with respect to the argument. This Hamiltonian function is different from that one that appears in the calculus of variations problems (2.1). The first term (8.6a) is the same as the *system equations* (8.1). The second term (8.6b) gives the evolution of *costates*. The boundary conditions for the *costate* variables Λ are specified only at the final time t_F

$$\Lambda(t_F) = \left[\frac{\partial \phi}{\partial \mathbf{x}}\right]_{t=t_F}. \tag{8.8}$$

The last term (8.6c) is the *optimality* condition or *control equations*, which gives the algebraic equations for the control functions. It is a simplified version of *Pontyragin maximum principle*

$$\mathbf{c} = \arg_{v \in \mathcal{U}} \min \mathcal{H}.$$

where $\mathcal{U}$ defines the domain of feasible controls. The maximum principle (Bryson and Ho, 2018) states that the control variables $\mathbf{c}(t)$ must be chosen so that the Hamiltonian function $\mathcal{H}$ is minimized at every instant of time. The optimal trajectory $\mathbf{x}(t)$, $\mathbf{c}(t)$ corresponds to the extremum of $\mathcal{H}$. The two-point Boundary Value Problem (BVP) with boundary conditions (8.2),(8.8) and algebraic equations (8.6c), must be solved to obtain the optimal solutions.

In addition, the states $\mathbf{x}(t)$ and control variables $\mathbf{c}(t)$ are limited by the environment and design constraints, and they are subject to the inequality constraints like

$$\mathbf{x}_{min} \leq \mathbf{x}(t) \leq \mathbf{x}_{max},$$
$$\mathbf{c}_{min} \leq \mathbf{c}(t) \leq \mathbf{c}_{max},$$

and the path constraints

$$p_{min} \leq \mathbf{p}(\mathbf{x}(t), \mathbf{c}(t)) \leq p_{max}.$$

The majority of the *optimal control problems* are non-linear, and therefore, analytical solutions are not available. Consequently, numerical methods are employed to solve these problems using computers. Any numerical method utilizes some Newton-based iteration methods to solve for a finite set of unknown variables. However, the current optimization problem (8.5) is infinite-dimensional, which should be converted to finite-dimensional. Therefore, the computational techniques typically require a combining optimization method with discretization techniques. There are two approaches to carry out this task, namely *Indirect method*, and *Direct method*.

In the *Indirect method*, also referred to as *Optimize-then-Discretize* approach, the optimal solutions are characterized as a set of ODEs (8.6) with appropriate BCs (8.2),(8.8) as discussed previously in this section. The two-point BVP, along with the algebraic equations, is solved using techniques such as shooting methods (Betts, 2010). The time domain is discretized into time steps, and the solution is approximated as a piecewise polynomial over these steps. As a result, an algebraic system of equations is obtained, which is solved by a suitable Newton-iterative method. However, this method is applicable only when the objective functions are available analytically. It requires extra costate variables to be solved, increasing the dimension of the problem to be solved. Another drawback is the requirement of the initial guess for these costates and the frequent occurrence of discontinuities in the optimal control.

On the other hand, the *Direct Method* approach transforms the infinite-dimensional system (8.1) into a set of finite-dimensional algebraic constraints using a *collocation* scheme (Hargraves and Paris, 1987; Enright and Conway, 1992; Betts, 1998). The objective functions, which were the functions of continuous states $\mathbf{x}(t)$ and control variables $\mathbf{c}(t)$ are now functions of their discretized versions. Subsequently, we obtain an NLP problem, involving the minimization of a finite-dimensional discretized objective function, subject to constraints arising from finite-dimensional discretized state equations. This NLP is then solved for a finite set of variables. This method is also termed as *Discretize-then-Optimize* approach. We employ this strategy to model the robot navigation problem, which is elaborated on in the next chapter.

8.2 Direct Transcription and Collocation

Collocation is used to transcribe differential *system equations* (8.1) into a set of algebraic constraints. A comprehensive description of collocation has been already presented in the sec-

tion 4.2, and we will briefly recall it here. The time domain $[0, t_F]$ is meshed into N intervals:

$$0 = t_0 < t_1 < t_2 \ldots\ldots < t_N = t_F.$$

The state $\mathbf{x}(t)$ is approximated as a polynomial of a certain degree with certain points in each mesh interval $[t_k, t_{k+1}]$ (called *collocation* points), and the *system equations* (8.1) are imposed at these points. As a result, we have algebraic constraints at these points. The objective function, which is in the form of an integral, is numerically integrated over this mesh to obtain an algebraic objective function. A simple transcription technique involves using just one collocation point, typically located at the midpoint of the mesh interval. In this case, the objective function is numerically integrated through the Trapezoidal method. Higher order *Gauss- Lobatto methods* (Herman and Conway, 1996) can also be employed, and in this case, the numerical integration is determined by the sum of weights of the variables $\mathbf{x}(t)$ and $\mathbf{c}(t)$ at the collocation points.

8.3 The Non-Linear Programming Problem (NLP)

Essentially, all numerical methods for solving the optimization problem incorporate a sort of Newton method to solve for a finite set of unknowns. The previous section 8.2 already explained how an *optimal control problem* can be translated into a finite-dimensional NLP problem with state variable $\mathbf{X} \in \mathbb{R}^N$. Contrary to the *optimal control problem*, no dynamics are involved here, and the independent parameter t is no longer present. The current objective is to choose $\mathbf{X}$ to minimize the scalar objective function:

$$F(\mathbf{X}), \quad F : \mathbb{R}^N \to \mathbb{R},$$

subject to M equality constraints

$$\mathbf{C}(\mathbf{X}) = 0, \quad \mathbf{C} : \mathbb{R}^N \to \mathbb{R}^M,$$

where $M \leq N$. The Lagrangian of the problem is

$$L(\mathbf{X}, \mathbf{\Lambda}) = \mathbf{F}(\mathbf{X}) - \mathbf{\Lambda} \cdot \mathbf{C}(\mathbf{X}),$$

which is a scalar function of N variables and M Lagrange multipliers. The necessary condition for the point $(\mathbf{X}^*, \mathbf{\Lambda}^*)$ to be the minimizer of the constrained optimum is that it satisfies

$$\nabla_X L(\mathbf{X}, \mathbf{\Lambda}) = \mathbf{g}(\mathbf{X}) - \mathbf{\Lambda} \cdot \mathbf{G}(\mathbf{X}) = \mathbf{0}, \tag{8.10a}$$

$$\nabla_\Lambda L(\mathbf{X}, \mathbf{\Lambda}) = -\mathbf{C}(\mathbf{X}) = \mathbf{0}, \tag{8.10b}$$

where $\mathbf{g}(\mathbf{X})$ is the gradient of the objective function $F(\mathbf{X})$, and $\mathbf{G}(\mathbf{X})$ is the gradient of the equality constraint vector $\mathbf{C}(\mathbf{X})$. The system (8.10) is solved numerically using *Newton-*

Raphson method to determine $(\mathbf{X}^*, \mathbf{\Lambda}^*)$. Newton's step from the iterate is given by

$$\begin{bmatrix} \mathbf{X}^{(k+1)} \\ \mathbf{\Lambda}^{(k+1)} \end{bmatrix} = \begin{bmatrix} \mathbf{X}^{(k)} \\ \mathbf{\Lambda}^{(k)} \end{bmatrix} + \begin{bmatrix} \Delta\mathbf{X} \\ \Delta\mathbf{\Lambda} \end{bmatrix},$$

where $(\Delta\mathbf{X}, \Delta\mathbf{\Lambda})$ is the solution of *Newton-KKT system*

$$\begin{bmatrix} \nabla_{XX} L(\mathbf{X}^{(k)}, \mathbf{\Lambda}(k)) & \nabla_{X\Lambda} L(\mathbf{X}^{(k)}, \mathbf{\Lambda}^{(k)}) \\ \nabla_{\Lambda X} L(\mathbf{X}^{(k)}, \mathbf{\Lambda}^{(k)}) & \nabla_{\Lambda\Lambda} L(\mathbf{X}^{(k)}, \mathbf{\Lambda}^{(k)}) \end{bmatrix} \begin{bmatrix} \Delta\mathbf{X} \\ \Delta\mathbf{\Lambda} \end{bmatrix} = \begin{bmatrix} \mathbf{g}(\mathbf{X}^{(k)}) - \mathbf{\Lambda}^{(k)} \cdot \mathbf{G}(\mathbf{X}^{(k)}) \\ -\mathbf{C}(\mathbf{X}^{(k)}) \end{bmatrix},$$

$$\Longrightarrow$$

$$\begin{bmatrix} \nabla_{XX} L(\mathbf{X}^{(k)}, \mathbf{\Lambda}^{(k)}) & -\mathbf{G}^T(\mathbf{X}^{(k)}) \\ \mathbf{G}(\mathbf{X}^{(k)}) & \mathbf{0} \end{bmatrix} \begin{bmatrix} \Delta\mathbf{X} \\ \Delta\mathbf{\Lambda} \end{bmatrix} = \begin{bmatrix} \mathbf{g}(\mathbf{X}^{(k)}) - \mathbf{\Lambda}^{(k)} \cdot \mathbf{G}(\mathbf{X}^{(k)}) \\ -\mathbf{C}(\mathbf{X}^{(k)}) \end{bmatrix}.$$

This last expression is referred to as the *Kurush-Kuhn-Tucker* (KKT) system which is rewritten as

$$\begin{bmatrix} \mathbf{H}_L(\mathbf{X}^{(k)}) & -\mathbf{G}^T(\mathbf{X}^{(k)}) \\ \mathbf{G}(\mathbf{X}^{(k)}) & \mathbf{0} \end{bmatrix} \begin{bmatrix} \Delta\mathbf{X} \\ \Delta\mathbf{\Lambda} \end{bmatrix} = \begin{bmatrix} \mathbf{g}(\mathbf{X}^{(k)}) - \mathbf{\Lambda}^{(k)} \cdot \boldsymbol{G}(\mathbf{X}^{(k)}) \\ -\mathbf{C}(\mathbf{X}^{(k)}). \end{bmatrix}. \tag{8.11}$$

Here, $\mathbf{H}_L$ is the Hessian of the Lagrangian

$$\mathbf{H}_L(X) = \nabla_X^2 F - \sum_{i=1}^{M} \Lambda_i \nabla_X^2 C_i.$$

The KKT matrix (8.11) must be non-singular to yield a successful iterate.

The given NLP problem can be generalized to the cases where inequality constraints are imposed; the M inequality constraints are of the form

$$\mathbf{C}(\mathbf{X}) \geq \mathbf{0}.$$

At the optimal point $\mathbf{X}^*$, the constraints are of two types. The constraints that are strictly satisfied, i.e., $C_i(\mathbf{X}^*) > 0, i \in \mathcal{I}$, are called inactive constraints. The constraints that are on the bounds, i.e., $C_i(\mathbf{X}^*) = 0, i \in \mathcal{E}$, are called active constraints. At the optimal solution, the Lagrange multipliers associated with active constraint must satisfy

$$\Lambda_i \geq 0.$$

The series of equality-constrained sub-problems are solved with an estimated guess of active constraints. If the active constraint is correct, the solution to the equality-constrained problem is also the solution to the inequality-constrained problem. Otherwise, the solution procedure is repeated after making another guess of estimated active constraints.

If the active set of constraints is known, then the problem is solved as an equality-constrained optimization problem, ignoring the inactive constraints. However, detecting the active set of

constraints is not easy and requires the repeated solution of the KKT system with the addition and removal of constraints.

In summary, the general NLP problem requires finding $\mathbf{X} \in \mathbb{R}^N$ to minimize

$$F(\mathbf{X}),$$

subject to the m constraints

$$C_{L,i} \leq C_i(\mathbf{X}) \leq C_{U,i}, \quad i = 1, \dots M,$$

and bounds

$$X_{L,i} \leq X_i \leq X_{U,i}, , \quad i = 1, \dots N.$$

Here the subscript i is the component of each vector. In this formulation, the equality constraints are imposed by setting $C_{L,L} = C_{U,j}$.

8.4 NLP Algorithms

In general, various methods are available for solving the NLP problems. Here, we discuss the two most commonly used traditional algorithms: *Sequential Quadratic Programming*(SQP) method and *Interior-points method*. The fundamental idea underlying these algorithms is presented here. The modern methods have more additional complexities (Nocedal and Wright, 2006).

8.4.1 Sequential Quadratic Programming

Sequential Quadratic Programming (Boggs and Tolle, 1995) is one of the most powerful algorithms for solving smooth, constrained, non-linear optimization problems. It is not a single algorithm but a conceptual method that forms the basis of many modern optimization algorithms. As discussed in the section (8.3), solving an NLP problem requires finding a search direction $\Delta\mathbf{X}$ in each Newton's iteration. Alternatively, each Newton's iteration step at $(\mathbf{X}^{(k)}, \Lambda^{(k)})$ can be interpreted as finding the minimum of

$$F(\mathbf{X}^{(k)}) + \frac{1}{2}\Delta\mathbf{X}^T\mathbf{H}_k\Delta\mathbf{X} + \mathbf{g}_k^T\Delta\mathbf{X}, \tag{8.12}$$

subject to the linearized constraints

$$\mathbf{G}_k\Delta X = -\mathbf{C}_k, \tag{8.13}$$

where $\mathbf{g}_k = \nabla_X F(\mathbf{X}^{(k)})$ and $\mathbf{G}_k = \nabla_X \mathbf{C}(\mathbf{X}^{(k)})$. This problem (8.12) is also referred to as a *quadratic programming* (QP) subproblem. If the matrix $\mathbf{G}_k$ is invertible, and the matrix $\mathbf{H_k}$ is

positive definite, the QP subproblem has a unique solution $(\Delta\mathbf{X}, \mathbf{l}^{(k)})$ that satisfies

$$\mathbf{H}_k\Delta\mathbf{X} + \mathbf{g}_k - \mathbf{G}_k^T\mathbf{l}^{(k)} = \mathbf{0}, \tag{8.14a}$$

$$\mathbf{G}_k\Delta\mathbf{X} + \mathbf{C}_k = \mathbf{0}. \tag{8.14b}$$

On comparing this expression with the KKT system (8.11), we find that $\mathbf{l}^{(k)} = \mathbf{\Lambda}^{(k+1)}$. If we subtract the $\mathbf{\Lambda}^{(k)} \cdot \mathbf{G}$ from both sides of the *Newton-KKT iteration* (8.11), we obtain

$$\begin{bmatrix} \mathbf{H}_k & -\mathbf{G}_k^T \\ \mathbf{G}_k & \mathbf{0} \end{bmatrix} \begin{bmatrix} \Delta\mathbf{X} \\ \mathbf{\Lambda}^{k+1} \end{bmatrix} = \begin{bmatrix} -\mathbf{g}_k \\ -\mathbf{C}_k \end{bmatrix}. \tag{8.15}$$

Therefore, the new iterate $(\mathbf{X}^k + \Delta\mathbf{X}, \mathbf{\Lambda}^{(k+1)})$ is the solution of the *quadratic programming* problem (8.12). The SQP methods solve a sequence of these QP sub-problems. The inclusion of inequality constraint in SQP is complicated and a rough sketch of the approach is presented here. The inequality constraints can also be considered in this SQP algorithm by formulating it as

$$\text{minimize } F(\mathbf{X}^{(k)}) + \frac{1}{2}\Delta\mathbf{X}^T\mathbf{H}_k\Delta\mathbf{X} + \mathbf{g}_k^T\Delta\mathbf{X}, \tag{8.16}$$

subject to the linearized constraints

$$\nabla C_i(\mathbf{X})\Delta\mathbf{X}^{k+1} + C_i(\mathbf{X}^{k+1}) = 0, \qquad i \in \mathcal{E}, \tag{8.17a}$$

$$\nabla C_i(\mathbf{X})\Delta\mathbf{X}^{k+1} + C_i(\mathbf{X}^{k+1}) \geq 0, \qquad i \in \mathcal{I}. \tag{8.17b}$$

The solution of this QP problem also gives an estimate of the set of Lagrange multipliers and active constraints. This active set at the solution of (8.16),(8.17) constitutes our guess at the solution of the nonlinear program. The SQP method should accurately identify this guess that does not alter at subsequent iterations, leading to an equality-constrained optimization behavior.

8.4.2 Interior Point Method

Interior Point Methods, also called *Barrier methods* are another powerful technique for solving large-scale optimization problems which are linear, non-linear convex, or non-convex (Potra and Wright, 2000). We begin by recalling the NLP problem that is rewritten as

$$\text{minimize } F(\mathbf{X}), \tag{8.18}$$

subject to

$$C_E(\mathbf{X}) = 0, \tag{8.19a}$$

$$C_I(\mathbf{X}) - s = 0, \tag{8.19b}$$

$$s \geq 0. \tag{8.19c}$$

The inequalities are transformed into equality using a vector s of slack variables. There are two types of methods in this *interior-point* approach, namely, *Continuation method* and *Barrier*

method. In the former approach, the KKT conditions for the NLP problem are written as

$$\nabla_X F(\mathbf{X}) - \mathbf{G}_E^T y - \mathbf{G}_I^T z = 0, \tag{8.20a}$$
$$SZ - \mu e = 0, \tag{8.20b}$$
$$\mathbf{C}_E(X) = 0, \tag{8.20c}$$
$$\mathbf{C}_I(X) - s = 0, \tag{8.20d}$$

together with $s \geq 0$ and $z \geq 0$. Here, $\mathbf{G}_E$ and $\mathbf{G}_I$ are the jacobian matrices of the functions $\mathbf{C}_E$ and $\mathbf{C}_I$ respectively, and y and z are the associated Lagrange multipliers. The matrices S and Z are diagonal matrices whose diagonal entries are s and z respectively, and e is the vector of ones $[1, \ldots, 1]^T$. This system is solved for a sequence of positive $\{\mu_k\}$ that converges to zero, while maintaining $s, z > 0$. The Newton-iteration step for this system of equations is

$$\begin{pmatrix} \nabla^2_{XX} L & 0 & -\mathbf{G}_E & -\mathbf{G}_I \\ 0 & Z & 0 & S \\ \mathbf{G}_E & 0 & 0 & 0 \\ \mathbf{G}_I & -\mathbf{I} & 0 & 0 \end{pmatrix} \begin{pmatrix} \Delta\mathbf{X} \\ \Delta s \\ \Delta y \\ \Delta z \end{pmatrix} = - \begin{pmatrix} \nabla_X F(\mathbf{X}) - \mathbf{G}_E(\mathbf{X}) \cdot y - \mathbf{G}_I(\mathbf{X}) \cdot z \\ SZ - \mu e \\ \mathbf{C}_E(\mathbf{X}) \\ \mathbf{C}_I(\mathbf{X}) - s \end{pmatrix}, \tag{8.21}$$

where L is the Lagrangian associated with (8.18), (8.19a):

$$L = F(\mathbf{X}) - y \cdot C_E(\mathbf{X}) - z \cdot (C_I(\mathbf{X}) - s).$$

This system is called the *primal-dual system*. After determining the vector $(\Delta\mathbf{X}, \Delta s, \Delta y, \Delta z)$, the new iterate is evaluated as

$$\begin{aligned} \mathbf{X}^{(k+1)} &= \mathbf{X}^{(k)} + p_s^{max} \Delta\mathbf{X}, \quad \mathbf{s}^{(k+1)} = \mathbf{s}^{(k)} + p_s^{max} \Delta s, \\ \mathbf{y}^{(k+1)} &= \mathbf{y}^{(k)} + p_z^{max} \Delta y, \quad \mathbf{z}^{(k+1)} = \mathbf{z}^{(k)} + p_z^{max} \Delta z, \end{aligned} \tag{8.22}$$

where

$$p_s^{max} = max \left\{ p \in [0,1] : s + p\Delta s \geq (1-\tau)s \right\}, \tag{8.23a}$$
$$p_z^{max} = max \left\{ p \in [0,1] : z + p\Delta z \geq (1-\tau)z \right\}, \tag{8.23b}$$

with $\tau \in [0,1]$. This condition (8.23), referred to as *fraction to the boundary rule* prevents the variables s and z from approaching their lower bound zero quickly. This process is repeated at each new iterate until convergence.

The second approach of *interior-point* methods corresponding to the minimization problem (8.18),(8.19a) constitutes the barrier problem

$$\begin{aligned} \text{minimize} \quad & F(\mathbf{X}) - \mu \sum_{i=1}^{m} \log s_i, \\ \text{subject to} \quad & \mathbf{C}_E(\mathbf{X}) = 0, \quad \mathbf{C}_I(\mathbf{X}) - s = 0, \end{aligned} \tag{8.24}$$

where μ is a positive parameter, and $\log(.)$ is a natural logarithm function. The minimization

of the barrier function prevents components of s from getting too close to zero. This is because $-\log t \to \infty$ as $t \to 0$. This barrier approach consists of finding solutions to (8.24) for a sequence of positive $\{\mu_k\}$ that converges to zero. Then the corresponding KKT conditions are

$$\nabla_X F(\mathbf{X}) - \mathbf{G}_E^T y - \mathbf{G}_I^T z = 0, \tag{8.25a}$$

$$-\mu S^{-1} e + z = 0, \tag{8.25b}$$

$$\mathbf{C}_E(X) = 0, \tag{8.25c}$$

$$\mathbf{C}_I(X) - s = 0. \tag{8.25d}$$

These conditions differ from the continuation method only in the second term. Multiplying (8.25b) with S gives the same KKT system as that of the previous one (8.20), and an identical iterative approach (8.22),(8.23) can be implemented to yield solutions.

8.5 Multi-Objective Optimization or Pareto Optimization

A Multi-Objective optimization problem (Marler and Arora, 2004) is an objective problem consisting of more than one objective function and is mathematically formulated as

$$\text{minimize}\,[f_1(\mathbf{X}), f_2(\mathbf{X}), \ldots, f_k(\mathbf{X})]\,,$$

subject to

$$g_j(\mathbf{X}) \le 0, \qquad j = 1, 2, \ldots, m,$$
$$h_i(\mathbf{X}) = 0, \qquad l = 1, 2, 3, \ldots, e,$$

where k is the number of objective functions, m is the number of inequality constraints and e is the number of equality constraints. We often encounter problems consisting of objective functions with competing effects. There is no single solution to these problems, and it helps to model the decision-maker's preferences. A solution is called non-dominating if none of the objectives can be further optimized without degrading the other objective functions. For instance, we may reach a situation where an objective's value can be optimized only after devaluing other objectives. These solutions are called *Pareto optimal solutions*. The boundary defined by all these optimal solutions is termed as *Pareto optimal front*. In short, the goal of Multi-Objective Optimization is to find solutions as close as possible to the *Pareto-optimal front*. There are various methods to accomplish this namely, *weighted sum method*, ϵ*-Constraint method*, *Weighted Metric method*, and non-traditional methods like *Genetic Algorithms*. In the present work, we do not perform any multi-objective optimization. We have multiple objectives in our system, and we study its behavior when different weights are given to these objectives. It will be helpful for the decision-maker to plan strategies (Ehrgott, 2005) on varying these weights to yield a more optimal solution.

CHAPTER 9

Optimal Control Problem for CTCRs

This chapter presents some robot maneuvering tasks cast as *optimal control problems*. The robot navigation is modeled as an optimization problem by quantifying it in terms of performance metrics. Several objective functions are designed according to the tasks, offering comprehensive explanations. Additionally, we outline the numerical solution strategy to solve the resultant optimization problem. Some portion of this work is already presented (Dhanakoti et al., 2022)

9.1 N-tube Robot

We recall the mechanical model of the CTCR from Chapter 6. The Hamiltonian system of an N-tube CTCR governing their equilibrium configurations is given by

$$
\begin{aligned}
\mathbf{r}' &= \mathbf{d}_3, && \text{in }]0, l_1[, && (9.1a)\\
\mathbf{n}' &= \mathbf{0}, && \text{in }]0, l_1[, && (9.1b)\\
\mathbf{q}' &== \sum_{j=1}^{3} \left(\mathbf{K}_{\mathbf{eff}}^{-\mathbf{1}}{}_{jj} m_j + \tilde{u}_j\right) \frac{1}{2}\mathbf{B}_j \mathbf{q}, && \text{in }]0, l_1[, && (9.1c)\\
\boldsymbol{\mu}' &= \sum_{j=1}^{3} \left(\mathbf{K}_{\mathbf{eff}}^{-\mathbf{1}}{}_{jj} m_j + \tilde{u}_j\right) \frac{1}{2}\mathbf{B}_j \boldsymbol{\mu} - \left[\frac{\partial}{\partial \mathbf{q}} \mathbf{d}_3(\mathbf{q})\right]^T \mathbf{n}, && \text{in }]0, l_1[, && (9.1d)\\
\alpha^{[i]\prime} &= \frac{\sum_{j=2}^{N} \beta^{[j]}}{K_{33}^{[1]}} - \frac{m_3}{K_{33}^{[1]}} + \frac{\beta^{[i]}}{K_{33}^{[i]}} + \hat{u}_3^{[i]} - \hat{u}_3^{[1]}, \qquad i = 2, 3, \ldots, N. && \text{in }]0, l_i[, && (9.1e)\\
\beta^{[i]\prime} &= \frac{K_{11}^{[i]} \hat{u}_1^{[i]}}{\sum_{j=1}^{k} K_{11}^{[j]}} \Bigg(\sum_{j=1}^{N} K_{11}^{[j]} \hat{u}_1^{[j]} \sin\left(\alpha^{[i]} - \alpha^{[j]}\right) \\
&\quad + m_1 \hat{u}_1^{[i]} \sin \alpha^{[i]} - m_2 \hat{u}_1^{[i]} \cos \alpha^{[i]} \Bigg), \qquad i = 2, 3, \ldots, N. && \text{in }]0, l_i[, && (9.1f)
\end{aligned}
$$

This first-order system is solved to obtain the backbone structure of the robot using the following boundary conditions

$$
\begin{aligned}
&\mathbf{r}(0) = [0, 0, 0]^T, \qquad \mathbf{q}(0) = \left[0, 0, \sin\frac{\theta_1}{2}, \cos\frac{\theta_1}{2}\right]^T, \\
&\mathbf{n}(l_1) + \mathbf{F} = \mathbf{0}, \qquad m_i(l_1) + (\Upsilon(\mathbf{q}(l_1)) \times \mathbf{F}) \cdot \mathbf{d}_i = \mathbf{0}, \quad i = 1, 2, 3. \\
&\alpha^{[i]}(0) = \left(\alpha_o^{[i]}\right), \qquad \boldsymbol{\beta}^{[i]}(l_i) = 0, \qquad i = 2, 3, \ldots N.
\end{aligned}
\tag{9.2}
$$

By solving the resultant (BVP) (9.1),(9.2), the equilibrium configuration of the robot, i.e., its states $\mathbf{r}(\mathbf{y}; s)$ and $\mathbf{q}(\mathbf{y}; s)$ are obtained as a function of control parameter vector $\mathbf{y}$ which is defined as

$$\mathbf{y} := [L_1, \ldots, L_N, \theta_1, \ldots, \theta_N] \in \mathbb{R}^{2N}.$$

Here, $\theta_i = \theta_1 + \alpha_o^{[i]}, i = 2, \ldots, N$ is the angle of rotation of the i-th tube at the base $s = 0$. As a result, a CTCR with N tubes has $2N$ control parameters determining its spatial configuration.

9.2 System Kinematics in Pseudo-time

We describe the robot's motion in space as a function of time. The tubes are considered sufficiently stiff, and inertial effects are negligible. Hence, we assume a quasi-static model, as the speed with which the robot moves is irrelevant. The motion is parameterized over time like *pseudo-time* parameter $t \in T := [0, 1]$. Then, the control parameters $\mathbf{y}$ at time t are written as function $\mathbf{y}(t)$. In addition, a control rate vector $\mathbf{w}(t) = [w_1(t), \ldots, w_N(t), \beta_1(t), \ldots, \beta_N(t)]$ is introduced to characterize the *system equations* or *system dynamics* defined as

$$\dot{\mathbf{y}}(t) = \mathbf{w}(t), \quad \mathbf{y}(0) = \mathbf{y_o}, \tag{9.3}$$

where $\mathbf{y_o}$ is the vector of control parameters at initial time $t = 0$. The rates $w_i : T \to \mathbb{R}$ and $\beta_i : T \to \mathbb{R}, i = 1, \ldots, N$ model the traverse and rotational velocities of each tube, respectively. The system dynamics (9.3) ensures the continuity of control parameters on the entire time interval T. The control parameters corresponding to the rotation of the tubes $\theta_i, i = 1, \ldots, N$ can assume any real value (being 2π-periodic), whereas the feed parameters $L_i, i = 1, \ldots, N$ can take only non-negative values and are bounded by the maximum length of the tubes $L_{i,\max}$ resulting in the inequality constraint,

$$0 \leq L_i(t) \leq L_{i,\max} \quad \forall t \quad i = 1, \ldots, N. \tag{9.4}$$

The presence of hysteresis regions in these robots (as described in Chapter 7) is not desirable during their operations. These situations can be mitigated by using the tubes below a critical length L_{crit}. These values are found by carrying out the numerical experiments as carried out in Chapter 7 for the given tip load.

9.3 Objective Functions

We quantify robot navigation as an objective function that must be minimized. Here, we consider a few prototypical objectives that describe simple tasks. The primary goal of many robot tasks is to guide it in such a way that its tip reaches a desired location $\mathbf{r_{tar}} \in \mathbb{R}^3$ and orientation $\mathbf{q_{tar}} \in \mathbb{R}^4$ at the final time $t = 1$. However, it may not always be feasible to attain a configuration simultaneously satisfying the position and orientation requirements, especially with a small number of tubes, say, $N \leq 3$. As a result, the required criterion is incorporated by prioritizing the actions using a weighting term $\bar{\lambda}$. It is included as a *Mayer term* (8.3) in the *optimal control*

problem as

$$M_1(\mathbf{y};\bar{\lambda}) := |\mathbf{r}(\mathbf{y}(1),l_1) - \mathbf{r_{tar}}|^2 + \bar{\lambda}|\mathbf{q}(\mathbf{y}(1),l_1) - \mathbf{q_{tar}}|^2, \tag{9.5}$$

where $\bar{\lambda}$ is the weighing term useful for prioritizing between tip position and orientation, and $|\cdot|$ is the Euclidean norm. The robot state $\mathbf{r}(\mathbf{y}(t);s,t), \mathbf{q}(\mathbf{y}(t);s,t)$ is obtained after solving the BVP (9.1)–(9.2) with control parameters $\mathbf{y}(t)$ and specified tip load $\mathbf{F}$. Alternatively, reaching the target position and orientation could be specified as equality constraints. However, due to the limited attainable combinations of position and orientation, this strategy would render the optimization task infeasible. Therefore, an appealing strategy is to relax this constraint and include a penalty term in the objective function to account for deviations from the desired position and orientation.

An alternative approach is to utilize only the desired tangent of the tip, i.e., $\mathbf{d}_3(\mathbf{y}(1),l_1)$, instead of the entire orientation $(\mathbf{q}(\mathbf{y}(1),l_1))$ in the objective function. This relaxed version imposes condition only on a single tangential director-axis $\mathbf{d}_3$ instead of all three directors $\mathbf{d}_k, (k = 1,2,3)$ allowing for rotations around the tangent of the robot tip. This task is formulated as maximizing the scalar product of the director and a specified target direction, i.e., $\mathbf{d}_3(\mathbf{y}(1),l_1)\cdot\mathbf{n_{tar}}$. Instead, this task can also be accomplished by minimizing the norm $|\mathbf{d}_3(\mathbf{y}(1),l_1) - \mathbf{n_{tar}}|^2$. Both of these approaches have an equivalent effect, and we choose the former approach due to the relatively simpler implementation of the dot product. Then, the objective function is of the form:

$$M_1(\mathbf{y},\bar{\lambda}) := |\mathbf{r}(\mathbf{y}(1),l_1) - \mathbf{r_{tar}}|^2 - \bar{\lambda}\mathbf{d}_3(\mathbf{y}(1),l_1)\cdot\mathbf{n_{tar}}. \tag{9.6}$$

Path tracing: Certain applications may require the robot to maneuver such that its tip follows a prescribed curve $\mathbf{r_{path}}(t)$ and orientation $\mathbf{n_{path}}(t)$. These problems are addressed by including a *Lagrange term* (8.4) in the objective function:

$$J_1(\mathbf{y},\bar{\lambda}) := \int_0^1 \left(|\mathbf{r}(\mathbf{y}(t),t) - \mathbf{r_{path}}(t)|^2 - \bar{\lambda}\mathbf{d}_3(\mathbf{y}(t),l_1)\cdot\mathbf{n_{path}}(t)\right) dt. \tag{9.7}$$

This operation can also be realized by constraining the deviation from the prescribed path curve.

$$|\mathbf{r}(\mathbf{y}(t),t) - \mathbf{r_{path}}(t)|^2 < tol_r, \qquad (\mathbf{y}(t),l_1)\cdot\mathbf{n_{path}}(t) < tol_o. \tag{9.8}$$

As already mentioned, many configurations of the robot that satisfy the given constraint requirement are not feasible and attainable, and the optimization may fail if tol_r is set too small. Moreover, this approach requires an initial solution that fulfills all the constraints, and providing such a solution may not always be feasible in practice. A flexible optimization approach can be utilized by using the combination of both approaches where we minimize the objective function satisfying the constraints on other functions.

Covered volume: Another key factor to take into account is the robot's working volume, i.e., the space traversed by its backbone while executing a job. Minimizing the working volume is

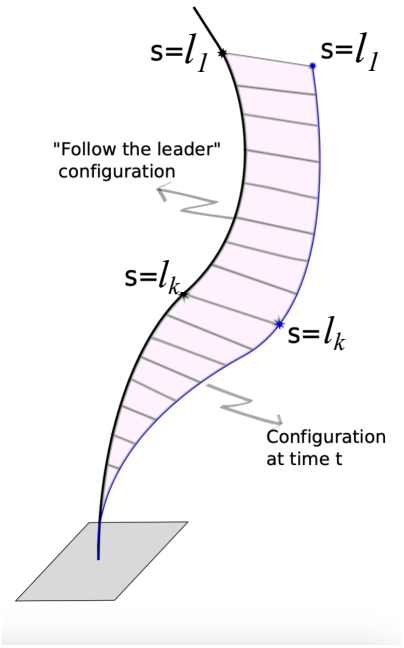

Fig. 9.1 Schematic showing the Deviation from the FTL configuration

particularly beneficial when operating in confined or constrained spaces. The working volume may be quantified in a variety of ways. One potential method is the accumulated deviation from the reference *Follow the Leader* (FTL) configuration, denoted as $\mathbf{r}(\mathbf{y}_{\mathrm{FTL}}, s)$. The CTCRs can be deployed in an FTL strategy where the tubes are sequentially extended such that the body of the robot traces its tip (Gilbert et al., 2015; Garriga-Casanovas and Rodriguez y Baena, 2018). Ideally, this strategy occupies the minimum working volume. However, this strategy can be employed only for deploying or removing the CTCR during the initial or final stages of a task as the robot deviates from the reference curve when its tip navigates to adjacent locations. The operational space is defined as the volume within which the robot's tip is required to move. After the robot is initially deployed using the FTL strategy, it initiates operations by moving to the nearby locations within the operation space. The robot should perform tasks centered around the initial FTL configuration with minimum deviation from it. We take the $\mathbf{r}(\mathbf{y}_{\mathrm{FTL}}, s)$ configuration as a reference curve and measure the robot's deviation from this configuration, providing a rough estimate of the working volume. The smaller the deviation from the reference is, the less likely the interference with neighbouring objects such as tissues. The associated objective is

$$J_2(\mathbf{y}) := \int_{t=0}^{1} \int_{s=0}^{l_1(t)} d\big(\mathbf{r}(\mathbf{y}_{\mathrm{FTL}}, s), \mathbf{r}(\mathbf{y}(t), s)\big)\, ds\, dt, \tag{9.9}$$

where $d(\hat{\mathbf{r}}, \mathbf{r}(s)$ is the distance of $\mathbf{r}(s))$ from the reference configuration $\hat{\mathbf{r}}$. It is defined as the distance to the arc length projection

$$d(\hat{\mathbf{r}}, \mathbf{r}(s)) = |\hat{\mathbf{r}}(s') - \mathbf{r}(s)| \quad \text{with} \quad \int_{\sigma=0}^{s'} \hat{\mathbf{r}}'(\sigma)\, d\sigma = s. \tag{9.10}$$

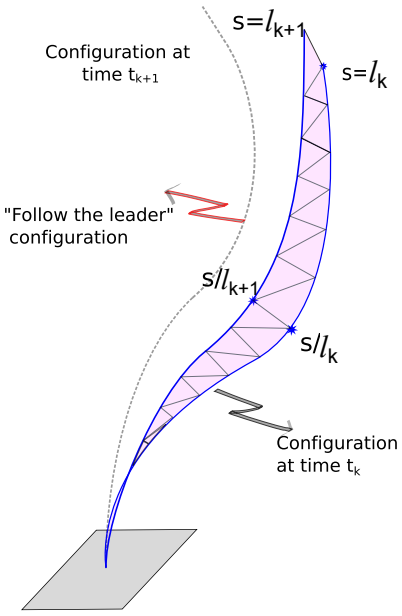

Fig. 9.2 Schematic showing the swept area by the CTCR.

Note that in the FTL configuration, the innermost tube can be assumed to have an infinite length, such that the FTL arc length always exceeds s, and the projection (9.10) is well-defined.

An alternative way to quantify the working volume of the robot is to consider the region swept by the robot's backbone during navigation (shown in Figure 9.2). The area swept by points on the CTCR corresponding to the normalized arc length (s/l_k) is considered as swept area and is mathematically given by

$$J_2(\mathbf{y}) := \int_{t=0}^{1} \int_{s=0}^{\Sigma L_i(t)} \mathbf{r}'(s,t) \times \frac{\partial}{\partial t}\mathbf{r}'(s,t)\, ds\, dt. \tag{9.11}$$

Unlike the prior case, where navigation is centered around the FTL reference curve, there is no preferred center for the working region here.

Regularization: In addition, the square of the L_2-norm of the $\mathbf{w}(t)$ vector is included as a regularization term in the objective function to avoid high-frequent instabilities,

$$J_3(\mathbf{w}) := \int_{t=0}^{1} |\mathbf{w}(t)|^2\, dt.$$

Furthermore, the solution can be further restricted by path constraints of the form

$$\mathbf{g_l} \leq \mathbf{g}(\mathbf{Y}, t) \leq \mathbf{g_u}, \tag{9.12}$$

where $\mathbf{g} \in \mathbb{R}^g$ is an objective function in terms robot's state and control parameters. For instance, imposing constraints on the robot tip orientation during a task, as illustrated in (9.8), exemplifies one such scenario.

In total, we define the overall objective as a linear combination of the individual contribu-

tions discussed above,

$$J(\mathbf{y}, \mathbf{w}) = \bar{\lambda}_0 M_1(\mathbf{y}, \bar{\lambda}) + \bar{\lambda}_1 J_1(\mathbf{y}, \bar{\lambda}) + \bar{\lambda}_2 J_2(\mathbf{y}) + \bar{\lambda}_3 J_3(\mathbf{w}).$$

Depending on the application, certain objective terms can be more important than others and may be emphasized by a corresponding selection of the weights $\bar{\lambda}_i$ $(i = 0, 1, 2, 3)$. In the end, we formulate the *optimal control problem* as

$$\min_{\mathbf{y} \in H^1(T), \mathbf{w} \in L^2(T)} J(\mathbf{y}, \mathbf{w}), \tag{9.13}$$

subject to equality constraints (9.3) and inequality constraints (9.4) and (9.12).

9.4 Discretization

The *direct method* approach is employed to numerically solve the current CTCR navigation problem. We discretize the *optimal control problem* (9.13) in pseudo-time t and arc length s and transform it into an NLP problem (section 8.3) to be solved (Nocedal and Wright, 2006; Betts, 2010). We divide the time interval $[0, 1]$ into m sub-intervals at time points $0 = t_0 < t_1 \cdots < t_m = 1$, in the simplest case with equidistant steps of length $t_{i+1} - t_i = \frac{1}{m}$. The objective function is then approximated on these time intervals using the trapezoidal rule as

$$J_m = \bar{\lambda}_0 M_1 + \frac{1}{m} \left(\frac{1}{2} \bar{j}(0) + \sum_{i=1}^{m-1} \bar{j}(t_i) + \frac{1}{2} \bar{j}(1) \right),$$

where $\bar{j}(t) = \bar{\lambda}_1 J_1 + \bar{\lambda}_2 J_2 + \bar{\lambda}_3 J_3$. The state $\mathbf{r}(s), \mathbf{q}(s)$ of the robot is obtained for the controls $\mathbf{y}(t_k)$ at the time points t_k by discretizing and solving the BVP problem (9.1) using suitable collocation methods Kierzenka and Shampine (2001, 2008), thereby converting the infinite-dimensional problem to a finite-dimensional algebraic system. From the robot state, the objective functions $j(t_k)$ are evaluated, where the integrals along the robot's length arising in (9.9) are approximated again using the trapezoidal rule. The ODEs (9.3) in the system dynamics are approximated using central differences as

$$\frac{\mathbf{y}_i(t_{k+1}) - \mathbf{y}_i(t_k)}{t_{k+1} - t_k} = \mathbf{w}_i(t_{k+1/2}),$$

for $i = 0, \ldots, m-1$ in terms of the pseudo-velocities $\mathbf{w}_i(t_{k+1/2})$.

The direct discretization results in a nonlinear program with $4Nm$ variables and $2Nm$ equality constraints. This NLP problem is numerically solved using *matlab fmincon* library employing either SQP or *interior-points* algorithm.

9.5 Supply of Gradients

The Gradient-based optimization techniques rely on gradient information of the objective functions and constraints with respect to the NLP variables. Supplying these gradients improves

the accuracy and computational speed of the optimization process. The required gradients are computed separately and then provided to the subroutines within the *matlab* program. However, it is often impractical and time-consuming to compute these derivatives analytically. As certain objective terms are functions of solutions of the BVP, analytical derivatives are not readily available. Instead, derivatives can be obtained through algorithmic differentiation (Griewank and Walther, 2008) or approximated using finite difference methods. Automatic differentiation involves a set of techniques based on the systematic application of chain rule to obtain derivatives of functions. Computer programs evaluate any mathematical functions through a set of elementary operations (such as addition, subtraction, multiplication, and division) and elementary functions $(\exp, \log, \sin)$. By applying the sequence of chain rule of calculus to these operations, we can obtain the derivatives of the functions analytically to working precision. Nonetheless, this approach cannot be implemented directly in our case as some objective functions depend on the solutions of the BVP and require some adjustments.

The objective function $\mathbf{g}(\mathbf{y}, \mathbf{c})$ depends on the state $\mathbf{y}(s)$ and the control parameters $\mathbf{c} \in \mathbb{R}^C$, where the state $\mathbf{y}(s)$ is solution of a two-point BVP

$$\mathbf{y}' = \mathbf{f}(\mathbf{y}, \mathbf{c}; s), \quad s \in [0, l] \tag{9.14a}$$

$$\mathbf{b_0}(\mathbf{y}(\mathbf{c}, 0)) = 0, \quad \mathbf{b_l}(\mathbf{y}(\mathbf{c}, l)) = 0. \tag{9.14b}$$

The BVP is numerically solved to yield the vector $\mathbf{Y} \in \mathbb{R}^M$, a finite-dimensional discretized version of the solution $\mathbf{y}(s)$ over the meshed interval of $[0, l]$. Here, M = dimension of $\mathbf{y} \times$ (Number of mesh intervals + 1). Since this solution depends on the control parameters $\mathbf{c}$, we write it as a function $\mathbf{Y}(\mathbf{c})$. Then, the objective $\mathbf{g}(\mathbf{y}, \mathbf{c})$ is approximated over this mesh as $\mathcal{G}(\mathbf{Y}(\mathbf{c}), \mathbf{c})$ using suitable collocation schemes. The functions such as (9.9), which contain integrals, are computed using numerical integration. The required gradients $\frac{d\mathbf{g}}{d\mathbf{c}}$ are approximated employing the following methods and provided.

9.5.1 Using BVPs

The most straightforward approach utilizes finite differences, where the components of gradient $\frac{d\mathbf{g}}{d\mathbf{c}}$ are approximated through a forward difference scheme as

$$\frac{d\mathbf{g}}{dc_i} \approx \frac{\mathcal{G}(\mathbf{Y}(\mathbf{c} + \epsilon \mathbf{e_i})) - \mathcal{G}(\mathbf{Y}(\mathbf{c}))}{\epsilon}, \qquad i = 1, \dots C,$$

or through a central difference scheme as

$$\frac{d\mathbf{g}}{dc_i} \approx \frac{\mathcal{G}(\mathbf{Y}(\mathbf{c} + \epsilon \mathbf{e_i})) - \mathcal{G}(\mathbf{Y}(\mathbf{c} - \epsilon \mathbf{e_i}))}{2\epsilon}, \qquad i = 1, \dots C,$$

where ϵ is a small scalar, and the vector $\mathbf{e_i}$ is the direction of perturbation in $\mathbf{c}$. Here, $\mathbf{e_i} \in \mathbb{R}^C$ is a column vector with one in ith row and zeros in the remaining rows. The value of ϵ should be chosen so that it is small enough to give a good approximation to the derivatives. But, it should not be too small to avoid round-off errors.

The central difference scheme provides a more accurate approximation of the derivative. However, solving a BVP is a time-consuming process, and the central difference scheme necessitates solving twice as many BVPs as the forward difference schemes. Hence, the forward difference scheme is generally favored over the central difference scheme in problems consisting of many variables and when accuracy is not a critical concern.

9.5.2 Using IVPs

Gradients can also be approximated using finite differences through an indirect approach. In the given BVP (9.14), some variables at the end $s = 0$ are given as boundary conditions, while some are unknown. We denote the unknown variables $\mathbf{y_{u,0}} \in \mathbb{R}^{Uk}$. Now, we consider an IVP by removing all the specified boundary conditions at the end $s = l$ and specifying unknown variables at $s = 0$. Then, the functions $\mathbf{g}$ and $\mathbf{b}_l$ are also functions of $\mathbf{y_{u,0}}$ and so, we write them as $\mathbf{b}_l(\mathbf{c}, \mathbf{y_{u,0}})$ and $\mathbf{g}(\mathbf{c}, \mathbf{y_{u,0}})$. A slight disturbance $\Delta\mathbf{c}$ in the control parameters $\mathbf{c}$ perturbs the state $\mathbf{y}$ by $\Delta\mathbf{y}$ and unknown variables $\mathbf{y_{u,0}}$ by $\Delta\mathbf{y_{u,0}}$. As a result, the boundary conditions at the other end $s = l$ are altered by

$$\Delta\mathbf{b}_l = \frac{d\mathbf{b}_l}{d\mathbf{c}}\Delta\mathbf{c} + \frac{d\mathbf{b}_l}{d\mathbf{y_{u,0}}}\Delta\mathbf{y_{u,0}}.$$

The boundary condition $\mathbf{b}_l$ is imposed, and the perturbation $\Delta\mathbf{c}$ does not affect its value. Therefore, the perturbation $\Delta\mathbf{b}_l$ is set to zero, leading to the relation:

$$\Delta\mathbf{y_{u,0}} = -\left[\frac{d\mathbf{b}_l}{d\mathbf{y_{u,0}}}\right]^{-1}\frac{d\mathbf{b}_l}{d\mathbf{c}}\Delta\mathbf{c}. \tag{9.15}$$

A minor perturbation in $\mathbf{c}$ results in a perturbation in $\mathbf{y_{u,0}}$ such that the imposed boundary conditions at the end $s = l$ are maintained.

Now consider the function $\mathbf{g}(\mathbf{y}(\mathbf{c}), \mathbf{c})$. A perturbation $\Delta\mathbf{c}$ in the control variable $\mathbf{c}$ leads to a perturbation

$$\Delta\mathbf{g} = \left[\frac{d\mathbf{g}}{d\mathbf{c}}\right]\Delta\mathbf{c} + \left[\frac{d\mathbf{g}}{d\mathbf{y_{u,0}}}\right]\Delta\mathbf{y_{u,0}}. \tag{9.16}$$

Using the relation (9.15) for $\Delta\mathbf{y_{u,0}}$ in (9.16), we obtain

$$\begin{aligned}\Delta\mathbf{g} &= \left[\frac{d\mathbf{g}}{d\mathbf{c}}\right]\Delta\mathbf{c} + \left[\frac{d\mathbf{g}}{d\mathbf{y_{u,0}}}\right]\Delta\mathbf{y_{u,0}},\\ &= \left[\frac{d\mathbf{g}}{d\mathbf{c}}\right]\Delta\mathbf{c} - \left[\frac{d\mathbf{g}}{d\mathbf{y_{u,0}}}\right]\left[\frac{d\mathbf{b_l}}{d\mathbf{y_{u,0}}}\right]^{-1}\frac{d\mathbf{b_l}}{d\mathbf{c}}\Delta\mathbf{c},\\ &\left[\left[\frac{d\mathbf{g}}{d\mathbf{c}}\right] - \left[\frac{d\mathbf{g}}{d\mathbf{y_{u,0}}}\right]\left[\frac{d\mathbf{b_l}}{d\mathbf{y_{u,0}}}\right]^{-1}\frac{d\mathbf{b_l}}{d\mathbf{c}}\right]\Delta\mathbf{c}.\end{aligned}$$

Then, the gradient component $\frac{d\mathbf{g}}{d\mathbf{c}}$ for a perturbation $\Delta\mathbf{c} = \epsilon\mathbf{e_i}$ is approximated as

$$\frac{d\mathbf{g}}{d\mathbf{c}} = \left[\left[\frac{d\mathbf{g}}{d\mathbf{c}}\right] - \left[\frac{d\mathbf{g}}{d\mathbf{y_{u,0}}}\right]\left[\frac{d\mathbf{b_l}}{d\mathbf{y_{u,0}}}\right]^{-1}\frac{d\mathbf{b_l}}{d\mathbf{c}}\right].$$

The required matrices $\frac{d\mathbf{g}}{d\mathbf{c}}$, $\frac{d\mathbf{b}_l}{d\mathbf{c}}$, $\frac{d\mathbf{g}}{d\mathbf{y_{u,0}}}$, and $\frac{d\mathbf{g}}{d\mathbf{y_{u,0}}}$ are evaluated using finite differences as

$$\begin{aligned}
\frac{d\mathbf{g}}{dc_i} &\approx \frac{\mathcal{G}(\mathbf{Y}(\mathbf{c}+\epsilon\mathbf{e}_i),\mathbf{y_{u,0}})) - \mathcal{G}(\mathbf{Y}(\mathbf{c}),\mathbf{y_{u,0}}))}{\epsilon}, \qquad i = 1,\dots C,\\
\frac{d\mathbf{b}_l}{dc_i} &\approx \frac{\mathbf{b_l}(\mathbf{Y}(\mathbf{c}+\epsilon\mathbf{e}_i),\mathbf{y_{u,0}}) - \mathbf{b_l}(\mathbf{Y}(\mathbf{c}),\mathbf{y_{u,0}})}{\epsilon}, \qquad i = 1,\dots C,\\
\frac{d\mathcal{G}}{d\mathbf{y_{u,0}}} &\approx \frac{\mathcal{G}(\mathbf{Y}(\mathbf{c}),\mathbf{y_{u,0}}+\epsilon\mathbf{u}_i)) - \mathbf{G}(\mathbf{Y}(\mathbf{c}),\mathbf{y_{u,0}})}{\epsilon}, \qquad i = 1,\dots Uk,\\
\frac{d\mathbf{b}_l}{d\mathbf{y_{u,0}}} &\approx \frac{\mathbf{b_l}(\mathbf{Y}(\mathbf{c}),\mathbf{y_{u,0}}+\epsilon\mathbf{u}_i)) - \mathbf{G}(\mathbf{Y}(\mathbf{c}),\mathbf{y_{u,0}}))}{\epsilon}, \qquad i = 1,\dots Uk.
\end{aligned}$$

Here, $\mathbf{u}_i \in \mathbb{R}^{Uk}$ is a column vector with one in the i th row and zeros in the remaining rows. The state $\mathbf{Y}(\mathbf{c})$ or $\mathbf{Y}(\mathbf{c}+\epsilon\mathbf{e}_i)$ is evaluated by solving an IVP, using initial conditions which include boundary conditions at the end $s = 0$ and variables $\mathbf{y}_{u,0}$. The BVP for the state $\mathbf{y}(\mathbf{c})$ is already solved to evaluate the objective $\mathbf{g}(\mathbf{y}(\mathbf{c}),\mathbf{c})$, and the values of $\mathbf{y}_{u,0}$ are readily available. In total, we need to evaluate $C + Uk$ sets of IVPs to evaluate the gradient $\frac{d\mathbf{g}}{d\mathbf{c}}$. On the contrary, only C sets of BVPs are required to approximate the gradient using the prior approach described in the subsection 9.5.1. However, IVPs are quicker to solve compared to BVPs. The shooting method techniques used to solve BVPs consist of multiple Newton steps which depend on initial guess and convergence criteria. In contrast, IVPs are solved using *Runga-Kutta methods*, which do not involve any iterative Newton methods.

9.5.3 Automatic Differentiation

Generally, the numerical computation of a BVP consists of meshing the time domain and transcribing it into a finite-dimensional algebraic system of the form:

$$F(\mathbf{Y},\mathbf{c}) = \mathbf{0}, \qquad F : M \times C \to M, \tag{9.17}$$

where $\mathbf{Y} \in \mathbb{R}^M$ is the discretized state $\mathbf{y}(s)$ over the mesh. Then, the gradient of the function $\mathcal{G}(\mathbf{Y},\mathbf{c})$ with respect to $\mathbf{c}$ reads

$$\frac{d\mathcal{G}}{d\mathbf{c}} = \mathcal{G}_Y\mathbf{Y_c} + \mathcal{G}_c, \tag{9.18}$$

where $\mathcal{G}_Y \in \mathbb{R}^{M\times 1}$ and $\mathcal{G}_c \in \mathbb{R}^{M\times C}$ are the partial derivatives of the function $\mathcal{G}$ with respect to the state $\mathbf{Y}$ and control parameter $\mathbf{c}$ respectively. Since, $\mathcal{G}$ is a function of $\mathbf{Y}$ and $\mathbf{c}$, the gradients $\mathcal{G}_c$ and $\mathcal{G}_Y$ can be evaluated. However, computing $\mathbf{Y_c}$ is not a straightforward process and is evaluated from the collocation equations of the BVP (9.18). After differentiating (9.17) with

respect to $\mathbf{c}$, we obtain

$$\mathbf{F_Y Y_c} + \mathbf{F_c} = 0,$$

where $\mathbf{F_Y}$ is a $M \times M$ matrix, and $\mathbf{F_c}$ is a $M \times C$ matrix. Then, for an invertible $\mathbf{F_Y}$, the gradient $\mathbf{Y_c}$ is evaluated as

$$\mathbf{Y_c} = -\mathbf{F_Y^{-1} F_c}. \tag{9.19}$$

On substituting 9.19 in 9.18, we get

$$\frac{d\mathcal{G}}{d\mathbf{c}} = -\left[\mathcal{G}_Y \mathbf{F_Y^{-1}}\right]\mathcal{G}_c + \mathbf{F_c} = -\mathcal{G}_Y\left[\mathbf{F_Y^{-1} F_c}\right] + \mathcal{G}_c.$$

As indicated by the different parenthesizing, this expression can be evaluated in two ways. In the first method (also termed as *Adjoint Gradient Computation*), the matrices are multiplied first $\Gamma = \left[\mathcal{G}_Y \mathbf{F_Y^{-1}}\right] \in \mathbb{R}^{M\times 1}$, which corresponds to a solution of *adjoint* equation

$$\mathbf{F_Y}\tilde{\Gamma}^T = \mathcal{G}_Y^T, \tag{9.20}$$

and then we multiply $\tilde{\Gamma}$ with $\mathcal{G}_c$. Combining everything, we get

$$\frac{d\mathcal{G}}{d\mathbf{c}} = -\Gamma \mathbf{F_c} + \mathcal{G}_c.$$

The last step involves the multiplication of $M \times 1$ matrix with $M \times C$, and it requires $M \times C$ evaluations. The adjoint problem (9.20) can use the intermediate elementary operations that result from Newton's step of solving (9.17), and its solution would not be harder.

In the second method, the matrix $\tilde{\Lambda} = \mathbf{F_Y^{-1} F_c}$ is evaluated and then substituted in (9.18) to give $-\mathcal{G}_Y\tilde{\Lambda} + \mathcal{G}_c$. The multiplication of $M \times M$ matrix by a $M \times C$ requires M^2C evaluations and costs $\mathcal{O}(M^2C)$. Evaluating gradients $\mathcal{G}_Y$ using either method is not always straightforward. Moreover, calculating the jacobian $F_Y \in \mathbb{R}^{M\times M}$ becomes challenging for larger systems.

In summary, a gradient-based optimization framework has been developed to model various robot navigation tasks. The numerical algorithm to solve the resultant system has also been outlined. In the next chapter, this methodology will be applied to model several prototypical tasks for CTCRs.

CHAPTER 10

Case studies

In this chapter, we test the proposed *optimal control*-based navigation framework using a three-tube CTCR. The mechanical properties of the constituent tubes of the CTCR are listed in Table 10.1. We consider test tasks like controlling the robot to guide its tip to a desired location and orientation, moving along a desired path. These numerical examples are solved with *matlab*'s *fmincon* library, employing either an SQP or a *interior point* algorithm (section 8.4). All the presented numerical computations and results are in dimensionless units. In our context, for instance, if 1 unit force corresponds to 1 Newton, then 1 unit length corresponds to $100mm$.

10.1 Minimum Working Volume

In the first example, we consider maneuvering the robot such that its tip moves from an initial point $\mathbf{r_{init}}$ to a target point $\mathbf{r_{tar}}$ with a minimum working volume.

10.1.1 Using deviation term from the FTL curve

To gain a better understanding of the objective functions in the optimization framework, we focus only on a subset of them and investigate their interplay. In the current example, only the objectives that quantify the target-pursuit $M_1(\mathbf{y}, \bar{\lambda})$, working volume $J_2(\mathbf{y})$, and regularization term $J_3(\mathbf{w})$ are included. Subsequently, the resultant optimization task involves minimizing the combined objective:

$$J(\mathbf{y}, \mathbf{w}) = \bar{\lambda}_0 M_1(\mathbf{y}, \bar{\lambda}) + \bar{\lambda}_2 J_2(\mathbf{y}) + \bar{\lambda}_3 J_3(\mathbf{w}).$$

Each section's length L_i is also subjected to an upper bound, as the rod lengths are finite.

$$0 \leq L_i(t) \leq 0.8.$$

Option	Tube 1	Tube 2	Tube 3
Bending Stiffness $K_{11}^{[i]}$ ($\times 10^4 N.mm^2$)	1.0	1.2	1.4
Torsion Stiffness $K_{33}^{[i]}$ ($\times 10^4 N.mm^2$)	1.0/1.3	1.2/1.3	1.4/1.3
Precurvature vector (mm^{-1})	[1/200,0,0]	[1/125,0,0]	[1/100,0,0]
Maximum Length (mm)	330	220	110

Table 10.1 Parameters of the CTCR used in the examples.

Moreover, this bound serves to prevent the occurrence of snapping during intermediate paths. In some instances, the BVP solver utilized within the optimization problem may encounter issues attributed to the singular Jacobian matrix of the BVP collocation equations, resulting in an abrupt termination of the solver. Typically, these situations arise in the close vicinity of the hysteresis regions. As a consequence, the optimization task remains incomplete. Therefore, this bound is crucial in preventing the optimization solver from reaching these undesirable intermediate iterations. In these numerical experiments, we set $\bar{\lambda} = 0$ in (9.5), as the tip's orientation is irrelevant here. The effectiveness of the proposed *minimum deviation objective* (9.9) in reducing the working volume is examined by comparing the cases with different values of $\bar{\lambda}_2$. Throughout this numerical testing, the weights $\bar{\lambda}_0$ and $\bar{\lambda}_3$ are held constant at their set values: $\bar{\lambda}_0 = 400$, $\bar{\lambda}_3 = 5$. The investigation is conducted with distinct values of $\bar{\lambda}_2$: 0, 20, and 50. The curve corresponding to the *follow-the-leader* configuration with controls $\mathbf{y}_{\mathrm{FTL}} = [0.5, 0.5 + \pi, 0.5 + \pi, 0.4, 0.6, 0.5]$ is employed as the reference or mean curve, and for evaluating the objective (9.9). For this numerical experiment, initial control parameters are set at $\mathbf{y}(0) = [0.5, 3.64, 3.84, 0.4, 0.6, 0.5]$, and a target point $\mathbf{r_{tar}} = [-0.4, 0.0, 1.0]$ is specified. No tip load $\mathbf{F} = \mathbf{0}$ is applied for this present example (Dhanakoti et al., 2022). CTCR configurations corresponding to the initial parameter $\mathbf{y}(0)$ are given as initial guesses for all time steps $t_k \in [0, 1]$. The optimization is executed with these parameters and the initial states, discretizing the time interval $[0, 1]$ into 10 equal steps.

Figure 10.1 displays the evolution of CTCR configurations for the resulting optimal solutions. The state at each mesh point t_k is obtained by solving BVP (9.1) and is plotted. From this plot, it is evident that the primary goal of reaching the prescribed target $\mathbf{r_{tar}}$ has been accomplished in all cases. At these solutions, the target pursuit objective $M_1(\mathbf{y}, 0)$, which is the distance between the tip at final time $t = 1$ is close to zero, typically in the order of 10^{-4}. Nevertheless, they followed different paths depending on the value of $\bar{\lambda}_2$. Figure 10.2 portrays the evolution of control parameters $\mathbf{y}$ as a function of time t.

When the coefficient of the *minimum deviation measure* J_2, i.e., $\bar{\lambda}_2$, is zero, the goal is to steer the robot tip to the target $\mathbf{r_{tar}}$ with a minimal regularization term. This scenario arises when the control parameters follow a linear function of time t. The plots of control parameters for $\bar{\lambda}_2 = 0$ in Figure 10.2 appear as straight lines and support this argument. For non-zero values of $\bar{\lambda}_2$, the robot minimizes the deviation measure J_2 by navigating along different paths. The reduction in the objective functions can be qualitatively observed in Figure 10.1, and quantitative results are presented in Table 10.2. The comparison of results between the *interior points* and SQP algorithms is also given in this table. Clearly, the SQP algorithm occasionally leads to different local minima with higher objective J. Additionally, we observe that the deviation from FTL measure J_2 decreases as the value of $\bar{\lambda}_2$ increases. Moreover, the value of the optimal objective function J, which is the value of J at the optimal solutions, increases with an increase in $\bar{\lambda}_2$.

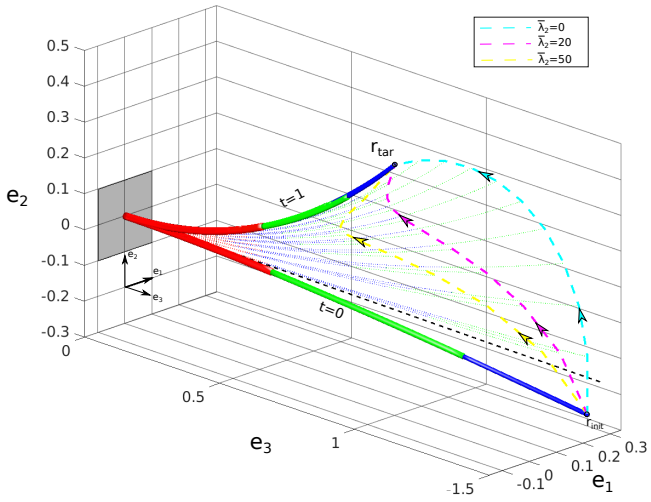

(a)

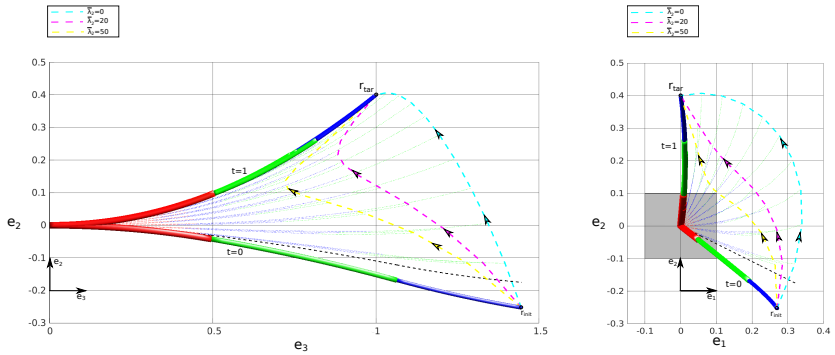

(b) Planar views

Fig. 10.1 The CTCR navigation with its tip traversing from $\mathbf{r_{int}}$ to $\mathbf{r_{tar}}$ for different values of $\bar{\lambda}_2$ and zero tip load. The robot's sections are shown in distinct colors. Solid lines depict the initial and final states, while light dotted lines represent intermediate states. Traces of the tip for different penalization $\bar{\lambda}_2$ are depicted by dashed lines in green, magenta, and cyan colors, accompanied by arrows indicating the direction of tip motion.

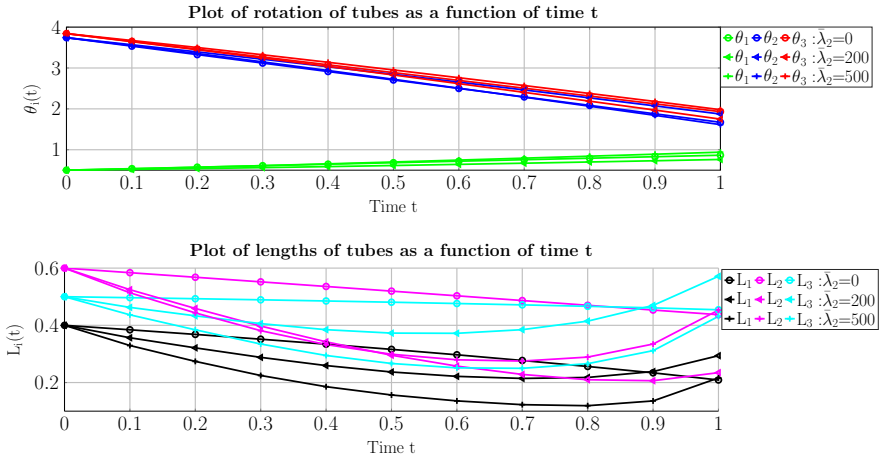

Fig. 10.2 The evolution of the control parameters $\mathbf{y}(t)$ for different values of $\bar{\lambda}_2$ and zero tip load.

$\bar{\lambda}_2$	Interior points		SQP	
	Deviation term J_2	Objective J	Deviation term J_2	Objective J
0	0.1626	22.2913	0.1350	37.7769
20	0.0889	23.4912	0.0744	74.7285
50	0.0572	26.5512	0.0490	84.6655
100	0.0391	26.3962	0.0347	27.5167
200	0.0283	30.9722	0.0250	30.3194

Table 10.2 Effect of the penalizing weight λ_2 on the deviation term (as calculated in (9.9) and the objective J

A closer inspection of Figure 10.2 reveals an interesting pattern in the evolution of control parameters $\mathbf{y}(t)$. For non-zero $\bar{\lambda}_2$, the angular components of the control parameters $(\theta_i(t))$ appear almost straight and deviate very slightly from the straight lines for the case of $\bar{\lambda}_2 = 0$. On the other hand, the length control parameters $L_i(t)$, for non-zero $\bar{\lambda}_2$, are non-straight and deviate significantly from the straight lines observed for the case of $\bar{\lambda}_2 = 0$. This finding suggests that the objective function J_2 is more sensitive to variations in the length control $L_i(t)$ compared to that of the angle controls $\theta_i(t)$. As a result, the optimization algorithm is predominantly influenced by alterations in $L_i(t)$ rather than in $\theta_i(t)$. For higher $\bar{\lambda}_2$, the lengths of the sections reduce during the initial phase of the motion and subsequently elongate to reach the target during the final phase, thereby reducing the deviation measure J_2. We also notice that the control parameters at the final time $t = 1$ are different for each path, and yet they correspond to the same tip position within a certain tolerance. As highlighted earlier, the various combinations of control parameters at the final time $t = 1$ can lead to the same tip location. These end control parameters depend on the nature of the objectives under consideration.

Now, we incorporate a concentrated tip load into the setup and perform the optimization. A load $\mathbf{F} = -0.1\mathbf{e}_1 - 0.15\mathbf{e}_2 - 0.12\mathbf{e}_3$ is applied to the tip ($\Delta = [0, 0, 0]$), and optimization is performed with the same penalizing weights as before. Figure 10.3 illustrates the evolution of the robot configurations with the tip load during this maneuver, and Figure 10.4 displays the control parameters $\mathbf{y}$ vs. time t plot. The optimal solutions exhibit qualitative similarities to those of the previous unloaded case, and similar qualitative trends are noted. For instance, the length controls $L_i(t)$ decrease during the initial phase of the motion and increase during the final phase. Figure 10.5 shows the plot of deviation from FTL as time t evolves. The area under this curve corresponds to the value of the objective J_2, which decreases as $\bar{\lambda}_2$ increases. The value of J_2 depends on the deviation from the reference FTL curve as well as CTCR's length $(L_1 + L_2 + L_3)$. The smaller value for $\bar{\lambda}_2 = 200$ is due to the smaller length of CTCR in the intermediate steps, as evident from Figures 10.3,10.4. Additionally, the angle controls $\theta_i(t)$ remain relatively straight and deviate only slightly compared to length controls $L_i(t)$, which exhibit significant deviations from the straight lines observed for $\bar{\lambda}_2 = 0$. However, the results quantitatively differ. The tip load deforms the robot's shape, leading to different values of objective functions. Consequently, the optimal solutions yield different sets of control parameters $\mathbf{y}(t)$.

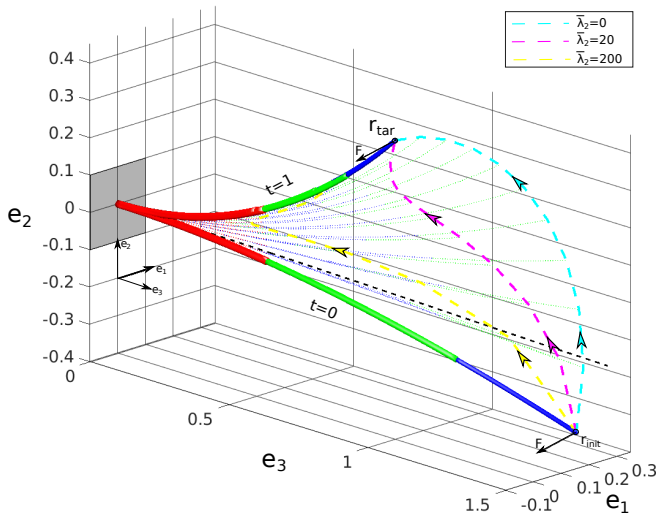

(a) 3D view

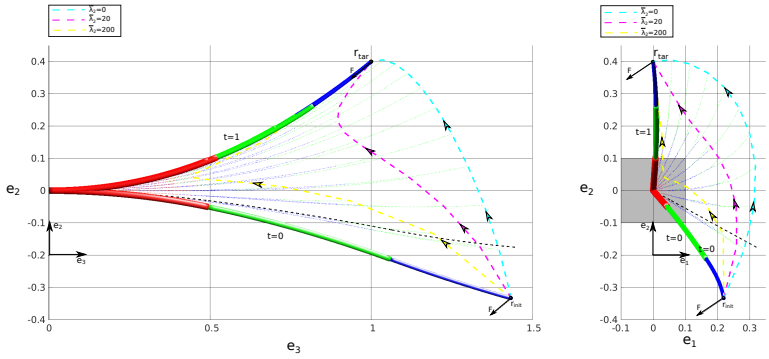

(b) Planar views

Fig. 10.3 The CTCR navigation with its tip traversing from $\mathbf{r_{int}}$ to $\mathbf{r_{tar}}$ for different values of $\bar{\lambda}_2$ and with a non-zero tip load. The description of the elements in the plot is identical to that of Figure 10.1. The load vector is also indicated at initial and final states.

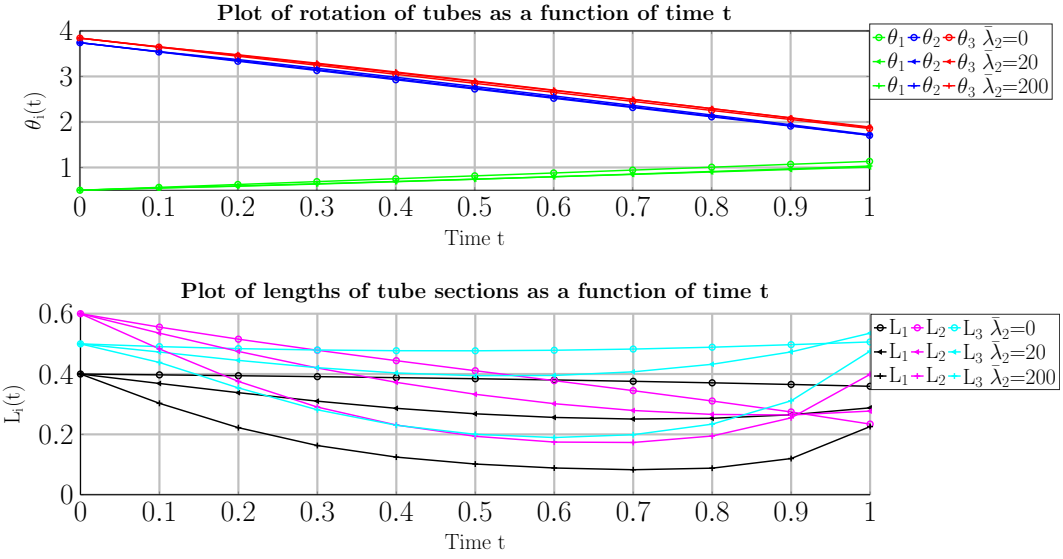

Fig. 10.4 The evolution of the control parameters $\mathbf{y}(t)$ for different values of $\bar{\lambda}_2$ in a scenario with non-zero tip load.

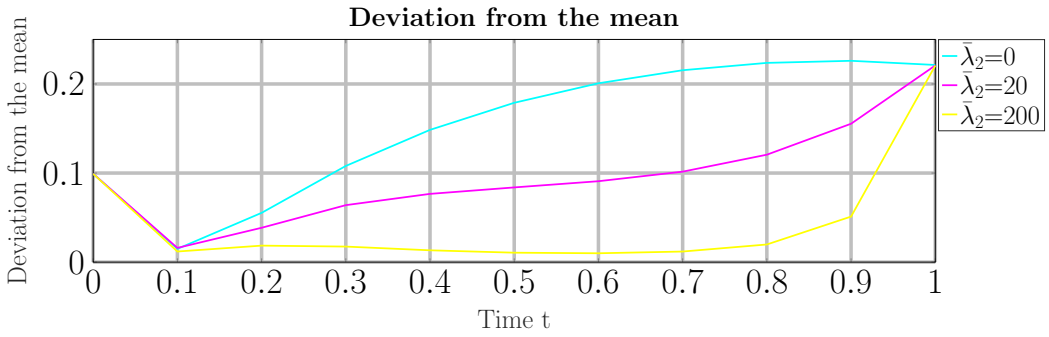

Fig. 10.5 The plot of the *deviation from the FTL* term (9.10) vs. time for different values of $\bar{\lambda}_2$.

The conserved quantities (discussed in section 6.5) are employed to set tolerances in the BVP solvers embedded within the optimization setup. The states of the robot are solved as a BVP using the *bvp4c* function inside the optimization scheme. This BVP solver employs a collocation formula to compute solutions. The numerical solution is based on the mesh of points at which the given ODEs are satisfied. *Matlab* adaptively varies this mesh size based on the residual of the solutions, ensuring that the computed solution is an exact representation of the given problem within a certain tolerance. Relative tolerance is the measure of the residual relative to the size of the function. We set these tolerance values by comparing the Hamiltonian H of the CTCR (6.19) (not to be confused with the Hamiltonian function of the *optimal control problem*) along the BVP solutions for different values of tolerance. Figure 10.6 shows the comparison of errors in the Hamiltonian for various values of relative tolerance. The error in Hamiltonian is on the order of 10^{-5} with a relative tolerance of 10^{-2}, and it improves to an order of 10^{-9} as the tolerance is tightened to 10^{-5}. Additionally, there is a rise in the number of mesh points (shown in circles) for this tolerance setting.

Now, we shall discuss the effect of using gradients computed through finite differences (using IVPs subsection 9.5.2) and Automatic Differentiation (subsection 9.5.3). Table 10.3 provides a comparison of the values of the objectives J for the optimal solutions computed using both of these methods. In all cases, the overall objective J computed using Automatic Differentiation is lower than that computed using finite differences. The gradients approximated through finite differences bring the system closer to the minimum value. However, as the optimization progresses, approaching further closer to the minimum becomes increasingly challenging. The deviation of the approximated gradients from the actual gradients hinders the accurate determination of the minimizing direction. As a consequence, the system may not continue its approach towards the optimal value. In addition, the current problem is highly nonlinear and has multiple local minima. It is also possible that the solver gets trapped in a region around a local optimal solution. The inaccuracies in the approximated minimizing directions might hinder the system from escaping this trapped region.

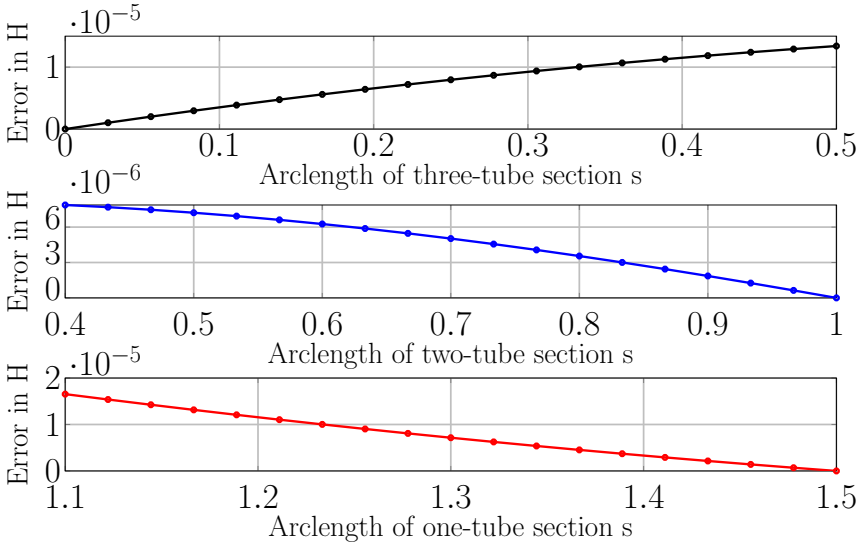

(a) Relative tolerance of 10^{-2}

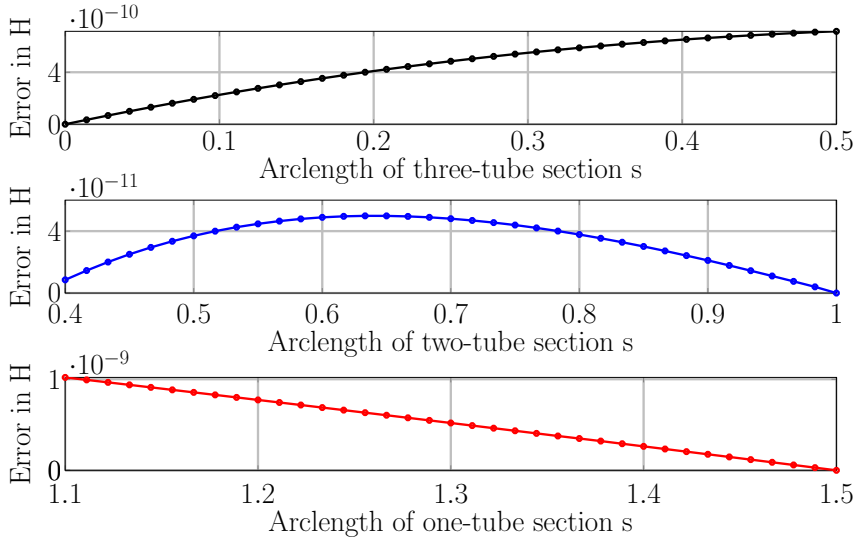

(b) Relative tolerance of 10^{-5}

Fig. 10.6 Error in the Hamiltonian of CTCR for different relative tolerances in BVP solver.

$\bar{\lambda}_2$	J (using Finite differences)	J (using Automatic Differentiation)
0	20.8425	19.2343
20	23.6093	21.4892
50	24.4342	23.4240
100	26.0259	25.5992

Table 10.3 Effect of the gradients computed using Finite Differences (IVPs) and Automatic Differentiation on the optimization task.

10.1.2 Sweep area

Now, we utilize the sweep area (9.11) as a working volume measure and perform the optimization. A concentrated load $\mathbf{F} = -0.1\mathbf{e}_1 - 0.15\mathbf{e}_2 - 0.12\mathbf{e}_3$, which is the same as the prior case, is applied to the tip ($\Delta = [0, 0, 0]$) for this study. The evolution of the control parameters and the CTCR configurations for the resulting optimal solutions are presented in Figure 10.7 and Figure 10.8, respectively. In addition, Table 10.4 presents the computed value of sweep area J_2 and the overall objective J at the optimal solutions. An increase in penalizing weights leads to a decrease in the sweep area measure J_2, highlighting the optimization framework's effectiveness. Similar to the cases in the preceding section 10.1.1, the sweep area objective function is sensitive to the length controls $L_i(t)$. The swept area of CTCR is minimized by reducing its length in its initial phase of motion and then elongating it in the final phase. For higher values of $\bar{\lambda}_2$, the optimization leads to a path where $L_i(t)$ is initially reduced close to zero length and subsequently increased in the final stage. The θ_i vs. t plots are straight and deviate very slightly compared to L_i vs. t plots. Its value is smaller in comparison to the *deviation from the FTL* objective for the identical path.

$\bar{\lambda}_2$	Sweep area J_2	Final Objective J
0	0.4566	22.4121
5	0.3316	22.855
10	0.2117	23.8461
20	0.1987	25.8542
40	0.1479	29.2434

Table 10.4 Effect of the penalizing term $\bar{\lambda}_2$ on the sweep area and the objective.

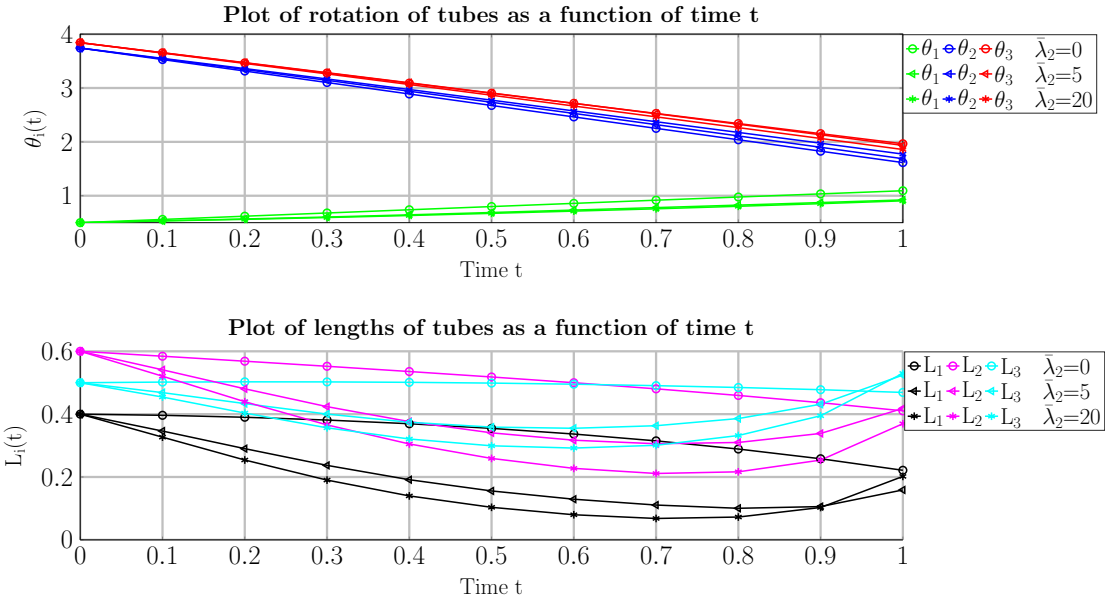

Fig. 10.7 The evolution of control parameters $\mathbf{y}(t)$ for different values of $\bar{\lambda}_2$.

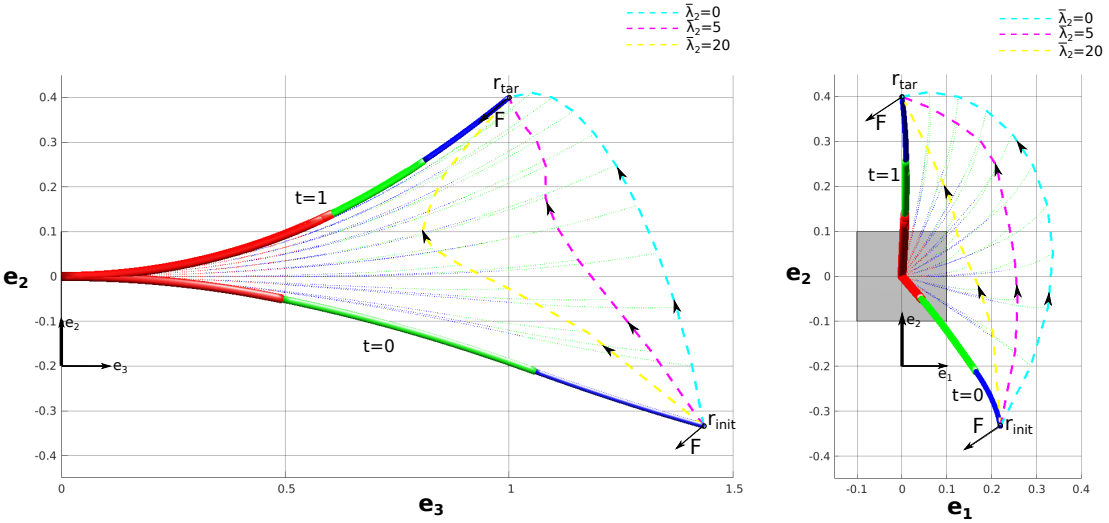

(a) Projection in $\mathbf{e_2}$-$\mathbf{e_3}$ plane

(b) Projection in $\mathbf{e_1}$-$\mathbf{e_2}$ plane

Fig. 10.8 The loaded robot navigating with its tip traversing from $\mathbf{r_{int}}$ from $\mathbf{r_{tar}}$ for different penalization of sweep area. The initial and final states of the robot are illustrated in solid lines whereas the intermediate states are illustrated in light dotted lines. The traces of the tip for different penalization $\bar{\lambda}_2$ are shown in dashed lines of green, magenta, and cyan colors, accompanied by arrows indicating the direction of the tip motion.

10.1.3 Restricting the length-control parameters

In all the illustrated examples, a common observation is that the objective J_2 (deviation term as well as sweep area) is more sensitive to variations in the length controls $L_i(t)$ than to variations in the rotation controls $\theta_i(t)$. Therefore, we conduct the study by restricting the length controls $L_i(t)$. In this scenario, we assume that the objective function J_2 depends exclusively on the rotation controls $\theta_i(t)$. We assume that the gradient of this objective function has only components with respect to angle controls $\theta_i(t)$ and no components related to the length controls L_i, i.e., $\frac{\partial J}{\partial L_i} = 0$. Consequently, the search directions during intermediate optimization stages are primarily influenced by changes in the angle controls $\theta_i(t)$ rather than the length controls $L_i(t)$. Figure 10.9 displays the CTCR configurations obtained for this optimization problem,

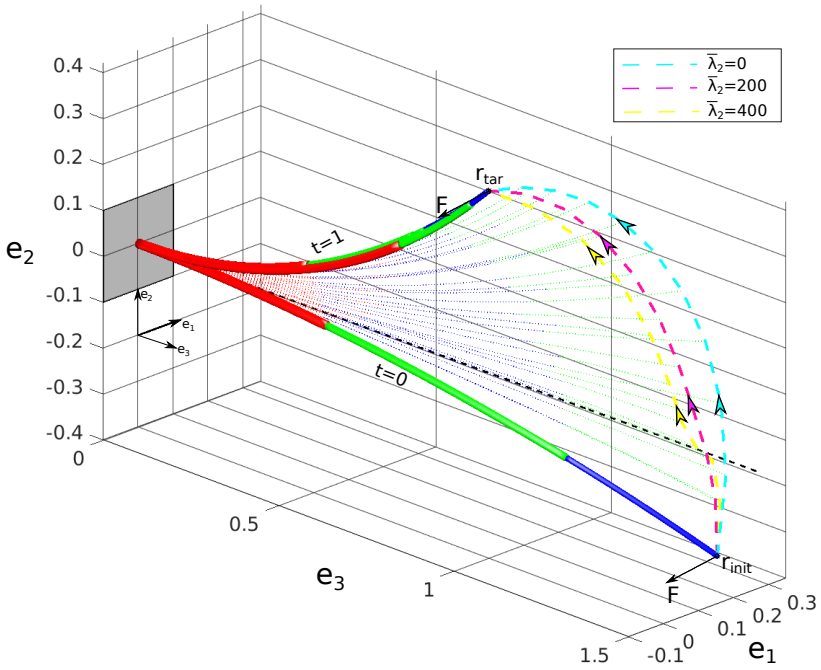

(a) 3D view

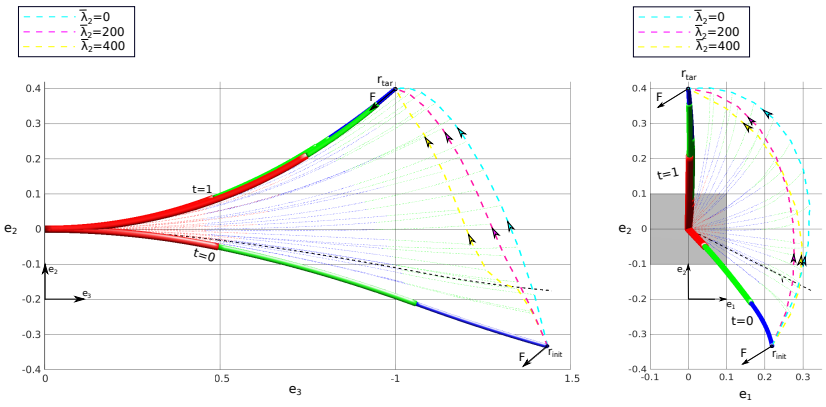

(b) Planar views

Fig. 10.9 The navigation of the loaded robot with its tip reaching $\mathbf{r_{tar}}$ from $\mathbf{r_{int}}$ for different $\bar{\lambda}_2$. The robot's sections are shown in different colors black, red, and blue corresponding to sections with 3, 2, and 1 tube, respectively.

whereas Figure 10.10a displays the evolution of the control parameters. On comparing with Figure 10.3b, we notice that the angle control parameters $\theta_i(t)$ are not straight and deviate significantly from straight lines. On the other hand, the length controls $L_i(t)$ are straight as their evolution is solely dictated by the regularization term (J_3). Higher values of the penalizing weights $\bar{\lambda}_2$ are necessary to notice any significant qualitative changes in the robot path. Figure 10.10b depicts the plot of evolution of the objective *deviation from FTL* (J_2). The area under the curve significantly decreases with the increase in the weight $\bar{\lambda}_2$. The deviation tends to approach zero during intermediate time steps when subjected to higher penalization. This indicates that the CTCR configuration closely aligns with the reference FTL curve at intermediate steps during the maneuver. These findings suggest that by constraining the length controls and emphasizing the rotation controls, it is possible to steer the robot closer to the FTL curve, thereby reducing the working volume for a given task.

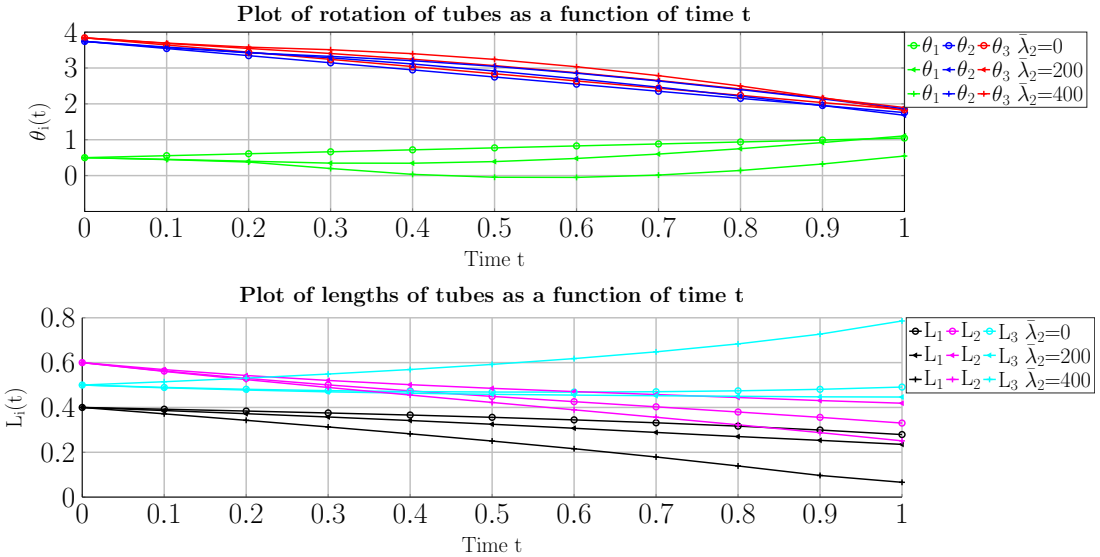

(a)

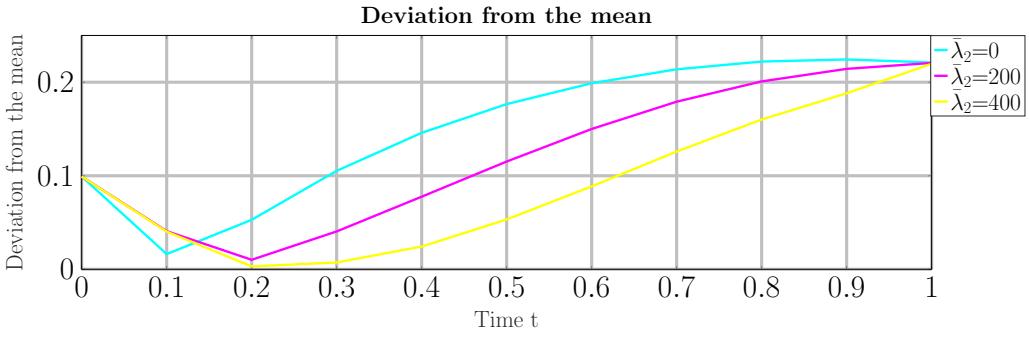

(b)

Fig. 10.10 Robot navigation when its length controls $L_i(t)$, $i = 1, 2, 3$ are restricted. a) The evolution of control parameters $\mathbf{y}(t)$ for different values of λ_2. b) The plot of deviation from the FTL vs. t. The area beneath this curve represents the value of the objective J_2 (9.10).

10.2 Fixed Tip Orientation with Adjustable Position

In this example, we extend the optimization framework to include the robot's tip orientation $\mathbf{d}_3(\mathbf{y}(t), l_1)$, as well as the target path $\mathbf{r_{path}}(t)$ in the maneuvering task. We intend to steer the robot tip close to a prescribed path $\mathbf{r_{path}}(t)$ and tip orientation path $\mathbf{n_{path}}(t)$. The straight line between the initial point $\mathbf{r_{init}}$ and the target $\mathbf{r_{tar}}$ is specified as target path $\mathbf{r_{path}}(t)$ $\forall t \in [0, 1]$:

$$\mathbf{r_{path}}(t) = (1 - t) * \mathbf{r_{init}} + t * \mathbf{r_{tar}}, \tag{10.1}$$

and a fixed tip orientation of $\mathbf{d}_3(\mathbf{y}(t), l_1)$ is provided as $\mathbf{n_{path}}(t)$. The covered volume objective J_2 is not considered here: since the tip is constrained to move along a path $\mathbf{r_{path}}(t)$, they might have conflicting actions against each other. In addition, we can gain a proper insight into their individual effects by focusing on fewer objectives. The current goal of steering the robot such that its tip stays close to a fixed tip orientation can be formulated either as (i) a deviation penalty in the objective, or (ii) an inequality constraint.

In the first case, the optimization problem reads

$$\text{Minimize } J(\mathbf{y}, \mathbf{w}) = \bar{\lambda}_0 M_1(\mathbf{y}, \bar{\lambda}) + \bar{\lambda}_1 J_1(\mathbf{y}, \bar{\lambda}) + \bar{\lambda}_3 J_3(\mathbf{w}),$$

subject to the constraints

$$\begin{aligned} &\frac{\mathbf{y}_i(t_{k+1}) - \mathbf{y}_1(t_k)}{t_{k+1} - t_k} = \mathbf{w}_i(t_{k+1/2}), \\ &0 \leq L_i(t_k) \leq 0.9. \end{aligned}$$

The penalizing weights $\bar{\lambda}_o = 5$, $\bar{\lambda}_1 = 400$, $\bar{\lambda}_2 = 0$, $\bar{\lambda}_3 = 40$ and an initial configuration with control parameters $\mathbf{y}(0) = [0.5, 3.64, 3.84, 0.4, 0.6, 0.5]$ are used for all cases in this section. We study the effect of penalization for deviation of the tip orientation by exploring cases with weights $\bar{\lambda} = 0, 1$ and 5. The time interval $[0, 1]$ is discretized into 10 equal intervals, and the optimization is performed over this mesh. The $\mathbf{r_{path}}(t_k)$ is obtained at mesh points t_k using (10.1). The target point $\mathbf{r_{tar}}$ is chosen as $[-0.265, 0.2324, 1.45]^T$.

The robot's motion is depicted in Figure 10.11a after obtaining the equilibria for the resultant optimal solutions at the mesh points t_k. The evolution of the angle between the tip tangent and the target vector $\mathbf{n_{tar}}$:

$$\boldsymbol{\Theta}(t) = \cos^{-1}\left(\mathbf{d}_3(\mathbf{y}(t), l_1) \cdot \mathbf{n_{tar}}\right), \tag{10.2}$$

is also shown in Figure 10.11b. When $\bar{\lambda} = 0$, the goal is to steer the robot tip to a target $\mathbf{r_{tar}}$, while remaining close to the specified path $\mathbf{r_{path}}(t)$ without accounting for tip orientation. The tip is constrained to move along the straight line connecting $\mathbf{r_{init}}$ and $\mathbf{r_{tar}}$ by penalizing its deviation from this path. Using non-zero penalization weights $\bar{\lambda}$ in (9.7), the robot tip is guided closely to the specified target vector $\mathbf{n_{tar}}$. The $\Theta(t)$ reaches its maximum value at the final time

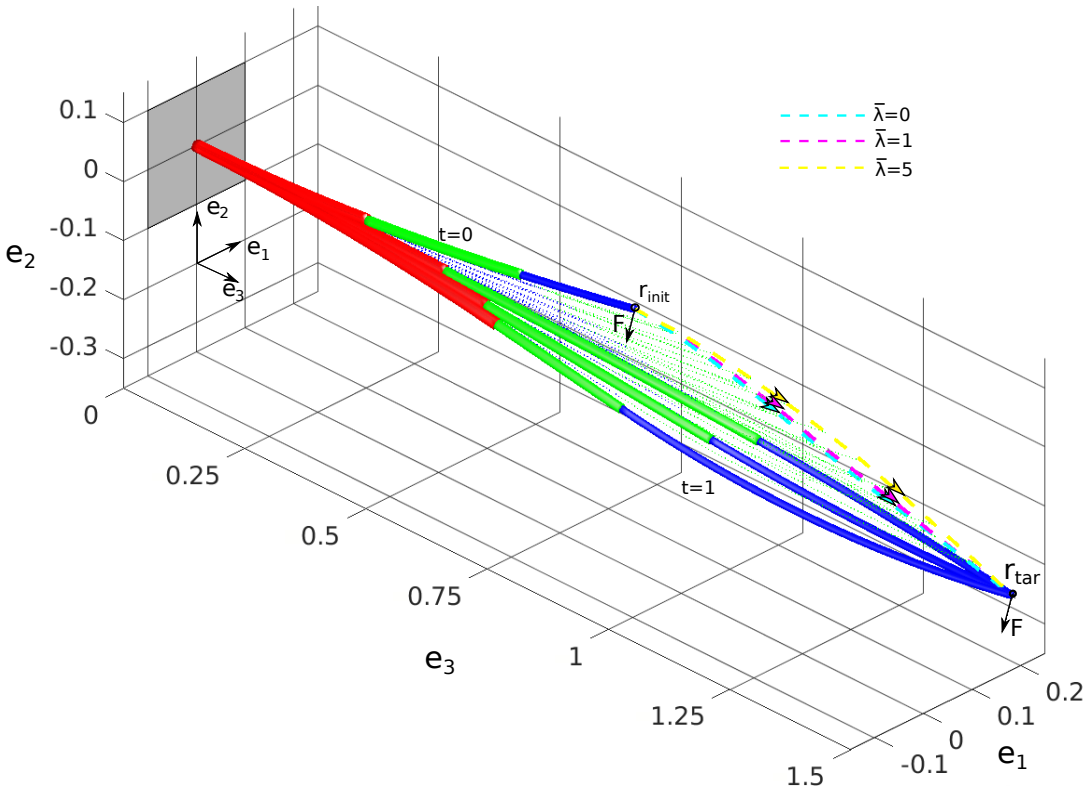

(a)

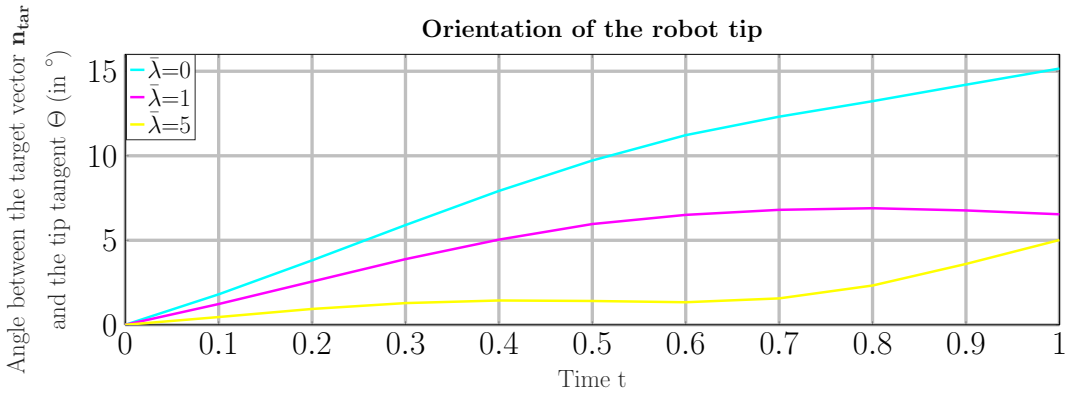

(b)

Fig. 10.11 a) The evolution of the CTCR as its tip moves from an initial point $\mathbf{r_{init}}$ to a target $\mathbf{r_{tar}} = [-0.01, 0.12, 0.78]^T$. The initial states and the final states are shown in solid lines, whereas intermediate states are shown in dotted lines. The traces of the tip for different values of $\bar{\lambda}$ are shown. b) The plots of the angle Θ vs. t for different values of $\bar{\lambda}$.

$t = 1$ during the navigation. When the tip's deviation from $\mathbf{n_{tar}}$ is penalized by using $\bar{\lambda} = 1$, the maximum value of $\Theta(t)$ is decreased to approximately 7°. Upon increasing the penalization $\bar{\lambda}$ to 5, the maximum angle is further reduced to around 5°. We can also notice that the CTCR configurations at the final time $t = 1$ are different for different cases of $\bar{\lambda}$. However, they point to the same tip location within different tolerances, but different tip orientations, as evident from the final states $(t = 1)$ in Figure 10.11a and the values of $\Theta(1)$ in Figure 10.11b.

We now formulate the robot navigation using an inequality constraint on $\Theta(t)$, which denotes the angle between the tip tangent $\mathbf{d}_3(\mathbf{y}(t), l_1)$ and the target vector $\mathbf{n_{tar}}$. A tolerance angle θ_{tol} is imposed, and penalizing term $\bar{\lambda} = 0$ is chosen in the objective function in (9.6). The inequality condition:

$$\Theta(t) \leq \theta_{\text{tol}}, \quad \text{or} \quad \cos\Theta(t) \geq \cos\theta_{\text{tol}}, \tag{10.3}$$

ensures the tip alignment. The plots of robot navigation for different values of θ_{tol} are depicted in Figure 10.12a. In Θ vs. t plot (Figure 10.12b), it is evident that for higher values of θ_{tol}, the

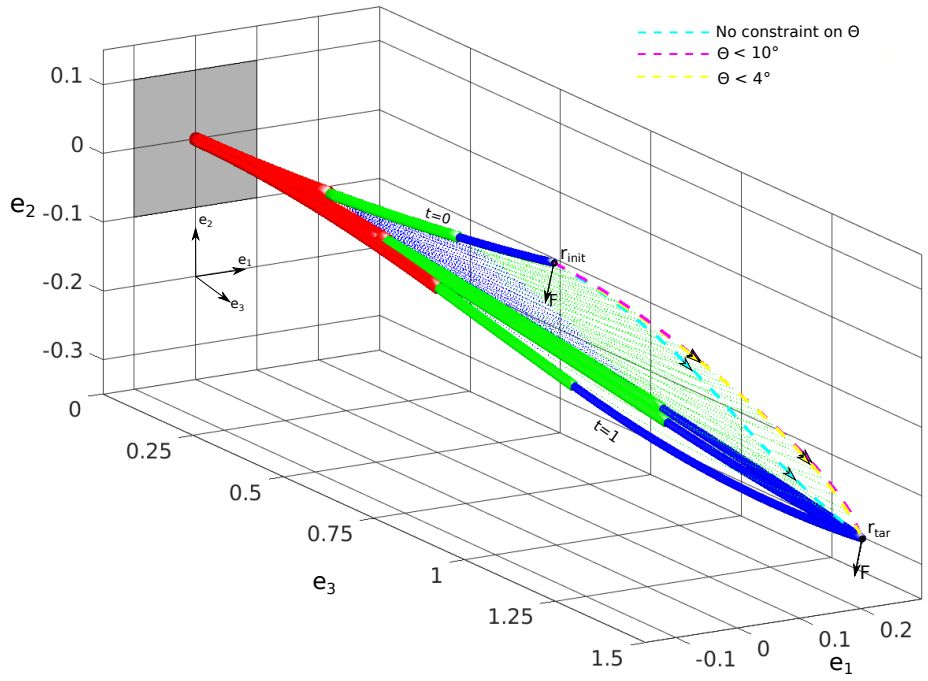

(a)

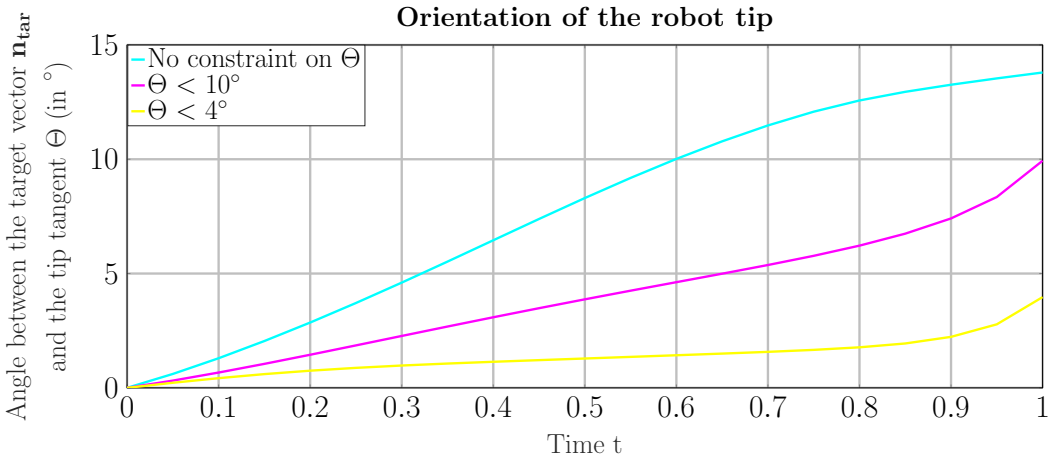

(b)

Fig. 10.12 a) The evolution of the CTCR as its tip moves from initial point $\mathbf{r_{init}}$ to $\mathbf{r_{tar}} = [-0.01, 0.12, 0.78]^T$. The traces of the tip for different values of $\bar{\lambda}$ are depicted. b) The plots of the angle Θ vs. t for different values of θ_{tol}.

inequality constraint remains inactive, i.e., the value of $\Theta(t)$ never reaches this specified tolerance θ_{tol} for any $t \in [0, 1]$. When the value of θ_{tol} is reduced to $10°$, the inequality constraint becomes active, attaining θ_{tol} value only at the final time $t = 1$. Further reduction of θ_{tol} to $5°$ accomplishes our objective, with the maximum value of $\Theta(t)$ solely attained at the final time $t = 1$.

In certain scenarios, it may not be possible to steer these robots to configurations with a desired tip point and orientation. For example, consider a task where a robot tip is required to reach a farther target point $\mathbf{r_{tar}} = [-0.265, -0.55, 1.45]^T$ with a minimum deviation of its tip from its initial tip tangent direction. We solve this optimization problem using an inequality constraint. Optimization is performed with three cases of θ_{tol}, namely *no constraint* $\theta_{\text{tol}} = 180°$, $\theta_{\text{tol}} = 15°$, and $\theta_{\text{tol}} = 7°$. Figure 10.13 portrays the evolution of robot configurations and $\Theta(t)$

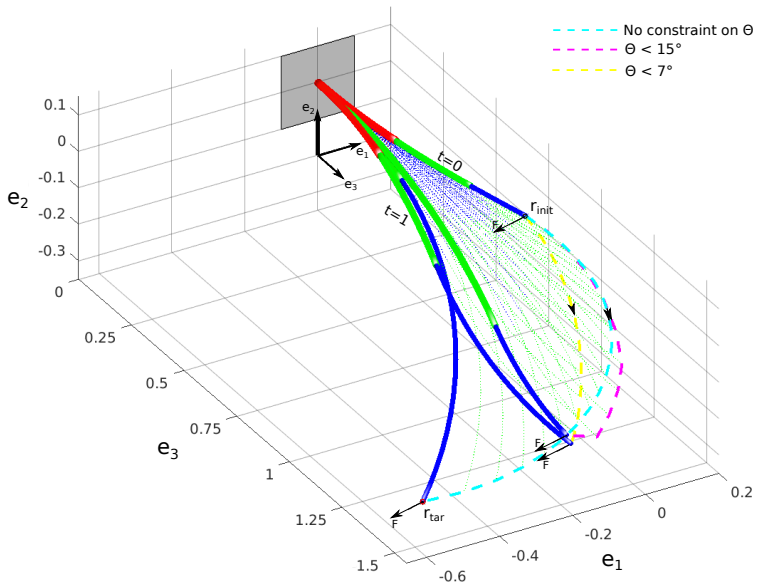

(a)

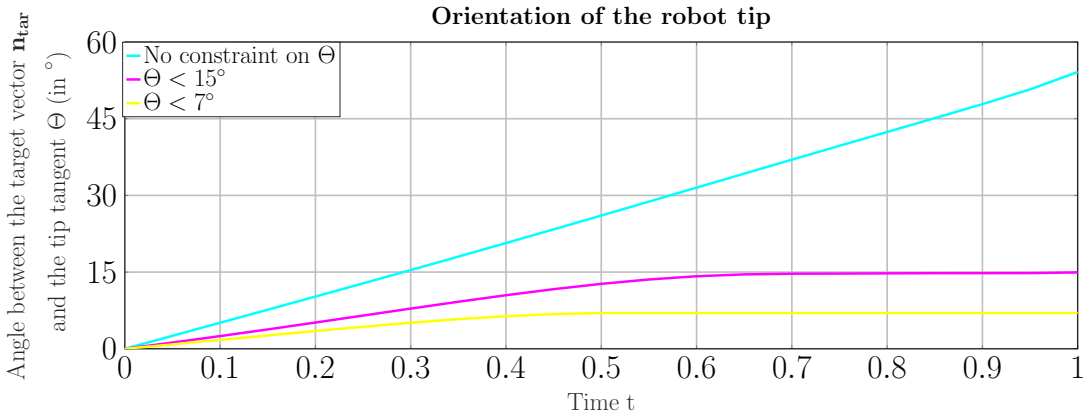

(b)

Fig. 10.13 The evolution of the CTCR as its tip moves from an initial point $\mathbf{r_{init}}$ to $\mathbf{r_{tar}} = [0.160, 0.167, 0.767]^T$ with its tip orientation restricted through the inequality constraint $\Theta \leq \theta_{\text{tol}}$. a) The time evolution of the robot state for different values of θ_{tol}. b) The Θ vs. t plot during the navigation for different values of θ_{tol}.

during this navigation task. When no inequality constraint is imposed on the tip orientation, the primary goal of guiding the robot tip to $\mathbf{r_{tar}}$ is accomplished. However, when the inequality is enforced with a tolerance of $15°$, the optimization algorithm fails to determine a local minimum solution in which the tip reaches the target $\mathbf{r_{tar}}$. The robot attains a configuration where its tip approaches close to the target $\mathbf{r_{tar}}$ without violating the inequality constraint. On further tightening the tolerance to $7°$, the distance between the final tip position and $\mathbf{r_{tar}}$ increases. From Figure 10.13b, we notice that the inequality constraint in the cases of $\theta_{\text{tol}} = 15°$ and $\theta_{\text{tol}} = 7°$ is active for a brief period of motion in the time interval $[0, 1]$, unlike the prior case, where it is active only momentarily at $t = 1$.

In these circumstances, the solutions cannot be further improved without compromising any objectives, and therefore, they lie on the *pareto front* or *pareto outcome* (Section 8.5). One of the competing objectives must be degraded to attain the desired goal. In the present context, if reaching the target point is the primary goal, then the value of θ_{tol} must be further increased.

10.3 Fixed Tip Position with Adjustable Orientation

In the final example, we intend to direct the robot tip to a prescribed orientation $\mathbf{n_{tar}}$ while maintaining its position fixed. The prescribed path in (9.7) is provided as a single point for this purpose, i.e., $\mathbf{r_{path}}(t) = \mathbf{r_{init}} = \mathbf{r_{tar}}$, which means the robot's tip is required to remain at this location throughout the maneuver. Optimization is performed by penalizing the deviation of the robot tip from the target $\mathbf{r_{tar}}$. The penalizing terms $\bar{\lambda}_0 = 400$, $\bar{\lambda}_1 = 100$, $\bar{\lambda}_2 = 0$ and $\bar{\lambda}_3 = 5$, and an initial configuration with control parameters $\mathbf{y}(0) = [0.5, 3.64, 3.84, 0.4, 0.6, 0.5]$ are used for the implementation. Figure 10.14 shows the evolution of robot configurations as its tip tangent approaches the target $\mathbf{n_{tar}} = [0, 0, 1]^T$ while ensuring that the tip remains closer to the target $\mathbf{r_{tar}}$. We implemented the optimization by employing $\bar{\lambda} = 0$ in intermediate path and $\bar{\lambda} = 2, 3$ at the final time. In every situation, aligning the tip precisely along the specified

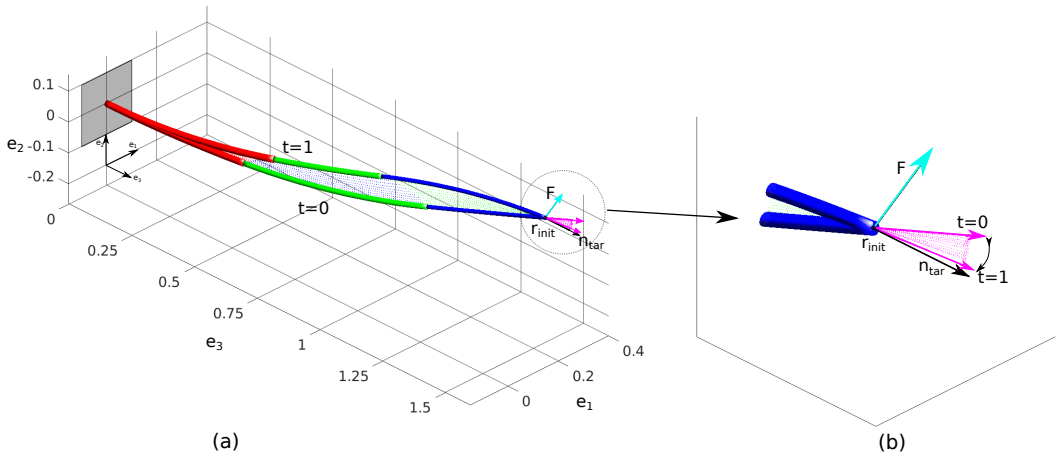

Fig. 10.14 a) The maneuver of the CTCR with its tip staying close to the initial point $\mathbf{r_{init}} \equiv \mathbf{r_{tar}}$ and the tip tangent (in magenta) approaching the target $\mathbf{n_{tar}} = [0, 0, 1]^T$(in black). b) The enlarged view of the region around the tip is shown clearly indicating the target $\mathbf{n_{tar}}$ and intermediate tip tangents during the maneuver.

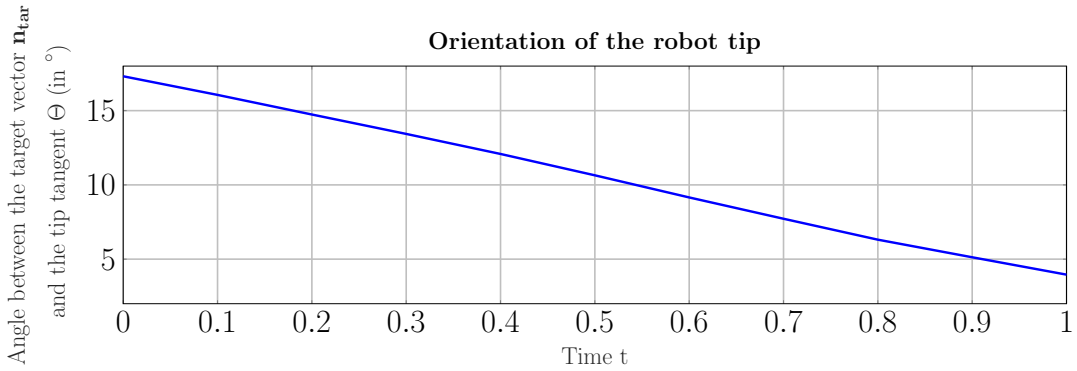

Fig. 10.15 The plot of Θ as a function of time t. Its value approaches $\approx 5^\circ$ at the final time ($t = 1$).

target $\mathbf{n_{tar}}$ may not be feasible. In these instances, the tip aligns as closely as possible with the target orientation $\mathbf{n_{tar}}$. In this illustration, the tangent of the robot tip at the final time $t = 1$ is $[0, 0.08, 0.99]^T$ and is indeed closer to $\mathbf{n_{tar}}$. In addition, the tip deviates slightly from $\mathbf{r_{tar}}$ during the maneuver. The evolution of the angle between the tip tangent and the target vector Θ is displayed in Figure 10.15. We notice that the angle Θ decreases, indicating that the robot tip is aligning with $\mathbf{n_{tar}}$. The value of Θ approaches zero, although never quite reaches it in this example.

10.4 Outlook

We formulated an open-loop, gradient-based navigation method for steering CTCRs in various tasks, which encompass tip path, tip orientation, and covered volume considerations. The obtained numerical results align with the expected outcomes and intuition. These optimization problems simulate several surgical tasks and may aid in the planning of precise and dexterous activities. For instance, the second example where the robot is guided to follow a specified path while maintaining a prescribed tip orientation, simulates gentle insertion of a needle into tissue with slight orientation adjustments. The third example, where the robot maintains its tip location while changing its orientation, mimics the cutting or tearing operation, where the robot tip holds a piece of tissue and changes its orientation with minimal positional adjustments. The presented examples illustrate the wide range of precise and dexterous activities achievable through optimization techniques.

CHAPTER 11

Conclusions and Future work

We have investigated the behavior of tip-loaded intrinsically curved elastic rod structures clamped at one end using variational principles. Intrinsic curvature is often neglected in studying rod problems as it stimulates complicated mechanics and geometrically nonlinear behavior. This study is of scientific significance as it has potential applications in the rapidly evolving field of soft robotics. Many soft robotic devices utilize intrinsically curved rods or a combination of them to generate flexible mechanisms, such as in CTCRs. We have presented the mechanical model of the elastic rods and CTCRs subject to a tip load and analyzed their stability properties. Furthermore, we integrated this mechanical model with the *optimal control* techniques to cast the robot navigation as an open-loop *optimal control problem*.

The equilibria of these relevant elastic rod structures were obtained as stationary points of an energy functional, resulting from strains in the elastic rods as well as the work performed by external forces and moments. We adapted the classic *Jacobi condition* Bolza (1904), generally shown only for fixed-fixed boundary conditions, to the problems with fixed-free boundary conditions to verify if these equilibria are local minimizers. The *Jacobi operator* of this class of problems has similar properties (self-adjoint) as that of the case with fixed-fixed ends, and, as a consequence, we extended the notion of *Morse index* to them. To replicate the real-world application, we expressed the variational problem in terms of varying parameters at the clamped end. In our applications, this parameter characterized the rotation, and the system is 2π- periodic about it. We verified that if *distinguished bifurcation diagrams* also agree with the unconstrained calculus of problems subject to fixed-free boundary conditions, and when the parameter acts through non-homogenous boundary conditions. Additionally, we generalized the concepts of *Jacobi condition*, the notion of the index, and *distinguished bifurcation diagrams* to the problems with the discontinuous integrand by utilizing the matching conditions at the points of discontinuity.

The results discussed in Chapter 5 have revealed new insights into the impact of intrinsic curvature on the hysteresis behavior of tip-loaded elastic rods. We applied *Kirchhoff Rod theory* to model the elastic rods, and the Hamiltonian formulation of the equilibria Dichmann et al. (1996) provided the equilibria for varying clamp angles. Their stability was analyzed by computing the *conjugate points*. For smaller curvatures, the rod exhibited only stable equilibria, whereas, for higher curvatures, it exhibited several unstable equilibria, implicating a snap-back instability. The rod assumed multiple spatial equilibria for the same clamp angle, depending

on its history, and hence; for this reason, we used the term hysteresis. Interestingly, only the intermediate values of the loads or rod lengths resulted in this hysteresis behavior. The increase in the tip load or tube length destabilized some equilibria and later stabilized them. This result is in stark contrast to the case of naturally straight rods, where an increase in length or load never had a stabilizing effect on the equilibria. For instance, in the case of intrinsically straight rods, if we increase the tip load or rod length beyond the critical buckling point, the trivial solutions become unstable and do not stabilize with a further increase in load or length. The *bifurcation surface* plots presented a better understanding of the dependence of hysteresis on the system parameters. In all cases, we found that the snapping region only existed as an isolated island within the parameter space. These findings have implications for the design and control of a soft robotic arm where its length or tip-load can be varied to approach or evade the snapping motion. Another significant finding was the impact of the torsion component and the arm of the lever arm on the hysteresis behavior. Both parameters acted as symmetry-breaking parameters of the system. In addition, for some values of these parameters, we obtained five spatial equilibria for the same clamp angle, three of which are unstable. In this scenario, the *distinguished bifurcation diagrams* accurately predicted the *index* for these equilibria. However, the *index* of one equilibrium must be determined using *conjugate points* along the solution path to employ these plots.

We limited our study to rod lengths smaller than the full circle. A further extension would be to consider studying full circle or n-circles. For such problems, the problem of self-contact should also be addressed. Multiple equilibria with an index greater than two are expected. In these cases, the *distinguished bifurcation diagrams* come in more handy. Finally, extending the study to elastic rods with mass or elliptic cross-sections could yield interesting results. Another possible extension would be to include the constrained case where the free end of the elastic rod is held at a fixed location (not clamped) instead of a dead load. This scenario would mimic the *ratchet* behavior of the guide wires (Warner, 1997). This so-called isoperimetric case would represent a slight generalization of the study by Manning et al. (1998).

The extended *Jacobi condition* was used to analyze the stability of CTCR configurations subject to tip loads. The backbone of CTCRs is analogous to a naturally curved elastic rod for any fixed imposed angles of the tubes at the root and, therefore, inherits its non-linear characteristics. Moreover, it consists of multiple sections with piecewise properties, further increasing the complexity. In CTCRs, snapping can occur when the relative rotation of tubes is varied or when the tip load changes its direction and a combination of them. The former case is well known. We studied the effect of tip load on hysteresis behavior using *distinguished bifurcation diagrams*. The ability of the tip load to act as a stabilizing agent or a destabilizing agent facilitates better for snapping-related tasks. We investigated the hysteresis behavior in a three-tube CTCR and demonstrated the effect of coupling between the sections and the tip load. In such instances, multiple instances of hysteresis were observed as the parameter was varied from 0 to 2π. *Distinguished bifurcation diagrams* are less informative when only two folds are present. The 2π periodicity of the system with respect to the bifurcation parameter, coupled with the property of the bifurcation diagrams indicating that stability changes at the fold, allows us to

demonstrate that the index oscillates between 0 and 1 between two folds. However, these diagrams are useful when there are more than two folds. In all these instances, the prediction of the index in the diagrams is verified through the computation of *conjugate points*. These results have the potential to enhance planning for more complex tasks with CTCRs. In addition, the conserved quantities arising from the Hamiltonian formulation were used to verify numerical accuracy and convergence. The impact of mesh size and the collocation points on the accuracy was highlighted. These quantities can be employed as benchmarks for setting several parameters within the numerical framework. For example, the effect of gradients supplied to Newton's method via finite differences or analytical expressions can also be verified.

The effect of clearances between the concentric tubes on the CTCR equilibria and their equilibria would be a natural extension of this work. In addition, the isoperimetric case where the tip of the CTCR is held (either clamped or fixed) would be an interesting case to be considered. This scenario is relevant in medical procedures where the manipulator at the tip holds onto tissue while performing tasks such as cutting or suturing.

We integrated the mechanical model of the CTCR with *optimal control* techniques to mathematically cast the robot's navigation as a constrained *optimal control problem*. A numerical approach was described to solve the problem, and the results demonstrate the feasibility of this method for optimization-based navigation tasks. The proposed objectives, particularly the minimum deviation objective and sweep area, achieved the desired tasks and exhibited the anticipated qualitative behavior. Some objectives may have conflicting aims in certain situations, where they should be penalized and degraded accordingly. The study also incorporated cases involving tip orientation during CTCR navigation, which has been previously under-explored in the literature. This investigation facilitates the design and planning of more complex tasks.

The current optimization framework often minimizes the covered volume or deviation term by shortening and elongating the robot in the initial and final period of motion in many instances. The effect of suppressing the dependence of this objective on length parameters, i.e.,$L_i(t)$ was also examined. The presented objectives may have less conflicting effects on each other when highly flexible CTCRs with more tubes are used. In such situations, multiple configurations can satisfy the required objectives, enabling a compromise solution that meets the requirements of conflicting objectives. However, it is computationally complex to solve problems with more than three tubes. Additionally, our study did not incorporate obstacle avoidance. It can be included in the current framework by adding an objective function given by Lyons et al. (2009); Flaßkamp et al. (2019).

The current optimization framework did not address the snapping-related issues but instead avoided them by imposing constraints on the length of the tubes. The stability of the equilibria was not determined in the *optimal control* framework, and the path obtained might lead to a snapping motion. However, the BVP solver in the optimization framework failed near the points closer to folds as the Jacobian of the collocation equations approached singularity in this

vicinity, causing an abrupt termination of the optimization program in *matlab*. A mathematical mechanism that keeps the system away from the fold-bifurcations is necessary to obtain the snap-free path. The *conjugate point* computation has the potential to serve as a proximity measure to the unstable region and can be used as a concept of proof to guide the system away from the unstable regime. For example, the determinant of the stability matrix at the fixed end, i.e., $s = 0$ in our case, can serve as a measure of proximity to the unstable regime. The closer this value is to zero, the closer the system is to the hysteresis region. This measure can be employed in *optimal control* frameworks to ensure that the system operates far from unstable regimes. Furthermore, this approach can be employed to guide the system close to the unstable regions. In these scenarios, the snapping can be utilized for energy-harnessing applications.

REFERENCES

Alfalahi, H., Renda, F., Messer, C., and Stefanini, C. (2021). Exploiting the instability of eccentric tube robots for distal force control in minimally invasive cardiac ablation. *Proceedings of the Institution of Mechanical Engineers, Part C: Journal of Mechanical Engineering Science*, 235(23):7212–7232.

Antman, S. (2006). *Nonlinear Problems of Elasticity*. Applied Mathematical Sciences. Springer, New York, second edition.

Armanini, C., Dal Corso, F., Misseroni, D., and Bigoni, D. (2017). From the elastica compass to the elastica catapult: an essay on the mechanics of soft robot arm. *Proceedings of the Royal Society A: Mathematical, Physical and Engineering Sciences*, 473(2198):20160870.

Ascher, U., Christiansen, J., and Russell, R. D. (1981). Collocation software for boundary-value odes. *ACM Transactions on Mathematical Software*, 7(2):209–222.

Baykal, C., Torres, L. G., and Alterovitz, R. (2015). Optimizing design parameters for sets of concentric tube robots using sampling-based motion planning. In *2015 IEEE/RSJ International Conference on Intelligent Robots and Systems (IROS)*, pages 4381–4387.

Bergeles, C., Gosline, A. H. C., Vasilyev, N. V., Codd, P. J., del Nido, P. J., and Dupont, P. E. (2015). Concentric tube robot design and optimization based on task and anatomical constraints. *IEEE Transactions on Robotics*, 31:67–84.

Betts, J. T. (1998). Survey of numerical methods for trajectory optimization. *Journal of guidance, control, and dynamics*, 21(2):193–207.

Betts, J. T. (2010). *Practical methods for optimal control and estimation using nonlinear programming*. SIAM, Philadelphia, PA, second edition.

Bliss, G. A. and Mason, M. (1906). A problem of the calculus of variations in which the integrand is discontinuous. *Transactions of the American Mathematical Society*, 7(2):325–336.

Boggs, P. T. and Tolle, J. W. (1995). Sequential quadratic programming. *Acta Numerica*, 4:1–51.

Bolza, O. (1904). *Lectures on the Calculus of Variations*, volume 14 of *2*. The Decenniel Publications of the University of Chicago Press, The University of Chicago Press.

Bryson, A. E. and Ho, Y. C. (2018). *Applied Optimal Control: Optimization, Estimation, and Control*. Routledge, New York.

Burgner, J., Rucker, D. C., Gilbert, H. B., Swaney, P. J., Russell, P. T., Weaver, K. D., and Webster, R. J. (2013). A telerobotic system for transnasal surgery. *IEEE/ASME transactions on mechatronics : a joint publication of the IEEE Industrial Electronics Society and the ASME Dynamic Systems and Control Division*, 19(3):996—1006.

Burgner, J., Swaney, P. J., Rucker, D. C., Gilbert, H. B., Nill, S. T., Russell, P. T., Weaver, K. D., and Webster III, R. J. (2011). A bimanual teleoperated system for endonasal skull base surgery. In *2011 IEEE/RSJ International Conference on Intelligent Robots and Systems*, pages 2517–2523.

Burgner-Kahrs, J., Gilbert, H. B., Granna, J., Swaney, P. J., and Webster, R. J. (2014). Workspace characterization for concentric tube continuum robots. In *2014 IEEE/RSJ International Conference on Intelligent Robots and Systems*, pages 1269–1275.

Caratheodery (1967). *Calculus of Variations and Partial Differential Equations of the first Order, Part II: Calculus of Variations*. Holden-Day Series in Mathematical Physics. Holden-Day, Inc, San Francisco.

Cole, N. L. (1940). The index theorem for a calculus of variations problem in which the integrand is discontinuous. *American Journal of Mathematics*, 62:249.

Dhanakoti, S., Maddocks, J., and Weiser, M. (2022). Navigation of concentric tube continuum robots using optimal control. In *Proceedings of the 19th International Conference on Informatics in Control, Automation and Robotics - ICINCO*, pages 146–154. INSTICC, SciTePress.

Dichmann, D. J., Li, Y., and Maddocks, J. H. (1996). Hamiltonian formulations and symmetries in rod mechanics. In Mesirov, J. P., Schulten, K., and Sumners, D. W., editors, *Mathematical Approaches to Biomolecular Structure and Dynamics*, pages 71–113. Springer New York, New York, NY.

Dichmann, D. J. and Maddocks, J. H. (1996). An impetus-striction simulation of the dynamics of an elastica. *Journal of Nonlinear Science*, 6(3):271–292.

Doedel, E., Keller, H. B., and Kernevez, J. P. (1991a). Numerical analysis and control of bifurcation problems (i): Bifurcation in finite dimensions. *International Journal of Bifurcation and Chaos*, 01(03):493–520.

Doedel, E., Keller, H. B., and Kernevez, J. P. (1991b). Numerical analysis and control of bifurcation problems (ii): Bifurcation in infinite dimensions. *International Journal of Bifurcation and Chaos*, 01(04):745–772.

Doedel, E. J. (2007). Lecture notes on numerical analysis of nonlinear equations. In Krauskopf, B., Osinga, H. M., and Galán-Vioque, J., editors, *Numerical Continuation Methods for Dynamical Systems: Path following and boundary value problems*, pages 1–49. Springer Netherlands, Dordrecht.

Doedel, E. J., Champneys, A. R., Dercole, F., Fairgrieve, T. F., Kuznetsov, Y. A., Oldeman, B., Paffenroth, R., Sandstede, B., Wang, X., and Zhang, C. (2007). Auto-07p: Continuation and bifurcation software for ordinary differential equations.

Domokos, G. and Healey, T. J. (2005). Multiple helical perversions of finite, intristically curved rods. *International Journal of Bifurcation and Chaos*, 15(03):871–890.

Ehrgott, M. (2005). *Multicriteria optimization*, volume 491. Springer Science and Business Media, second edition.

Enright, P. J. and Conway, B. A. (1992). Discrete approximations to optimal trajectories using direct transcription and nonlinear programming. *Journal of Guidance, Control, and Dynamics*, 15(4):994–1002.

Flaßkamp, K., Worthmann, K., Mühlenhoff, J., Greiner-Petter, C., Büskens, C., Oertel, J., Keiner, D., and Sattel, T. (2019). Towards optimal control of concentric tube robots in stereotactic neurosurgery. *Mathematical and Computer Modelling of Dynamical Systems*, 25(6):560–574.

Garriga-Casanovas, A. and Rodriguez y Baena, F. (2018). Complete follow-the-leader kinematics using concentric tube robots. *The International Journal of Robotics Research*, 37(1):197–222.

Gelfand, I. and Fomin, S. (1963). *Calculus of Variations*. Prentice Hall, Inc, New Jersey.

Gilbert, H. B., Hendrick, R. J., and Webster, R. J. (2016). Elastic stability of concentric tube robots: A stability measure and design test. *IEEE Transactions on Robotics*, 32:20–35.

Gilbert, H. B., Neimat, J., and Webster, R. J. (2015). Concentric tube robots as steerable needles: Achieving follow-the-leader deployment. *IEEE Transactions on Robotics*, 31(2):246–258.

Goldstein, H. (1951). *Classical Mechanics*. Addison-Wesley Press, Inc, Massachusetts.

Golubitsky, M. and Schaeffer, D. G. (2014). *Singularities and Groups in Bifurcation Theory*. Springer-Verlag, New York.

Granna, J. (2019). *Multi-objective particle swarm optimization for the structural design of concentric tube continuum robots for medical applications*. PhD thesis, Gottfried Wilhelm Leibniz Universität Hannover.

Granna, J., Godage, I. S., Wirz, R., Weaver, K. D., Webster, R. J., and Burgner-Kahrs, J. (2016). A 3d volume coverage path planning algorithm with application to intracerebral hemorrhage evacuation. *IEEE Robotics and Automation Letters*, 1(2):876–883.

Graves, L. M. (1930). Discontinuous solutions in space problems of the calculus of variations. *American Journal of Mathematics*, 52:1.

Griewank, A. and Walther, A. (2008). *Evaluating derivatives: Principles and Techniques of Algorithmic Differentiation*. SIAM, Philadelphia, PA, second edition.

Ha, J., Park, F. C., and Dupont, P. E. (2015). Elastic stability of concentric tube robots subject to external loads. *IEEE Transactions on Biomedical Engineering*, 63(6):1116–1128.

Hargraves, C. R. and Paris, S. W. (1987). Direct trajectory optimization using nonlinear programming and collocation. *Journal of Guidance, Control, and Dynamics*, 10(4):338–342.

Healey, T. J. and Mehta, P. G. (2005). Straightforward computation of spatial equilibria of geometrically exact cosserat rods. *International Journal of Bifurcation and Chaos*, 15(03):949–965.

Herman, A. L. and Conway, B. A. (1996). Direct optimization using collocation based on high-order gauss-lobatto quadrature rules. *Journal of Guidance, Control, and Dynamics*, 19(3):592–599.

Hestenes, M. R. (1966). *Calculus of Variations and Optimal Control Theory*. John Wiley and Sons, Inc, New York - London - Sydney.

Hoffman, K. A. (2005). Stability results for constrained calculus of variations problems: an analysis of the twisted elastic loop. *Proceedings of the Royal Society A: Mathematical, Physical and Engineering Sciences*, 461(2057):1357–1381.

Hoffman, K. A. and Manning, R. S. (2009). An extended conjugate point theory with application to the stability of planar buckling of an elastic rod subject to a repulsive self-potential. *SIAM Journal on Mathematical Analysis*, 41(2):465–494.

Hoffman, K. A., Manning, R. S., and Paffenroth, R. C. (2002). Calculation of the stability index in parameter-dependent calculus of variations problems: Buckling of a twisted elastic strut. *SIAM Journal on Applied Dynamical Systems*, 1(1):115–145.

Keller, H. B. (1977). Numerical solution of bifurcation and nonlinear eigenvalue problems. *Applications of Bifurcation Theory*.

Kierzenka, J. and Shampine, L. F. (2001). A BVP solver based on residual control and the Matlab PSE. *ACM Transactions on Mathematical Software*, 27:299–316.

Kierzenka, J. and Shampine, L. F. (2008). A bvp solver that controls residual and error. *Journal of Numerical Analysis, Industrial and Applied Mathematics*, 3(1-2):27–41.

Kumar, A. and Healey, T. J. (2010). A generalized computational approach to stability of static equilibria of nonlinearly elastic rods in the presence of constraints. *Computer Methods in Applied Mechanics and Engineering*, 199(25-28):1805–1815.

Kuznetsov, V. and Levyakov, S. (2002). Complete solution of the stability problem for elastica of euler's column. *International Journal of Non-linear Mechanics*, 37(6):1003–1009.

Lane, D. T. (2012). Stability of discontinuous elastic rods with applications to nanotube junctions. Master's thesis, University College London, London, UK.

Laschi, C., Cianchetti, M., Mazzolai, B., Margheri, L., Follador, M., and Dario, P. (2012). Soft robot arm inspired by the octopus. *Advanced Robotics*, 26:709 – 727.

Lazarus, A., Miller, J., and Reis, P. (2013a). Continuation of equilibria and stability of slender elastic rods using an asymptotic numerical method. *Journal of the Mechanics and Physics of Solids*, 61(8):1712–1736.

Lazarus, A., Miller, J. T., Metlitz, M. M., and Reis, P. M. (2013b). Contorting a heavy and naturally curved elastic rod. *Soft Matter*, 9:8274–8281.

Levyakov, S. V. and Kuznetsov, V. V. (2010). Stability analysis of planar equilibrium configurations of elastic rods subjected to end loads. *Acta Mechanica*, 211(1):73–87.

Li, Y. and Maddocks, J. H. (1996). On the computation of equilibria of elastic rods part i:integrals, symmetry and a hamiltonian formulation. *preprint*.

Lyons, L. A., Webster, R. J., and Alterovitz, R. (2009). Motion planning for active cannulas. In *2009 IEEE/RSJ International Conference on Intelligent Robots and Systems*, pages 801–806.

Maddocks, J. H. (1984). Stability of nonlinearly elastic rods. *Archive for Rational Mechanics and Analysis*, 85(4):311–354.

Maddocks, J. H. (1985). Restricted quadratic forms and their application to bifurcation and stability in constrained variational principles. *SIAM Journal on Mathematical Analysis*, 16(1):47–68.

Maddocks, J. H. (1987). Stability and folds. *Archive for Rational Mechanics and Analysis*, 99(4):301–328.

Majidi, C. (2014). Soft robotics: A perspective—current trends and prospects for the future. *Soft Robotics*, 1:5–11.

Majumdar, A. and Raisch, A. (2014). Stability of twisted rods, helices and buckling solutions in three dimensions. *Nonlinearity*, 27(12):2841.

Manning, R. S. and Hoffman, K. A. (2001). Stability of n-covered circles for elastic rods with constant planar intrinsic curvature. *Journal of Elasticity and the Physical Science of Solids*, 62(1):1–23.

Manning, R. S., Rogers, K. A., and Maddocks, J. H. (1998). Isoperimetric conjugate points with application to the stability of dna minicircles. *Proceedings of the Royal Society of London. Series A: Mathematical, Physical and Engineering Sciences*, 454(1980):3047–3074.

Marler, R. T. and Arora, J. S. (2004). Survey of multi-objective optimization methods for engineering. *Structural and Multidisciplinary Optimization*, 26(6):369–395.

McMillen, T., Goriely, A., et al. (2002). Tendril perversion in intrinsically curved rods. *Journal of Nonlinear Science*, 12(3):241–281.

Miller, J. T., Lazarus, A., Audoly, B., and Reis, P. M. (2014). Shapes of a suspended curly hair. *Physical Review Letters*, 112:068103.

Mitros, Z., Sadati, S., Henry, R., Cruz, L. D., and Bergeles, C. (2021). From theoretical work to clinical translation: Progress in concentric tube robots. *Annual Review of Control Robotics and Autonomous Systems*, 5:335–359.

Morse, M. (1951). *Introduction to Analysis in the Large*. Institute for Advanced Study, Princeton, NJ.

Neukirch, S. and Henderson, M. E. (2002). Classification of the spatial equilibria of the clamped elastica: Symmetries and zoology of solutions. *Journal of Elasticity*, 68(1):95–121.

Nocedal, J. and Wright, S. J. (2006). *Numerical Optimization*. Springer, New York, second edition.

O'Reilly, O. M. and Peters, D. M. (2011). On stability analyses of three classical buckling problems for the elastic strut. *Journal of Elasticity*, 105(1):117–136.

Potra, F. A. and Wright, S. J. (2000). Interior-point methods. *Journal of Computational and Applied Mathematics*, 124(1-2):281–302.

Riojas, K. E., Hendrick, R. J., and Webster III, R. J. (2018). Can elastic instability be beneficial in concentric tube robots? *IEEE Robotics and Automation Letters*, 3(3):1624–1630.

Rogers, K. A. (1997). *Stability exchange in Parameter-Dependent Constrained Variational Principles with Applications to Elastic Rod models of DNA Minicirlces*. PhD thesis, University of Maryland, College Park, USA.

Rucker, D. C., Jones, B. A., and Webster III, R. J. (2010). A geometrically exact model for externally loaded concentric-tube continuum robots. *IEEE transactions on Robotics : a publication of the IEEE Robotics and Automation Society*, 26(5):769–780.

Rucker, D. C., Webster III, R. J., Chirikjian, G. S., and Cowan, N. J. (2010). Equilibrium conformations of concentric-tube continuum robots. *The International Journal of Robotics Research*, 29(10):1263–1280.

Sagan, H. (1969). *Introduction to the Calculus of Variations*. McGraw-Hill, Inc., New York.

Shuster, M. D. (1993). A survey of attitude representation. *Journal of The Astronautical Sciences*, 41:439–517.

Sipos, A. A. and Várkonyi, P. L. (2020). The longest soft robotic arm. *International Journal of Non-Linear Mechanics*, 119:103354.

Swaney, P. J., Gilbert, H. B., Webster, R. J., Russell, P. T., and Weaver, K. D. (2014). Endonasal skull base tumor removal using concentric tube continuum robots: A phantom study. *Journal of Neurological Surgery—Part B*, 76:145 – 149.

Teschl, G. (2012). *Ordinary differential equations and dynamical systems*, volume 140 of *Graduate Studies in Mathematics*. American Mathematical Society, Providence, Rhode Island.

Warner, J. A. (1997). Numerical simulations of elastic rods. Master's thesis, University of Maryland, College Park, USA.

Yip, M. C., Sganga, J., and Camarillo, D. B. (2017). Autonomous control of continuum robot manipulators for complex cardiac ablation tasks. *Journal of Medical Robotics Research*, 2:1750002:1–1750002:13.

Appendices

Appendix A

Strum-Liouville Problem

We first present the results of the standard *Sturm-Liouville* operator usually applied on a scalar variable $y(s)$. A second-order self-adjoint operator given by

$$\mathcal{L}y(s) \equiv -\frac{d}{ds}\left[p(s)\frac{d}{ds}y(s)\right] - q(s)y(s),$$

and satisfying the following boundary conditions in the Hilbert space $L_2(0,l)$

$$\begin{aligned}\alpha_1 y(0) + \alpha_2 y'(0) = 0, \quad \alpha_1^2 + \alpha_2^2 > 0,\\ \beta_1 y(l) + \beta_2 y'(l) = 0, \quad \beta_1^2 + \beta_2^2 > 0,\end{aligned}$$

is called *Sturm-Liuoville* operator (Teschl, 2012). The functions $p(s), q(s)$ and $p'(s)$ are assumed to be continuous real functions and the $p(s)$ is positive definite for all $s \in [0,l]$. We have $\alpha_2 = 0$ for Dirichlet boundary conditions, $\alpha_1 = 0$ for *Neumann* boundary conditions, and a combination of these conditions for *Natural boundary conditions*. Then, consider the eigenvalue problem

$$\mathcal{L}y = \rho(s)y, \qquad \frac{d}{ds}\left(p(s)\frac{dy}{ds}\right) + q(s)y(s) + \rho y(s) = 0.$$

The combination of *comparison* and *separation* theorems (Teschl, 2012) leads to the following properties on the eigenvalues ρ and the eigenfunctions $y(s)$.

1. The eigenvalues $\rho_1, \rho_2, \ldots$ are real and can be numbered so that

$$\rho_1 < \rho_2 < \rho_3 < \ldots \rho_n \ldots \infty.$$

2. Corresponding to each eigenvalue ρ_n, there exists an unique eigenfunction $y_n(s)$ with exactly $n-1$ zeros in the interval $[0,l]$.

3. These normalized eigenfunctions form an orthonormal basis under the inner product in $L^2([0,l])$

$$\langle y_n(s), y_m(s)\rangle = \int_0^l y_n(s)y_n(s)ds = \delta_{n,m}.$$

The presented *Sturm-Liouville* problem for a scalar valued function $y(s)$ can be extended to the our required vector of functions $\mathbf{y}(s)$ after some matrix and operator arithmetic (for e.g. see Manning et al. (1998)(Appendix)) as long as the operator $\mathcal{S}$ is self-adjoint.

Now, we will summarize the properties stated in Chapter 2. First, consider the case with fixed-fixed boundary conditions where the variations $h(s)$ belong to the class of admissible variations:

$$\mathcal{A}_d \equiv \left\{h(s) \in \mathcal{H}^2[0,l]) : h(0) = \mathbf{0} = h(\sigma)\right\}.$$

Property 1 For a given σ, the operator $\mathcal{S}$ has countably infinite number of eigenvalues: $\rho_1(\sigma) \leq \rho_2(\sigma) \leq \ldots$ each with finite multiplicity.

Given the Legendre's strengthened condition, this property is a direct consequence of the *Sturm-Liouville* operator.

Property 2 Each eigenvalue $\rho_m(\sigma)$ is monotonically decreasing function of σ.
We need some machinery to prove this property. Let ρ_i be the i th smallest eigenvalue and h_i corresponding eigenfunctions. We define a sequence of subspaces as

$$\begin{aligned}
\mathcal{A}_1 &= \{h \in \mathcal{A}([0,\sigma]) : \|h\|_2 = 1\},\\
\mathcal{A}_2 &= \{h \in \mathcal{A}([0,\sigma]) : \|h\|_2 = 1, \langle h, h_1\rangle = 0\},\\
\mathcal{A}_3 &= \{h \in \mathcal{A}([0,\sigma]) : \|h\|_2 = 1, \langle h, h_1\rangle = \langle h, h_2\rangle = 0\},
\end{aligned}$$

and so on. $\mathcal{A}_m$ is the allowed variation orthogonal to first m eigenfunctions. Then, the eigenvalues of the operator $\mathcal{S}$ are given by the variational principle

$$\rho_m(\sigma) = \min_{h \in \mathcal{A}_m} \frac{\langle \mathcal{S}h, h\rangle}{\langle h, h\rangle}. \tag{A.1}$$

Consider $\sigma_1 < \sigma_2$ and define a function $j_i(s)$ in the interval $[0,\sigma_2]$ by appending a zero function to the eigenfunction h_i on $[0,\sigma_1]$ as

$$j_i(s) = \begin{cases} h_i(s,\sigma_1), & 0 \leq s < \sigma_1 \\ 0, & \sigma_1 < s \leq \sigma_2 \end{cases}, \quad i = 1,2,...m.$$

Now choose a_k not all zero so that $\sum_{k=1}^{m} a_k j_k$ is orthogonal to $h_1(s;\sigma_2), \ldots h_{m-1}(s;\sigma_2)$ on $[0,\sigma_2]$. Then, according to A.1, we have

$$\rho_m(\sigma_2) \leq \int_0^{\sigma_2} \left[\sum_{i=1}^{m} a_i j_i(s)\right] \mathcal{S} \left[\sum_{i=1}^{m} a_i j_i(s)\right] ds.$$

The integrand vanishes for the appended zero function and therefore, the integration limits can

be changed to $[0, \sigma_1]$

$$\rho_m(\sigma_1) \leq \int_0^{\sigma_1} \left[\sum_{i=1}^{m} a_i h_i(s, \sigma_1) \right] \mathcal{S} \left[\sum_{i=1}^{m} a_i h_i(s, \sigma_1) \right],$$

h_i are orthogonal eigenfunctions of $\mathcal{S}$ and, therefore

$$\rho_m(\sigma_2) \leq \sum_{i=1}^{m} a_i a_k \rho_k(\sigma) \int_0^{\sigma_2} h_i h_k ds = \sum_{i=1}^{m} (a_i)^2 \rho_k(\sigma) \leq \rho_m(\sigma_1).$$

Property 3 For σ sufficiently close to 0, the eigenvalues of $\mathcal{S}$ are all positive.

The *Sturm-Liouville* operator can be asymptotically written as a Taylor expansion around $s = 0$, and consider only zeroth order terms i.e., $p(s) \approx p(0)$ and $q(s) \approx q(0)$

$$\mathcal{L}y(s) \equiv -\frac{d}{ds}\left[p(0) \frac{d}{ds} y(s) \right] - q(0) y(s),$$

and, consequently, the following eigenvalue problem is obtained

$$p(0)h'' + (q(0) + \rho)\, h = 0. \tag{A.2}$$

This equation (A.2) has non-trivial solutions of the form

$$h(s) = a \sin\left(\sqrt{q(0) + \rho} \right) s + b \cos\left(\sqrt{q(0) + \rho} \right) s, \quad q(0) + \rho > 0,$$

and the boundary condition $h(0) = h(\sigma) = 0$ fetches the relation

$$\rho_n = -q(0) + \frac{n^2 \pi^2}{\sigma^2}.$$

For σ very close to zero, the value of ρ_n is positive for all n.

Now consider the second-order differential operator corresponding to the case with fixed-free boundary conditions where the variations $h(s)$ belong to the class of admissible variations:

$$\mathcal{B}_d \equiv \left\{ h(s) \in \mathcal{H}^2[0, l]) : h(l^*) = 0, h'(l) = 0, h(l) = 1 \right\}.$$

Property 1: For a given l^*, the operator $\mathcal{S}$ has countably infinite number of eigenvalues: $\rho_1(l^*) \leq \rho_2(l^*) \leq \ldots$ each with finite multiplicity. The second-order *Jacobi operator* is a *Sturm-Liouville* operator for this new set of boundary conditions as long as the Legendre's strengthened condition is satisfied. Therefore, the eigenvalues of the $\mathcal{S}$ satisfy $\rho_1 < \rho_2 < \ldots$.

Property 2: Each eigenvalue $\rho_m(l^*)$ is monotonically decreasing function of l^*.
This proof is a similar generalization of the previous case. If ρ_i is the i th smallest eigenvalue

and h_i corresponding eigenfunctions. We define a sequence of subspaces as

$$\mathcal{B}_1 = \{h \in \mathcal{A}([l^*, l]) : \|h\|_2 = 1\},$$
$$\mathcal{B}_2 = \{h \in \mathcal{A}([l^*, l]) : \|h\|_2 = 1, \langle h, h_1\rangle = 0\},$$
$$\mathcal{B}_3 = \{h \in \mathcal{A}([l^*, l]) : \|h\|_2 = 1, \langle h, h_1\rangle = \langle h, h_2\rangle = 0\},$$

and so on. $\mathcal{B}_m$ is the allowed variation orthogonal to first m eigenfunctions. Then, the eigenvalues of the operator $\mathcal{S}$ are given by the variational principle

$$\rho_m(\sigma) = \min_{h \in \mathcal{A}_m} \frac{\langle \mathcal{S}h, h\rangle}{\langle h, h\rangle}. \tag{A.3}$$

Consider $l_2^* < l_1^*$ and define a function j_i in the interval $[l_2^*, l]$ by joining a zero function to the eigenfunction h_i on $[l_1^*, l]$

$$j_i(s) = \begin{cases} h_i(s, (l_1^*)), & l_1^* < s \le l, \\ 0, & l_2^* \le s < l_1^*. \end{cases}$$

Now choose a_k not all zero so that $\sum_{k=1}^m a_k j_k$ is orthogonal to $h_1(s; l_2^*), \ldots h_{m-1}(s; l_2^*)$ on $[l_2^*, l]$. Then, according to A.3, we have

$$\rho_m(l_2^*) \le \int_{l_2^*}^{l} \left[\sum_{i=1}^m a_i j_i(s)\right] \mathcal{S}\left[\sum_{i=1}^m a_i j_i(s)\right] ds.$$

The integrand vanishes for the appended zero function and therefore, the integration limits can be changed to $[l_1^*, l]$

$$\rho_m(l_2^*) \le \int_{l_1^*}^{l} \left[\sum_{i=1}^m a_i h_i(s, l_1^*)\right] \mathcal{S}\left[\sum_{i=1}^m a_i h_i(s, l_1^*)\right].$$

Here, h_i are orthogonal eigenfunctions of $\mathcal{S}$ and, therefore

$$\rho_m(l_2^*) \le \sum_{i=1}^m a_i a_k \rho_k(l_2^*) \int_0^{l_2^*} h_i h_k ds = \sum_{i=1}^m (a_i)^2 \rho_k(\sigma) \le \rho_m(l_1^*),$$

and by changing the integration limits (ρ_1, l) followed by the similar calculations, we obtain

$$\rho_m(l_2^*) \ge \rho_m(l_1^*).$$

Property 3: For l^* sufficiently close to l, the eigenvalues of $\mathcal{S}$ are all positive.

The *Sturm-Liouville* operator can be asymptotically written as a Taylor expansion around $s = l$ and consider only zeroth order terms i.e., $p(s) \approx p(l)$ and $q(s) \approx q(l)$

$$\mathcal{L}y(s) \equiv -\frac{d}{ds}\left[p(l)\frac{d}{ds}y(s)\right] - q(l)y(s),$$

and as a result, we yield the following eigenvalue problem

$$p(l)h'' + (q(l) + \rho)\, h = 0.$$

This equation has non-trivial solutions of the form

$$h(s) = a \sin\left(\sqrt{q(l) + \rho}\right) s + b \cos\left(\sqrt{q(l) + \rho}\right) s, \quad q(l) + \rho > 0,$$

and the boundary conditions $h(l^*) = 0$ and $h'(l) = 0$ results in

$$\rho_n = -q(l) + \frac{(2n-1)^2 \pi^2}{4\,(l - l^*)^2}, \quad n = 1, 2, \ldots, \infty.$$

For l^* sufficiently close to l, the value of ρ_n is positive for all n.

Appendix B

Derivatives of Directors

This appendix records the derivatives of directors with respect to $\mathbf{q}$ and their projection on $\mathbf{B}_1\mathbf{q}, i = 1, 2, 3$. The directors of the frame with a quadratic normalization are given by

$$\mathbf{d}_1 = \frac{1}{|\mathbf{q}|^2}\begin{bmatrix} q_1^2 - q_2^2 - q_3^2 + q_4^2 \\ 2\left(q_1 q_2 + q_3 q_4\right) \\ 2\left(q_1 q_3 - q_2 q_4\right) \end{bmatrix}, \qquad \mathbf{d}_2 = \frac{1}{|\mathbf{q}|^2}\begin{bmatrix} 2\left(q_1 q_2 - q_3 q_4\right) \\ -q_1^2 + q_2^2 - q_3^2 + q_4^2 \\ 2\left(q_2 q_3 + q_1 q_4\right) \end{bmatrix},$$

$$\mathbf{d}_3 = \frac{1}{|\mathbf{q}|^2}\begin{bmatrix} 2\left(q_1 q_3 + q_2 q_4\right) \\ 2\left(q_2 q_3 - q_1 q_4\right) \\ -q_1^2 - q_2^2 + q_3^2 + q_4^2 \end{bmatrix}.$$

Then, the expressions for the derivative take the form

$$\frac{\partial \mathbf{d}_1}{\partial \mathbf{q}} = \frac{2}{|\mathbf{q}|^2}\begin{bmatrix} q_1 & -q_2 & -q_3 & q_4, \\ q_2 & q_1 & q_4 & q_3, \\ q_3 & -q_4 & q_1 & -q_2 \end{bmatrix} - \frac{\mathbf{d}_1}{|\mathbf{q}|^4}\begin{bmatrix} q_1 & q_2 & q_3 & q_4 \end{bmatrix},$$

$$\frac{\partial \mathbf{d}_2}{\partial \mathbf{q}} = \frac{2}{|\mathbf{q}|^2}\begin{bmatrix} q_2 & q_1 & -q_3 & -q_4, \\ -q_1 & q_2 & -q_3 & q_4, \\ q_4 & q_3 & q_2 & q_1 \end{bmatrix} - \frac{\mathbf{d}_2}{|\mathbf{q}|^4}\begin{bmatrix} q_1 & q_2 & q_3 & q_4 \end{bmatrix},$$

$$\frac{\partial \mathbf{d}_3}{\partial \mathbf{q}} = \frac{2}{|\mathbf{q}|^2}\begin{bmatrix} q_3 & q_4 & q_1 & q_2, \\ -q_4 & q_3 & q_2 & -q_1, \\ -q_1 & -q_2 & q_3 & q_4 \end{bmatrix} - \frac{\mathbf{d}_3}{|\mathbf{q}|^4}\begin{bmatrix} q_1 & q_2 & q_3 & q_4 \end{bmatrix}.$$

Dichmann et al. (1996) expressed these derivatives elegantly as

$$\left(\frac{\partial \mathbf{d}_1}{\partial \mathbf{q}}\right)^T = \frac{2}{|\mathbf{q}|^2}\mathbf{B}_3\mathbf{q} \otimes \mathbf{d}_2 - \frac{2}{|\mathbf{q}|^2}\mathbf{B}_2\mathbf{q} \otimes \mathbf{d}_3,$$

$$\left(\frac{\partial \mathbf{d}_2}{\partial \mathbf{q}}\right)^T = \frac{2}{|\mathbf{q}|^2}\mathbf{B}_1\mathbf{q} \otimes \mathbf{d}_3 - \frac{2}{|\mathbf{q}|^2}\mathbf{B}_3\mathbf{q} \otimes \mathbf{d}_1,$$

$$\left(\frac{\partial \mathbf{d}_3}{\partial \mathbf{q}}\right)^T = \frac{2}{|\mathbf{q}|^2}\mathbf{B}_2\mathbf{q} \otimes \mathbf{d}_1 - \frac{2}{|\mathbf{q}|^2}\mathbf{B}_1\mathbf{q} \otimes \mathbf{d}_2.$$

The projections of these derivatives on the $\{\mathbf{B}_1\mathbf{q}, \mathbf{B}_2\mathbf{q}, \mathbf{B}_3\mathbf{q}\}$ space by taking the dot-product gives

$$\frac{\partial \mathbf{d}_1}{\partial \mathbf{q}} \cdot \mathbf{B}_1\mathbf{q}/2 = \mathbf{0}, \qquad \frac{\partial \mathbf{d}_1}{\partial \mathbf{q}} \cdot \mathbf{B}_2\mathbf{q}/2 = -\mathbf{d}_3, \qquad \frac{\partial \mathbf{d}_1}{\partial \mathbf{q}} \cdot \mathbf{B}_3\mathbf{q}/2 = \mathbf{d}_2,$$
$$\frac{\partial \mathbf{d}_2}{\partial \mathbf{q}} \cdot \mathbf{B}_1\mathbf{q}/2 = \mathbf{d}_3, \qquad \frac{\partial \mathbf{d}_2}{\partial \mathbf{q}} \cdot \mathbf{B}_2\mathbf{q}/2 = \mathbf{0}, \qquad \frac{\partial \mathbf{d}_2}{\partial \mathbf{q}} \cdot \mathbf{B}_3\mathbf{q}/2 = -\mathbf{d}_1,$$
$$\frac{\partial \mathbf{d}_3}{\partial \mathbf{q}} \cdot \mathbf{B}_1\mathbf{q}/2 = -\mathbf{d}_2, \qquad \frac{\partial \mathbf{d}_3}{\partial \mathbf{q}} \cdot \mathbf{B}_2\mathbf{q}/2 = \mathbf{d}_1, \qquad \frac{\partial \mathbf{d}_3}{\partial \mathbf{q}} \cdot \mathbf{B}_3\mathbf{q}/2 = \mathbf{0}.$$

Appendix C

Hessian Matrices

This appendix presents the expressions for Hessian matrices that appear in the Jacobi equations.

C.1 Hessian matrices of the Elastic Rods

The expressions for the Hessian matrices of the elastic Rods are

$$\frac{\partial^2 H}{\partial \mathbf{q}^2} = \sum_{j=1}^{3} \frac{1}{4\mathbf{K_j}} \mathbf{B}_j \boldsymbol{\mu} \otimes \mathbf{B}_j \boldsymbol{\mu} - \begin{bmatrix} -n_3 & 0 & n_1 & -n_2 \\ 0 & -n_3 & n_2 & n_1 \\ n_1 & n_2 & n_3 & 0 \\ -n_2 & n_1 & 0 & n_3 \end{bmatrix}, \tag{C.1}$$

$$\frac{\partial^2 H}{\partial \mathbf{q} \partial \boldsymbol{\mu}} = \frac{\partial^2 H}{\partial \boldsymbol{\mu} \partial \mathbf{q}}^T = \sum_{j=1}^{3} \frac{1}{4\mathbf{K_j}} \mathbf{B}_j \boldsymbol{\mu} \otimes \mathbf{B}_j \mathbf{q} - \begin{bmatrix} 0 & u_3 & -u_2 & u_1 \\ -u_3 & 0 & u_1 & u_2 \\ u_2 & -u_1 & 0 & u_3 \\ -u_1 & -u_2 & -u_3 & 0 \end{bmatrix}, \tag{C.2}$$

$$\frac{\partial^2 H}{\partial \boldsymbol{\mu}^2} = \sum_{j=1}^{3} \frac{1}{4\mathbf{K_j}} \mathbf{B}_j \mathbf{q} \otimes \mathbf{B}_j \mathbf{q}, \tag{C.3}$$

where u_1, u_2, u_3 are the three components of the strain

$$\mathbf{u} = \mathbf{K}^{-1}\mathbf{m} + \hat{\mathbf{u}},$$

and n_1,n_2 and n_3 are the three components components of constant internal force $\mathbf{n}(s) = \mathbf{F}$ along directors $\mathbf{d_1}, \mathbf{d_2}$ and $\mathbf{d_3}$ respectively.

C.2 Hessian matrices of the Two-Tube CTCR section

The Hessian for this case is similar to the three-tube section, with strains taking the form

$$\mathtt{u} = \mathbf{K_{eff}}^{-1}\mathbf{m} + \tilde{\mathbf{u}},$$

and the effective stiffness $\mathbf{K_{eff}}$

$$\mathbf{K_{eff}} = \mathbf{K^{[1]}} + \mathbf{K^{[2]}} = \begin{bmatrix} K_{11}^{[1]} + K_{11}^{[2]} & 0 & 0 \\ 0 & K_{11}^{[1]} + K_{11}^{[2]} & 0 \\ 0 & 0 & K_{33}^{[1]} + K_{33}^{[2]} \end{bmatrix},$$

where

$$\tilde{\mathbf{u}} = \mathbf{K_{eff}}^{-1} \left(\mathbf{K^{[1]}} \hat{\mathbf{u}}^{[1]} + \mathbf{K^{[2]}} \left(\hat{\mathbf{u}}^{[2]} - \begin{bmatrix} 0 \\ 0 \\ \alpha^{[2]\prime} \end{bmatrix} \right) \right).$$

The expressions for $\alpha^{[2]\prime}$ is given in terms of Hamiltonian phase variables as

$$\alpha^{[2]\prime} = \frac{K_{33}^{[1]} + K_{33}^{[2]}}{K_{33}^{[1]} K_{33}^{[2]}} \beta^{[2]} - \frac{m_3}{K_{33}^{[1]}} + \hat{u}_3^{[2]} - \hat{u}_3^{[1]}.$$

$$\frac{\partial^2 H}{\partial \mathbf{q}^2} = \frac{1}{K_{eff1}} \mathbf{B}_1 \boldsymbol{\mu} \otimes \mathbf{B}_1 \boldsymbol{\mu} + \frac{1}{4K_{eff2}} \mathbf{B}_2 \boldsymbol{\mu} \otimes \mathbf{B}_2 \boldsymbol{\mu} + \frac{1}{4K_{eff3}} \mathbf{B}_3 \boldsymbol{\mu} \otimes \mathbf{B}_3 \boldsymbol{\mu} - \begin{bmatrix} -n_3 & 0 & n_1 & -n_2 \\ 0 & -n_3 & n_2 & n_1 \\ n_1 & n_2 & n_3 & 0 \\ -n_2 & n_1 & 0 & n_3 \end{bmatrix},$$

$$\frac{\partial^2 H}{\partial \boldsymbol{\mu}^2} = \frac{1}{4\mathbf{K_{eff_1}}} \mathbf{B}_1 \mathbf{q} \otimes \mathbf{B}_1 \mathbf{q} + \frac{1}{4\mathbf{K_{eff_2}}} \mathbf{B}_2 \mathbf{q} \otimes \mathbf{B}_2 \mathbf{q} + \frac{1}{4\mathbf{K_{eff_3}}} \mathbf{B}_3 \mathbf{q} \otimes \mathbf{B}_3 \mathbf{q},$$

$$\frac{\partial^2 H}{\partial \boldsymbol{\alpha}^2} == -\frac{K_{11}^{[1]} K_{11}^{[2]}}{K_{11}^{[1]} + K_{11}^{[2]}} \hat{u}_1^{[1]} \hat{u}_1^{[2]} \cos \alpha^{[2]} + \frac{K_{11}^{[2]} \hat{u}_1^{[2]}}{K_{11}^{[1]} + K_{11}^{[2]}} (m_1 \cos \alpha^{[2]} + m_2 \sin \alpha^{[2]}),$$

$$\frac{\partial^2 H}{\partial \boldsymbol{\beta}^2} = \frac{1}{K_{33}^{[1]}} + \frac{1}{K_{33}^{[2]}},$$

$$\frac{\partial^2 H}{\partial \mathbf{q} \partial \boldsymbol{\mu}} = \frac{\partial^2 H}{\partial \boldsymbol{\mu} \partial \mathbf{q}}^T = \frac{1}{4\mathbf{K_{eff_1}}} \mathbf{B}_j \boldsymbol{\mu} \otimes \mathbf{B}_j \mathbf{q} + \frac{1}{4\mathbf{K_{eff_2}}} \mathbf{B}_j \boldsymbol{\mu} \otimes \mathbf{B}_j \mathbf{q} + \frac{1}{4\mathbf{K_{eff_3}}} \mathbf{B}_j \boldsymbol{\mu} \otimes \mathbf{B}_j \mathbf{q} - \begin{bmatrix} 0 & u_3 & -u_2 & u_1 \\ -u_3 & 0 & u_1 & u_2 \\ u_2 & -u_1 & 0 & u_3 \\ -u_1 & -u_2 & -u_3 & 0 \end{bmatrix},$$

$$\frac{\partial^2 H}{\partial \mathbf{q} \partial \boldsymbol{\alpha}} = \frac{-K_{11}^{[2]} \hat{u}_1^{[2]}}{\mathbf{K_{eff}}} \left(\hat{u}_1^{[2]} \sin \alpha^{[2]} \mathbf{B}_1 \boldsymbol{\mu} - \hat{u}_1^{[2]} \cos \alpha^{[2]} \mathbf{B}_2 \boldsymbol{\mu} \right),$$

$$\frac{\partial^2 H}{\partial \mathbf{q} \partial \boldsymbol{\beta}} = \mathbf{B}_3 \mathbf{q} / 2K_{33}^{[1]},$$

$$\frac{\partial^2 H}{\partial \boldsymbol{\mu} \partial \boldsymbol{\alpha}} = \frac{K_{11}^{[2]} \hat{u}_1^{[2]}}{\mathbf{K_{eff}}} \left(\hat{u}_1^{[2]} \sin \alpha^{[2]} \mathbf{B_1 q} - \hat{u}_1^{[2]} \cos \alpha^{[2]} \mathbf{B_2 q} \right),$$
$$\frac{\partial^2 H}{\partial \boldsymbol{\mu} \partial \boldsymbol{\beta}} = -\mathbf{B}_3 \boldsymbol{\mu} / 2 K_{33}^{[1]},$$
$$\frac{\partial^2 H}{\partial \boldsymbol{\alpha} \partial \boldsymbol{\beta}} = \mathbf{0}.$$

C.3 Hessian Matrices of the Three-Tube CTCR section

The Hessian for this case is similar to the three-tube section, with strain $\mathbf{u}$ taking the form

$$\mathbf{u} = \mathbf{K_{eff}}^{-1} \mathbf{m} + \tilde{\mathbf{u}},$$

and the effective stiffness $\mathbf{K_{eff}}$ as

$$\mathbf{K_{eff}} = \mathbf{K^{[1]}} + \mathbf{K^{[2]}} + \mathbf{K^{[3]}} = \begin{bmatrix} K_{11}^{[1]} + K_{11}^{[2]} + K_{11}^{[3]} & 0 & 0 \\ 0 & K_{11}^{[1]} + K_{11}^{[2]} + K_{11}^{[3]} & 0 \\ 0 & 0 & K_{33}^{[1]} + K_{33}^{[2]} + K_{33}^{[3]} \end{bmatrix},$$

where

$$\tilde{\mathbf{u}} = \mathbf{K_{eff}}^{-1} \left(\mathbf{K}^{[1]} \hat{\mathbf{u}}^{[1]} + \mathbf{K}^{[2]} \left(\hat{\mathbf{u}}^{[2]} - \begin{bmatrix} 0 \\ 0 \\ \alpha^{[2]\prime} \end{bmatrix} \right) + \mathbf{K}^{[3]} \left(\hat{\mathbf{u}}^{[2]} - \begin{bmatrix} 0 \\ 0 \\ \alpha^{[3]\prime} \end{bmatrix} \right) \right).$$

The expressions for $\alpha^{[2]\prime}$ and $\alpha^{[3]\prime}$ in terms of Hamiltonian phase variables are

$$\alpha^{[2]\prime} = \frac{\beta^{[2]} + \beta^{[3]}}{K_{33}^{[1]}} - \frac{m_3}{K_{33}^{[1]}} + \frac{\beta^{[2]}}{K_{33}^{[2]}} + \hat{u}_3^{[2]} - \hat{u}_3^{[1]},$$
$$\alpha^{[3]\prime} = \frac{\beta^{[2]} + \beta^{[3]}}{K_{33}^{[1]}} - \frac{m_3}{K_{33}^{[1]}} + \frac{\beta^{[3]}}{K_{33}^{[3]}} + \hat{u}_3^{[3]} - \hat{u}_3^{[1]}.$$

Then, the Hessian matrices are given by

$$\frac{\partial^2 H}{\partial \mathbf{q}^2} = \frac{1}{4\mathbf{K_{eff_1}}} \mathbf{B}_1 \boldsymbol{\mu} \otimes \mathbf{B}_1 \boldsymbol{\mu} + \frac{1}{4\mathbf{K_{eff_2}}} \mathbf{B}_2 \boldsymbol{\mu} \otimes \mathbf{B}_2 \boldsymbol{\mu} + \frac{1}{4\mathbf{K_{eff_3}}} \mathbf{B}_3 \boldsymbol{\mu} \otimes \mathbf{B}_3 \boldsymbol{\mu} - \begin{bmatrix} -n_3 & 0 & n_1 & -n_2 \\ 0 & -n_3 & n_2 & n_1 \\ n_1 & n_2 & n_3 & 0 \\ -n_2 & n_1 & 0 & n_3 \end{bmatrix},$$
$$\frac{\partial^2 H}{\partial \boldsymbol{\mu}^2} = \frac{1}{4\mathbf{K_{eff_1}}} \mathbf{B}_1 \mathbf{q} \otimes \mathbf{B}_1 \mathbf{q} + \frac{1}{4\mathbf{K_{eff_2}}} \mathbf{B}_2 \mathbf{q} \otimes \mathbf{B}_2 \mathbf{q} + \frac{1}{4\mathbf{K_{eff_3}}} \mathbf{B}_3 \mathbf{q} \otimes \mathbf{B}_3 \mathbf{q},$$

$$\frac{\partial^2 H}{\partial \boldsymbol{\alpha}^2} = \begin{bmatrix} H_{\alpha^{[2]}\alpha^{[2]}} & H_{\alpha^{[2]}\alpha^{[3]}} \\ H_{\alpha^{[3]}\alpha^{[2]}} & H_{\alpha^{[3]}\alpha^{[3]}} \end{bmatrix},$$
$$\frac{\partial^2 H}{\partial \boldsymbol{\beta}^2} = \begin{bmatrix} \frac{1}{K_{33}^{[1]}} + \frac{1}{K_{33}^{[2]}} & \frac{1}{K_{33}^{[1]}} \\ \frac{1}{K_{33}^{[1]}} & \frac{1}{K_{33}^{[1]}} + \frac{1}{K_{33}^{[3]}} \end{bmatrix},$$

where

$$\begin{aligned} H_{\alpha^{[2]}\alpha^{[2]}} &= -\frac{K_{11}^{[1]}\hat{u}_1^{[1]}}{\mathbf{K_{eff}}}\left(K_{11}^{[1]}\hat{u}_1^{[1]}\cos(\alpha^{[2]}-\alpha^{[1]}) + K_{11}^{[3]}\hat{u}_1^{[3]}\cos(\alpha^{[2]}-\alpha^{[3]})\right) \\ &\quad + m_1\hat{u}_1^{[2]}\cos\alpha^{[2]} + m_2\hat{u}_1^{[2]}\sin\alpha^{[2]}, \\ H_{\alpha^{[3]}\alpha^{[3]}} &= -\frac{K_{11}^{[1]}\hat{u}_1^{[1]}}{\mathbf{K_{eff}}}\left(K_{11}^{[1]}\hat{u}_1^{[1]}\cos(\alpha^{[2]}-\alpha^{[1]}) + K_{11}^{[3]}\hat{u}_1^{[3]}\cos(\alpha^{[2]}-\alpha^{[3]})\right) \\ &\quad + m_1\hat{u}_1^{[3]}\cos\alpha^{[3]} + m_2\hat{u}_1^{[3]}\sin\alpha^{[3]}, \\ H_{\alpha^{[2]}\alpha^{[3]}} &= -\frac{K_{11}^{[2]}K_{11}^{[3]}\hat{u}_1^{[2]}\hat{u}_1^{[3]}\cos(\alpha^{[2]}-\alpha^{[3]})}{\mathbf{K_{eff}}}, \end{aligned}$$

$$\frac{\partial^2 H}{\partial \mathbf{q}\partial \boldsymbol{\mu}} = \frac{\partial^2 H}{\partial \boldsymbol{\mu}\partial \mathbf{q}}^T = \frac{1}{4\mathbf{K_{eff_1}}}\mathbf{B}_j\boldsymbol{\mu}\otimes\mathbf{B}_j\mathbf{q} + \frac{1}{4\mathbf{K_{eff_2}}}\mathbf{B}_j\boldsymbol{\mu}\otimes\mathbf{B}_j\mathbf{q}\frac{1}{4\mathbf{K_{eff_3}}}\mathbf{B}_j\boldsymbol{\mu}\otimes\mathbf{B}_j\mathbf{q} - \begin{bmatrix} 0 & u_3 & -u_2 & u_1 \\ -u_3 & 0 & u_1 & u_2 \\ u_2 & -u_1 & 0 & u_3 \\ -u_1 & -u_2 & -u_3 & 0 \end{bmatrix},$$

$$\begin{aligned} \frac{\partial^2 H}{\partial \mathbf{q}\partial \alpha^{[2]}} &= \left[\frac{-K_{11}^{[2]}\hat{u}_1^{[2]}}{\mathbf{K_{eff}}}\left(\hat{u}_1^{[2]}\sin\alpha^{[2]}\mathbf{B}_1\boldsymbol{\mu} - \hat{u}_1^{[2]}\cos\alpha^{[2]}\mathbf{B}_2\boldsymbol{\mu}\right)\right], \\ \frac{\partial^2 H}{\partial \mathbf{q}\partial \alpha^{[3]}} &= \left[\frac{-K_{11}^{[3]}\hat{u}_1^{[3]}}{\mathbf{K_{eff}}}\left(\hat{u}_1^{[3]}\sin\alpha^{[3]}\mathbf{B}_1\boldsymbol{\mu} - \hat{u}_1^{[3]}\cos\alpha^{[3]}\mathbf{B}_2\boldsymbol{\mu}\right)\right], \\ \frac{\partial^2 H}{\partial \mathbf{q}\partial \boldsymbol{\beta}} &= \left[\mathbf{B}_3\mathbf{q}/2K_{33}^{[1]} \quad \mathbf{B}_3\mathbf{q}/2K_{33}^{[1]}\right], \\ \frac{\partial^2 H}{\partial \boldsymbol{\mu}\partial \alpha^{[2]}} &= \left[\frac{K_{11}^{[2]}\hat{u}_1^{[2]}}{\mathbf{K_{eff}}}\left(\hat{u}_1^{[2]}\sin\alpha^{[2]}\mathbf{B}_1\mathbf{q} - \hat{u}_1^{[2]}\cos\alpha^{[2]}\mathbf{B}_2\mathbf{q}\right)\right], \\ \frac{\partial^2 H}{\partial \boldsymbol{\mu}\partial \alpha^{[3]}} &= \left[\frac{K_{11}^{[3]}\hat{u}_1^{[3]}}{\mathbf{K_{eff}}}\left(\hat{u}_1^{[3]}\sin\alpha^{[3]}\mathbf{B}_1\mathbf{q} - \hat{u}_1^{[3]}\cos\alpha^{[3]}\mathbf{B}_2\mathbf{q}\right)\right], \\ \frac{\partial^2 H}{\partial \boldsymbol{\mu}\partial \boldsymbol{\beta}} &= \left[-\mathbf{B}_3\boldsymbol{\mu}/2K_{33}^{[1]} \quad -\mathbf{B}_3\boldsymbol{\mu}/2K_{33}^{[1]}\right], \\ \frac{\partial^2 H}{\partial \boldsymbol{\alpha}\partial \boldsymbol{\beta}} &= \begin{bmatrix} 0 & 0 \\ 0 & 0 \end{bmatrix}. \end{aligned}$$

Appendix D

Code Availability

The examples presented in the thesis were implemented either using *AUTO-07p* or *Matlab-R2023b*. The codes utilized for them are available at `https://github.com/chekri/PhD_Thesis`. The examples featured in parts 1 and 2 of the thesis, focusing on *parameter continuation*, have been implemented using *AUTO-07p*. The software package *AUTO-07p* can be easily installed, and the source file of its latest version was also provided. *AUTO-07p* examples are provided along with the script files, and they can be executed using a single command from terminal. *Python* codes are employed to generate the plots from the obtained solutions, and they are also available here. Detailed instructions on running these programs were also furnished. If further details on these codes are required, contact me at chekri.dsp@gmail.com. The examples featured in part 3 of this thesis, which constitute optimization methodologies have been implemented using *Matlab-R2023b*.

Zusammenfassung

Mithilfe von Variationsrechnung untersuchen wir das Verhalten elastischer Stabtragwerke unter äußeren Lasten, die an einem Ende eingespannt und am anderen Ende frei sind. Die Stabilitätseigenschaften der Gleichgewichte werden unter Verwendung von Bedingungen zweiter Ordnung durch Verallgemeinerung der Jacobi'sche Theorie der konjugierten Punkte analysiert. Der Indexbegriff, der die Dimension des Unterraums der Variationen quantifiziert, über dem die zweite Variation negativ-definit ist, wird auf diese Klasse von Problemen erweitert. Die Variationsstruktur der parameterabhängigen Variationsrechnung wird ausgenutzt, um die Änderungen des Index an den Falten in *Spezielle Bifurkationsdiagramme* vorherzusagen. Wir verallgemeinern diese Diagramme auf Probleme mit aktuellen feste-frei Enden. Außerdem untersuchen wir die Stabilität von Variationsproblemen mit diskontinuierlichen Integranden, indem wir das Konzept der konjugierten Punkte, des Index und der *Spezielle Bifurkationsdiagramme* auf diese erweitern. Zu diesem Zweck werden Anpassungsbedingungen zweiter Ordnung an den Unstetigkeitsstellen hergeleitet.

Diese Techniken werden mit dem Ziel entwickelt, sie in Soft-Roboter-Anwendungen einzusetzen, einem Bereich, der zunehmend an Beliebtheit gewinnt. Einige Anwendungen wie Concentric Tube Continuum Robots (CTCRs), verwenden intrinsisch gekrümmte Stäbe, um flexible Mechanismen zu erzeugen. Das Zusammenspiel von geometrischen Nichtlinearitäten, externen Lasten und intrinsischer Krümmung führt zu faszinierendem und komplexem Verhalten, wie z.B. der Snap-Back-Instabilität. Die Untersuchung der Abhängigkeit dieses Verhaltens von Parametern wie Eigenkrümmung, Länge, Spitzenlast und Hebelarm der Last hilft bei der effizienten Nutzung in praktischen Anwendungen. Wir erweitern diese Untersuchung auf CTCRs, die einem in sich gekrümmten elastischen Stab ähneln, aber eine etwas andere Physik aufweisen. Diese Forschung hilft bei der Entwicklung und Steuerung von Robotern für komplexere Aufgaben. Diese Roboter bestehen aus mehreren Abschnitten und ihre Eigenschaften ändern sich abrupt an den Grenzen der einzelnen Abschnitte.

Schließlich wird eine gradientenbasierte Navigation mit offenem Regelkreis eingesetzt, um das Robotermanöver mit optimalen Kontrollmethoden zu modellieren. Mit diesem Ansatz werden mehrere komplexe Aufgaben in Form von Zielfunktionen quantifiziert, die optimiert werden. Wir betrachten die optimale Steuerung von CTCRs, die über Pseudozeit parametrisiert sind, und konzentrieren uns dabei auf die Minimierung des Arbeitsvolumens des Roboters während seines Betriebs. Eine numerische Strategie zur Durchführung der resultierenden Optimierung wird ebenfalls vorgestellt.

Selbstständigkeitserklärung

Name: Dhanakoti
Vorname: Siva Prasad Chakri

Ich erkläre gegenüber der Freien Universität Berlin, dass ich die vorliegende Dissertation selbstständig und ohne Benutzung anderer als der angegebenen Quellen und Hilfsmittel angefertigt habe. Die vorliegende Arbeit ist frei von Plagiaten. Alle Ausführungen, die wörtlich oder inhaltlich aus anderen Schriften entnommen sind, habe ich als solche kenntlich gemacht. Diese Dissertation wurde in gleicher oder ähnlicher Form noch in keinem früheren Promotionsverfahren eingereicht.

Mit einer Prüfung meiner Arbeit durch ein Plagiatsprüfungsprogramm erkläre ich mich einverstanden.

.....
Siva Prasad Chakri Dhanakoti,
Berlin, 18 July 2023.